ISSN 0016-2523

FUJITSU

SCIENTIFIC & TECHNICAL JOURNAL

Spring 1992 VOL. 28, NO. 1

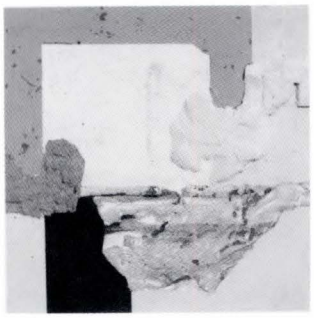

The Issue's Cover :
ZONA CONFINARIA (Boundary Zone)
by Junroh MANABE

FUJITSU Scientific & Technical Journal is published quarterly by FUJITSU LIMITED of Japan to report the results of research conducted by FUJITSU LIMITED, FUJITSU LABORATORIES LTD., and their associated companies in communications, electronics, and related fields. It is the publisher's intent that FSTJ will promote the international exchange of such information, and we encourage the distribution of FSTJ on an exchange basis. All correspondence concerning the exchange of periodicals should be addressed to the editor.

FSTJ can be purchased through KINOKUNIYA COMPANY LTD., 38-1, Sakuragaoka 5-Chome, Setagaya-ku, Tokyo 156, Japan, (Telephone : +81-3-3439-0162, Facsimile : +81-3-3706-7479).

The price is US$7.00 per copy, excluding postage.

FUJITSU LIMITED 1015 Kamikodanaka, Nakahara-ku,
Kawasaki 211, Japan
Cable Address : FUJITSULIMITED KAWASAKI
Telephone : +81-44-777-1111
Facsimile : +81-44-754-3562

Printed by MIZUNO PRITECH Co., Ltd. in Japan

FUJITSU

SCIENTIFIC & TECHNICAL JOURNAL

Spring 1992 VOL. 28, NO. 1

CONTENTS

UDC 548-144:681.327
FUJITSU Sci. Tech. J., **28**, 1, pp. 1-12(1992)

Liquid Crystal Large Screen Projection Displays

• Akihiro Mochizuki • Yasuhiro Yoneda • Toshiaki Narusawa

A liquid crystal large screen projection display for presentations is reviewed. Two types of addressing mode, an optically addressed and an electrically addressed projection display are introduced. Several types of electrically addressed liquid crystals are possible for the presentation device. Those currently available include the supertwisted nematic (STN) and nematic-cholesteric phase transition (NCPT) liquid crystal projectors. The applications of these for a still image display device are compared.

UDC 548.52:621.315.5
FUJITSU Sci. Tech. J., **28**, 1, pp. 13-49(1992)

Recent Advances in the Application of Transmission Electron Microscopy to the Evaluation of III-V Compound Semiconductor Thin Films

• Osamu Ueda

This paper reviews recent advances in the application of transmission electron microscopy to the evaluation of structures, interfaces and defects in compound semiconductor thin films. It has been shown microscopically for the first time that the growth of $(GaAs)_m/(GaP)_n$ strained layer superlattices by atomic layer epitaxy proceeds in a precisely layer-by-layer manner. Detailed characterizations of interfaces and defects in AlAs, GaAs and GaP on Si, also GaAsSb and Fe-doped InP on InP are described; later, the mechanisms which generate such defects and techniques for their elimination are discussed. Studies of atomic ordering in InGaP and InGaAs are presented, with reference to the mechanisms which generate ordered structures and their influence on the properties of the material.

UDC 621.315.55:621.375.826
FUJITSU Sci. Tech. J., **28**, 1, pp. 50-61(1992)

Pulsed-Jet Epitaxy of III-V Compounds

• Masashi Ozeki • Nobuyuki Ohtsuka • Yoshiki Sakuma

Pulsed-jet epitaxy (PJE) for III-V compounds (GaAs, InP, GaP, and InAs) and its possibilities for process technology are described. A model involving selective reactions has been proposed to explain the self-limiting process in PJE. A reduction of carbon contamination has been achieved for GaAs growth using PJE and carrier concentrations ranging from 10^{14} cm^{-3} to 10^{20} cm^{-3} for *n*-type GaAs, and from 10^{15} cm^{-3} to 10^{21} cm^{-3} for *p*-type GaAs. These can be obtained by controlling growth conditions and doping levels. The growth of $(GaAs)_m(GaP)_n$ superlattices has demonstrated the high potential of PJE in superlattice growth. PJE offers unique possibilities for low temperature growth, selective growth, and uniform thickness growth.

UDC 548.522:621.315.55
FUJITSU Sci. Tech. J., **28**, 1, pp. 62-97(1992)

Metalorganic Vapor Phase Epitaxy Using Organic Group-V Sources

• Toshihide Kikkawa • Hitoshi Tanaka • Junji Komeno

Safer MOVPE growth of GaAs, AlGaAs, and InGaAs on 3-inch GaAs substrates was investigated using organic group-V sources.

Tertiarybutylarsine (TBAs) and monoethylarsine (EtAs) were used with a horizontal atmospheric pressure reactor. GaAs and AlGaAs grown using TBAs were of high purity and extremely uniform, equivalent to those using arsine. With either silane or disilane doping, Si incorporation efficiency using TBAs or EtAs was always higher than that using arsine. The group-V pyrolysis simulation implies that H_2AsSiH_3 dominates in the gas phase when using TBAs, corresponding to high doping efficiency. High quality, high electron-mobility transistors were achieved with TBAs. These results verify that epitaxial layers grown using TBAs are of sufficiently high quality for device applications.

UDC 621.3.049.73:681.327.17
FUJITSU Sci. Tech. J., **28**, 1, pp. 98-106(1992)

Molecular Dynamics Simulation on an AP1000 Distributed Memory Parallel Computer

• Hiroyuki Sato • Yasumasa Tanaka • Toru Yao

Parallel processing techniques have been applied to the molecular dynamics calculation module of AMBER developed by the University of California. The target machine is the AP1000 distributed memory parallel computer developed at Fujitsu Laboratories Limited. AP1000 consists of up to 1 024 processor elements connected with three different networks. To obtain a higher degree of parallelism and better load balance between processors, a particle division method was developed to randomly allocate particles to processors. Experiments showed that a problem with 41 095 atoms can be processed 226 times faster with a 512-processor AP1000 than by one processor.

UDC 548.52:621.315.5
FUJITSU Sci. Tech. J., **28**, 1, pp. 107-114(1992)

Automated Visual Inspection System for Bonded IC Wires

• Hiroyuki Tsukahara • Masato Nakashima
• Takehisa Sugawara

This paper discusses an automated visual inspection system for bonded IC wires. The system uses high-contrast image capture, an algorithm for accurately measuring the bonding balls, and a wire inspection algorithm. The high-contrast image capture system consists of a wide-area camera and two types of lighting optics, one for ball sensing and the other for wire sensing. The algorithm for measuring the bonding balls is based on morphological techniques, and the wire inspection algorithm is based on a border following algorithm. The automated inspection system measures ball diameters to within ±5 μm accuracy, which corresponds to half a pixel of the captured picture. The system takes 0.2 seconds to inspect a wire and ball. Combining the inspection system with an automatic wire bonder enables a fully automatic bonding system.

UDC 577.322:681.32
FUJITSU Sci. Tech. J., **28**, 1, pp. 115-121(1992)

Low Drive Voltage and Low Chirp Modulator Integrated DFB Laser Light Source for Multiple-gigabit Systems

• Toru Watanabe • Keiji Sato • Haruhisa Soda

This paper discusses a low drive voltage and low chirp modulator integrated DFB laser (MI-DFB laser). In this research, the composition of the absorption layer was adjusted experimentally to obtain a low drive voltage, and the absorption layer thickness was analytically optimized. The drive voltage for an extinction ratio of -13 dB is found to be -3 V, which is small enough for high-speed IC drivers. A SiN film on the front facet is optimized for an antireflective (AR) coat, and gives a low chirp width of 0.016 nm at -15 dB (0.004 nm at -3 dB) under 10 Gbit/s NRZ pseudo random modulation. The low drive voltage and low chirp performance is promising for use in the next generation of multiple-gigabit long-haul optical fiber transmission systems.

UDC 548-144:681.327

Liquid Crystal Large Screen Projection Displays

• Akihiro Mochizuki • Yasuhiro Yoneda • Toshiaki Narusawa

(Manuscript received September 9, 1991)

A liquid crystal large screen projection display for presentations is reviewed.
Two types of addressing mode, an optically addressed and an electrically addressed projection display are introduced. Several types of electrically addressed liquid crystals are possible for the presentation device. Those currently available include the supertwisted nematic (STN) and nematic-cholesteric phase transition (NCPT) liquid crystal projectors.
The applications of these for a still image display device are compared.

1. Introduction

Large projection displays are currently popular for presentations, public announcements, and showing moving pictures. For presentations, a liquid crystal display (LCD) pad is now commonly used together with a personal computer and an overhead projector. The LCD pad can conveniently be used with a conventional overhead projector and a personal computer, this kind of system may be called an electronic overhead projector (EOHP). Since the LCD pad is light and thin, it can easily be carried and by using the simple optical system of an overhead projector, a low cost LCD projector is possible. However, such a display requires high information content, high resolution, a large display area, a high luminance screen and good compatibility with various office automation equipment. To meet these demands, we proposed a projection display using nematic-cholesteric phase transition (NCPT) type liquid crystals[1]. Consequently, several types of liquid crystal projection display for EOHPs have been proposed and realized[2)-5)]. The most popular liquid crystal projection display is the so-called electronic overhead projector using a supertwisted nematic (STN) LCD, and this projection display is quite portable. A high resolution projection display using laser beam addressed smectic liquid crystals is now also available.

Despite such progress, the liquid crystal projection display is still in the development stage due to such drawbacks as poor screen luminance and information content. We have proposed and achieved an NCPT projection display which overcomes these drawbacks. We now compare and discuss the characteristics of the several types of liquid crystal large screen projection displays, particularly those used for meetings, education, conferences and public announcements.

2. LCD modes for projection displays

Several types of liquid crystal drive mode are first introduced, then the advantages and disadvantages of the LCDs for EOHP applications are discussed.

Liquid crystal projection displays can be classified into two types, an optically addressed LCD projector, and an electrically addressed LCD projector. Generally, the laser beam addressed type offers higher information content and a higher luminance screen image than the electrically addressed type. However, the electrically addressed type is more compact and less expensive.

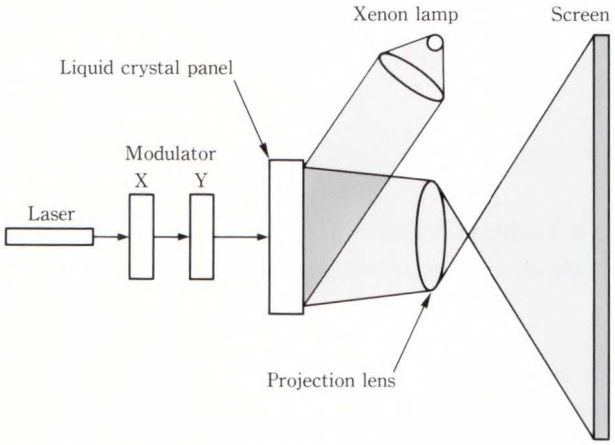

Fig. 1—Structure of laser beam addressed liquid crystal projection display system.

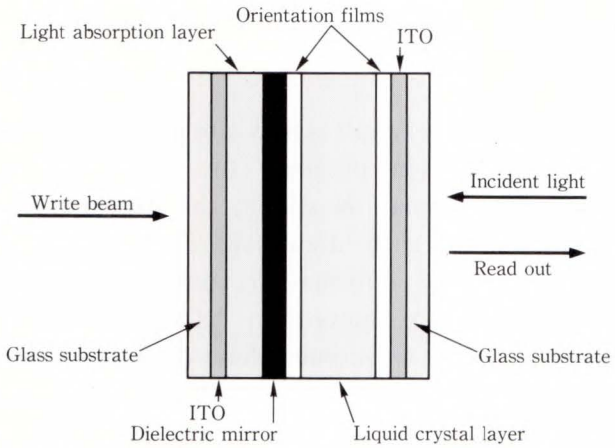

Fig. 2—Structure of liquid crystal panel for laser beam addressed display.

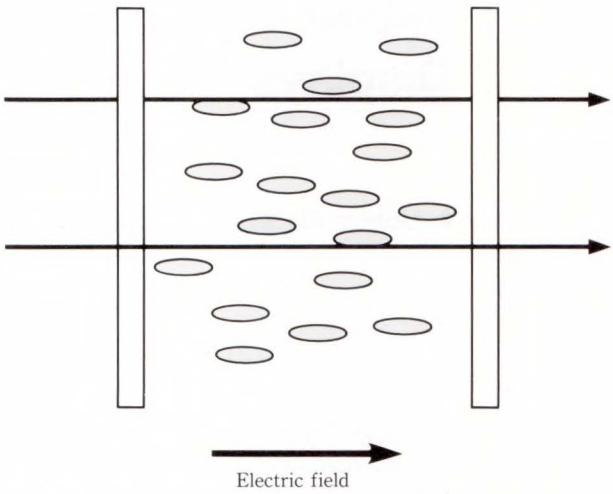

Fig. 3—Liquid crystal molecular alignment of the laser beam addressed projection system: Transparent state.

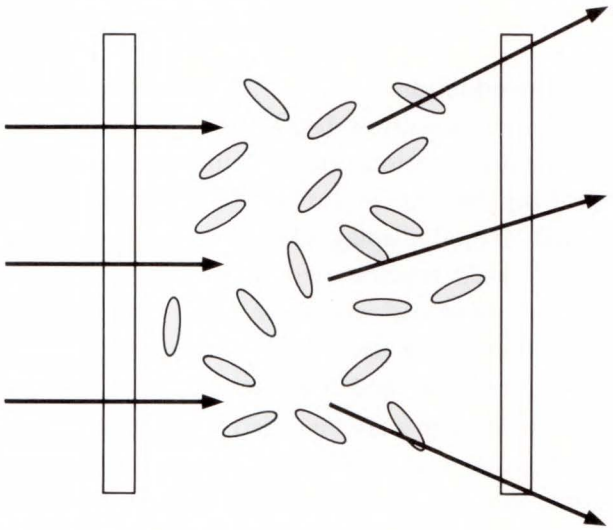

Fig. 4—Liquid crystal molecular alignment of the laser beam addressed projection system: Scattering state.

2.1 Optically addressed projector

2.1.1 Laser beam addressed projector

In 1972, Kahn, F.J. proposed a laser beam addressed projection display using cholesteric liquid crystals[6),7)]. Since then, improvements have been made for this type. Currently, smectic A and C phase liquid crystals are used for this type of projection display. Figure 1 shows the structure of the projection display system and Fig. 2 shows the structure of the liquid crystal display. The laser beam addressed liquid crystal projector uses phase transition induced by thermal transfer from the laser beam to the liquid crystals. The projector is initially transparent since the liquid crystal alignment in the panel is homeotropic as shown in Fig. 3.

The laser beam is scanned to a particular point in the panel, and the liquid crystal at that point is heated to the isotropic phase. When an electric field is applied to the panel and the laser beam removed, the heated liquid crystal cools with a parallel molecular alignment, giving a transparent state. When an electric field is not applied, the liquid crystal alignment becomes irregular with no alignment force during the cooling process, resulting in the light scattering as shown in Fig. 4.

The transparent and light scattering states are projected on to a large screen by the reflective optical system shown in Fig. 1. In this sys-

tem, the transparent state in the liquid crystal panel provides a bright image on the screen and the scattering state provides a dark image. Color images can be provided by using color filters.

The advantages of this display are a bright screen, high resolution and high information content. The laser beam addressed system uses light scattering induced by thermal transfer, thus there is no need to use polarizers which reduce the screen luminance. Also, since the laser beam addressed system uses the liquid crystal's memory effect, which preserves both light transparent and scattering states, there is no limitation to the information content. A system with nine million pixels was proposed by Usubuchi in 1987[8]. However, the speed of writing is slow, and the system is heavy and bulky, and thus expensive. Laser beam addressing works one point at a time, thus the writing time is proportional to the number of pixels. To write nine million pixels, for instance, it takes 10 μs times nine million, or 90 s for a whole screen. Furthermore, heat transfer from the laser beam to the liquid crystal requires a high power laser; rapid heat transfer requires a several hundred mW class laser. The laser beam scanning requires beam transducers and beam modulators, and these make the liquid crystal projection system bulky and expensive.

The laser beam addressed liquid crystal projector has an extremely high information content and resolution with a bright screen, and it produces shades of gray by dithering. Such a high resolution image with gray shades is considered suitable for computer aided design (CAD) displays. To improve the writing speed, a laser beam addressed system using a chiralsmetic C phase liquid crystal has been proposed by Bone[9]. The fast response of the chiralsmetic C phase liquid crystal and the limited information content combine to achieve a video rate liquid crystal projection display. Moreover, the contrast ratio of this display is as high as 100:1 due to the higher order liquid crystal molecular alignment of the chiralsmetic C phase.

2.1.2 CRT addressed projector

A CRT addressed liquid crystal projector has been proposed for moving picture images by

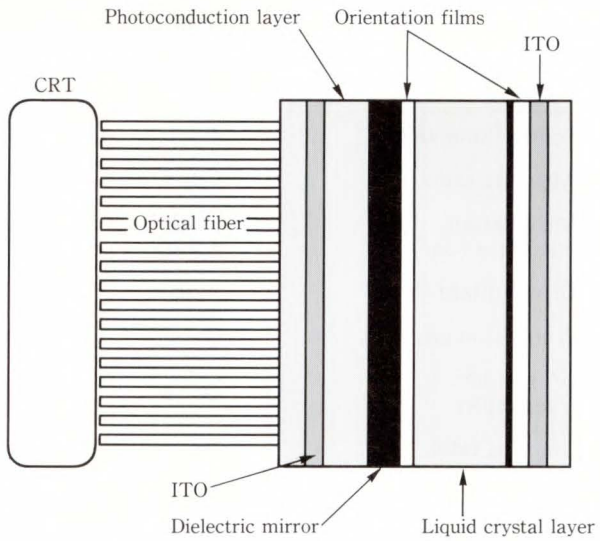

Fig. 5—Structure of CRT addressed liquid crystal projector.

Koda[10]. The structure of the liquid crystal panel is the same as the laser beam addressed projector, but the writing method is different. This system uses the rapid scanning of a CRT beam to give a moving picture. While CRT addressing can produce video rate projection, the resolution is not so good because of divergence of the CRT beam. To suppress beam divergence, an optical fiber guide was used between the CRT and LCD, as shown in Fig. 5. Using the optical fiber guide, Koda realized a 640 x 480 pixel video rate liquid crystal projector. The liquid crystal panel used tunable birefringence with a dielectrically positive anisotropy nematic liquid crystal material. This mode requires two polarizers. Thus the screen luminance is as low as a conventional twisted nematic liquid crystal display and the CRT writing equipment makes it a rather heavy and bulky system.

This display is being used for a spatial light modulator (SLM) with optical processability in conjunction with an optical fiber guide. SLMs have great potential optically addressed liquid crystal devices for optical switching systems.

2.2 Electrically addressed LC projector

There are several types of electrically addressed liquid crystal projector. Generally, the electrically addressed projector is smaller and lighter than the optically addressed projector,

Table 1. Electrically addressed liquid crystal drive modes for a projection display

	STN	DAP	SH	NCPT	Ferroelectric	AM-TN
Screen luminance	Poor	Poor	Poor	Excellent	Fair	Poor
Aperture ratio	Good	Good	Good	Good	Good	Fair
Information content (dot)	640 × 480	1 200 × 1 000	≥640 × 480	≥2 240 × 2 240	≥2 000 × 2 000	1 200 × 1 000
Drive voltage (V)	20	60	60	25	25	10
Production cost	Good	Fair	Fair	Good	Fair	Poor
Gray shade capability	Good	Good	Good	Good	Good	Excellent
Contrast ratio	Good	Good	Good	Good	Fair	Excellent
Video rate display capability	Poor	Poor	Fair	Poor	Fair	Good

and is thus suitable for EOHPs.

In principle every liquid crystal drive mode can be used in the liquid crystal projector. Several electrically addressed liquid crystal drive modes which are suitable for projection display are introduced below. The advantages and disadvantages of each liquid crystal drive mode are summarized in Table 1.

2.2.1 Tunable birefringence mode

In this mode, the liquid crystal molecular alignment is controlled by an electric field. The liquid crystal's birefringence changes as its alignment changes, and this property is used for polarized light switching. A dielectrically positive nematic liquid crystal material is used with homogeneous alignment, a dielectrically negative liquid crystal material is used with homeotropic alignment. A hybrid molecular alignment panel, whose upper substrate has homeotropic alignment and lower substrate has homogeneous alignment, also demonstrates the tunable birefringence effect[11].

1) Nematic LC with homogeneous alignment

In this liquid crystal molecular alignment, a dielectrically positive liquid crystal material is used. The most popular device of this type is supertwisted birefringence effect (SBE) or supertwisted nematic (STN) LCDs. The liquid crystal's birefringence is controlled by an external applied voltage. The transmission of incident light is controlled by the retardation Δnd of the liquid crystal which is sandwiched between two polarizers. The STN type of liquid crystal is now used for projection displays, and its relatively high information content makes it attractive for presentation displays. Some of the STN projection systems are well designed and equipped with sophisticated devices, a detailed discussion is given in the next chapter.

2) Nematic LC with homeotropic alignment

This type of LCD makes use of the deformation of the vertical aligned phase (DAP)[12]. It uses a dielectrically negative liquid crystal material with homeotropic alignment. When there is no applied voltage, linearly polarized incident light passes through the liquid crystal medium with no polarization change, hence it cannot pass through the polarizer on the viewer's side, and this makes the dark state. When a drive voltage higher than the threshold is applied, the molecular optical axis inclines in proportion to the drive voltage. The polarized axis of the incident light and the molecular optical axis are then no longer coincident, resulting in birefringence of the liquid crystal. This birefringence rotates the polarization axis of the incident light, and the rotational axis allows transmission through the polarizers on the viewer's side. The intensity of the transmitted light is dependent on the external applied voltage.

Tunable birefringence is considered suitable for projection displays. However, the birefringence of liquid crystal material is usually

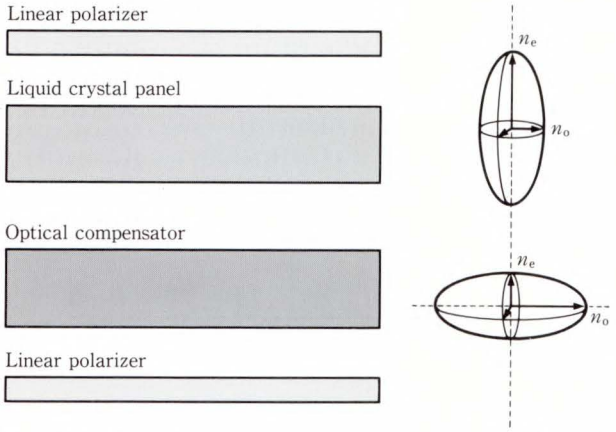

Fig. 6—Display configuration of super homeotropic (SH) mode with optical compensator.

quite sensitive to the ambient temperature, so this mode may need strict temperature control when used for OHP display. However, heat absorption by the two polarizers makes temperature control difficult.

2.2.2 Electrically controlled birefringence mode

Electrically controlled birefringence (ECB) mode with homeotropic alignment has good multiplexing capability, achromaticity and gray scale performance[13] particularly when used for projection. However, the viewing angle of an ECB mode LCD is narrow, thus it is quite difficult to use it for a flat panel display which is viewed directly. This type of LCD may therefore be suitable for projection display[12]. Recently, an ECB mode with an optical compensator has been demonstrated for a direct viewing display[14),15]. The display configuration is shown in Fig. 6. The liquid crystal panel and the optical compensator are sandwiched between crossed polarizers, and the LCD uses a dielectrically negative liquid crystal with homeotropic alignment. This type of LCD is called super homeotropic (SH). Generally when the ECB with homeotropic alignment is perpendicular to the substrate, and crossed polarizers are at 45° to the molecular tilt direction, no birefringence occurs, resulting in the dark state. When an external voltage is applied to the LCD, the liquid crystal molecules tilt and light is transmitted.

However, the molecular alignment of the liquid crystal sometimes deviates from perpendicular to the substrate when an external voltage is applied, due to reverse tilt of the liquid crystal. To avoid this molecular alignment oblique to homeotropic alignment is needed, but this induces both light leakage and a narrow viewing angle, which reduces the legibility. However, a narrow viewing angle is not a disadvantage for projection displays. The fixed optical system of an OHP does not need a wide viewing angle, but light leakage due to deviations reduces the contrast ratio of the display. Light leakage is an intrinsic problem of the ECB types of projection display.

The response of the super homeotropic LCD is rapid compared to tunable birefringence LCDs. The SH LCD also gives a high information content because of the steep threshold in the electrooptical relation. However, this LCD has a high drive voltage, reaching 60 V for a 640 x 400 pixel panel. The high drive voltage raises the cost, particularly for a high information content LCD. However, the ECB mode LCD has a great potential for high contrast projection displays. Further improvements in the materials to overcome both the deviations and the high drive voltage will be quite important to achieve an ECB mode projection display in practice.

2.2.3 Nematic bistable LCDs

Heffner[16] suggested that when a nematic or cholesteric liquid crystal material is placed between two surfaces, the directors can be constrained throughout the cell to certain equilibrium configurations. The configuration of the liquid crystal directors throughout the cell is determined by the surface boundary conditions, the material constants such as helical pitch, and the cell gap. For certain geometries and material parameters, two or more configurations are taken as the solutions to the Oseen-Frank equations[17]. In these configurations, a first-order phase change may occur from the state of higher free energy to the configuration with the lower free energy. This first-order phase change provides the bistable cholesteric twist cell[18].

In this cell, bistability can occur between two topologically equivalent states with differ-

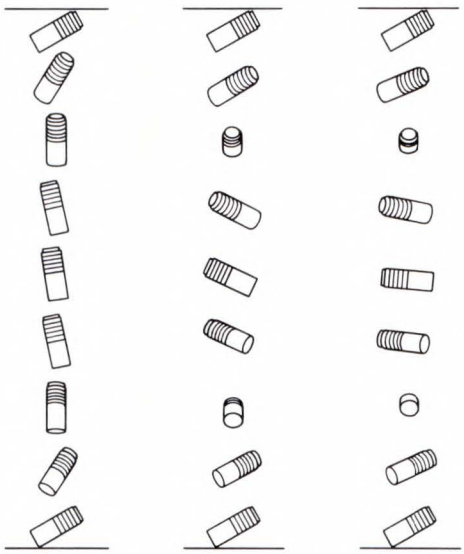

Fig. 7—Nematic bistable configuration. Orientation of molecules in three states of holding voltage cell. The up and down orientations are the two bistable states.

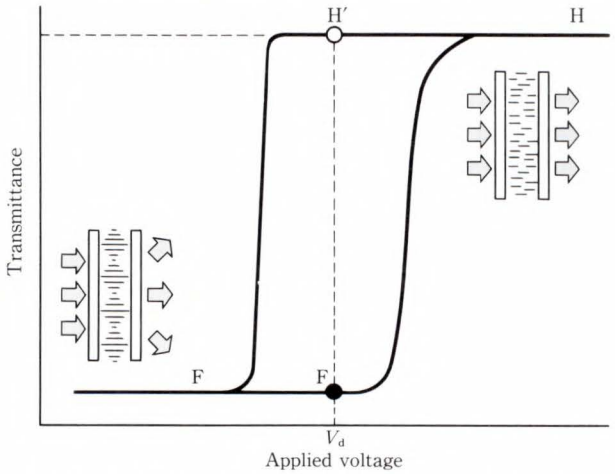

Fig. 8—Electrooptical property of the NCPT liquid crystal display.

ent twist behavior. A dielectrically positive nematic liquid cystal material with added cholesteric liquid crystal is used with pretilted homogeneous alignment. The two states, which are described as *Up* or *Down*, may exist either with *No field* or in the presence of a holding field as shown in Fig. 7. Barberi[19] also reported the nematic bistable configuration. He suggests that the bistability is caused by surface anchoring and flexoelectricity. Sandwiched between two polarizers, these configurations can be used

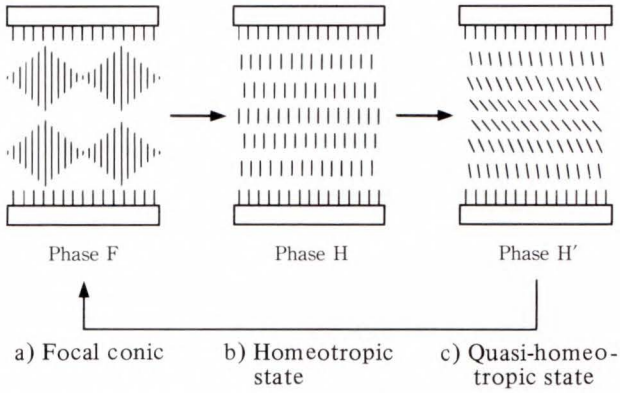

Fig. 9—Liquid crystal molecular alignment of the NCPT display.

for LCDs. However, reliable bistable behavior is required for a practical LCD, and particularly for projection displays, bistability will govern the performance of both the LCD and the liquid crystal projection display.

2.2.4 Nematic-cholesteric phase transition (NCPT) mode

A nematic-cholesteric phase transition type liquid crystal mixture with positive dielectric anisotropy changes state when the applied voltage is increased as shown in Fig. 8. It moves from a cloudy cholesteric state, cholesteric phase F, to a transparent state, nematic phase H. When the voltage is decreased, this mixture moves from phase H to a metastable transparent state, nematic phase H', then to phase F. In phase F, the liquid crystal in the panel has the helical structure shown in Fig. 9a). Because the axis of the helix is parallel to the glass substrates, incident light is scattered, making phase F cloudy. In phase H, the liquid crystal does not have a helical structure but has a homeotropic structure instead, as shown in Fig. 9b). Incident light passes through the homeotropic structure, making phase H transparent. In phase H', the structure of the liquid crystal layer is homeotropic. However, in the center, the liquid crystal molecules are thought to be slightly inclined as shown in Fig. 9c). Phase H' is a metastable state, a supersaturated state. Supersaturation might stabilize hysteresis in the cholesteric-nematic phase transition[1),20)]. Thus the stability of the hysteresis effect is though to be affected by the specific balance between

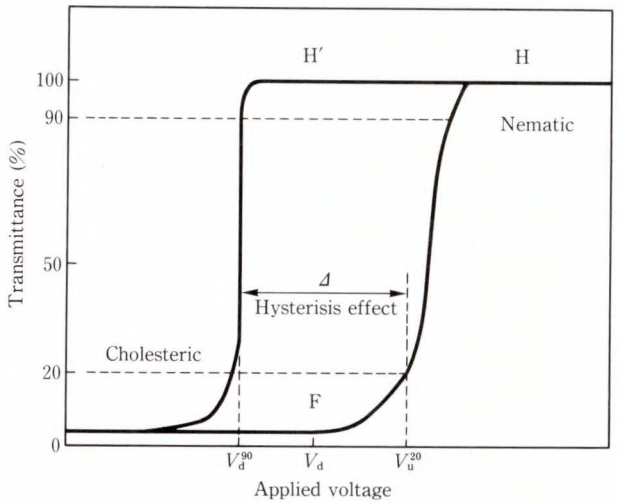

Fig. 10—Bistability of NCPT mode.

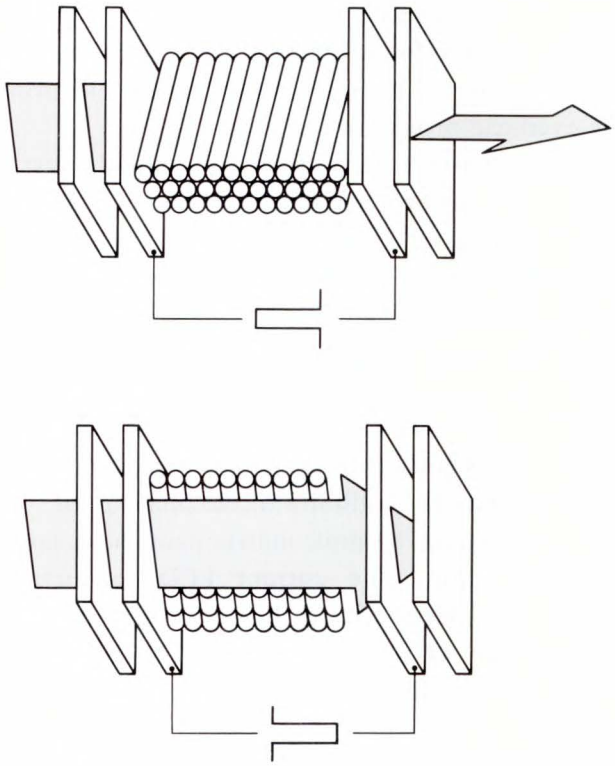

Fig. 11—Bistable projection configurations of the ferroelectric liquid crystal display.

surface anchoring and the thermal properties of the helical structure.

The width of the hysteresis effect is Δ, as shown in Fig. 10. This is the difference between the voltage $V_u{}^{20}$ which gives 20 percent transmittance in the cholesteric to nematic phase transition, and the voltage $V_d{}^{90}$ which gives 90 percent in the nematic to cholesteric phase

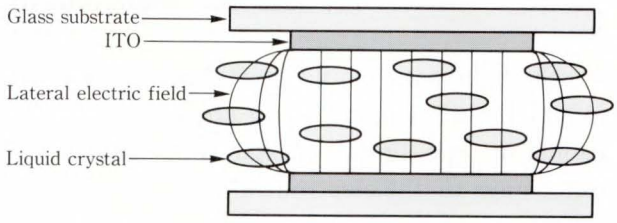

Fig. 12—High resolution mechanism of ferroelectric liquid crystal display.

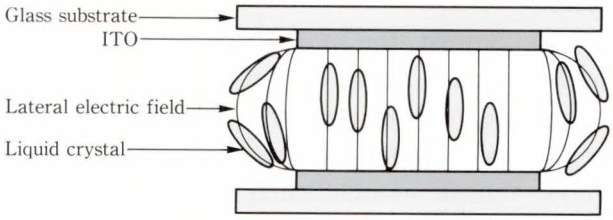

Fig. 13—Nematic liquid crystal molecular alignment along with lateral electric field.

transition. The drive voltage V_d is set between $V_u{}^{20}$ and $V_d{}^{90}$ as shown in Fig. 10.

Addressing of the NCPT panel is done using electrooptical hysteresis. After initializing all the pixels, a writing task is done using the electro-optical behavior. This is done one line at a time, thus the writing time of the whole screen is proportional to the number of scanning lines. Since the average writing time for each scanning line is 2.2 ms, it takes 2.2 s (2.2 ms x 1 000 lines) to write 1 000 scanning lines.

2.2.5 Ferroelectric LC mode

Unlike nematic liquid crystal materials, ferroelectric liquid crystal shows spontaneous polarization coupled with externally applied voltage. Strong coupling with the applied voltage gives a sub-millisecond response time for the ferroelectric liquid crystal display. Furthermore, the ferroelectric liquid crystal molecule has bistable polarization configurations as shown in Fig. 11, and this bistability makes a memory type drive possible. Thus the ferroelectric liquid crystal display has no limitation of information contents with a direct drive panel. The liquid crystal molecular movement is also parallel to the substrates, as shown Fig. 12, and parallel movement and bistability combine to give a high resolution of the display. A fine, transparent

electrode pattern provides the lateral electric field.

Since nematic liquid crystal materials which exhibit induced polarization are polarized longitudinally, the liquid crystal molecules at the outer edge of the electrode align with the lateral electric field as shown in Fig. 13. The optical axis of a nematic liquid crystal is the long molecular axis, hence the light transmission changes continuously with the lateral electric field.

In contrast, the spontaneous polarization of a ferroelectric liquid crystal is perpendicular to the molecular long axis, thus even though there is a lateral electric field, the molecular alignment stays almost perpendicular to the substrate. Therefore, the ferroelectric liquid crystal display has a high resolution and high contrast ratio[21].

The ferroelectric liquid crystal display needs two polarizers to reduce screen luminance for projection display. However, high resolution is necessary for projection displays. Since the ferroelectric liquid crystal display has both high information content and high resolution, a good large projection screen image can be produced. Iwai[22] reported a four million pixel full color projection display using a ferroelectric liquid crystal. This projection display consisting of three ferroelectric liquid crystal panels, and each panel switched light. Red, green and blue lights were switched by each liquid crystal panel, and full color was achieved by dithering.

2.2.6 Other liquid crystal modes

Several other types of liquid crystal drives may be used for projection displays. A polymer dispersed liquid crystal (PDLC)[23] may be an excellent candidate due to its light scattering ability. It can be made into sheet film for a large liquid crystal display viewed directly, such as for may also be used with public announcement boards[24]. A large screen projection display may also be used with a polysilicone thin-film transistor (TFT) panel[25].

The π-cell[26] is another candidate for a large liquid crystal projection display, it offers fast optical switching at 1 ms. The π-cell is being used for a time sequential optical shutter in conjunction with a CRT display[27]. The π-cell may require TFTs for a high information content display, and the need to use polarizers makes it hard to use it for large projection displays.

3. Comparison of currently available drive modes

There are three types of liquid crystal drive mode currently in use: a nematic-cholesteric phase transition (NCPT) type liquid crystal, a supertwisted nematic (STN) liquid crystal, and an active matrix (AM) drive twisted nematic (TN) liquid crystal. Both the NCPT and the STN type are driven by a multiplexed system in a simple matrix panel. The active matrix TN is driven by thin-film transistors (TFTs).

The characteristic of a simple matrix and an active matrix for a liquid crystal projector are first compared, then application in the electronic overhead projector is discussed.

The active matrix driven TN liquid crystal projector can produce images at video speed, so it is suitable for a video projector. However, the aperture ratio of the active matrix panel is lower than that of the simple matrix panel, and for a high resolution display such as the one million pixel projector, the aperture ratio is lower than 50 percent. The low aperture ratio and two polarizers significantly reduce screen luminance which makes the legibility of the image poor.

In contrast, a simple matrix panel has a large aperture ratio. The current LCD production technology gives a much higher productivity of an A4-size LCD panel with 640 x 400 pixels than for an active matrix panel. An A4-size LCD panel is required for an electronic overhead projector for compatibility with conventional OHP transparencies.

Since the electronic overhead projector is used mainly for meetings, conferences, public announcements and so on, a character image is mainly required. For the first stage, a still black and white image is necessary. Then, a still multicolor, and a still full color image should be provided. Next, a video rate multicolor and full color image will be required, and finally, a real-time three dimensional full color projector can be expected.

In the next section, the characteristics of the two types of currently available EOHPs using a simple matrix liquid crystal panel for presentations are compared.

3.1 NCPT projection display

The NCPT liquid crystal projector was reported by Mochizuki in 1985[1]. This projection display needs no polarizer, so screen luminance is high. Without polarizers, not only is the screen brighter, but also is absorbed the liquid crystal panel heats up less since less projected light is absorbed. The optical system of the conventional overhead projector gives poor lighting uniformity. Sometimes, the light intensity in the center of the image is twice as bright as the outer part. Therefore, a liquid crystal projector equipped with polarizers should not be used for many hours continuously. Continuous usage may cause part of the image to deteriorate due to high temperatures in the liquid crystal panel.

The total transmittance of the NCPT panel is more than 80 percent, which depends on the aperture ratio and also thus affects the resolution of the panel. The productivity of the NCPT panel is also much higher than the STN panel. The NCPT needs no rubbing treatment for liquid crystal molecular alignment, whereas, the STN panel requires careful rubbing for correct alignment. The molecular orientation of the liquid crystal is one of the most sensitive thus most difficult processes in the production of LCDs. Therefore, the NCPT LCD panel production process, which does not require rubbing, is more efficient. Particularly for the production of large panels, such as A4-size, non-rubbing is preferable to produce a uniform molecular orientation.

The other advantage of the NCPT projector is that it has no limitation in information content. Yabe[28] reported a five million pixel NCPT projection display in 1991 (see Fig. 14). The bistability of the NCPT type gives an extremely high information content, as high as the laser beam addressed liquid crystal projector system is quite simple, as with conventional STN LCDs, and is therefore inexpensive. Moreover, since the NCPT needs no polarizers, the screen can be as

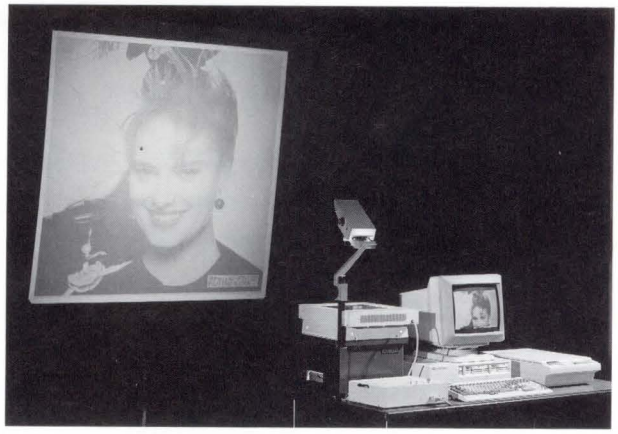

Fig. 14—The 5-million pixel NCPT liquid crystal projection display.

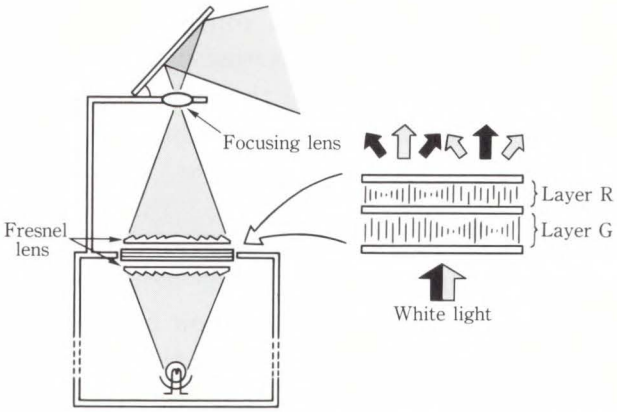

Fig. 15—Structure of double-layer NCPT liquid crystal projection display.

a laser beam addressed system. To produce five million pixels high resolution projection uniform molecular alignment over a large area is done without rubbing and no heat up without polarizers. Although this display uses the bistability of the NCPT liquid crystal, the extremely high resolution enables a fine gray scale image by dithering as shown in Fig. 14.

The NCPT projector can also produce color images without using color filters, since it controls the direction of the incident light. The direction of scattered light is governed by the helical pitch of the liquid crystal and the retardation Δnd of the material, where Δn is the birefringence of the liquid crystal and d is the panel gap. Due to birefringence the direction of the incident light is dependent on the wavelength of the light. Thus when only the

green component of the incident light is scattered, the red component passes through the liquid crystal panel, and a red image can be obtained on the screen.

The most effective scattering wavelength dependends on the liquid crystal material and the panel gap, therefore one NCPT panel can produce a single color image. A double layer NCPT projector can produce a multicolor image[29]. The structure of the double layer NCPT liquid crystal projection display is shown in Fig. 15. When the liquid crystal is in the cholesteric phase, the green light scattering panel (layer R: upper panel) allows only the red component of the incident light to pass through, and scatters the other color components. The red light scattering panel (layer G: lower panel) allows only the green component to pass through, and scatters the other color components. With this system, red, green, white and black can be displayed. The scattered components are dependent on both the selective Bragg reflection caused by the liquid crystal's helical pitch, and the retardation of the liquid crystal. This system can produce four colors. However, by adding a blue light scattering panel, an eight-color multicolor projector is possible, and dithering technology can produce a full color image.

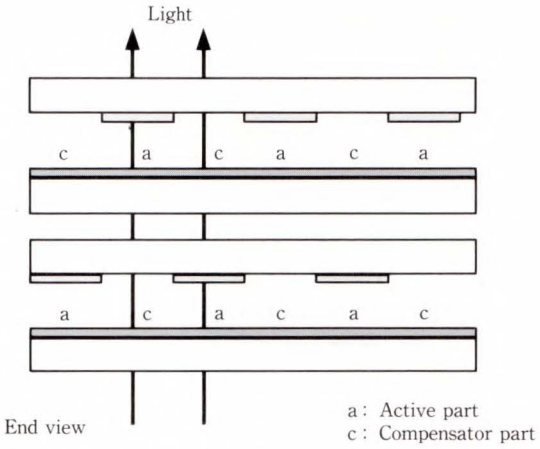

Fig. 16—Double-layer STN fine resolution panel for projection display.

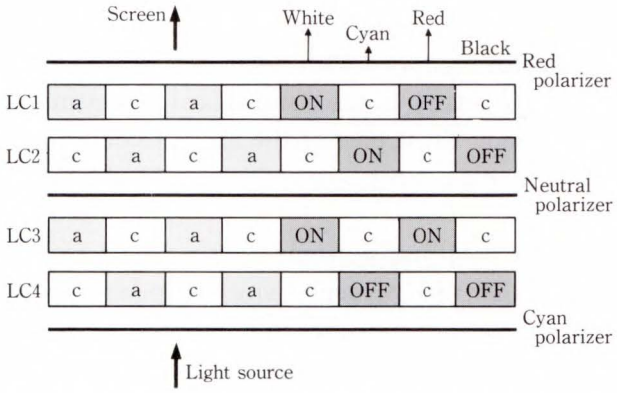

Fig. 17—Structure of multicolor STN projection display.

3.2 STN projection displays

The STN is the most popular type of LCD. Many office automation devices use STN LCDs with an A4 panel size. Thus it is quite natural to use STN LCDs for electronic overhead projectors. Several types of STN electronic overhead projectors are currently available from several companies. These STN projectors offer 640 × 480 pixels or 640 × 400 pixels. However, the size in panel temperature governs the characteristics of these projectors and it is quite difficult to produce 1 200 × 800 pixel STN projectors.

Conner[30] proposed a high resolution, 1 200 × 1 000 pixel multicolor electronic overhead projector using STN technology. Figure 16 shows the structure of the high resolution STN projection system. Two STN panels are stacked with each panel's pixels being compensated as shown in Fig. 16. Each panel is driven by a 1/256 duty ratio, which has enough drive window with a wide temperature range, giving a total resolution of 1 200 × 1 000 pixels. A color image is produced by birefringence of the liquid crystal – in principle, STN LCDs have a birefringence effect – and incident white light turns colored by this effect. Using three STN layers, Conner realized a multicolor projection display as shown in Fig. 17. The first layer is a *red* panel, which turns incident white light to red. The second layer is a *cyan* panel, which turns incident light to cyan. The third layer is a *yellow* panel, which turns the light to yellow. This subtracting system achieves a multicolor projection image.

Although these clever techniques have been used, heat absorption of the STN panel

limits the information content. The limitations of the STN projection system are thus low information content, image deterioration due to higher temperatures and poor luminance of the projection screen.

4. Conclusion

The liquid crystal projection display is an effective system for producing a large image. The optically addressed projection system offers high information content and high resolution, but is so complicated that it is bulky, heavy and expensive. This system may be suitable for special applications such as a huge control panel for a command control.

The electrically addressed liquid crystal projector is generally compact and inexpensive. The active matrix TN type is particularly useful for video rate screen images. However, the active matrix projector requires its own optical system, so for electronic overhead projectors, the simple matrix LCD is more suitable. The STN projector is currently the most popular. However, this display needs two polarizers which reduce screen luminance absorb projection light, and raise the temperature of the LCD.

In contrast, the NCPT projector needs no polarizers, giving high screen luminance, and its bistability gives an extremely high information content, reaching five million pixels. This non-polarized projection display is suitable for displays requiring good screen luminance and high image quality. Although the NCPT projector can display only still images, the high resolution can produce gray scales.

The NCPT projector offers the same high luminance, resolution and information content image as a laser beam addressed projector, yet is as simple, compact and inexpensive as a conventional STN projector. It can also produce full color images. Therefore, the NCPT projector is an effective presentation device.

References

1) Mochizuki, A., Gondo, H., Watanuki, T., Saito, K., Ikegami, K., and Okuyama, H.: New Nematic-Cholesteric LCD Using Hysteresis Behavior. *Proc. SID* (Soc. Infor. Display), **26**, 4, pp. 243-248 (1985).
2) Kunigata, M., Hirai, Y., Ooi, Y., Niiyama, S., Asakawa, T., Masumoto, K., Kumai, M., and Gunjima, T.: A Full-Color Projection TV Using LC/Polymer Composit Light Valve. Conf. Rec. SID '91, 1991, pp. 227-230.
3) Schadt, M., and Funfschilling, J.: Novel Polarized Liquid Crystal Color Projection and New TN-LCD Operating Modes. Conf. Rec. SID '90, 1990, pp. 324-326.
4) Sterling, D.R., Te Kolste, D. R., Hagger, M. J., Borah, C. T., and Bleha, P. W.: Video-Rate Liquid Crystal Light Valve Using an Amorphous Silicon Photoconductor. Conf. Rec. SID '90, 1990, pp. 327-329.
5) Conner, R. A.: Subtractive Color STN-LCD Display. To be published in the *Proc. SID*, 1991.
6) Melchior, H., Kahn, F. J., Maydan, D., and Fraser, D. B.: Thermally Addressed Electrically Erased High-Resolution Liquid-Crystal Light Valves. *Appl. Phys. Lett.*, **21**, 8, pp. 392-394 (1972).
7) Kahn, F. J.: ir-Laser-Addressed Thermo-Optic Smectic Liquid-Crystal Storage Displays. *Appl. Phys. Lett.*, **22**, 3, pp. 111-113 (1973).
8) Usubuchi, T., Komatsubara, S., Wakatsuki, K., Kubota, K., and Nishida, N.: A Compact High Resolution Projector Utilizing a Laser-Diode Addressed Liquid Crystal Light Valve. *Proc. SPIE*, Kahn, F. J. ed., **760**, Large Screen Projection Displays, pp. 62-69 (1987).
9) Bone, M., Haven, D., and Slobodin, D.: Video-Rate Photoaddressed Ferroelectric LC Light Valve with Gray Scale. Conf. SID, 1991, pp. 254-256.
10) Koda, J., Henderson, A., Ledebuhr, A., Bleha, W., and Huelsman, K.: Full Color Projector with Single Liquid Crystal Light Valve. *Proc. SPIE*, Kahn, F. J. ed., **760**, Large Screen Projection Displays, pp. 78-84 (1987).
11) Matsumoto, S., Kawamoto, M., and Mizunoya, K.: Field-induced deformation of hybrid-aligned nematic liquid crystals: New multicolor liquid crystal display. *J. Appl. Phys.*, **47**, pp. 3842-3845 (1976).
12) Robert, J., and Clerc, F.: Liquid crystal matrices for TV and colored graphic displays. Conf. SID, 1989, pp. 30-30B.
13) Shiekel, M. F., and Fahrenschon, K.: Deformation of nematic liquid crystals with vertical orientation in electrical fields. *Appl. Phys. Lett.*, **19**, 10, pp. 391-393 (1971).
14) Yamauchi, S., Aizawa, M., Cleac, J. F., Uchida, T.,

and Duchene, J.: Homeotropic-alignement full-color LCD. Conf. Rec. SID, 1989, pp. 378-341.
15) Clerc, F. J., Aizawa, M., Yamauchi, S., and Duchene, J.: Highly Multiplexed Super Homeotropic LCD. Conf. Rec. Japan Display, Kyoto, 1989, pp. 188-191.
16) Heffner, R. W., and Berreman, W. D.: Switching Characteristics of a Bistable Cholesteric Twist Cell. *J. Appl. Phys.*, **53**, 12, pp. 8599-8606 (1982).
17) Heffner, R. W.: Anisotropic domaun grouth in the bistable cholesteric twist cells. *Mol. Cryst. Liq. Cryst.*, **130**, pp. 305-319 (1985).
18) Berreman, W. D., and Heffner, R. W.: Disclination-free bistable twist cells. *Proc. SID*, **22**, 3, pp. 191-193 (1981).
19) Barberi, R., Giocondo, M., and Durand, G.: A Flexoelectrically Controlled Surface Bistable Nematic Display. Conf. Rec. SID, 1991, pp. 606-607.
20) Mochizuki, A., and Kobayashi, S.: A surface effect on the threshold electric field of a cholesteric-nematic phase transition. Accepted for publication to *Mol. Cryst. Liq. Cryst.*, (1991).
21) Clark, A. N., and Lagerwall, T. S.: Submicrosecond Bistable Electro-Optic Switching in Liquid Crystals. *Appl. Phys. Lett.*, **36**, 11, pp. 899-901 (1980).
22) Iwai, Y., Wakita, N., Uemura, T., Fujiwara, S., Gohara, Y., Kimura, S., Masumoto, Y., Miyatake, Y., Tsuda, T., Hori, Y., and Oota I.: Multi-Color, High Resolution Projection Display with Ferroelectric Liquid Crystal Light Valves with 4M Pixels. Conf. Rec. Japan Display, Kyoto, 1989, pp. 180-183.
23) Chidichimo, G., Arabia, G., Golemme, A., and Doane, J. W.: Electrooptic properties of polymer dispersed liquid crystals. *Liquid Crystals*, **5**, 5, pp. 1443-1452 (1989).
24) Drzaic, P. S., and Muller, A.: Droplet shape and reorientation fields in nematic droplet/polymer films. *Liquid Crystals*, **5**, 5, pp. 1467-1475 (1989).
25) Kunigita, M., Hirai, Y., Ooi, Y., Niiyama, S., Asakawa, T., Masumo, K., Kumai, H., Yuki, M., and Gunjima, T.: A Full-Color Projection TV Using LC/Polymer Composite Light Valves. SID '90 Digest, 1990, pp. 227-230.
26) Bos, P. J., and Haven, T.: Field-sequential stereoscopic viewing systems using passive glasses. *Proc. SID*, **30**, 1, pp. 39-43 (1989).
27) Bos, P. J., Johnson, P. A., and Koehler/Beran, K. R.: A Liquid-Crystal Optical-Switching Device (π-cell). SID '83 Digest, 1983, pp. 30-33.
28) Yabe, Y., Yamada, H., Hoshi, T., Yoshihara, T., Mochizuki, A., and Yoneda, Y.: A 5-M Pixel Overhead Projection Display Utilizing a Nematic-Cholesteric Phase Transition Liquid Crystal. Conf. Rec. SID, 1991, pp. 261-264.
29) Mochizuki, A., Yoshihara, T., Iwasaki, M., Yamagishi, Y., Koike, Y., Haraguchi, M., and Kaneko, Y.: A 1 120 x 768 Pixel Four-Color Double-Layer Liquid Crystal Projection Display. *Proc. SID*, **31**, 2, pp. 155-161 (1990).
30) Conner, R. A., and Gulick, E. P.: High-Resolution Display System Based on Stacked Mutually Compensated STN-LCD Layers. Conf. Rec. SID, 1991, pp. 755-757.

Akihiro Mochizuki
Organic Materials Laboratory
FUJITSU LABORATORIES, ATSUGI
Bachelor of Natural Science
The University of Tokyo 1980
Dr. of Engineering
Tokyo University of Agriculture and Technology 1991
Specializing in Liquid Crystal Materials Science

Yasuhiro Yoneda
Organic Materials Laboratory
FUJITSU LABORATORIES, ATSUGI
Bachelor of Industrial Chemistry
Seikei University 1970
Specializing in Photo-Polymers

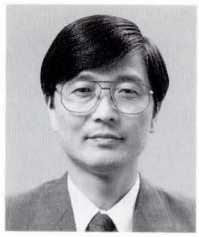

Toshiaki Narusawa
Organic Materials Laboratory
FUJITSU LABORATORIES, ATSUGI
Bachelor of Science Eng.
Shinshu University 1967
Master of Science Eng.
Shinshu University 1969
Specializing in Organic Materials

UDC 548.52:621.315.5

Recent Advances in the Application of Transmission Electron Microscopy to the Evaluation of III-V Compound Semiconductor Thin Films

• Osamu Ueda

(Manuscript received October 24, 1991)

This paper reviews recent advances in the application of transmission electron microscopy to the evaluation of structures, interfaces and defects in compound semiconductor thin films. It has been shown microscopically for the first time that the growth of $(GaAs)_m/(GaP)_n$ strained layer superlattices by atomic layer epitaxy proceeds in a precisely layer-by-layer manner. Detailed characterizations of interfaces and defects in AlAs, GaAs and GaP on Si, also GaAsSb and Fe-doped InP on InP are described; later, the mechanisms which generate such defects and techniques for their elimination are discussed. Studies of atomic ordering in InGaP and InGaAs are presented, with reference to the mechanisms which generate ordered structures and their influence on the properties of the material.

1. Introduction

III-V compound semiconductor thin films such as GaAlAs/GaAs and InGaAs(P)/InP grown by the advanced growth techniques of metalorganic vapor phase epitaxy (MOVPE), molecular beam epitaxy (MBE) and atomic layer epitaxy (ALE)[1)-4)], are widely used as materials for optical devices, electron devices, and their integrated circuits. In order to ensure the best possible device characteristics and high device performance, one must achieve precise control of the layered structures, i.e. control of layer thicknesses and uniformity, and abruptness of the hetero-interface, at the atomic level. To achieve high device reliability, it is also necessary to solve certain materials issues in the thin films, i.e. generation of defects in the crystal, and thermal instability of the crystal.

To confirm controllability in the growth of layered structures and to solve the materials issues described above, one must perform structural evaluation of these materials microscopically or even at the atomic level. Transmission electron microscopy (TEM) {i.e. both conventional TEM and high-resolution TEM (HRTEM)}, is a powerful structural evaluation technique which can provide a considerable degree of information regarding structures, interfaces and defects in the thin films.

In this paper, the current state of our application of TEM to the evaluation of structures, interfaces and defects (including those due to thermal instability) in a variety of III-V semiconductor thin films is systematically reviewed.

2. TEM

In this chapter, three major techniques involved in TEM are described. They are specimen preparation techniques, observation techniques, and computer simulation techniques of HRTEM images.

2.1 Specimen preparation techniques[5)]

For TEM observation, preparation of specimens is a crucial factor. A good TEM specimen must:

1) be thin enough;
2) have a flat surface;
3) be undamaged;
4) have no surface contamination;
5) have no bowing.

In particular, the thickness of the sample is most important since the incident electron beam should pass through the specimen. Whether or not the sample is transparent to the electron beam also depends on the voltage used to accelerate the electrons, and the material. When 200 kV TEM is used, the maximum thicknesses for Si and GaAs are 1 μm and 0.5 μm, respectively. However, the optimum thickness for conventional TEM is 0.1-0.2 μm, and for HRTEM, the thickness should be less than 50 nm.

Specimen preparation techniques can be classified into two types, chemical etching and ion milling. In chemical etching, Br_2/CH_3OH solution is mostly used for III-V compounds, after polishing the sample down to about 100 μm. In the case of layered structures such as InGaAsP/InP double-heterostructures, preferential etching techniques can be used, in which the substrates are removed preferentially leaving only the epitaxial layers. This technique is useful for the preparation of plan-view TEM specimens. To prepare cross-sectional TEM specimens, we must thin the sample by the other technique, ion milling.

Preparation consists of the following steps:
1) Sticking the sample epitaxial wafers face-to-face with epoxy glue;
2) Cutting the sample processed in step 1) into cross-section slices with a thickness of about 0.5 mm;
3) Polishing the specimen from both sides down to about 50 μm;
4) Mounting the specimen onto a single-hole TEM mesh;
5) Reducing the specimen to final thickness by ion milling from both sides.

2.2 Observation techniques[6]

In this study, we used a Topcon EM-002B ultra-high resolution analytical electron microscope equipped with an energy dispersive X-ray spectrometer (EDX) and electron energy loss spectrometer (EELS). We applied both conventional TEM techniques and HRTEM techniques.

2.2.1 Conventional TEM techniques

In conventional TEM, there are two main methods used: bright-field and dark-field imaging. A bright-field image is obtained from the transmitted electron beam, whereas a dark-field image is from one of the Bragg reflected beams.

Thus, these images are complimentary. In these observations, several diffraction conditions are used:
1) Two-beam condition
   One particular reflection is excited.
2) Multi-beam condition
   More than two reflections are excited.
3) Quasi-kinematic condition
   No reflections are excited.

2.2.2 HRTEM

The HRTEM technique provides us with precise atomic level contrast; the contrast is "phase-contrast" which is produced as a result of multiple-scattering of transmitted electrons in the specimen[7]. In this situation, a zone-axis diffraction condition is used where the direction of the incident electron beam is set exactly normal to the crystallographic plane of the specimen (in this condition, all equivalent reflected beams are equally excited). The actual image is made by allowing many beams through a circular objective aperture at high magnification (typically × 300 000). The HRTEM image consists of lattice-fringes corresponding to low-index spacings of the materials (200, 111, 220, 400,...); thus this is called a "lattice image" or "structure image".

2.3 Computer simulation of HRTEM images

The HRTEM images described in subsection 2.2.2 strongly depend on the defocus value of the objective lens, the thickness of the specimen, the optical parameters of the electron microscope, etc. Therefore, computer simulation is required for a complete understanding of the HRTEM images. The most important method for computing such images is the multi-slice method[8]. In this study, we have also applied

this method to simulate the HRTEM images of various types of III-V superlattices.

3. Evaluation of layered structures

In order to ensure the best possible device characteristics and high device performance, one must achieve precise control of the layered structure, i.e. atomic-level control of layer thicknesses and uniformity, and abruptness of the hetero-interface. In this chapter, recent results on structural evaluation of GaAs/GaP strained layer superlattices grown by atomic layer epitaxy, which allows layer-by-layer growth of compound semiconductors, is described.

3.1 GaAs/GaP strained layer superlattices grown by ALE

ALE is a very attractive technique in which crystals can be grown layer-by-layer through a self-limiting mechanism[1)-4)]. It can offer great benefits in fabricating various III-V heterostructures with extremely high uniformity in thickness, excellent abruptness of the hetero-interface and novel artificial structures such as monolayer superlattices, quantum wires and boxes. We have previously reported the development of a new ALE technique called pulsed-jet epitaxy (PJE) which can achieve layer-by-layer growth of III-V compounds with extremely good controllability[9)-11)]. Moreover, we have described successful growth of $(GaAs)_m/(GaP)_n$ (m, n = 1, 2, 3, . . .) strained layer superlattices by PJE[12)]. Structural analyses using X-ray diffraction[12)] and Raman scattering spectroscopy[13)] have indicated that growth of the superlattices was completely controllable at an atomic level even for the case of a $(GaAs)_1/(GaP)_1$ monolayer superlattice. Furthermore, luminescence and reflectance measurements strongly suggested that the $(GaAs)_1/(GaP)_1$ superlattice has a direct bandgap[12),14)]. However, no one has ever reported any direct evidence for layer-by-layer growth of III-V compound semiconductors by ALE.

In this section, we describe for the first time a detailed TEM evaluation of various $(GaAs)_m/(GaP)_n$ (m, n = 1,2,3, . . .) superlattices grown on (001) GaAs substrates by ALE. In this work, $(GaAs)_1/(GaP)_1$, $(GaAs)_3/(GaP)_3$ and $(GaAs)_4/(GaP)_2$ strained layer superlattices were examined by TEM. The $(GaAs)_m/(GaP)_n$ superlattices were grown on (001) GaAs (just) substrates by ALE (PJE). Both GaAs and GaP were grown at 500 °C, where both materials can be grown layer-by-layer. Trimethylgallium (TMGa), arsine (AsH_3) and phosphine (PH_3) were used as source gases. The alternating pulses of TMGa and arsine (phosphine) were separated by a hydrogen purge pulse to prevent the reactants from mixing. A vapor pressure of 20 Torr was maintained during the growth {growth procedures are described in detail elsewhere[12)]}. The thicknesses of these superlattices are approximately 50 nm. In this work, we have performed cross-sectional TEM observations.

3.1.1 Structural evaluation of $(GaAs)_1/(GaP)_1$ monolayer superlattices

Figure 1 shows a typical transmission electron diffraction (TED) pattern obtained from the (110) cross-section of such a $(GaAs)_1/(GaP)_1$ monolayer superlattice. Since the superlattice is 50 nm thick and the selected area aperture used in this experiment was 150 nm in dia, this TED pattern is mostly from the GaAs substrate. However, superstructure spots are observed at positions indexed

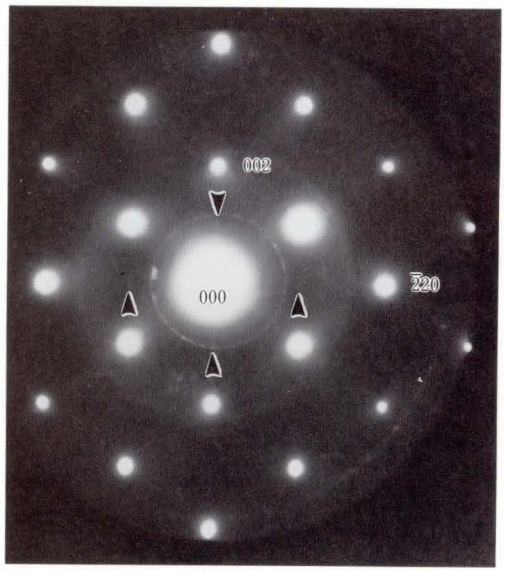

Fig. 1—A TED pattern from a (110) cross-section of a $(GaAs)_1/(GaP)_1$ monolayer superlattice.

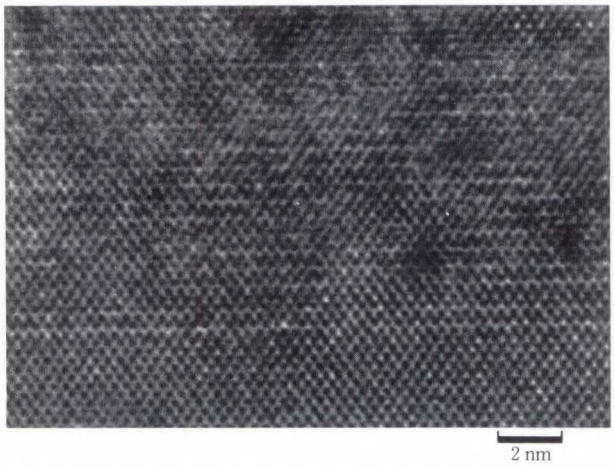

Fig. 2—A (110) cross-sectional HRTEM image of a $(GaAs)_1/(GaP)_1$ monolayer superlattices.

as 001, $\bar{1}10$, $\bar{1}12$, . . . (see diffraction spots indicated by arrows.). This particular set of superstructure spots is associated with the $(GaAs)_1/(GaP)_1$ monolayer superlattice. In order to clarify if such superlattices are generated in real space, HRTEM observation was carried out. Figure 2 is a (110) cross-section HRTEM image of the superlattice. In this image, one bright spot corresponds to two adjacent atoms, i.e. Ga-As or Ga-P along the <110> direction. The interface between the epitaxial layer and the GaAs substrate is indicated by an arrow. Computer simulation of $(GaAs)_1/(GaP)_1$ confirms that in Fig. 2, the bright spots with stronger and weaker intensities correspond to Ga-As and Ga-P (specimen thickness = 2 nm, amount of defocus = 38 nm), respectively (see also arrows in the epitaxial layer). Note that the hetero-interface is extremely abrupt with no imperfections and no alloyed region, and that the $(GaAs)_1/(GaP)_1$ monolayer superlattice is formed uniformly in the entire epitaxial layer region. This is the first direct evidence for layer-by-layer growth of III-V compound semiconductors by ALE.

3.1.2 Structural evaluation of $(GaAs)_3/(GaP)_3$ and $(GaAs)_4/(GaP)_2$

We have also evaluated multiple-layer superlattices of $(GaAs)_3/(GaP)_3$ and $(GaAs)_4/(GaP)_2$. A TED pattern from the (110) cross-section of $(GaAs)_3/(GaP)_3$ is shown in Fig. 3. A sharp satellite-spot pair is present around the

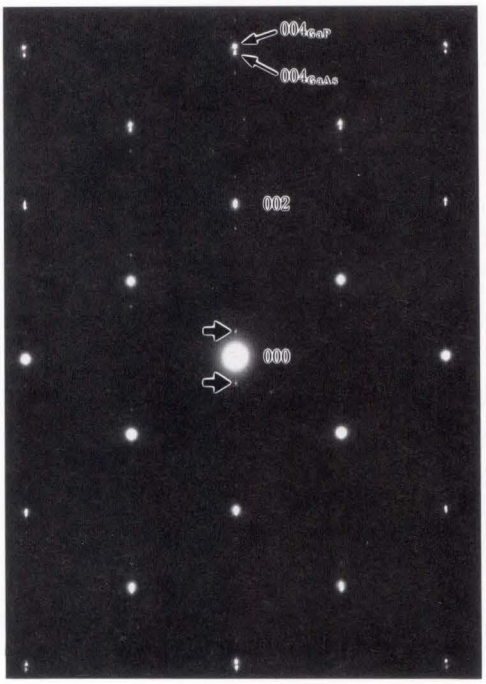

Fig. 3—A TED pattern from a (110) cross-section of the $(GaAs)_3/(GaP)_3$ superlattice.

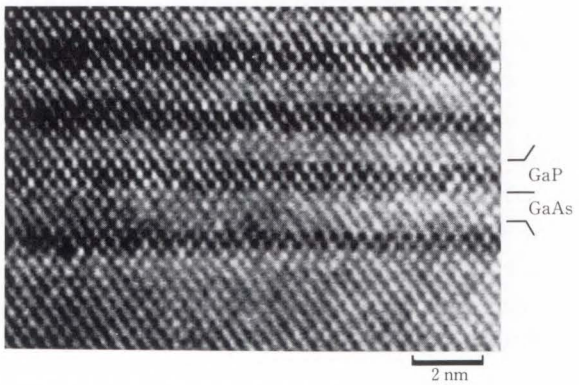

Fig. 4—A (110) cross-sectional HRTEM image of a $(GaAs)_3/(GaP)_3$ superlattice.

000 (direct) spot (see spots around the 000 indicated by arrows), which corresponds to the periodicity of $(GaAs)_3/(GaP)_3$. The spacing between the satellite and 000 spots is approximately one sixth of that between the 002 and 000 spots. This result indicates that the superlattice has periodicity of 6 atomic layers. In the higher order spot region, the fundamental spot splits into two individual spots as shown in the upper part of the TED pattern. In this region, spots for 004 reflections of GaAs and GaP are observed with very narrow spacing. Since the midpoint between two satellite spots

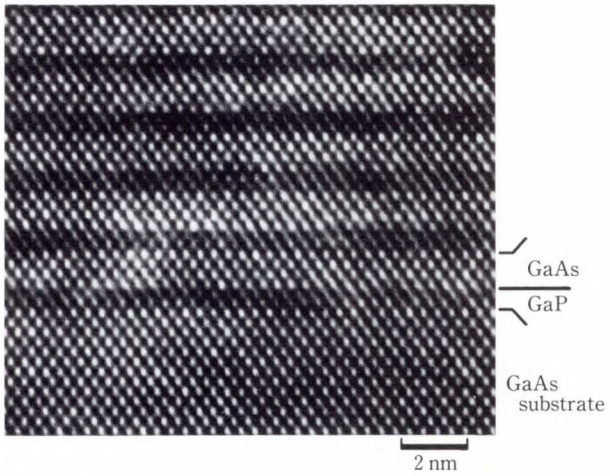

Fig. 5—A (110) cross-sectional HRTEM image of a $(GaAs)_4/(GaP)_2$ superlattice.

nearly coincides with that between the 004 spots, the periodicity of the superlattice can be treated as that of a GaAsP mixed crystal.

Figures 4 and 5 show (110) cross-section HRTEM images of $(GaAs)_3/(GaP)_3$ and $(GaAs)_4/(GaP)_2$ superlattices. These images also confirm that bright spots with stronger and weaker intensities correspond to Ga-As and Ga-P, respectively. The locations of the GaAs and GaP layers are indicated in each figure. GaAs and GaP layers of exactly three monolayers have grown uniformly throughout the epitaxial layer. In both cases, neither alloyed regions nor oxidized regions were found at the hetero-interface. Also note that at each hetero-interface in the superlattice, {111} planes deform to an "S"-shape. This is probably due to lattice distortion of the crystal at each interface due to lattice-mismatch. Computer simulation is required to confirm this.

4. Interface structure and defects

Defect generation is one of the important materials issues in III-V semiconductor thin film growth. Defects introduced during growth can be classified into two types: interface defects and bulk defects.

Defects belonging to the first type are stacking faults, V-shaped dislocations, dislocation clusters, microtwins, inclusions, and misfit dislocations. Interface defects due to contamination, thermal damage of the substrate, local

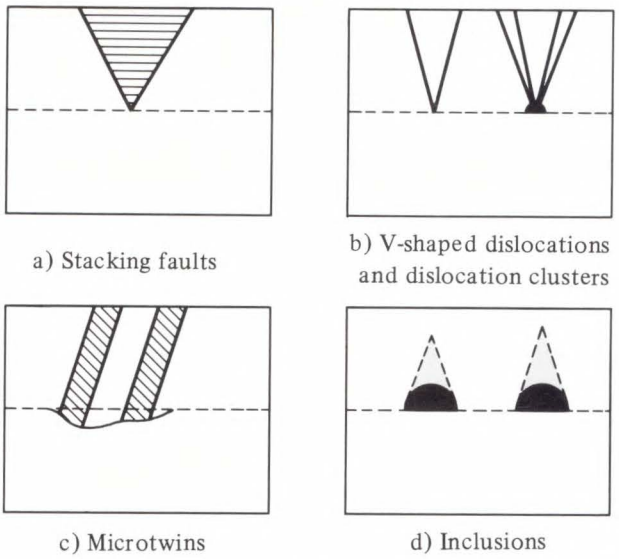

Fig. 6—Schematic diagrams of interface defects due to contamination, thermal damage of the substrate, or local segregation.

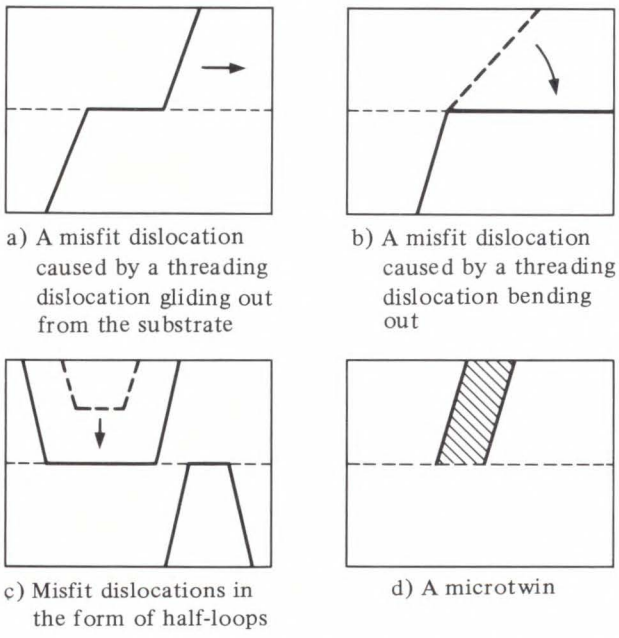

Fig. 7—Schematic diagrams of interface defects due to lattice mismatch.

segregation at the interface, and those due to lattice-mismatch are schematically shown in Figs. 6 and 7.

The stacking faults shown in Fig. 6a) are generated from the hetero-interface, extending along the four equivalent {111} planes, forming a stacking fault tetrahedron. In MBE-grown crystals, they often correspond to surface

defects (see section 4.3). Pit-pairs are often observed on the etched surface of thin films. In the TEM image of the area which includes a pit-pair, small dislocation segments are observed. From the shape of the dislocations, this dislocation pair is assumed to comprise a V-shaped dislocation {see Fig. 6b)}. Occasionally, preferential etching takes place at such V-shaped dislocations[15]. Microtwins are generated at the hetero-interface through relaxation of stress, extending along the {111} planes, as shown in Fig. 6c). They occasionally terminate with {211} type boundaries in mid-layer. Inclusions are accidentally introduced during liquid phase epitaxy (LPE) growth by incorporation of remaining droplets into the solid solution when the Ga- or In-rich melt is wiped off from the substrate[16] {see Fig. 6b)}. Since the first three kinds of defect described above are eliminated by clearing the substrate surface prior to growth and/or the protection of the substrate against evaporation of substrate atoms, they are presumably generated by contamination of, and/or thermal damage to the substrate.

Thus, control of the hetero-interface is extremely important for the elimination of defects.

If there is a difference in lattice constant between the epitaxial layer and the substrate, misfit dislocations are generated when the film thickness exceeds the critical thiciness t_c, which depends on the structure and elastic properties of the material, and the type of dislocations. There are several possible mechanisms for the generation of misfit dislocations as shown in Figs. 7a) to c). First, threading dislocations propagating from the substrate may glide out {see Fig. 7a)} or bend out {see Fig. 7b)} to the edge of the wafer. It is also expected that two dislocations with the same Burgers vectors in the substrate can terminate as one misfit dislocation at the hetero-interface, forming a half-loop {see right figure of Fig. 7c)}.

If the dislocation density in the substrate is low, other mechanisms which may occur are:

1) nucleation of micro-half-loops at the surface;
2) expansion of loops down to the interface;

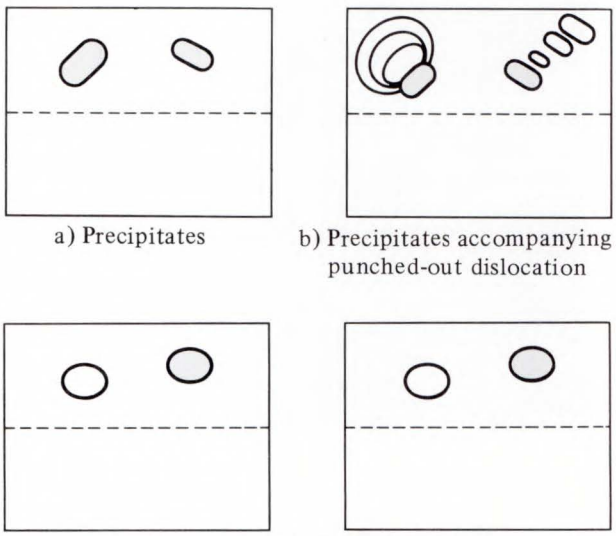

a) Precipitates
b) Precipitates accompanying punched-out dislocation
c) Faulted and/or unfaulted loops due to local segregation of dopant atoms
d) Faulted and/or unfaulted loops due to modulated structure generation

Fig. 8—Schematic diagrams of bulk defects due to local segregation of dopant atoms or native point defects.

3) gliding out of the threading segments to the edge {left figure of Fig. 7c)}[17].

In highly mismatched heteroepitaxy such as GaAs/Si, microtwins {see Fig. 7d)} and/or stacking faults are very often generated, particularly during the initial stage of growth[18]. They propagate along the four equivalent {111} planes. However, they often annihilate in mid-layer, i.e. terminating in {211} type boundaries for microtwins[19),20] and coalescence of two stacking faults on different planes[19].

Figures 8a) to d) show typical features of bulk defects. In most cases, they are generated in heavily-doped crystals as shown in Figs. 8a) to c). When supersaturated dopants are present in the crystal, they tend to segregate locally, either during growth or during the cooling process after growth, forming precipitates {see Fig. 8a)}. When there is large lattice-mismatch between the precipitates and the matrix, dislocation loops are often punched out by the relaxation of stress {see Fig. 8b)}. These precipitates are often observed in heavily doped LPE-grown InGaAsP crystals on InP[21]. In the formation of precipitates, excess native point defects can be introduced. They may condense

at some nucleation centers to form dislocation loops (either faulted or unfaulted) as shown in Fig. 8c). Interstitial type dislocation loops are often observed in heavily doped LPE-grown GaAlAs crystals with Ge[22]. On the other hand, dislocation loops are present even in undoped crystals. We have found both vacancy type and interstitial type loops in undoped LPE-InGaP crystals[23]. Since modulated structures (see Chap. 5) are generated in the crystal, these loops are presumably caused by the condensation of excess point defects induced as byproducts of modulated structures.

In this chapter, to illustrate some of the topics described above, we present recent results on the TEM evaluation of interfaces and defects in highly mismatched AlAs, GaAs and GaP grown on (001)Si. Analyses of interface defects in GaAsSb on (001)InP heterostructures and bulk defects in heavily Fe-doped InP crystals are also described.

4.1 Interfaces and defects in AlAs on Si(001) grown by ALE

Highly mismatched heterostructures such as GaAs/Si[24)-29)], InP/Si[30)], and SiGe/Si[31)] are very attractive materials for use in opto-electronic integrated circuits, solar cells and heterobipolar transistors. The main problems in these systems are the differences in lattice constants and in thermal expansion coefficients between the substrate and epitaxial layers. At the initial stage of crystal growth, although the lattice mismatch may be relaxed by the presence of misfit dislocations at the hetero-interface, three-dimensional island growth often takes place, generating in the crystal a high density of defects such as threading dislocations, stacking faults and microtwins. In GaAs/Si the defect density can be reduced to about $10^6/cm^2$ by using the standard two-step growth method[24], applying *in situ* cyclic annealing[25),26)], and introducing strained layer superlattices[27),28)]. However, during the cooling process after growth the difference in the thermal expansion coefficients causes additional stress in the system, thus enhancing the multiplication of dislocations via glide motion[29)]. Therefore, in order to achieve a drastic reduction of the defect density, the following approaches are required:

1) Operating a two-dimensional growth mode from the initial stage;
2) Fabricating the heterostructure above the buffer layer at lower temperatures.

We have previously reported that GaAs and AlAs single crystals can be directly grown on Si substrates at 500 °C using ALE[32)-35)]. From Auger electron spectroscopy and Raman scattering spectroscopy, it has been shown that growth by ALE on Si substrates is initially three-dimensional but that it changes to layer-by-layer growth at a relatively early stage. We have also found that coverage improves remarkably when initiating the growth with AlAs instead of GaAs. However, the atomic structure of the hetero-interface, the critical thickness for two-dimensional growth and the defect structures in the GaAs and AlAs layers have not yet been clarified. In this section, we describe for the first time a detailed structural evaluation of ALE-grown AlAs layers on (001)Si substrates by TEM.

Thin AlAs layers were grown on a (001)Si substrate (tilted 2° toward the $<110>$ direction) at 500 °C. Prior to growth, the substrates were heated to 1 000 °C for 20 min in H_2 to evaporate the oxidized surface layer. Since exposure to air heavily damages the surface of AlAs, a 10-atom layer of GaAs was deposited as protection. We also grew GaAs (3 μm)/AlAs/Si heterostructures to evaluate defect generation in thick GaAs layers. In this structure, GaAs layers were grown by MOVPE. Arsine (AsH_3) and trimethylgallium (TMGa) or trimethylaluminum (TMAl) were used as source gases and sprayed on the substrates as pulsed-jets[36)].

4.1.1 Atomic structure of the hetero-interface

First, the hetero-interface between the AlAs layer and the Si substrate was evaluated at the atomic level. As a reference, we also examined a GaAs/Si heterostructure grown by standard two-step MOVPE. Figure 9 shows a typical (110) cross-sectional HRTEM image of the reference sample. The hetero-interface is not abrupt, but highly uneven. The typical interface

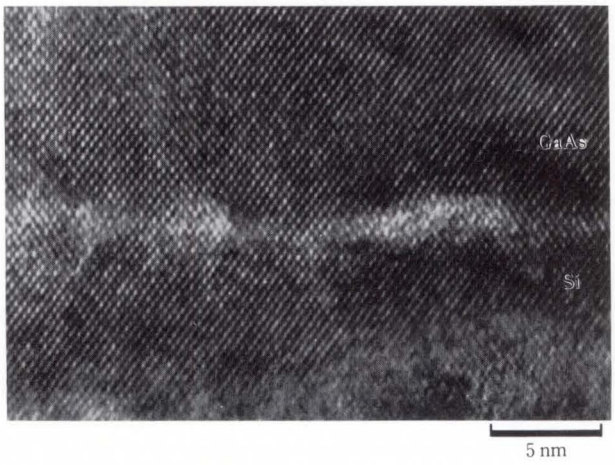

Fig. 9—A (110) cross-sectional HRTEM image of a hetero-interface of the GaAs/(001)Si heterostructure grown by standard two-step MOVPE.

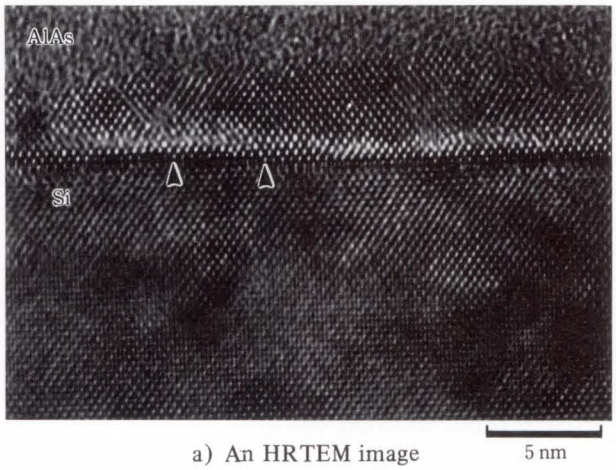

a) An HRTEM image

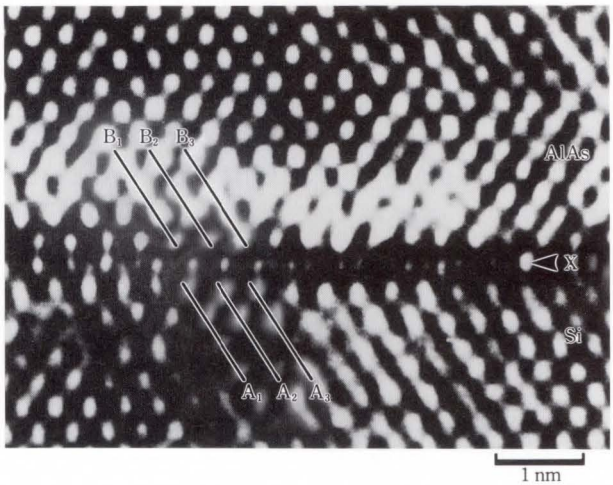

b) A high magnification image of the part of the HRTEM image a)

Fig. 10—(110) cross-sectional HRTEM images of a hetero-interface of the AlAs/(001)Si hetero-structures grown by ALE.

roughness is in the range of 5-10 atomic layers. An amorphous-like contrast is also observed locally. These features are presumably caused by three-dimensional growth and the reaction between the GaAs buffer layer and the substrate during the annealing process (2nd step) of the buffer layer growth. On the other hand, the AlAs/(001)Si interface is found to be extremely sharp {see Fig. 10a)} compared to that of GaAs/Si. Also note that atomic steps are clearly observed {see arrows in Fig. 10a)} and that no amorphous or alloyed regions are found. Figure 10b) is a high magnification image of part of Fig. 10a).

At the hetero-interface, two distinct features are found:

1) The (111) fringes in both Si and AlAs regions do not coincide with each other as indicated by A_1-A_3 and B_1-B_3;
2) An extra layer with anomalous fringe contrast, which is not observed at the GaAs/Si interface, appears (see the layer indicated by X). In this layer, the spacing of the brighter spots along the $<110>$ direction (from left to right) is half of that in the Si and GaAs regions.

As previously reported for ALE of GaAs on a GaAs substrate, one atomic layer of GaAs is grown in one growth cycle[36]. However, for AlAs on GaAs, one cycle allows the growth of two atomic layers of AlAs. The interpretation of the difference in growth rate between GaAs and AlAs is as follows[36]: during GaAs deposition, one Ga atom for every As atom is adsorbed on the (001)GaAs surface, whereas, during AlAs deposition, the (001)Al face touches the GaAs, resulting in adsorption of two Al atoms per As atom[37]. This is due to a very small lattice mismatch (1.3 percent) between the Al and GaAs. Therefore, the extra layer is presumably one atomic layer of metallic (001)Al. We assume that a similar mechanism operates during the growth of AlAs on Si. To confirm this, computer simulation is required.

4.1.2 Initial stage of growth

Figure 11 shows a bright-field plan-view TEM image of a thin AlAs layer on (001)Si taken under zone-axis illumination. In this sample, a 6-atom layer of AlAs is covered by a 10-atom layer of GaAs to protect the AlAs surface. Since the plan-view specimen includes Si, AlAs and GaAs, Moiré fringes are observed as a result of the interference between the transmitted wave and the doubly reflected waves at the AlAs/Si interface. As shown in Fig. 11, numerous patchy regions with Moiré fringes in two directions of nearly $<110>$ and $<1\bar{1}0>$ are formed. These regions are thought to be three-dimensional islands of AlAs on the substrate. They are 5-20 nm in dia. Rotational misalignment of the Moiré fringes is observed, indicating that the islands rotate slightly at the initial stage of growth to minimize the strain energy. Cross-sectional observation was also carried out on the GaAs/AlAs/(001)Si heterostructures. Figures 12a) and b) show cross-sectional HRTEM images of AlAs/(001)Si at an initial stage of growth. In Figs. 12a) and b), 6- and 26-atom layers of AlAs were grown, respectively (in both cases, 10-atom layers of GaAs were grown to protect the surface of the AlAs). In Fig. 12a), islands of 5-20 nm in dia are observed uniformly in the entire region. Thus, one can conclude that a three-dimensional growth mode is dominant at the initial stage of growth of AlAs. However, as the AlAs layer grows thicker, the growth mode becomes more two-dimensional, forming a rather smoother surface{see Fig. 12b)}.

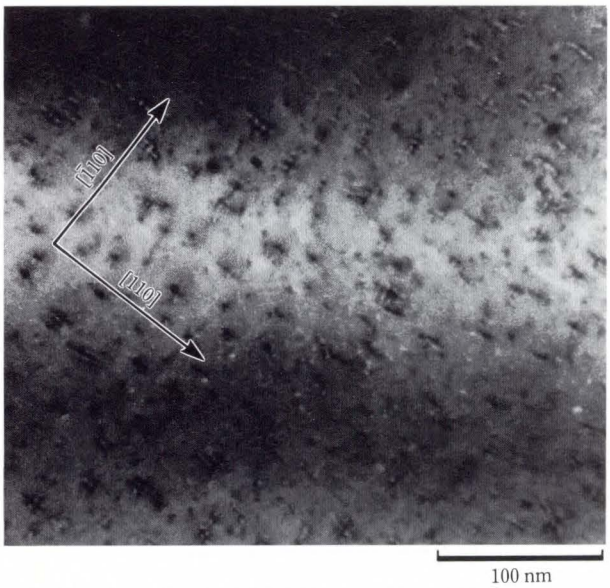

Fig. 11 – A bright-field plan-view TEM image of AlAs/(001)Si heterostructures taken under zone-axis illumination.

Figures 13a) and b) show cross-sectional dark-field TEM images of GaAs/AlAs/(001)Si heterostructures with 36- and 80-atom layers of AlAs, respectively, capped by a 3 μm thick GaAs layer, obtained under the 002 reflection. Since the intensity of the 002 reflection is very low in GaAs and Si, the AlAs layer appears brighter. In Fig. 13a), the interface between AlAs and GaAs is nearly smooth although regions with dark contrast are often observed in the AlAs layer. When the AlAs was grown thicker {see Fig. 13b)}, the hetero-interface was found to be just as smooth. These results can lead us to conclude that the critical thickness for achieving two-dimensional growth in AlAs on (001)Si is approximately 36 atomic layers.

Next, in order to compare the growth mode of AlAs on (001)Si with that of GaAs on (001)Si, we have grown heterostructures consisting of three stacked buffer layers, the first AlAs (a 70-atom layer), the second GaAs (a 70-atom layer), and the third AlAs (a 70-atom layer), capped by a GaAs (3 μm) layer. A cross-sectional TEM image of this structure is shown in Fig. 14. The interface between the first AlAs layer and the second (GaAs) layer (the region with darker contrast) is smooth, whereas the interface between the second (GaAs) and the third (AlAs) layer is very uneven. However, the interface smoothness between the third layer and the thick, upper GaAs layer has improved. These results indicate that the critical thickness for a change from three-dimensional to two-dimensional growth in GaAs on (001)Si is much larger than that for AlAs on (001)Si. As described in section 3.1, two atomic layers are grown per ALE cycle for AlAs, achieving coverage twice as good as for GaAs (the bond strength of Al-Si, which is greater than that of Ga-Si, could also enhance the coverage)[32]. Thus, the difference in the critical thickness

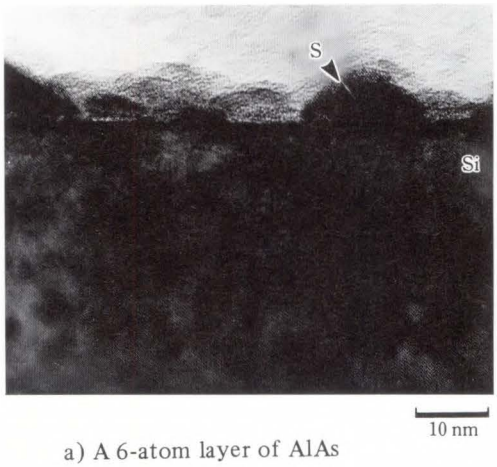

a) A 6-atom layer of AlAs

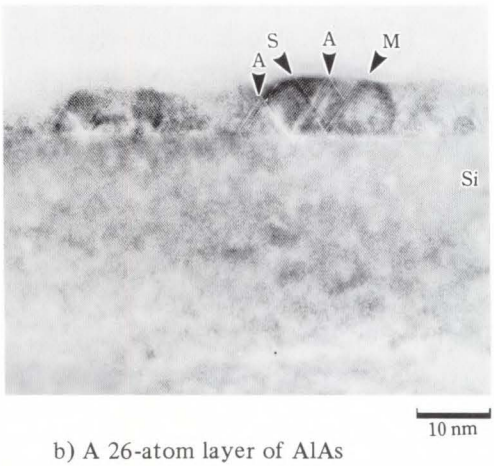

b) A 26-atom layer of AlAs

Fig. 12—(110) cross-sectional HRTEM images illustrating the initial stage of growth of AlAs layers on (001)Si substrates. In both cases, a 10-atom layer of GaAs was grown to protect the surface of the AlAs layer.

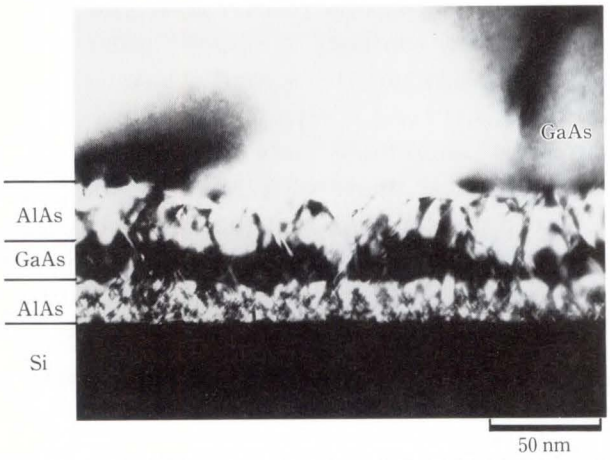

Fig. 14—A (110) cross-sectional dark-field TEM image of GaAs with AlAs/GaAs/AlAs buffer layers grown on (001)Si substrate taken under the 002 reflection.

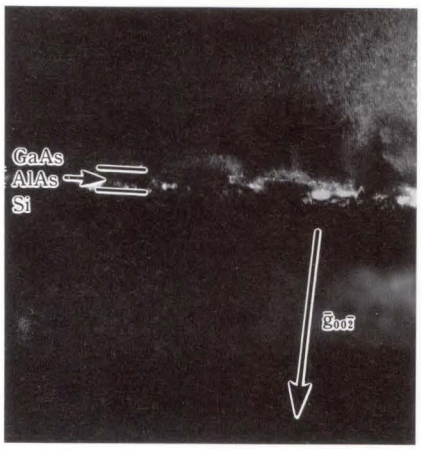

a) A 36-atom layer of AlAs

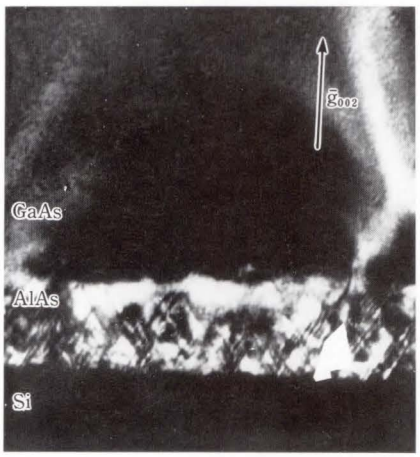

b) An 80-atom layer of AlAs

Fig. 13—(110) cross-sectional dark-field TEM images of GaAs (2 μm)/AlAs/(001)Si heterostructures grown on (001)Si substrates taken under the 002 reflection.

between AlAs and GaAs could be explained by the improvement in coverage in the case of AlAs deposition.

4.1.3 Defects in the AlAs layer

Two types of defect are present in the AlAs layer, stacking faults and microtwins. They are generated at the initial stage of growth as shown in Figs 12a) and b). In both micrographs, stacking faults and microtwins are indicated by S and M, respectively. Self-annihilation of these defects is observed at regions indicated by A in Fig. 12b). As the AlAs grows thicker, the density of these defects increases as shown in Fig. 13b). Generation of such a high density of defects in AlAs may be associated with a low stacking fault energy and the softness of the

material. However, surprisingly, the defects annihilate at the interface between the AlAs and the thick upper GaAs layer. From the images shown in Figs. 12b) and 13b), possible models for the self-annihilation of stacking faults and microtwins are as follows:

1) Stacking faults propagating on different {111} planes annihilate where they meet each other;
2) Microtwins terminate on the {211} planes normal to the twin boundary at the interface between the AlAs and the thick upper GaAs layer to minimize the strain energy.

The results described above lead us to the conclusion that using an AlAs layer grown by atomic layer epitaxy as a buffer layer is a very promising way to achieve high-quality GaAs/Si heterostructures with a low defect density.

4.2 Anti-phase boundaries in GaAs and GaP crystals grown on (001)Si by MOVPE

In highly mismatched hetero-epitaxy, apart from the problems of lattice mismatch and thermal mismatch, the generation of anti-phase domains (APDs)[38] in the growth of polar semiconductors such as GaAs on (001) nonpolar semiconductors such as Si, has received considerable attention in the past. It is now recognized that they can be controlled in practice by using substrates with an off-angle of more than 2° off Si[39]. However, the exact nature and mechanism for their generation (and annihilation, if any) is not yet fully understood. At present, two unique TEM techniques can be employed for surveying APDs. One is the convergent beam electron diffraction (CBED) approach[40]. The other is the ±002 dark-field imaging technique proposed by Kuan et al[41]. The latter method is a very simple one: we have also employed this method in our experiments. The technique enables us to produce distinct dark and bright contrast on both sides of the anti-phase boundary (APB), although the contrast is strongly related to the foil thickness. In this section, we describe for the first time a detailed TEM investigation of APDs and present direct evidence for their self-annihilation.

Crystals were grown by MOVPE. Two types of heterostructure are examined in this study. Heterostructures I consist of a GaP buffer layer (0.1 mm), followed by strained layer superlattices (SLSs) of $GaP/GaAs_{0.5}P_{0.5}$ and $GaAs_{0.5}P_{0.5}/GaAs$ (5 periods for each SLS and 20 nm for each layer), and finally a thick GaAs layer (4 mm). The growth temperatures for the GaP, SLSs and GaAs were 900 °C, 750 °C and 750 °C, respectively. TMGa, AsH_3 and PH_3 were used as reactants {the growth procedure is described in detail elsewhere[42),43)]}. Heterostructures II are grown by standard two-step MOVPE. They consist of a GaAs buffer layer (12.5 nm) grown first at 400 °C, and a thick GaAs layer (3 μm) grown at 650 °C. In both cases, the heterostructures were grown on Si substrates with the following orientations: Types Ia and IIa were grown on (001) ± 0.5° Si substrates and Types Ib and IIb on (001)2° off toward the [110] direction.

4.2.1 Evaluation of Types Ia and IIa structure

First, plan-view and cross-section TEM observations were performed for Type Ia and IIa structures. The plan-view observations reveal uniformly distributed domain-like regions of the type shown in Fig. 15. We conclude that these regions correspond to APDs for the following reasons:

1) No extra spots for small-angle tilt boundaries are found in the electron diffraction pattern from the area containing the domain-like regions.
2) A part of the boundary has fringe contrast, but this is not due to a stacking fault since the fringe is not asymmetric in the dark-field image (stacking faults exhibit asymmetric fringe contrast).
3) In electron diffraction patterns from areas which include the domain-like regions in the (110) and the $(1\bar{1}0)$ cross-sections, no twin-related spots are observed.
4) From cross-sectional observations, the contrast of the domain itself in a dark field image is reversed when the reflection vector changes from 002 to $00\bar{2}$ as illustrated in Fig. 18 (Fig. 18 is described in detail later).

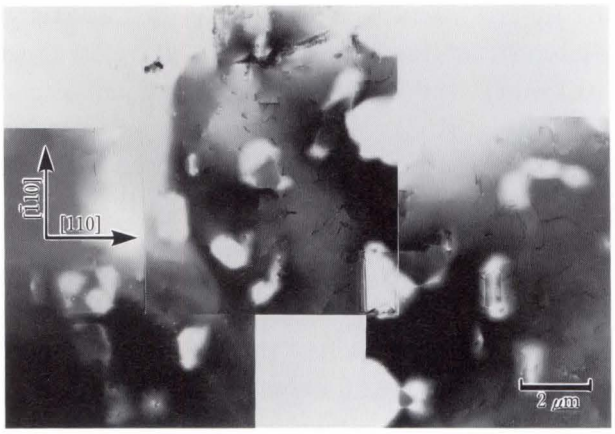

Fig. 15—A (001) plan-view TEM image of APDs in the GaAs top layer of the Type Ia structure, taken under the < 001 > zone-axis illumination.

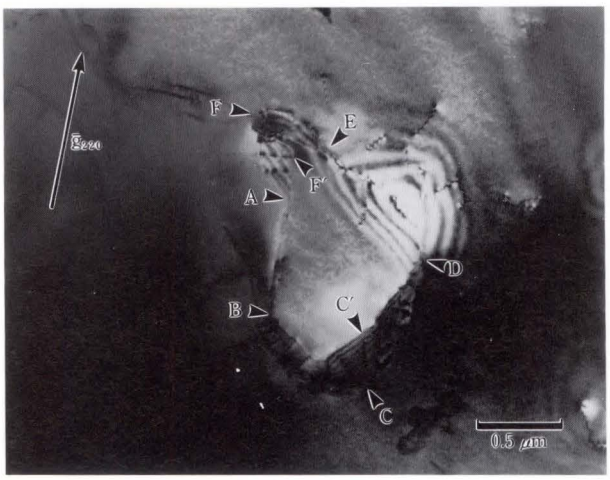

Fig. 16—A (001) plan-view bright-field TEM image of an APD in the GaAs top layer of the Type Ia structure, taken under the 220 reflection.

The domain size is 0.5-2 μm. Each APD has a different geometry; they are found to be three-dimensional extended polygon-shaped structures consisting of sub-boundaries nearly normal to the (001) plane and inclined to the (001) plane. Figure 16 shows a typical plan-view bright-field TEM image of an APD taken under the 220 reflection. Since the sub-boundaries indicated by A-B and D-E do not display fringe contrast, they are presumably normal to the (001) plane. In view of their elongations, they are possibly (110)- and (100)-oriented boundaries, respectively. From plan-view observations, it is found that most of the APBs normal to the (001) plane are (110) or (100) boundaries. The

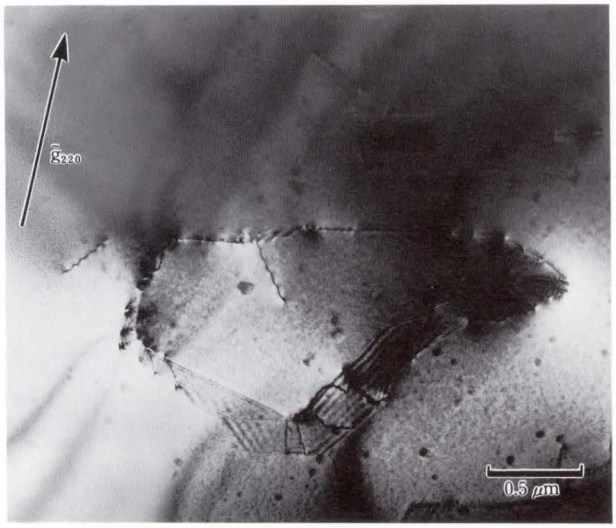

Fig. 17—A (001) plan-view bright-field TEM image of an APD in the GaAs top layer of the Type IIa structure, taken under the 220 reflection.

other boundaries indicated by B-C-D-C'-B and A-F'-E-F are curved and exhibit fringe contrast. This may be due to the phase-shift of the electron beam when it enters the APD from the matrix crystal. Thus, they are inclined to the (001) plane and are perhaps a mixture of tilted APBs indexed as (11n), such as (111) and (112) and (10n), such as (101) and (102). In each boundary, a number of dislocations can be seen. In this case, these boundary dislocations are invisible under the reflection of 400 or 040. Since most of the APBs are not lying on the {111} plane, these boundary dislocations cannot glide. Also in the case when stacking faults and microtwins are generated in the APD, they cannot be expected to extend to the region outside the APD, since there is a clear difference in atomic arrangement between the APD and the matrix crystal. From stereoscopic observations, it is found that the circuit indicated by A-B-C-D-E-F-A in Fig. 16 is lying below the top surface and that the circuit indicated by A-B-C'-D-E-F'-A is lying on the top surface. This finding suggests that the domain size becomes smaller during crystal growth with self-annihilation occurring as a final stage.

In Type IIa structures, similar APDs to those described above were also observed as shown in Fig. 17, although not all of the APDs annihilate.

Surprisingly, we have discovered direct

evidence for this speculation in the cross-section TEM image shown in Fig. 18. Figures 18a) and b) are dark-field images taken under weak 002 and $00\bar{2}$ reflections obtained from the (110) cross-section specimen of Type Ia. A high density of defects (mostly dislocations) is present in both the GaP buffer layer and the SLSs, since the crystal is grown on (001) ±0.5° Si. In both figures, a domain extending from the interface between the Si substrate and the GaP buffer layer into the GaAs is observed (see the domain denoted by APD). Note that in Fig. 18a) the domain contrast is bright whereas that of the matrix region is dark. On the other hand, the opposite result is obtained in Fig. 18b). Since the crystal structures on both sides of an APD are related to each other by 180° rotation about the <110> direction, the 002 reflection from the crystal on one side of an APB should be equivalent to that of the $00\bar{2}$ reflection from the other side of the APB. We have calculated the amplitude of the transmitted beam and the 002 and $00\bar{2}$ beams in an (110) diffraction pattern from perfect GaP and GaAs crystals as a function of foil thickness (see Fig. 19). It is found that due to the lack of twofold axes along the <110> direction in the zinc-blende structure, the amplitudes of the 002 and the $00\bar{2}$ reflections are not equal for most crystal thicknesses. Thus, one can conclude that the image intensities from both sides of the APB must be different except for certain foil thickness. In Figs. 18a) and b), the upper part of the micrograph corresponds to the edge of the TEM specimen. The thickness is almost constant in the direction parallel to the interface and gradually increases from the upper part (edge of the foil) to the lower part. The estimated thickness of the major part of the foil where the APD is clearly observed (region denoted by APD) is roughly 30-50 nm. Based on this consideration, the domain observed in Figs. 18a) and b) is identified to be an APD similar to that shown in Fig. 16. As can be seen in Figs. 18a) and b), the APD annihilates in the intermediate layer of GaAs by changing the orientation of sub-boundaries from normal to (001) to higher-index-planes (see also the region denoted by arrows).

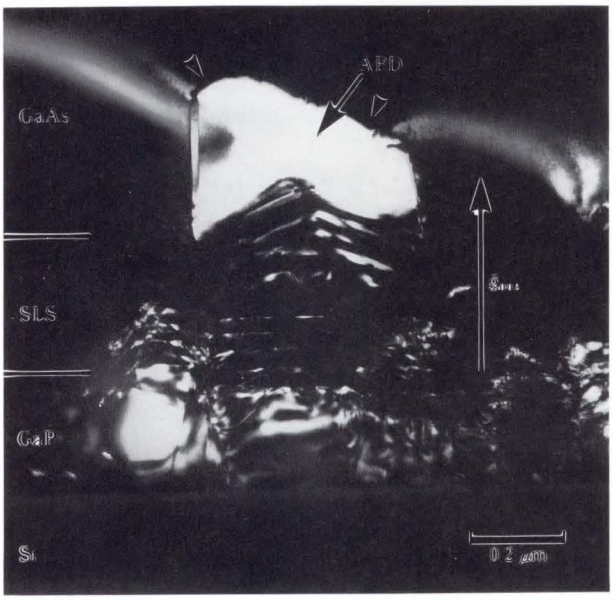

a) $\bar{g} = 002$

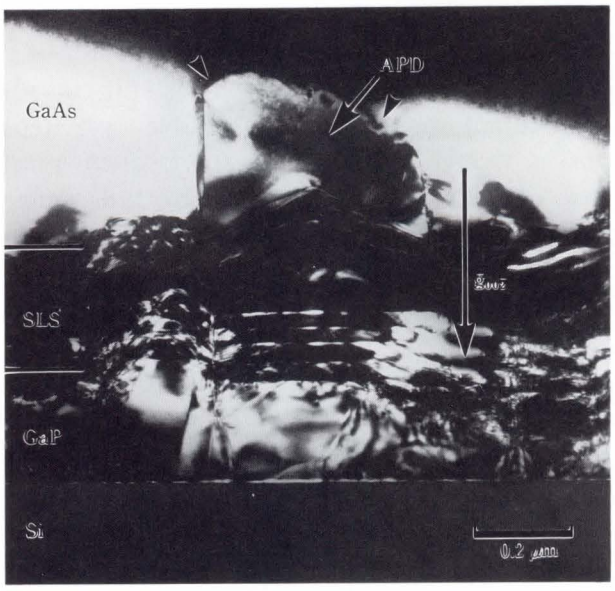

b) $\bar{g} = 00\bar{2}$

Fig. 18—(110) cross-sectional dark-field TEM images of the Type Ia structure.

On the basis of these results, the following scenarios are derived for the self-annihilation mechanism of APDs during crystal growth:

1) At the initial stage of crystal growth, three-dimensional island growth proceeds, at the step-edges. By the coalescence of islands with two different phases (i.e. matrix-phase and anti-phase), APDs are structurally introduced. The APDs may be originally co-

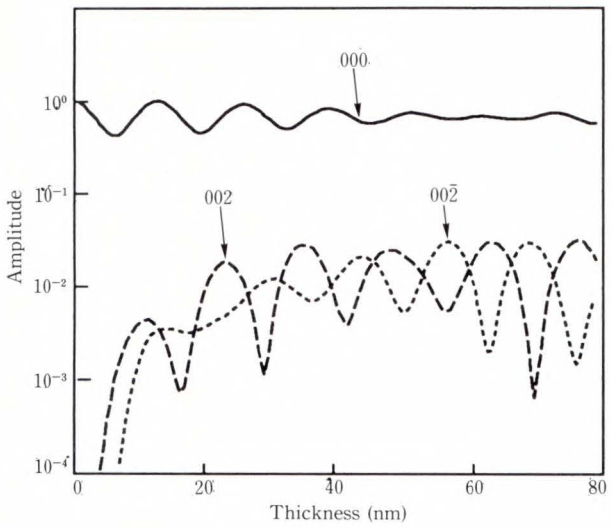

a) GaAs

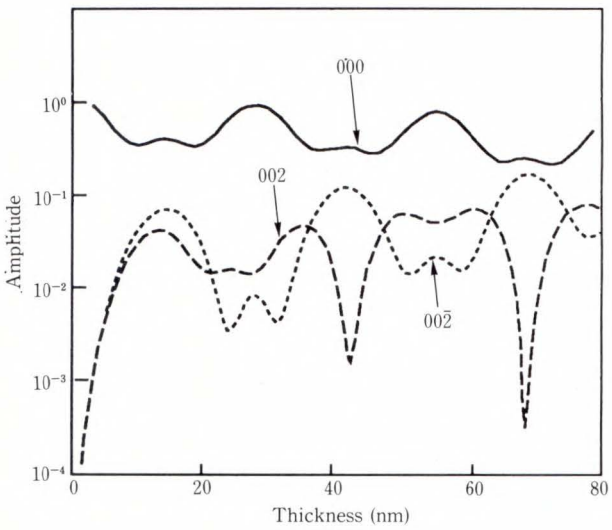

b) GaP

Fig. 19—Calculated thickness dependence of the amplitudes of the 000, 002, and 00$\bar{2}$ reflections from GaAs and GaP crystals.

lumnar-shaped consisting predominantly of sub-boundaries nearly normal to the (001) plane such as (110) and (100). Alternately, the sub-boundaries may be inclined to the (001) plane from an early stage of crystal growth, in which case step 3) takes place immediately.

2) When the thickness of the APD reaches a critical value, these sub-boundaries change their orientation to a higher-index plane inclined to the (001) plane {such as the (112) plane, which is the orientation with lowest energy[44]}, so as to minimize the total energy in the system.

3) By the coalescence of APBs with opposite orientation, the APD finally annihilates itself at the intermediate layer. At present, the reason for the existence of (100) APBs at the initial stage of crystal growth is not clear. Since not all of the APDs annihilate, it is also difficult to estimate the critical thickness for step 2).

4.2.2 Evaluation of Type Ib and IIb structures

Plan-view observations of both Type Ib and IIb structures reveal no APDs similar to those shown in Figs. 16 and 17 in the surface region of the GaAs layer.

Figures 20a) and b) are 002 and 00$\bar{2}$ dark-field TEM image from the (110) cross-section of a Type Ib structure, illustrating the interface between the GaP buffer layer and Si substrate. Hillock-like micro-domains are observed in the GaP buffer layer near the interface (see arrows). The variation in the diffraction contrast of these micro-domains is very similar to that in the APDs shown in Fig. 4. Moreover, in this case, reasons 1)-4) described previously (see the beginning of subsection 4.2.1), are satisfied. Therefore, it is concluded that they are also APDs, although very small, with diameters of 10-20 nm. Provided that there are a certain number of monolayer steps on the surface of a (001) 2° off Si substrate (there is still controversy about the existence of double-layer steps on the vicinal surface of Si), the frequent presence of APDs is well explained by the average spacing between monolayer steps, i.e. approximately 4 nm. In the Type IIb structures, hillock-like APDs similar to those in Type Ib were also observed.

Regarding the self-annihilation of APDs at the initial stage of growth on tilted substrates, there have been two competing models, one by Pukite and Cohen[45] and the other by Kawabe et al[46]. Although the sub-boundaries of the hillock-like APDs shown in Fig. 20 are lying nearly on {211} planes, our findings strongly support the latter model[46].

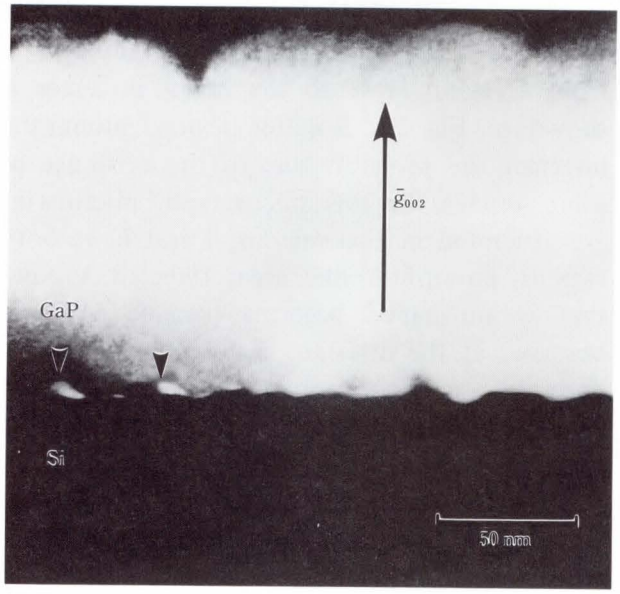

a) $\bar{g} = 002$

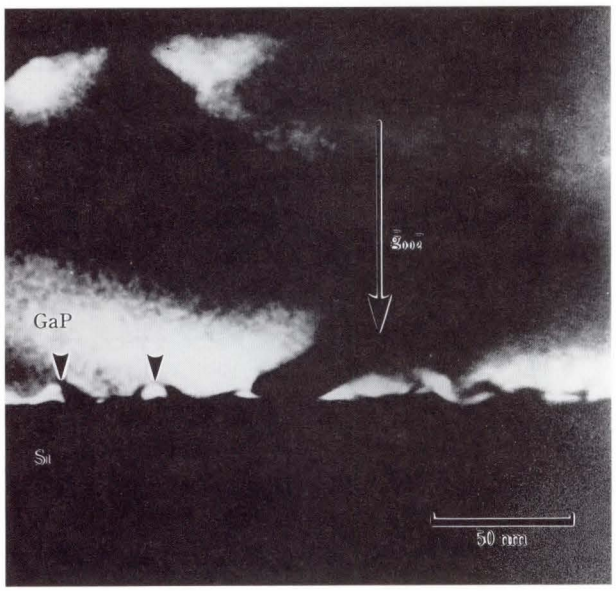

b) $\bar{g} = 00\bar{2}$

Fig. 20—(110) cross-sectional dark-field TEM images of the GaP/Si interface of a Type Ib structure.

4.3 Defects in GaAsSb crystals grown on (001)InP by molecular beam epitaxy

GaAsSb is an important material for opto-electronic and high-speed devices[47]. Recently, we have reported on the growth of GaAsSb crystals on (001)InP substrates by molecular-beam epitaxy (MBE)[48]. To produce devices with suitable properties and reliability, it is important to obtain defect-free and thermally stable materials. In this section, we describe the TEM evaluation of defects in GaAsSb crystals grown on (001)InP substrates by MBE.

$GaAs_{1-x}Sb_x$ ($x = 0.49$) is grown on (001)InP substrates by MBE at temperatures in the range 460-590 °C[48]. During growth, the substrates are rotated at 15 r/min to ensure uniform composition, thickness and carrier concentration. The growth rate and the V/III partial pressure ratios are kept at 1.2 mm/h and 7.5, respectively. The epitaxial layers are 2.5 μm thick.

Three types of defect generated at the hetero-interface have been observed. They are stacking fault tetrahedra, microtwins and misfit dislocations.

4.3.1 Stacking faults

Figure 21 illustrates a typical optical micrograph of the surface of a GaAsSb crystal grown at 590 °C. A high density of surface defects is observed. They are hillock-like defects lying along the <110> direction, and are very similar to the oval defects in MBE-Ga(Al)As crystals[49]. The defect structure observed by TEM at these surface defects is shown in Fig. 22. Stacking faults lying on the four equivalent {111} planes are seen. Since the thin foil includes only the surface region of the epitaxial layer, one can expect that the surface defects correspond to stacking fault tetrahedra[50]. The stacking faults often multiplied as denoted by X. In addition, threading dislocations and small stacking faults are found inside the tetrahedra. By considering the length of the stacking faults at the surface, their basal {111} planes, and the epitaxial layer thickness, it is deduced that they originated at the hetero-interface. The density of these defects can be reduced by lowering the growth temperature and cleaning the substrate with appropriate As over-pressure. Therefore, the dominant factors affecting their generation could be the evaporation of phosphorous atoms from the substrate and/or the existence of some oxide or contamination on the substrate surface.

4.3.2 Microtwins

Microtwins are occasionally observed in epitaxial layers grown at higher growth temperatures. They also originate from the hetero-interface, extending to the surface area with {111} boundaries. Some of them terminate in

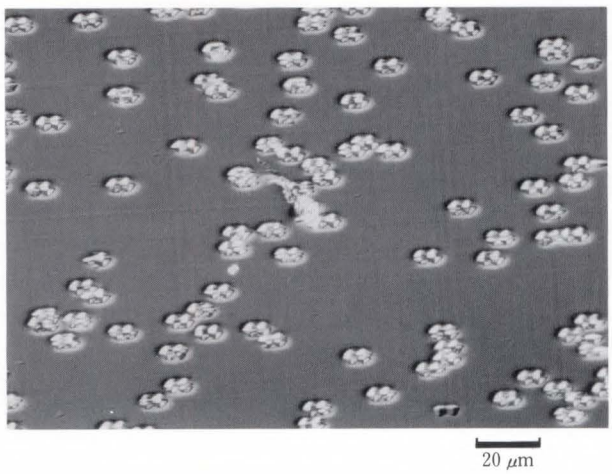

Fig. 21—An optical micrograph of defects revealed on the surface of an MBE-grown GaAsSb crystal on (001)InP substrate.

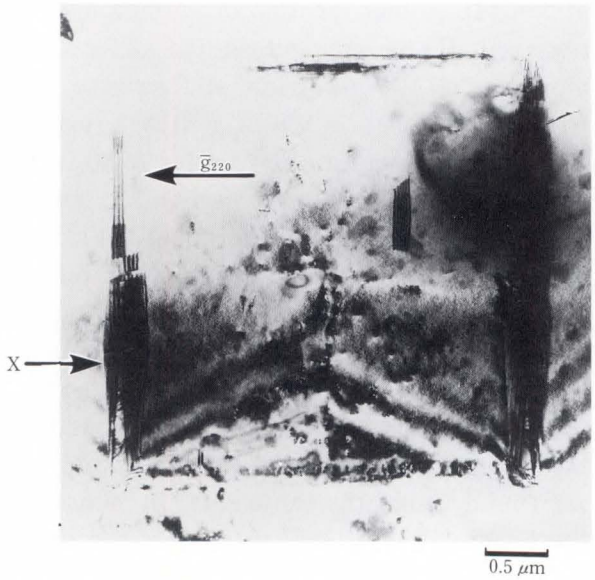

Fig. 22—A (001) plan-view bright-field TEM image of a stacking fault tetrahedron corresponding to the surface defect shown in Fig. 21, taken under the 220 reflection.

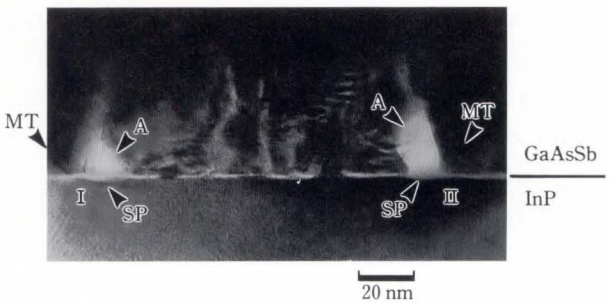

Fig. 23—A low magnification (001) plan-view HRTEM image of the GaAsSb/(001)InP interface.

mid-layer with {211} boundaries. A HRTEM image of a GaAsSb crystal grown at 590 °C from a region close to the hetero-interface is shown in Fig. 23. Brighter regions along the interface are probably due to the existence of some oxides. In this micrograph, microtwins are generated in two regions, I and II. In both regions, amorphous-like areas (labeled A), and shallow pit-shaped patterns (labeled SP), are observed at the interface just below the amorphous-like area. Microtwins (labeled MT) are generated only in the region adjacent to the areas.

Based on these results, the following mechanism is suggested for the generation of microtwins:

1) Evaporation of phosphorous atoms from the substrate surface (formation of In-rich droplets on the surface);
2) Generation of amorphous areas as a consequence of an In-rich melt;
3) Growth of crystals with different lattice constants around the amorphous areas;
4) Generation of microtwins by the relaxation of the stress resulting from the lattice mismatch between the normal GaAsSb areas and those formed in step 3).

Thus, microtwins can be eliminated by methods similar to those described for stacking faults.

4.3.3 Misfit dislocations

Since we have successfully grown GaAsSb on (001)InP with nearly lattice-matching conditions ($\Delta a/a < 1 \times 10^{-3}$), generation of misfit dislocations is unexpected. However, we have occasionally found dislocations at the hetero-interface with spacing in the range 30-100 nm. All of these dislocations have dissociated into two partials. Figure 24 is an HRTEM image which displays a stacking fault between the two partials X and Y. There is clear anisotropy in the widths of the stacking fault segments contained in the substrate and epitaxial layer. This may be due to the different behavior of 90°- and 30°-partials under different strain fields[17].

A possible model for the formation of these dislocations is as follows:

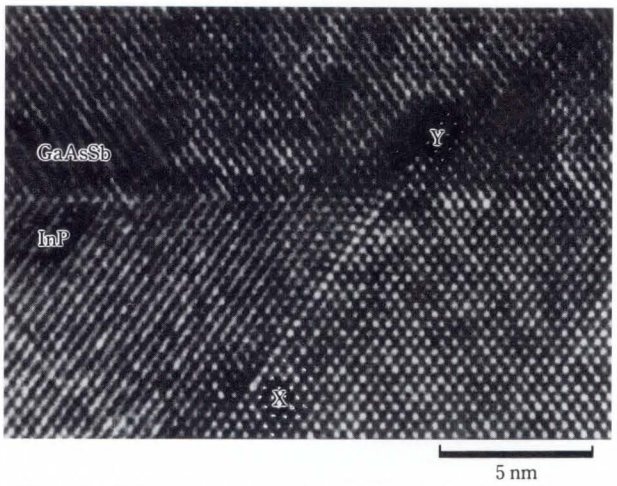

Fig. 24—A (110) cross-sectional HRTEM image of a dissociated misfit dislocation generated at the GaAsSb/(001)InP interface.

1) At the initial stage of growth, due to poor control of the gas flow (particularly overshooting of the Sb-beam), an Sb-rich ternary alloy is grown, resulting in a compressive and a tensile strain field in the epitaxial-side and the substrate-side, respectively;
2) As the crystal grows thicker, 60°-type misfit dislocations are generated by the relaxation of the resulting stress;
3) Due to different behaviors of 90°- and 30°-partials, the 90°-partial first extends into the substrate, then the 30°-partial extends into the epitaxial layer.

To prevent the introduction of such defects, more precise control of the gas flow at the initial stage is required.

4.4 Precipitates in heavily Fe-doped InP crystals grown by metalorganic chemical vapor deposition

Semi-insulating InP is an important material for opto-electronic and high-speed devices. Until now, much effort has been devoted to achieving high resistivity[51)-53)]. It has previously been reported that resistivities of $10^9\ \Omega\cdot$cm have been successfully obtained for Fe-doped InP grown by MOVPE[54)]. However, iron-phosphorous precipitates are produced in the crystal during growth. Nakahara et al.[55)] have undertaken a detailed investigation of the precipitates by TED analysis and EDX and have concluded that they are composed of FeP. However, little is known about the nature and distribution of the precipitates, or their generation mechanism. In this section, more detailed characteristics of the precipitates and the relationship between the Fe-doping gas flow rate and precipitate density are described based on the TEM analysis.

InP crystals are grown on (001)InP substrates at 650 °C by atmospheric pressure MOVPE. Phosphine (PH_3) and trimethylindium (TMIn) are used as reactants. The V/III partial pressure ratio is kept at 20. The electron concentration of the non-doped layer is about 2×10^{15} cm^{-3}. Ferrocine $Fe(C_5H_5)_2$ vapor is used as the Fe-doping gas and its flow rate is varied in the range 0-100 ml/min.

4.4.1 Microstructure of precipitates

First of all, an Fe-doped InP layer grown with the maximum gas flow rate (100 ml/min) was examined. As previously reported by Nakahara et al.[55)], a large number of circular precipitates are observed in a dark-field image, particularly in the area close to the edge of the thin specimen. They may be expected to stay on the surface of the specimen after etching since they are thought not to be dissolved by the Br_2/CH_3OH etchant[55)]. However, in the region slightly away from the edge of the specimen, the density of precipitates is found to be nearly constant as shown in Fig. 25. Figures 25a) and b) are bright-field and weak-beam dark-field TEM images of precipitates taken under the 220 and the 660 reflections with positive s, which is a deviation parameter from an exact Bragg condition.

From these images, one can differentiate between precipitates buried in the matrix and those lying on the surface as follows:

1) Precipitates exhibiting parallel Moiré fringes with constant spacing are buried in the matrix (we call these Type A precipitates);
2) Precipitates which do not exhibit Moiré fringes are lying on the surface (Type B).

In the latter situation, the probability of direct double reflection between precipitates and matrix is considered to be much lower as a result of possible oxide presence and the small

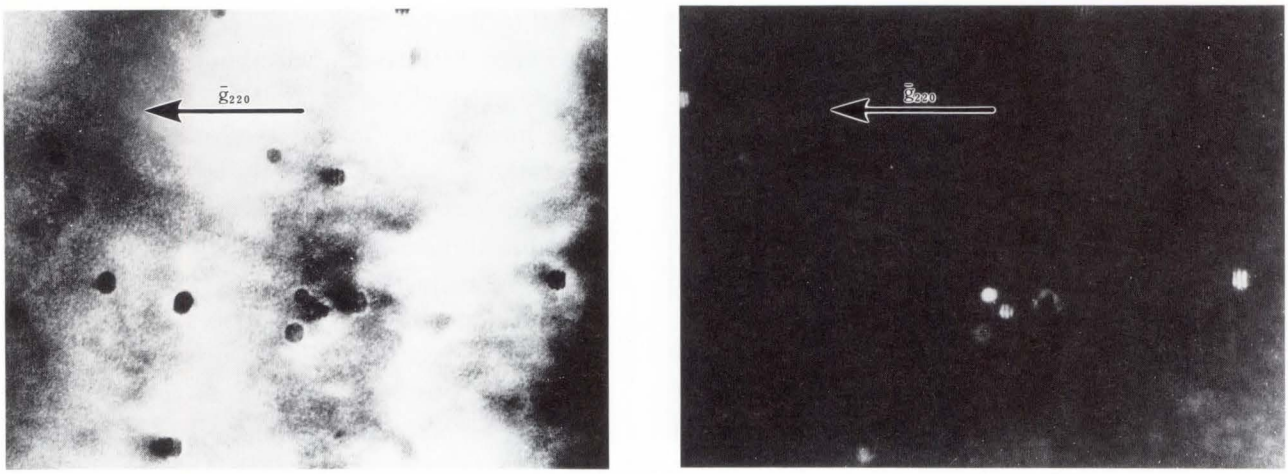

a) Bright-field image b) Weak-beam dark-field image

Fig. 25—Plan-view TEM images of Fe-precipitates in sample 1 (the gas flow rate is 100 ml/min) after chemical etching.

contact area between the two materials. Type B precipitates are generally out of contrast in the weak-beam image since there is no strain associated with them. However, they occasionally do exhibit bright contrast presumably as a result of sticking force between the precipitate and the matrix at the surface. In order to confirm this, bright-field images were obtained under many beam conditions.

Typical images of Type A precipitates obtained from the same specimen are illustrated in Fig. 26. Note that all of these precipitates

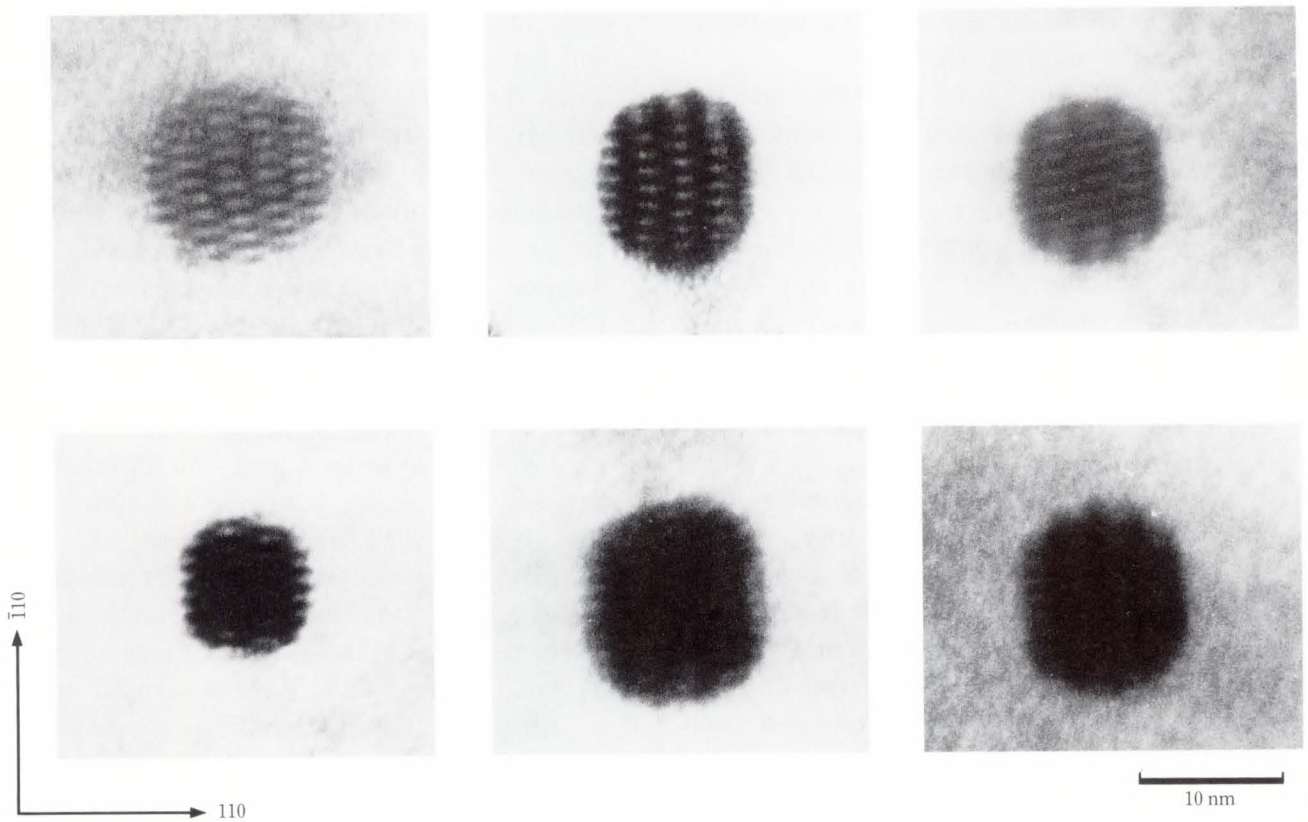

Fig. 26—A series of plan-view bright-field TEM images of precipitates taken under many beam diffraction conditions [001] zone-axis condition. Note the Moiré fringes in three different orientations.

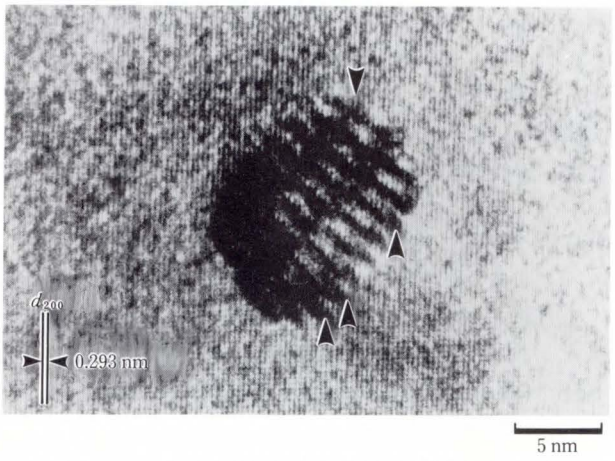

Fig. 27—A plan-view HRTEM image of the precipitate taken under nearly zone-axis condition. Two sets of 200-lattice frings can be seen. A small amount of lattice distortion is visible at the precipitate-matrix interface (see arrows).

exhibit three kinds of Moiré fringe with different orientations and periodicities. Therefore, there is a certain orientation relationship between the precipitates and the matrix crystal. Although nano-probe electron diffraction experiments (2-5 nm probe dia) were performed on the precipitates, the exact orientation of the precipitates could not be determined due to double reflection of electrons at the precipitate-matrix interface. Figure 27 is a plan-view HRTEM image of a precipitate. The precipitate also exhibits Moiré fringes similar to those shown in Fig. 26. Lattice fringes corresponding to d_{200} for InP can be seen. Slight misalignments of lattice fringes are occasionally found at the precipitate-matrix interface (see arrows). This result suggests that there is little strain field at the interface, which is consistent with the fact that the lattice parameter of InP is very close to that of FeP. Thus, the precipitates are coherent. Although precipitates were determined to be FeP by TED analysis[55], compositional analysis using EDX was carried out on them. Figures 28a) and b) are typical EDX spectra obtained from the matrix and the precipitate using an electron probe 2 nm in dia. Fe is clearly detected within the precipitate {see Fig. 28b)}.

4.4.2 Spatial distribution of precipitates

A (110) cross-sectional TEM observation was performed on Fe-doped InP crystals grown

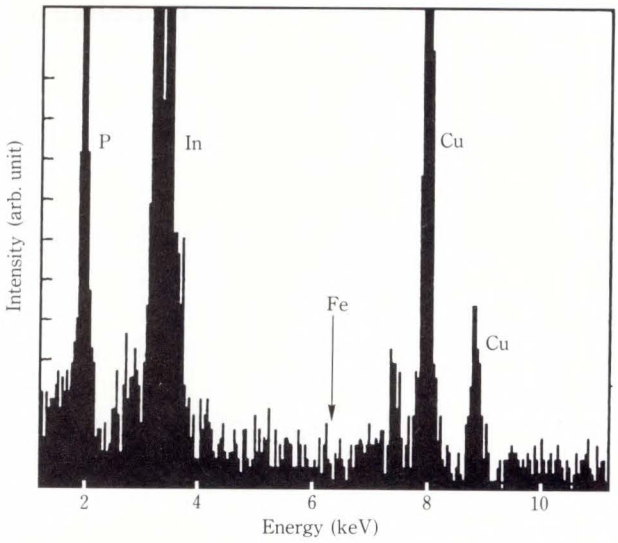

a) Matrix area

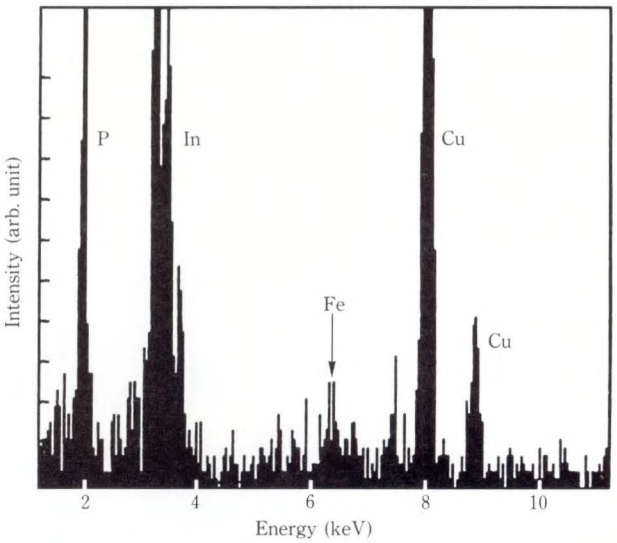

b) Precipitate area

Fig. 28—EDX spectra from the Fe-doped InP crystal (probe dia is nearly 2 nm).

with the maximum gas flow rate; the resulting image is shown in Fig. 29. High magnification images of the three areas indicated by a, b and c are shown in inserts a′, b′, c′, respectively. Precipitates are again observed as circular images indicating that they are spherical particles. Also note that the precipitates are uniformly distributed in the crystal. Since the interface between the epitaxial layer and the substrate is not clearly observed {the broken line in Fig. 29 is assumed to be close to the real interface from consideration of the thickness of the epitaxial layer determined from a scanning elec-

tron micrograph (SEM) image of a cleaved and stain-etched cross-section of the homo-junction}, it seems that there is no preferential segregation of Fe-atoms at the interface. Moreover, precipitates attached to the surface were not found at all.

4.4.3 Dependence of the density and diameter of precipitates on gas flow rate

The effect of the Fe-doping gas flow rate on the density and diameter of precipitates was also studied. Figures 30a) to d) show plan-view bright-field TEM images of precipitates in Fe-doped InP crystals grown with gas flow rates of 100, 30, 20 and 5 ml/min, respectively. Precipitates are observed in crystals grown with gas flow rates higher than 20 ml/min. Their density increases as the gas flow rate increases. However, their diameter is almost constant. Precipitates are not observed in crystals grown with gas flow rates lower than 5 ml/min. These results are summarized in Table 1. From secondary ion mass spectroscopy (SIMS) measurements, the total Fe concentration in sample 4 (gas flow rate 5 ml/min) in Table 1 is calculated to be approximately 1×10^{17} cm^{-3}, which is the solubility limit of Fe in InP at 650 °C.

4.4.4 Generation mechanism of precipitates

Based on the results described in subsections 4.4.1 to 4.4.3, three generation mechanisms for FeP precipitates can be proposed as follows:

1) FeP particles are first formed in the gas phase, then they are deposited onto the growth surface and are buried in the growing InP crystal.
2) FeP precipitates are formed directly on the growth surface through migration and segregation of Fe-atoms, and the strong reaction between Fe-atoms and P-atoms.

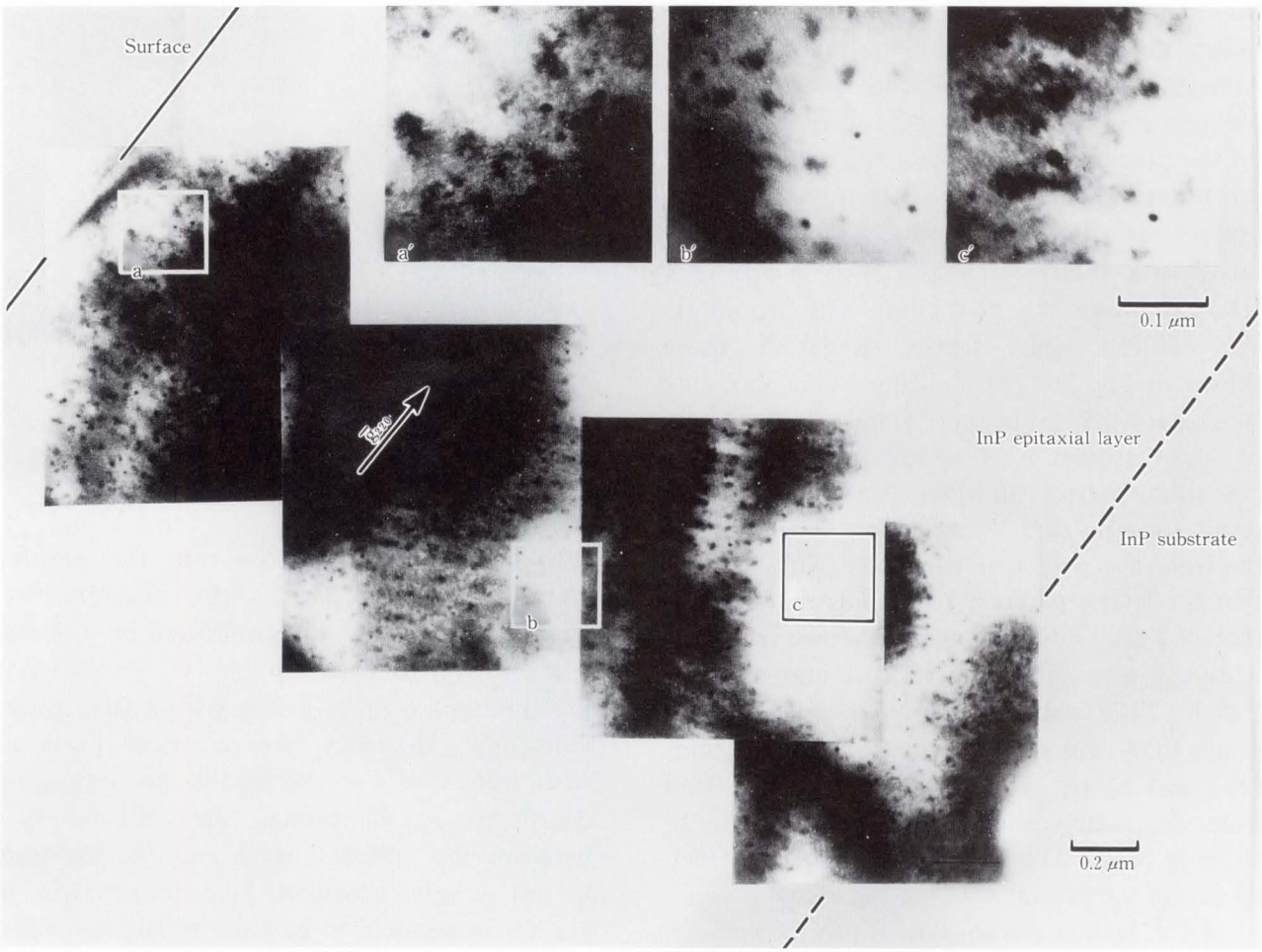

Fig. 29—A (110) cross-sectional bright-field TEM image from an Fe-doped InP crystal taken under $\bar{g} = 220$, $s > 0$. Inserts labeled a', b' and c' correspond to high magnification images of the areas denoted by a, b, and c.

3) In the growing InP layer, when the doped Fe-concentration exceeds the solubility limit, supersaturated Fe-atoms tend to segregate at some nucleation centers via rapid diffusion, and FeP precipitates start to grow. When the diameter of precipitates reaches a critical value, they can not grow any more due to the strain field accumulated around them.

Models 1) and 2) are unlikely since no FeP particles are found on the surface of As-grown InP layers, and no precipitates are observed in

Table 1. Dependence of Fe-doping gas flow rate on the density and diameter of precipitates

Sample No.	Gas-flow rate (ml/min)	Epitaxial layer thickness (μm)	Precipitate density (cm^{-3})	Precipitate diameter (nm)	
				Average	(max/min)
1	100	3	1×10^{14}	8.3	(3.8/11.2)
2	30	2	3×10^{13}	5.8	(4.1/11.6)
3	20	2.5	8×10^{12}	12.9	(5.8/18.6)
4	5	4	$<5 \times 10^{10}$	–	
5	1	3	$<5 \times 10^{10}$	–	
6	0.5	3	$<5 \times 10^{10}$	–	
7	0.2	3	$<5 \times 10^{10}$	–	

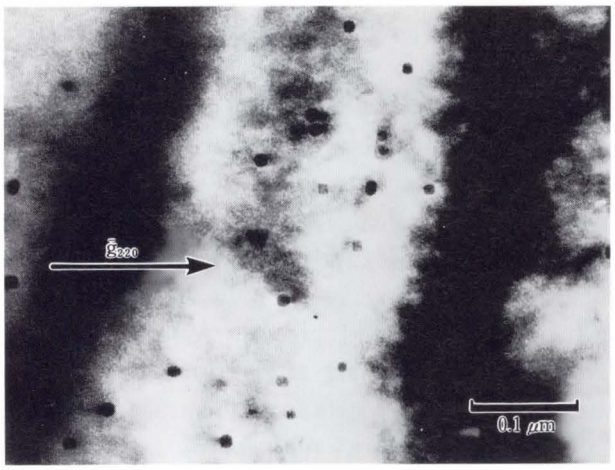

a) 100 ml/min

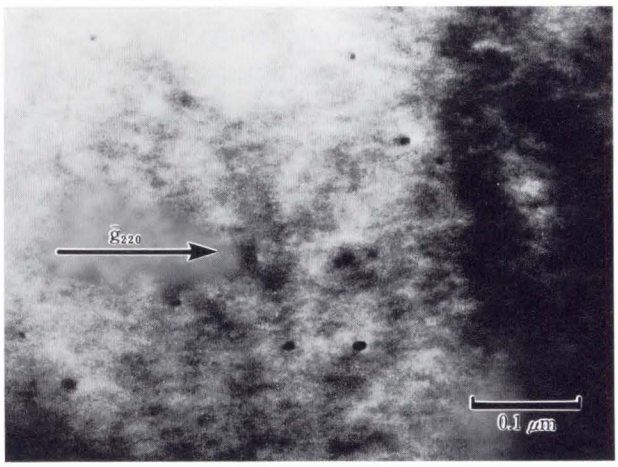

b) 30 ml/min

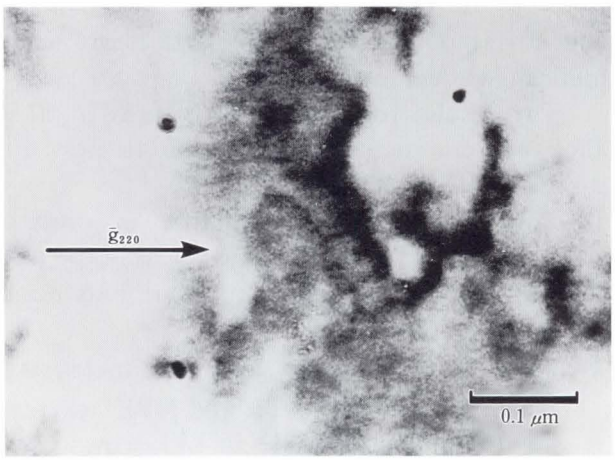

c) 20 ml/min

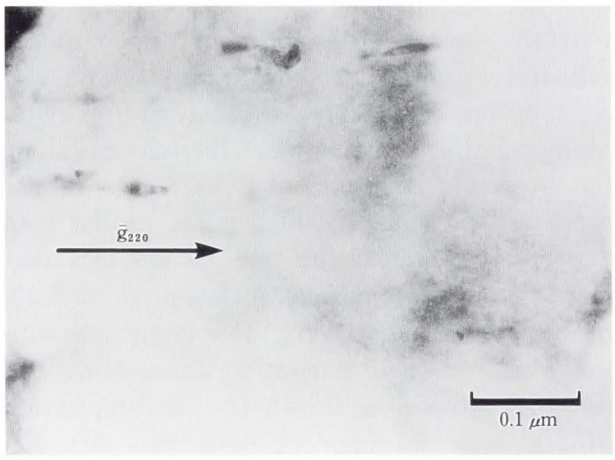

d) 5 ml/min

Fig. 30—Typical plan-view bright-field TEM images of FeP-precipitates in Fe-doped InP crystals grown under different gas flow rates, obtained by $\bar{g} = 220$, $s > 0$.

crystals grown with gas flow rates lower than 5 ml/min.

At present, model 3) is the most probable, based on the following evidence:

1) Precipitates are generated when the doped Fe-concentration exceeds the solubility limit;
2) Precipitates are uniformly distributed in the crystal and have almost constant diameter; and
3) Precipitates are spherical and coherent.

5. Evaluation of ordered structures in III-V alloy semiconductors

Apart from the materials issue of defect generation, in most III-V alloy semiconductors there are two major issues regarding the thermal instability of the materials; namely the generation of "modulated structures[56)-60)]" and the generation of "ordered structures[61)-63)]".

The modulated structures are generated in alloy semiconductors such as InGaAs, InGaP and GaAsSb whose compositions are inside the spinodal region[56)]. They are observed as quasi-periodic diffraction contrast in bright- or dark-field images under two-beam or multi-beam conditions. They develop in the two equivalent directions of <100> and <010>, and they are columnar in the <001> growth direction. It is also clear that structures with both long (50-200 nm) and short (5-20 nm) periodicities are formed when the composition is outside the spinodal region[57)-60)]. Thus, one can expect that the former structures are formed during growth by spinodal decomposition, and the later ones during the cooling process after growth. Moreover, the compositional fluctuations along the structure measured by EDX are in the range 2-3 percent[58)], which is far smaller than expected. This may be due to the fact that in semiconductors, atomic diffusion in the bulk or on the surface is very slow compared with metal alloys. Their generation does not depend on the growth method. The decomposition process may be enhanced by atomic diffusion at the liquid-solid interface for LPE growth and at the growth surface for MOVPE, VPE and MBE.

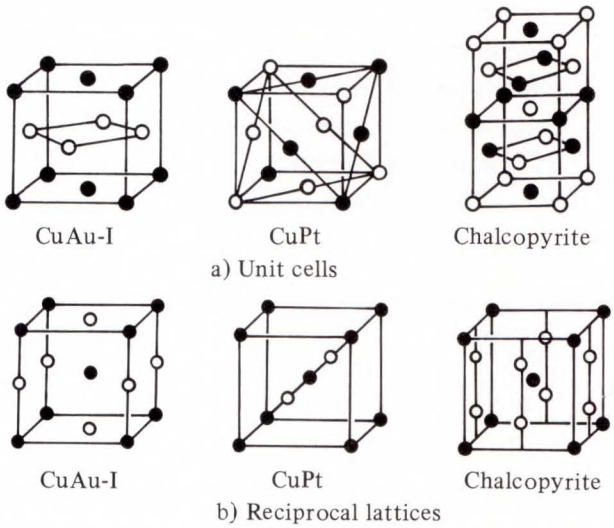

Fig. 31 – Schematic diagrams of three types of substitutionally ordered structure in the fcc lattice of AB-type binary compounds.

On the other hand, recently, ordered structures (or natural superlattices), in which atoms of two different elements in column III or V arrange periodically in lattices, have been observed in various III-V alloy semiconductors[61)-83)]. In most cases, the ordered structures are generated locally in the crystal, and the degree of ordering is strongly affected by the growth method and growth conditions. It is known that there are three types of substitutionally ordered structures in face centered cubic (fcc) lattices of AB-type binary alloy systems. They are CuAu-I (Ll_0), CuPt (Ll_1) and Chalcopyrite (El_1), whose atomic arrangements and corresponding reciprocal lattices are schematically shown in Fig. 31[84)].

The results for ordered structures in III-V alloy semiconductors obtained up to now are summarized as follows:

1) The most common structure in crystals grown on a (001) substrate is CuPt-type (see Fig. 31), and other structures are only occasionally observed.
2) They are very often generated in crystals grown by MOVPE, VPE and MBE, whereas no ordering takes place in LPE-grown crystals {except for one report of ordered structures in InGaAs by Nakayama et al.[71)], which is not yet confirmed elsewhere}.

3) Regarding CuPt-type structures, one can observe only two variants in the (110) cross-section. In particular, atomic steps on the growth surface are believed to play an important role in the generation of the ordered structures, since one of the two variants is preferentially enhanced when substrates tilted toward the <110> direction are used.
4) The ordering is not perfect and the ordered regions are plate-like microdomains lying on planes nearly parallel to the growth surface.
5) Defects such as anti-phase boundaries are often generated in the ordered region.
6) The degree of ordering depends on the growth temperature, V/III partial pressure ratio (in the case of MOVPE and MBE), and rotation velocity of the substrate.
7) Only strongly ordered InGaP crystals grown by MOVPE exhibit abnormal band gap energies (up to 50 meV lower than the normal value).

In this chapter, we describe the results of detailed TEM evaluations of ordered InGaP crystals grown on (001)GaAs and ordered InGaAs crystals grown on (110)InP.

5.1 Ordered structures in InGaP crystals grown on (001)GaAs by MOVPE

Regarding atomic ordering, Gomyo et al.[61] have been the first to report that in InGaP crystals grown by MOVPE, there is a strong relationship between the optical properties of the crystals and the degree of ordering. They have also concluded from the electron diffraction analysis that they are most likely to be superlattices of (110) planes ... Ga/Ga/In/In/Ga/Ga/In/In/ ... in the direction of [110] in the column III sublattice, i.e. $(InP)_2(GaP)_2$ super-lattices on the (110) plane. However, evidence of ordering is available only from a (001) plan-view specimen, and the three-dimensional atomic structure of the ordered InGaP was not clear.

In this section, the three-dimensional atomic structure of the MOVPE-grown InGaP crystals on (001)GaAs is described in more detail based on plan-view and cross-section TED analyses, and HRTEM.

Epitaxial growth is carried out by atmospheric pressure MOVPE. The InGaP layers are grown on (001)-oriented GaAs substrates tilted 2.5° towards $<1\bar{1}0>$, and the growth temperature is kept at 630 °C. PH_3, TMIn and TMGa are used as reactants, and the V/III partial pressure ratio is kept at 100. The epitaxial wafers examined in this experiment consist of a GaAs buffer layer and an InGaP layer of 800-900 nm and 10-400 nm, respectively. Two types of InGaP crystals are examined. One is an InGaP crystal grown with rotation of the substrate (20 r/min, Type I), and the other is an InGaP crystal grown without rotation of the substrate (Type II). In both types of InGaP crystal, the photoluminescence peak wavelength of the crystals is 652 nm at 77 K and the typical lattice-mismatch $\Delta a/a$ between GaAs and InGaP is 2×10^{-3}.

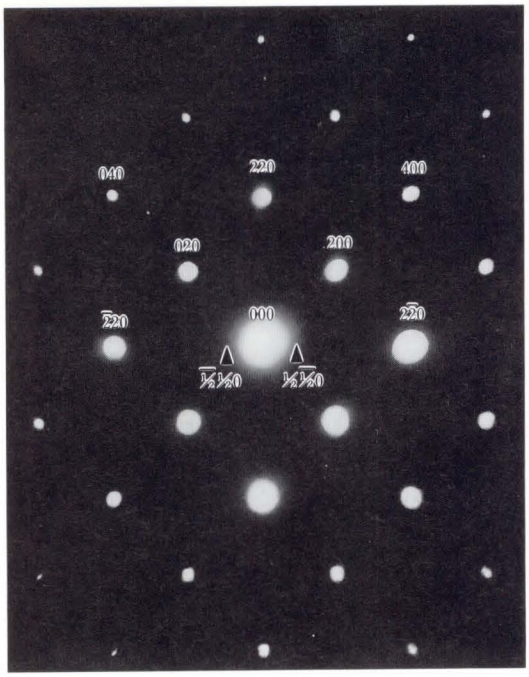

Fig. 32—A TED pattern from the (001) plan-view of a Type I InGaP crystal.

5.1.1 Evaluation of Type I crystals

1) Plan-view observation

First of all, plan-view observations were carried out. In the dark-field TEM image of the InGaP crystal taken under the 220 reflection, both coarse and fine modulated structures with periodicities of 30-50 nm and 5-10 nm, respectively, are clearly observed along the two equivalent directions of [100] and [010][57)-60].

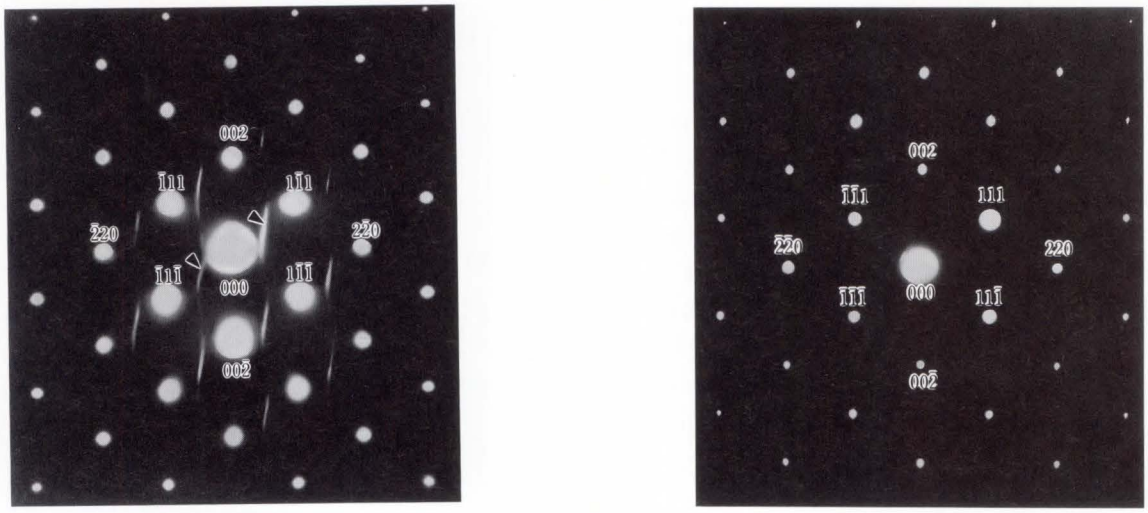

a) $(\bar{1}\bar{1}0)$ cross-section

b) $(1\bar{1}0)$ cross-section

Fig. 33—TED patterns from the $(\bar{1}\bar{1}0)$ and the $(1\bar{1}0)$ cross-section of a Type I InGaP crystal.

Next, a TED analysis was performed on the (001) plan-view specimen as illustrated in Fig. 32. Extra-spot pairs are observed on both sides of the matrix spots along only one <110> direction.

The extra-spot pairs are indexed as nearly $[h \pm 1/2, k \mp 1/2, 0]$ for an [hk0] matrix spot[61]. However, careful measurement of the positions of these extra spots confirmed that each one is located slightly inside the ideal position described above.

2) Cross-sectional observation

Cross-sectional TEM observation has been carried out on both the $(\bar{1}\bar{1}0)$ and the $(1\bar{1}0)$ orientations. Pronounced extra spots (here referred to as "superstructure spots") and streaks are present in the $(\bar{1}\bar{1}0)$TED pattern {see Fig. 33a)}, but not in the $(1\bar{1}0)$TED pattern {see Fig. 33b)}.

The characteristic features of the diffraction pattern are as follows:

i) the presence of superstructure spot pairs at positions indexed as $[h \pm 1/2, k \mp 1/2, l \pm 1/2]$ for an [hkl] matrix spot {for example, the positions indicated by arrows in Fig. 33a)};

ii) the appearance of streaks around the superstructure spots lying along both the [001] and the $[00\bar{1}]$ directions, but slightly tilting (a few degrees) toward the $[1\bar{1}0]$ and the $[\bar{1}10]$ directions, respectively {however, no superstructure spots are found at positions indexed as $[h \pm 1/2, k \pm 1/2, l \pm 1/2]$, as shown in Fig. 33b), nor are any observed at positions indexed as $[h \pm 1/2, k \mp 1/2, 0]$ as shown in Fig. 33a) which are expected from the (001)TED pattern shown in Fig. 32};

iii) in both types of diffraction pattern, weak and short streaks are observed along the [001] and the $[00\bar{1}]$ directions around each matrix spot.

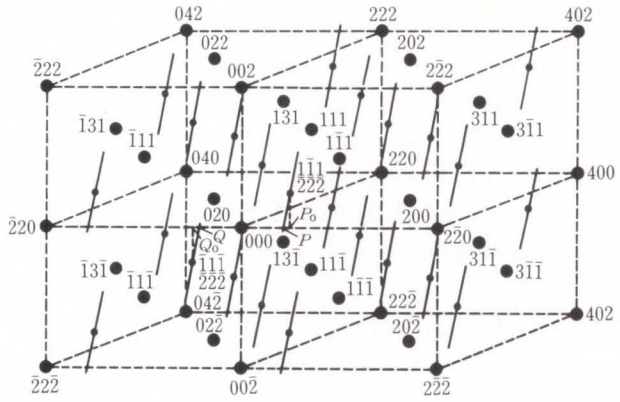

Fig. 34—Schematic diagram of the reciprocal lattice of an ordered InGaP crystal (CuPt-type). Large and small closed circles represent the positions of the fundamental diffraction spots and superstructure spots.

On the basis of the three diffraction patterns described above, a reciprocal lattice of the InGaP was constructed schematically as shown in Fig. 34. This leads us to the conclusion that the extra-spot pairs appearing in the (001)TED pattern (see Fig. 32) correspond to intersecting points of the streaks on the (001) reciprocal plane and that they are not real superstructure spots[61]. The fact that the extra spots appearing in the (001)TED pattern are located slightly inside the ideal positions of the [h ±1/2, k ∓1/2, 0] is well understood by the tilting of the streaks. The positions denoted by P_0 and Q_0 are indexed as [1/2, $\overline{1/2}$, 0] and [$\overline{1/2}$, 1/2, 0], respectively, and P and Q show observed locations of pair spots on both sides of the 000 spot in Fig. 32. Since streaks are present around the superstructure spots, it is assumed that the ordering is not perfect, and that ordered regions correspond to microdomains of a finite size. The reciprocal lattice illustrated in Fig. 34 is associated with a CuPt-type ordered structure[84], which is one of these previously shown in Fig. 31. The ordering occurs on the (111) plane of column III atoms with doubling in periodicity, i.e. the ordered structure corresponds to a monolayer superlattice of $(InP)_1(GaP)_1$ on the (111) plane.

A $(\bar{1}\bar{1}0)$ cross-sectional HRTEM image of the InGaP crystal is illustrated in Fig. 35. Doubling in periodicity of the $(1\bar{1}1)$ lattice fringe, i.e. the presence of arrays of brighter spots on each second $(1\bar{1}1)$ fringe is clearly observed. This is presumably associated with the superstructure spots in the $(\bar{1}\bar{1}0)$TED pattern {see Fig. 33a)}, whereas no abnormal contrast is observed in the $(1\bar{1}0)$ cross-sectional HRTEM image. The presence of non-ordered regions is very often observed, indicating that the ordering is not perfect. These ordered structures are observed in all InGaP crystals with different thickness.

As described above, it should be recognized that the ordering occurs on only one of the four equivalent (111) planes. In order to clarify the cross-sectional shape of the ordered region, a dark-field image is taken directly from one of the superstructure spots, as shown in Fig. 36. In this image, brighter regions correspond to ordered regions since the intensity is associated

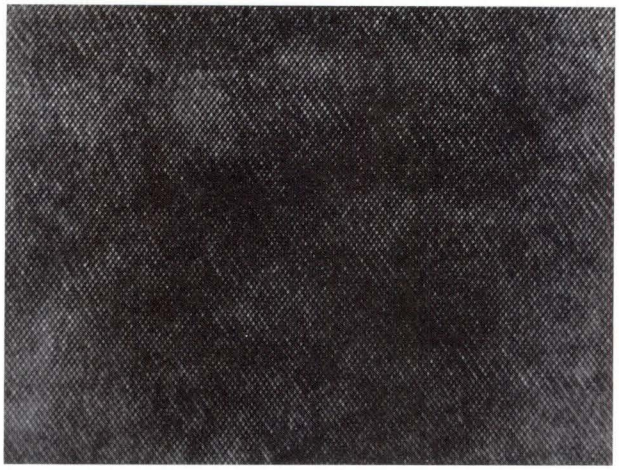

Fig. 35 – A $(\bar{1}\bar{1}0)$ cross-sectional HRTEM image of ordered regions in a Type I InGaP crystal.

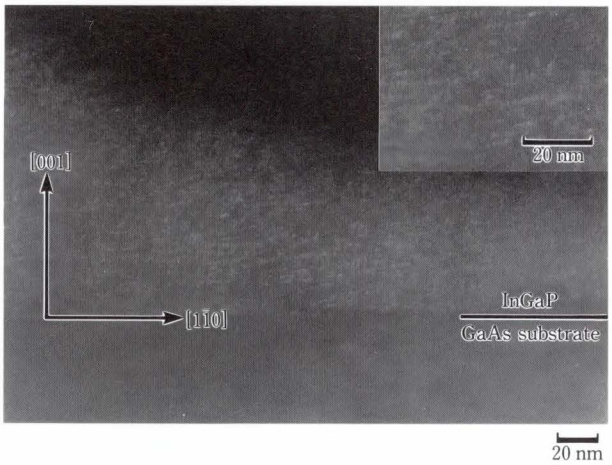

Fig. 36 – A $(\bar{1}\bar{1}0)$ cross-sectional dark-field TEM image of ordered regions in a Type I InGaP crystal, obtained from one of the superstructure spots.

with only the superstructure spot. The ordered regions are found to be plate-like microdomains of 5-15 nm wide and about 2 nm thick, lying on the plane slightly inclined to the (001) plane. These results are consistent with the appearance of streaks around the superstructure spots and their tilting in the TED pattern shown in Fig. 33a).

5.1.2 Evaluation of Type II crystals

1) Plan-view observation

Plan-view observations reveal both coarse and fine modulated structures with periodicities similar to those observed in Type I crystals.

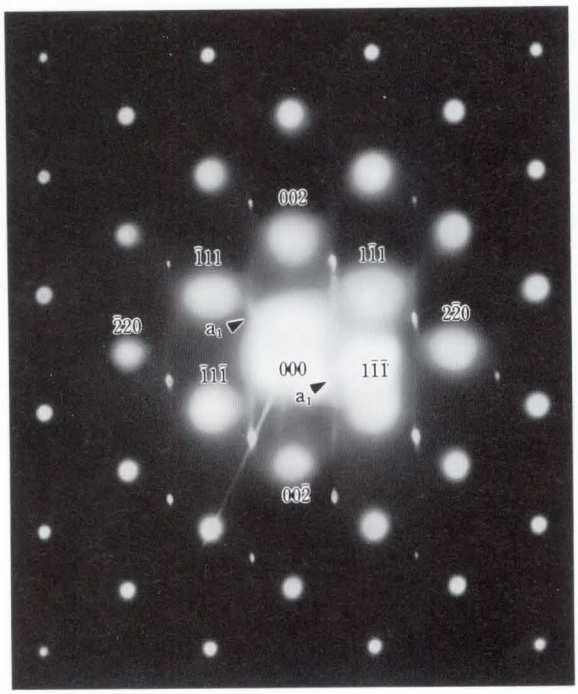

a) Region 1

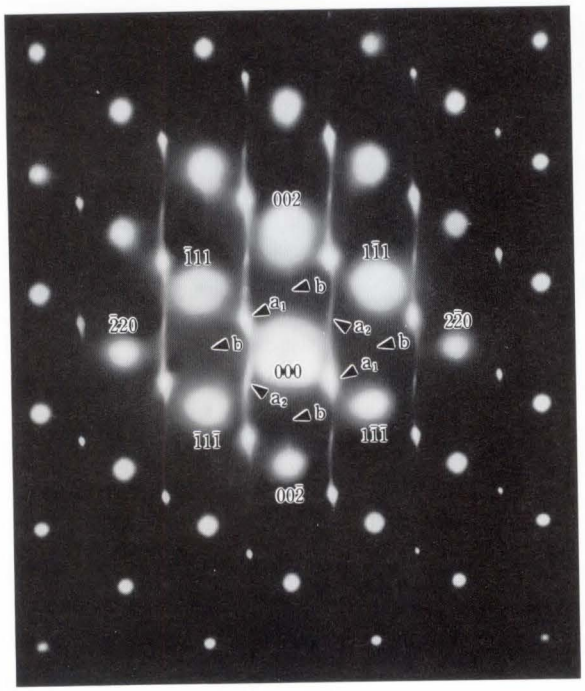

b) Region 2

Fig. 37—TED patterns from a (110) cross-section of a Type II InGaP crystal.

Thus, there is no influence of substrate rotation on the generation of modulated structures. The electron diffraction patterns obtained from Type II crystals also exhibit superstructure spots similar to those observed in the Type I crystals.

2) Cross-sectional observation

Quite different intensity profiles of the superstructure spots are found in the TED patterns obtained from two different regions of a Type II crystal {see Figs. 37a) and b)}. Although one series of superstructure spots is present, they are "spotty" rather than "streaky", indicating fairly long range ordering. Moreover, the intensity of the superstructure spots is much stronger than in Type I crystals, and weaker streaks can also be seen along the [001] direction. Occasionally, two series of superstructure spots are observed as illustrated in Fig. 37b) (see spots indicated by a_1 and a_2). However, there is asymmetry in the intensity of each series. Furthermore, very weak superstructure spots, which are associated with a CuAu-I-type structure[80),81)], are occasionally observed at positions indexed as 001, 003, and $1\bar{1}0$ {see also spots indicated by b in Fig. 37b)}. These results suggest that CuPt-type structures are predominantly generated in the crystals grown on (001)-oriented substrates.

Figure 38a) illustrates an HRTEM image obtained from a $(\bar{1}\bar{1}0)$ cross-section of Type II crystal. Doubling in $(1\bar{1}1)$ lattice fringes is clearly observed over a considerable region; this indicates long range ordering. It is also emphasized that planar defects are often observed in the high resolution image, i.e. the region indicated by APBs in Fig. 38b), where a phase-shift of the $(1\bar{1}1)$ fringes is observed. They might be anti-phase boundaries as suggested by Kuan et al[80)]. The HRTEM image from a $(1\bar{1}0)$ cross-section does not exhibit periodic intensity in any lattice fringes.

A cross-section dark-field image of ordered regions obtained from one of the superstructure spots in a Type II crystal is shown in Fig. 39. The size and shape of the ordered domains are found to be very different. In most cases, the domains are much larger than those observed in Type I crystals (see Fig. 36). These domains also consist of plate-like segments lying nearly on the (001) plane, possibly associated with anti-phase boundaries. In this case, approximately 80 percent of the total area is dominated by ordered regions, which is much more than in Type I

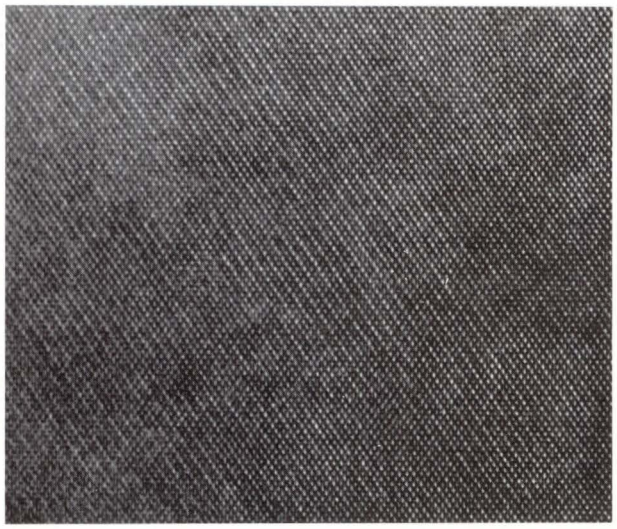

a) An HRTEM image

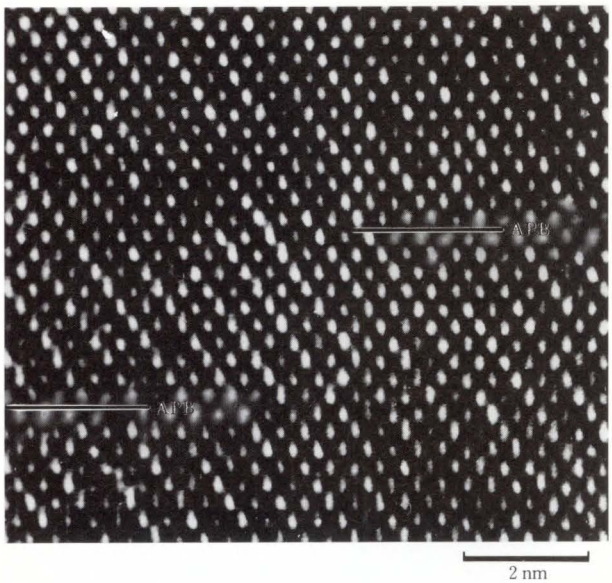

b) A higher magnification image of a part of the ordered region with anti-phase boundaries shown in a)

Fig. 38—($1\bar{1}0$) cross-sectional HRTEM images of ordered structures in a Type II InGaP crystal.

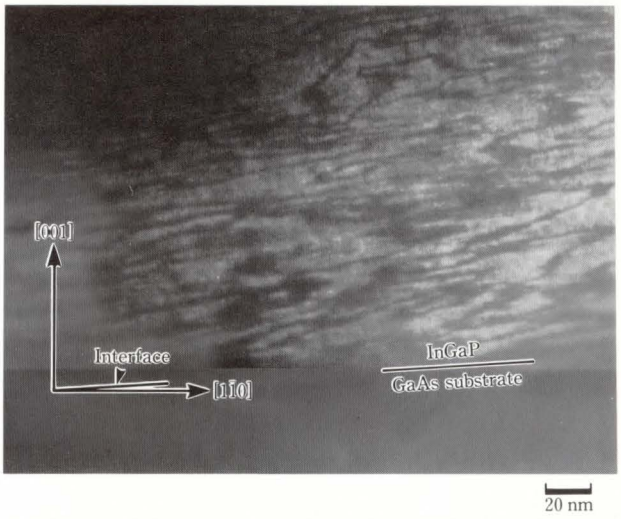

Fig. 39—A ($\bar{1}\bar{1}0$) cross-sectional dark-field TEM image of ordered regions in a Type II InGaP crystal, obtained from one of the superstructure spots.

crystals. Moreover, the boundaries between ordered domains and non-ordered regions are also slightly tilted.

5.1.3 On the difference in the generation of ordered structures between Type I and II crystals

In order to clarify the difference in the generation of ordered structures, one must consider their generation mechanism.

Based on the findings of the ordered structures in MOVPE-grown InGaP crystal described in subsections 5.1.1 and 5.1.2, and those in other III-V alloy semiconductors[61)-83)], it is realized that ordering occurs in III-V alloy semiconductors grown by MOVPE or MBE where deposited atoms can migrate and rearrange easily on the surface during growth. Thus, the mobility of the matrix atoms on the surface is expected to be one of the most dominant parameters for the generation of ordered structures. One of the most direct pieces of evidence for this hypothesis can be found in the cross-sectional feature of ordered domains shown in Fig. 38, i.e. the boundaries between the ordered and non-ordered regions are tilted from the [001] direction, indicating that the boundaries are moving towards the [1$\bar{1}$0] direction during crystal growth.

In view of these considerations, one can suggest the following as factors which might affect the formation of ordered structures during crystal growth with or without substrate rotation:

1) Mobility of atoms on the growth surface;
2) Distribution of the gas flow near the growth surface;
3) Effective temperature at the growth surface.

Since there is no major difference between the average thickness in Type I crystals and that in Type II crystals, factor 3) seems to have little contribution to the ordering.

Thus, one can assume that a combination of factors 1) and 2) affect the formation of ordered structures on the growth surface as follows:

i) When the InGaP crystal is grown on a rotating substrate, local fluctuation is present in the gas flow near the growth surface, reducing the surface rearrangement of the deposited atoms. In this case, migration of the deposited atoms on the growth surface is much more disturbed by the gas molecules with relatively high velocities than is the case with a non-rotating substrate. Thus, the effective mobility of the deposited atoms is lower.

ii) When the crystal is grown on a non-rotating substrate, gas flow distribution on the growth surface is uniform and effective mobility of the deposited atoms is high compared with case i); thus ordering is enhanced.

5.2 Ordered structures in InGaAs crystals grown on (110)InP by MBE

As described in section 5.1, the ordered structures in crystals grown on (001) substrates are mostly CuPt-type. On the other hand, CuAu-I-type ordered structures have been found by Kuan et al. in AlGaAs crystals grown on (110)GaAs substrates by MOVPE and MBE[80], and InGaAs crystals grown on (110)InP substrates by MBE[81]. However, they only showed TED patterns corresponding to the CuAu-I-type structure; the microstructural features of the ordered regions and dependence of the degree of ordering on growth conditions have not yet been clarified. In this work, we describe a detailed TEM study on the dependence of the degree of ordering on the growth conditions and a microstructural evaluation of the CuAu-I-type ordered structures.

Undoped InGaAs crystals grown on (110)InP substrates by MBE were examined in this study. The crystals were grown at 360-485 °C on exactly (110)InP substrates, or on InP substrates tilted toward the [001], [00$\bar{1}$] or [1$\bar{1}$0] direction. During growth, the substrates were rotated to achieve a good uniformity in composition, thickness and carrier concentration. The V/III partial pressure ratio was kept at 400 or 60{only for crystals grown on substrates tilted toward the [001] direction}. The epitaxial layer was approximately 1 μm thick. The lattice mismatch between the InGaAs layer and the InP substrate was within $\pm 1 \times 10^{-3}$.

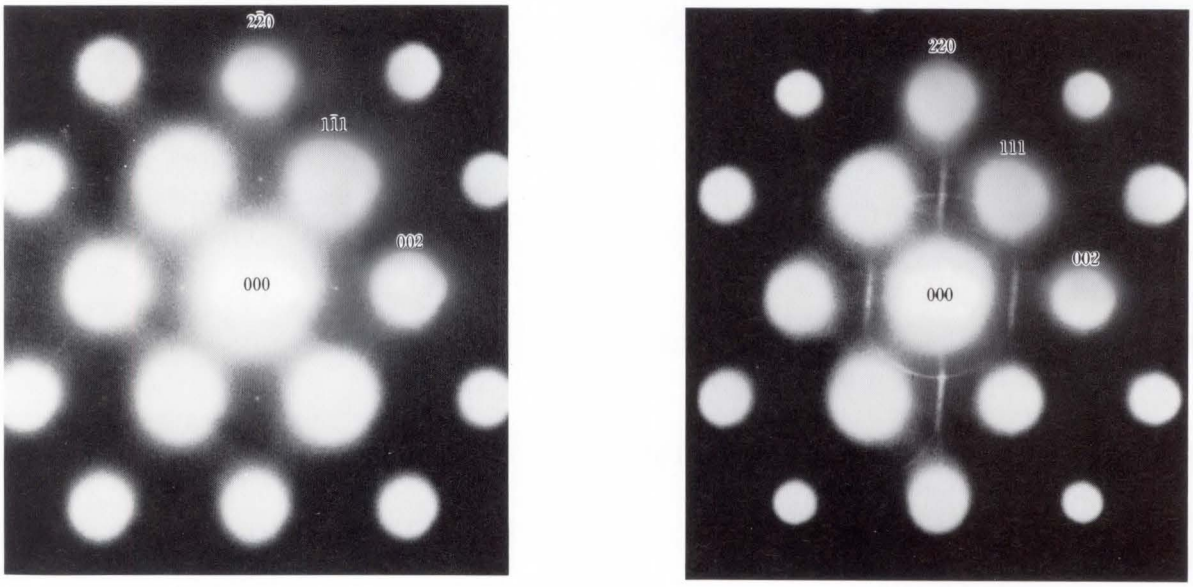

a) (110) plan-view b) ($\bar{1}$10) cross-section

Fig. 40—TED patterns from the (110) plan-view and the ($\bar{1}$10) cross-section of InGaAs grown on (110)InP tilted 3° toward [1$\bar{1}$0].

5.2.1 Identification of CuAu-I-type structures by TED and dependence of the degree of ordering on substrate orientation

Figures 40a) and b) show the TED patterns from a (110) plan-view and a ($\bar{1}$10) cross-section of an InGaAs crystal grown on a (110)InP substrate tilted 3° toward the [1$\bar{1}$0] direction. In both figures, superstructure spots are observed at positions indexed as 001, 1$\bar{1}$0, $\bar{1}$10, 1$\bar{1}$2, $\bar{1}$12, . . . This particular set of superstructure spots is associated with a CuAu-I-type ordered structure[80),81)]. In this structure, Ga atoms preferentially occupy the (000) and (1/2, 1/2, 0) sites and In atoms preferentially occupy the (1/2, 0, 1/2) and (0, 1/2, 1/2) sites in each unit cell. A schematic diagram of the atomic arrangement in the CuAu-I-type structure viewed along the [110] direction normal to the growth axis is shown in Fig. 41. From this diagram, one can see that the perfectly ordered material consists of alternating InAs and GaAs monolayers, i.e. $(InAs)_1/(GaAs)_1$ monolayer superlattices, when viewed along either the [110] growth direction or the [001] direction. Note that the superstructure spots shown in Fig. 40b) are extremely streaky, and that the streaks are "S"-shaped, tilted slightly from the [110] direction. Superstructure spots of a similar shape are also observed in the TED patterns from (110) cross-sections of ordered InGaP (CuPt-type) crystals grown on (001)GaAs tilted substrates.

The streaky shape of the superstructure spots may be due to either

1) the generation of anti-phase boundaries in the ordered region or
2) the fact that ordered regions are plate-like microdomains (see Fig. 46 in subsection 5.2.3), although computer simulations of epitaxial growth are required to resolve this issue.

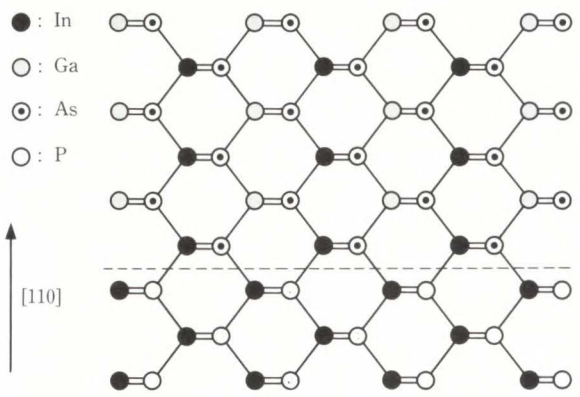

Fig. 41—A schematic diagram of the atomic arrangement of CuAu-I-type ordered structure in an InGaAs crystal viewed from the [1$\bar{1}$0] direction.

Figures 42a) to c) show TED patterns from plan-views of InGaAs crystals grown on (110)InP substrates with tilting angles of 0°, 3° and 5° toward the [001] direction. In crystals grown on a (110) pure InP substrate {see Fig. 42a)}, the intensity of the superstructure spots is very weak, indicating very weak ordering. However, when a substrate tilted 3° toward the [001] direction is used, ordering

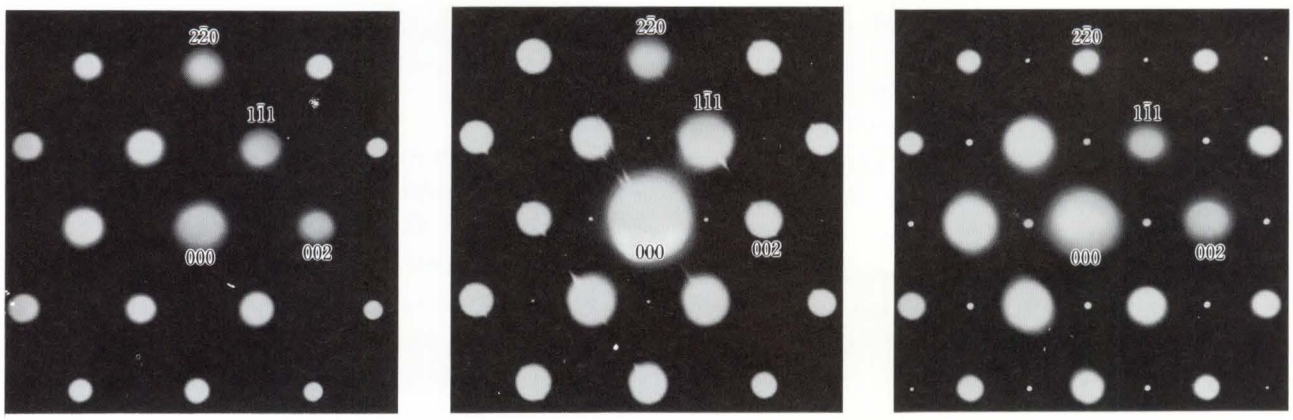

a) Exactly (110) b) (110)InP tilted 3° toward [001] c) (110)InP tilted 5° toward [001]

Fig. 42—TED pattern from the (110) plan-view of InGaAs crystals grown at different tilting angles.

becomes stronger as shown in Fig. 42b). Further, ordering becomes much stronger in a crystal grown on a substrate tilted 5° toward the [001] direction {see Fig. 42c)}. Since tilting of the substrate orientation toward the [001] or the [00$\bar{1}$] direction introduces periodic arrays of steps on the substrate surface, one can conclude that atomic steps on the growth surface play an important role in the formation of the ordered structures. It is also established that the ordering is stronger in crystals grown on substrates tilted toward the [001] or the [00$\bar{1}$] direction than those on substrates tilted toward the [1$\bar{1}$0] direction. This may be explained as follows: when the (110) surface is tilted toward the [001], the steps are very straight, giving rise to strong ordering, but when the (110) surface is tilted toward [1$\bar{1}$0], highly kinked steps are formed, preventing the crystal from ordering (in the latter case, only the kinks themselves can enhance the ordering).

5.2.2 Dependence of the degree of ordering on growth temperature

In order to clarify the influence of growth temperature on the formation of ordered structures, we grew InGaAs crystals at various temperatures in the range of 435-485 °C on (110)InP substrates tilted 3° toward the [1$\bar{1}$0] direction. From TED analysis, it was found that in this temperature range, the degree of ordering increases with growth temperature. Figures 43a) and b) show TED patterns from ($\bar{1}$10) cross-sections of InGaAs crystals grown at 435 °C and 485 °C, respectively. TED analysis has also been carried out for crystals grown on substrates tilted toward the [001] direction. It has been found that, in the range of 360-450 °C also, the degree of ordering increases with growth temperature. These results can be explained by the fact that the mobility of atoms deposited on the growth surface also increases with temperature, and that the formation of ordered structures is thought to be strongly related to the migration and reconstruction of the deposited atoms[62),69)].

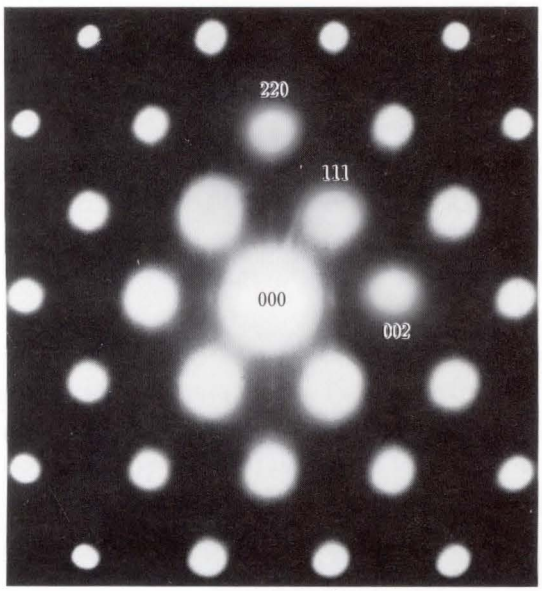

a) T_g = 435 °C

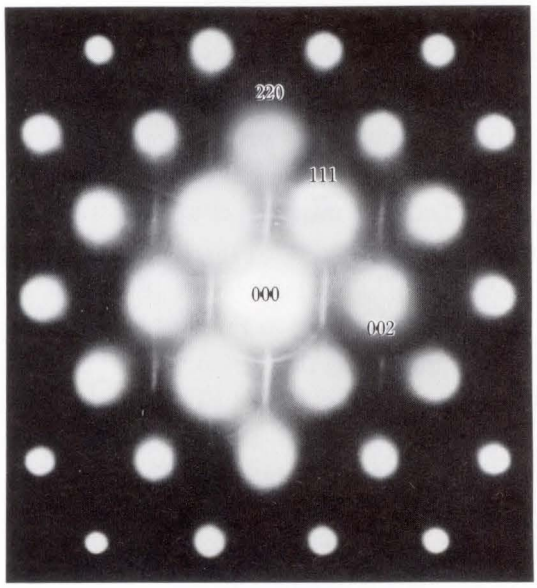

b) T_g = 485 °C

Fig. 43 – TED patterns from the ($\bar{1}$10) cross-sections of InGaAs crystals grown on (110)InP tilted 3° toward [1$\bar{1}$0].

5.2.3 Microstructural characterization of CuAu-I-type structures

HRTEM analysis was carried out to evaluate the ordered structures at an atomic level. Figure 44 shows a typical HRTEM image of ordered InGaAs grown on a (110)InP substrate tilted 3° toward the [00$\bar{1}$] direction. Doubling of the (002) (see arrows X_1-X_3) and the (220) (see arrows Y_1-Y_4) lattice fringes, which is associated with CuAu-I-type structures, is ob-

served locally, suggesting that the crystal consists of both well-ordered and non-ordered regions. It should be emphasized that planar defects are often observed in high resolution images, e.g. the region denoted by APB, where a phase-shift of the (002) lattice fringes is observed. These are expected to be anti-phase boundaries as suggested by Kuan et al[81]. In the (001) cross-section HRTEM images, doubling of both the (220) and the (2$\bar{2}$0) lattice fringes is observed. Figure 45 shows computer simulated images of a CuAu-I-type ordered structure in InGaAs. Figure 45a) shows a schematic diagram of the ordered structure viewed along the [001] direction. Figures 45b) to d) show the thickness dependence of a CuAu-I-type structure with an incident electron beam of [$\bar{1}$10] and optimum focusing. It is found that in each case, the In-As pairs cause a brighter spot than the Ga-As pairs.

In order to clarify the cross-sectional shape of the ordered region, a dark-field image was taken with one of the superstructure spots, as shown in Fig. 46. In this image, ordered regions are observed to be brighter since the image con-

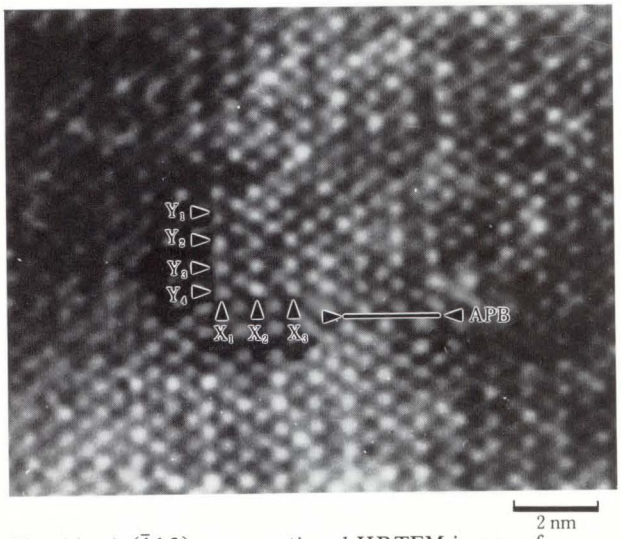

Fig. 44—A ($\bar{1}$10) cross-sectional HRTEM image of ordered InGaAs grown on (110)InP tilted 3° toward [00$\bar{1}$].

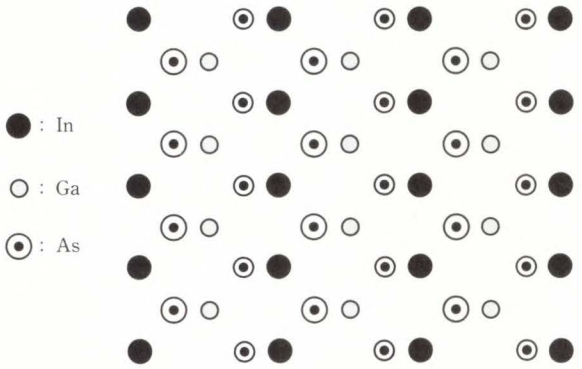

a) A schematic diagram of the ordered structure (large and small dotted circles represent foreground and background atoms)

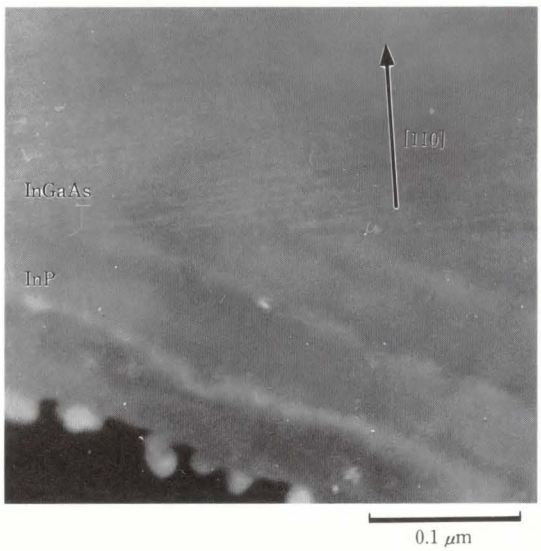

Fig. 46—A ($\bar{1}$10) cross-sectional dark-field TEM image of an ordered InGaAs crystal from one of the superstructure spots.

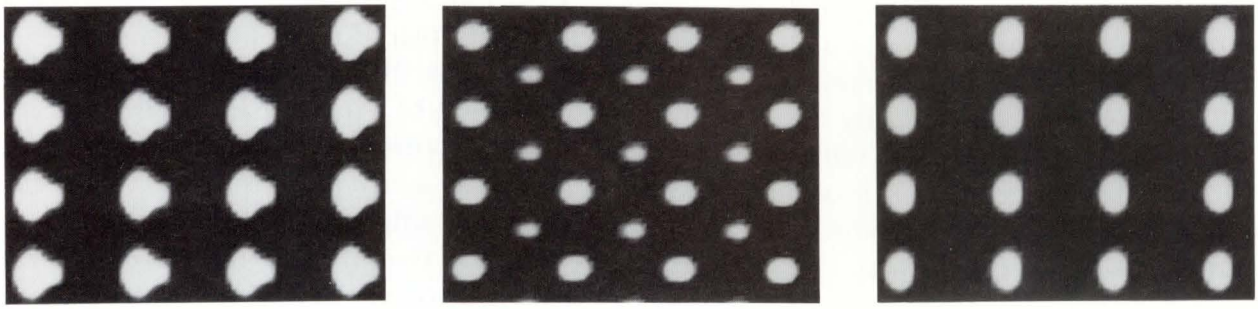

b) Δf (defocus) = 38 nm, t (thickness) = 8.3 nm

c) Δf = −38 nm, t = 16.3 nm

d) Δf = −38 nm, t = 25 nm

Fig. 45—Computer simulated images of ordered InGaAs by multi-slice method.

trast is formed by only the superstructure spot. It is found that the ordered regions are plate-like microdomains 2-4 nm thick, lying on a plane slightly tilted from the (110) plane. It is thought that the streaks observed in the TED pattern {see Fig. 40b)} are due to the plate-like shape of these microdomains. The tilting of the streaks can also be explained by the tilting of the microdomains.

On the basis of these results, it is proposed that the formation of CuAu-I-type structure takes place by

1) migration of the deposited atoms on the growth surface, and
2) rearrangement of the migrating atoms from the step edges over two atomic layers.

Further experiments and theoretical calculations are required to completely understand the formation mechanism of the ordered structures.

5.2.4 Enhancement of two-dimensional electron gas mobility in InGaAs/N-InAlAs heterostructures

In order to investigate the electrical properties of ordered (110)InGaAs, we studied two-dimensional electron gas (2DEG) mobility in InGaAs/N-InAlAs heterostructures with a strongly ordered InGaAs layer[85),86)]. We grew selectively doped InGaAs/N-InAlAs heterostructures on (110)InP substrates tilted 3° and 5° toward the [001] direction. These heterostructures consisted of a 600 nm undoped InAlAs buffer layer, a 600 nm undoped InGaAs channel layer, a 10 nm undoped InAlAs spacer layer, a 90 nm Si-doped InGaAs cap layer with a carrier concentration of 3×10^{17} cm^{-3}, and a 10 nm Si-doped InGaAs cap layer with a carrier concentration of 3×10^{17} cm^{-3}. The 2DEG mobility and sheet electron concentration (N_s) are plotted as a function of temperature in Fig. 47. The 2DEG mobility is highly anisotropic: in the <001> direction, the mobility (denoted by closed squares) saturates at 100 000 cm^2/V·s and is comparable to that in the sample grown on a (001) substrate (see line); while in the <$\bar{1}$10> direction, the mobility (denoted by closed triangles and closed circles) is much higher than the alloy scattering limited mobility

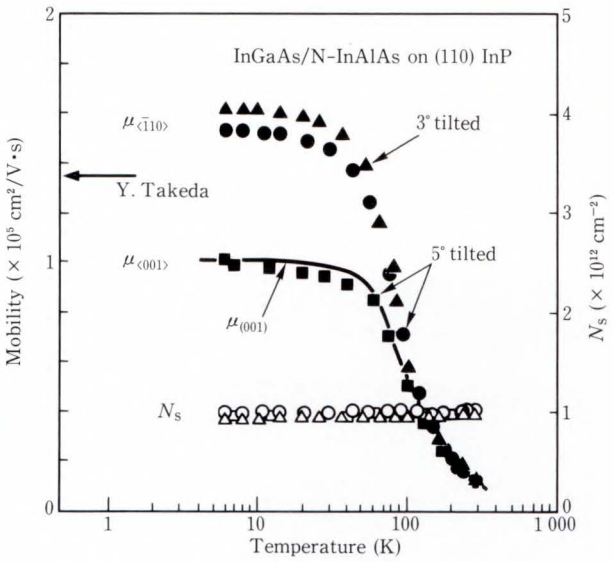

Fig. 47—Temperature dependence of the 2DEG mobility and the sheet electron concentration in the <$\bar{1}$10> and <001> directions in selectively doped InGaAs/N-InAlAs hetero-structures grown on (110)InP substrate tilted 3° and toward <00$\bar{1}$>.

calculated at an N_s of 1×10^{12} cm^{-2} by Takeda et al.[87)] (denoted by an arrow) at lower temperatures. The 2DEG mobility in the <$\bar{1}$10> direction in a sample grown on 3° tilted substrate reached 161 000 cm^2/V·s with an N_s of 9.5×10^{11} cm^{-2} at 6 K (101 000 cm^2/V·s with an N_s of 9.6×10^{11} cm^{-2} at 77 K)[86)]. This is the highest mobility, to our knowledge, ever reported for lattice-matched InGaAs/N-InAlAs heterostructure systems. This mobility enhancement in the <$\bar{1}$10> direction is thought to be caused by the suppression of alloy scattering due to the formation of CuAu-I ordering in the InGaAs channel layer. On the other hand, the 2DEG mobility in the <001> direction compares with that of the non-ordered sample. The difference in 2DEG mobility in different directions could be explained as follows: Since the plate-like ordered and disordered regions are stacked on nearly the (110) plane on the tilted substrates, stripes of ordered and disordered regions are formed along the <$\bar{1}$10> direction at the InGaAs side of the hetero-interface where the 2DEG accumulates. Thus, along the <001> direction, i.e. normal to the stripes, electrons

travel across the disordered regions. Along the $<\bar{1}10>$ direction, i.e. parallel to the stripes, the 2DEG formed in both the ordered and disordered regions move along the stripes. The electrons in the ordered regions should be unaffected by alloy scattering in the disordered regions.

The highest 2DEG mobility obtained in the $<\bar{1}10>$ direction, however, is lower than the theoretical prediction in alloy scatter-free $(InAs)_1(GaAs)_1$ monolayer superlattices[86]. One of the reasons for this is that the InGaAs layers are not completely ordered even in the $<\bar{1}10>$ direction. Moreover, the ordered regions include many anti-phase boundaries. The 2DEG mobility in the $<\bar{1}10>$ direction could be improved by reducing the number of such boundaries.

6. Conclusion

We have reviewed recent advances in the application of TEM to the evaluation of structures, interfaces and defects in III-V compound semiconductor thin films, solving various materials issues in these systems.

First, $(GaAs)_m/(GaP)_n$ strained layer superlattices grown by ALE have been structually evaluated by HRTEM at the atomic level. It has been shown microscopically for the first time that $(GaAs)_1/(GaP)_1$ monolayer superlattices are formed uniformly throughout the epitaxial layer, indicating that this method achieves precise layer-by-layer growth. Similar results have also been obtained for $(GaAs)_3/(GaP)_3$ and $(GaAs)_4/(GaP)_2$ superlattices.

AlAs/Si heterostructures grown by ALE have been evaluated by TEM. The hetero-interface is found to be extremely abrupt compared to GaAs/Si grown by a two-step MOVPE method. Atomic steps are clearly observed at the interface and no amorphous or alloyed regions are found. At the initial stage of growth, a three-dimensional island growth mode is dominant. However, two-dimensional growth takes place after depositing only 36 atomic layers of AlAs. Two types of defect are observed in the AlAs layer, stacking faults and microtwins. Although the density of these defects is high, they tend to self-annihilate at the interface between the AlAs layer and the thick, upper GaAs layer.

The nature and behavior of APBs in GaAs and GaP on (001)Si grown by MOVPE have been investigated. It has been found that APDs are very complicated three-dimensional polygons with several sub-boundaries in different orientations. Self-annihilation of APDs during growth is directly observed for the first time through plan-view and cross-sectional observations. Based on these results, a mechanism of annihilation of these domains is proposed.

Interface defects in MBE-grown GaAsSb crystals and bulk defects in MOVPE-grown InP doped with Fe have been characterized. In MBE-grown GaAsSb crystal, we have found three types of interface defects, i.e. stacking fault tetrahedra, microtwins and dissociated dislocations. FeP precipitates are found in Fe-doped InP. They are found to be spherical coherent precipitates uniformly distributed in the crystal. Their density increases as the doping gas flow rate increases from 20 ml/min to 100 ml/min. In crystals grown with gas flow rates lower than 5 ml/min, in which the Fe-concentration is below the solubility limit, no precipitates are found at all. For each defect, the mechanism of defect generation and possible ways to eliminate it were discussed.

We have also described detailed TEM studies on atomic ordering in MOVPE-grown InGaP on (001)GaAs and MBE-grown InGaAs on (110)InP. From TED and HRTEM analyses, CuPt-type and CuAu-I-type ordered structures have been found in InGaP on (001)GaAs and InGaAs on (110)InP, respectively. In each case, the atomic structure of the ordered regions and dependence of the degree of ordering on growth conditions were described. The generation mechanisms of ordered structures and their influence on the optical and electrical properties of the materials were also discussed.

7. Acknowledgement

The author would like to express his gratitude to Professors M. Umeno, T. Jimbo and T. Soga of Nagoya Institute of Technology for their co-operation and valuable suggestions.

Fruitful discussions and a number of editorial suggestions by Dr. A. Hobbs are greatly appreciated. Finally, he would like to thank Dr. O. Ohtsuki for his encouragement throughout this work.

References

1) Nishizawa, J., Abe, H., and Kurabayashi, T.: Molecular Layer Epitaxy. *J. Electrochem Soc.*, **132**, 5, pp.1197-1200 (1985).
2) Usui, A., and Sunakawa, H.: GaAs Atomic Layer Epitaxy by Hydride VPE. *Jpn. J. Appl. Phys.*, **25**, 3, pp.L212-L214 (1986).
3) Doi, A., Aoyagi, Y., and Namba, S.: Stepwise Monolayer Growth of GaAs by Switched Laser Metalorganic Vapor Phase Epitaxy. *Appl. Phys. Lett.*, **49**, 13, pp.785-787 (1986).
4) Bedair, S.M., Tischler, M.A., Katsuyama, T., and El-Masry, N.A.: Atomic Layer Epitaxy of III-V Binary Compound. *Appl. Phys. Lett.*, **47**, 1, pp.51-53 (1985).
5) Katoda, T., Okumura, T., Komiya, S., Ozeki, M., and Ueda, O.: "Evaluation Techniques for Semiconductors". (in Japanese), Katoda, T., ed., 1st ed., Tokyo, Sangyo Tosho, 1989, pp.179-189.
6) Katoda, T., Okumura, T., Komiya, S., Ozeki, M., and Ueda, O.: "Evaluation Techniques for Semiconductors". (in Japanese), Katoda, T., ed., 1st ed., Tokyo, Sangyo Tosho, 1989, pp.189-204.
7) Spence, J.C.H.: Experimental High-Resolution Electron Mocroscopy". Bawn, C.E.H., Fröhlich, H., Hirsch, P.B., and Mott, N.F., ed., 1st ed., Oxford. O.U.P., 1980, pp.136-143.
8) Spence, J.C.H.: Experimental High-Resolution Electron Microscopy". Bawn, C.E.H., Fröhlich, H., Hirsch, P.B., and Mott, N.F., ed., 1st ed., Oxford, O.U.P., 1980, pp.143-148.
9) Ozeki, M., Mochizuki, K., Ohtsuka, N., and Kodama, K.: New Approach to the Atomic Layer Epitaxy of GaAs Using a Fast Gas Stream. *Appl. Phys. Lett.*, **53**, 16, pp.1509-1511 (1988).
10) Ozeki, M., Mochizuki, K., Ohtsuka, N., and Kodama, K.: Growth of GaAs Thin Films by a New Atomic Layer Epitaxy Technique. *Thin Solid Films*, **174**, pp.63-70 (1989).
11) Ozeki, M., Sakuma, Y., and Ohtsuka, N.: Pulsed-Jet Epitaxy of III-V Compounds. *FUJITSU Sci. Tech. J.*, **28**, 1, pp. 50-61 (1992).
12) Ozeki, M., Kodama, K., Sakuma, Y., Ohtsuka, N., and Takanohashi, T.: GaAs/GaP Strained-Layer Superlattices Grown by Atomic Layer Epitaxy. *J. Vac. Sci. & Technol.*, **B8**, 4, pp.741-746 (1990).
13) Kodama, K., Ozeki, M., Sakuma, Y., and Ohtsuka, N.: Raman Scattering of $(GaAs)_n(GaP)_n$ Short-Period Superlattices Prepared by Pulsed Jet Epitaxy. *J. Appl. Phys.*, **69**, 9, pp. 6713-6715 (1991).
14) Takanohashi, T., and Ozeki., M.: Exciton-Absorption Transitions in $(GaAs)_n(GaP)_n$/GaAs Atomic Layer Superlattices. Proc. 7th Int. Conf. Vapor Growth & Epitaxy, Nagoya, 1991, to be published in a special issue of *J. Cryst. Growth*, (1992).
15) Ueda, O., Wakao, K., Yamaguchi, A., Isozumi, S., and Komiya, S.: Defect Structures in Rapidly Degrated InGaAsP/InGaP Double-Heterostructure Lasers. *J. Appl. Phys.*, **57**, 5, pp.1523-1532 (1985).
16) Ueda, O., Wakao, K., Komiya, S., Yamaguchi, A., Isozumi, S., and Umebu, I.: Catastrophic Degradation of InGaAsP/InGaP Double-Heterostructure Lasers Grown on (001)GaAs Substrates by Liquid Phase Epitaxy. *J. Appl. Phys.*, **58**, 11, pp.3996-4002 (1985).
17) Marée, P.M.J., Barbour, J.C., van der Veen, J.F., Kavanagh, K.L., Bulle-Lieuwma, C.W.T., and Viegers, M.P.A.: Generation of Misfit Dislocations in Semiconductors. *J. Appl. Phys.*, **62**, 11, pp.4413-4420 (1987).
18) Takasugi, H., Kawabe, M., and Bando, Y.: Initial Growth and Dislocation Accomodation of GaAs on Si(100) by Molecular Beam Epitaxy. *Jpn. J. Appl. Phys.*, **26**, 5, pp.L584-L586 (1987).
19) Lee, J.W., and Tsai, H.L.: Crystal Orientations and Defect Structures of GaAs Layers Grown on Misoriented Si Substrates by Molecular-Beam Epitaxy. *J. Vac. Sci. & Technol.*, **B5**, 3, pp.819-821 (1987).
20) Carey, K.W., Ponce, F.A., Amano, J., and Aranovich, J.: Structural Characterization of Low-Defect-Density Silicon on Sapphire. *J. Appl. Phys.*, **54**, 8, pp.4414-4420 (1983).
21) Ueda, O., Umebu, I., and Kotani, T.: Transmission Electron Microscopic Observation of Defects in Heavily Doped LPE InGaAsP Layers with Zn, Cd, Sn and Te. *J. Cryst. Growth*, **62**, 2, pp.329-342 (1983).
22) Kotani, T., Ueda, O., Akita, K., Nishitani, Y., Kusunoki, T., and Ryuzan, O.: Direct Observation of Defects in Si-Doped and Ge-Doped $Ga_{0.9}Al_{0.1}As$ Epitaxial Layers by Transmission Electron Microscopy. *J. Cryst. Growth*, **38**, 1, pp.85-92 (1977).
23) Ueda, O., Komiya, S., and Isozumi, S.: TEM Investigation of Dislocation Loops in Undoped InGaAsP and InGaP Layers Grown by Liquid Phase Epitaxy.

Jpn. J. Appl. Phys., **23**, 6, pp.L394-L396 (1984).
24) Akiyama, M., Kawarada, Y., and Kaminishi, K.: Growth of Single Domain GaAs Layer on (100)-Oriented Si Substrate by MOCVD. *Jpn. J. Appl. Phys.*, **23**, 11, pp.L843-L845 (1984).
25) Yamaguchi, M. Yamamoto, A., Tachikawa, M., Itoh, Y., and Sugo, M.: Defect Reductio Effects in GaAs on Si Substrates by Thermal Annealing. *Appl. Phys. Lett.*, **53**, 23, pp.2293-2295 (1988).
26) Choi, C., Otsuka, N., Munns, G., Houdre, R., Morkoç, H., Zhang, S.L., Levi, D., and Klein, M.V.: Effect of *In Situ* and *Ex Situ* Annealing on Dislocations in GaAs on Si Substrates. *Appl. Phys. Lett.*, **50**, 15, pp. 992-994 (1987).
27) Hayafuji, N., Ochi, S., Miyashita, M., Tsugami, M., Murotani, T., and Kawagishi, A.: Effectiveness of AlGaAs/GaAs Super-lattices in Reducing Dislocation Density in GaAs on Si. *J. Cryst. Growth*, **93**, pp. 494-498 (1988).
28) Ueda, O., Soga, T., Jimbo, T., and Umeno, M.: Characterization of MOCVD-Grown GaAs/Strained Layer Superlattices/GaP/Si Heterostructures by Transmission Electron Microscopy. *J. Cryst. Growth*, **106**, 4, pp. 491-497 (1990).
29) Tachikawa, M., and Mori, H.: Dislocation Generation of GaAs on Si in the Cooling Stage. *Appl. Phys. Lett.*, **56**, 22, pp. 2225-2227 (1990).
30) Crumbaker, T.E. Lee, H.Y., Hafich, M.J., and Robinson, G.Y.: Growth of InP on Si Substrates by Molecular Beam Epitaxy. *Appl. Phys. Lett.*, **54**, 2, pp. 140-142 (1989).
31) Bean, J.C., Feldman, L.C., Fiory, A.T., Nakahara, S., and Robinson, I.K.: Ge_xSi_{1-x}/Si Strained-Layer Superlattice Grown by Molecular Beam Epitaxy. *J. Vac. Sci. & Technol.*, **A2**, 2, pp. 436-440 (1984).
32) Kitahara, K., Ohtsuka, N., and Ozeki, M.: Initial Stages of GaAs and AlAs Growth on Si Substrates: Atomic-Layer Epitaxy. *J. Vac. Sci. & Technol.*, **B7**, 4, pp. 700-703 (1989).
33) Kitahara, K., Ohtsuka, N., Ueda, O., and Ozeki, M.: Control of GaAs on Si Interface Using Atomic Layer Epitaxy. Extended Abst. 22nd Conf. Solid State Devices and Mat., Sendai, 1990, pp. 877-880.
34) Kitahara, K., Ohtsuka, N., Ueda, O., Funagura, M., and Ozeki, M.: Control of GaAs on Si Interface Using Atomic Layer Epitaxy. *Jpn. J. Appl. Phys.*, **29**, 12, pp. L2457-L2459 (1990).
35) Kitahara, K., Ohtsuka, N., Ueda, O., and Ozeki, M.: A New Approach to Control GaAs on Si Interface Using Atomic Layer Epitaxy. Proc. 13th State-of-The-Art Program on Compound Semicond. (SOTAPOCS XIII), Lee, H.H., Ueda, O., Clechet, P., and Woodall, J.M., ed., Seattle, 1990, Electrochem. Soc., N.J., 1991, pp. 1-8.
36) Ozeki, M., Mochizuki, K., Ohtsuka, N., and Kodama, K.: Kinetic Processes in Atomic-Layer Epitaxy of GaAs and AlAs Using a Pulsed Vapor-Phase Method. *J. Vac. Sci & Technol.*, **B5**, 4, pp. 1184-1186 (1987).
37) Duran, J.C., Platero, G., and Flores, F.: Initial Stages of the Schottky-Barrier Formation for an Abrupt Al-GaAs (100) Interface. *Phys. Rev. B*, **34**, 4, pp. 2389-2393 (1986).
38) Kroemer, H.: Polar-on-Nonpolar Epitaxy. *J. Cryst. Growth*, **81**, pp. 193-204 (1987).
39) Ueda, T., Nishi, S., Kawarada, Y., Akiyama, M., and Kaminishi, K.: Effects of the Substrate Offset Angle on the Growth of GaAs on Si Substrate. *Jpn. J. Appl. Phys.*, **25**, 9, pp. L789-L791 (1986).
40) Pond, R.C., Gowers, J.P., Holt, D.B., Joyce, B.A., Neave, J.H., and Larsen, P.K.: A General Treatment of Antiphase Domain Formation and Identification at Polar-Nonpolar Semiconductor Interface. Mat Res. Soc. Symp. Proc., 25, 1984, pp. 273-278.
41) Kuan, T.S., and Chang, C.-A.: Electron Microscope Studies of a Ge-GaAs Superlattices Grown by Molecular Beam Epitaxy. *J. Appl. Phys.*, **54**, 8, pp. 4408-4413 (1983).
42) Soga, T., Imori, T., Umeno, M., and Hattori, S.: Stress and Strain of GaAs on Si Grown by MOCVD Using Strained Superlattice Intermediate Layers and a Two-Step Growth Method. *Jpn. J. Appl. Phys.*, **26**, 5, pp. L536-L538 (1987).
43) Sota, T., Kohama, Y., Uchida, K., Tajima, M., Jimbo, T., and Umeno, M.: MOCVD Growth and Characterization of GaAs and GaP Grown on Si Substrates. *J. Cryst. Growth*, **93**, pp. 499-503 (1988).
44) Petroff, P.M.: Nucleation and Growth of GaAs on Ge and the Structure of Antiphase Boundaries. *J. Vac. Sci. & Technol.*, **B4**, 4, pp. 874-877 (1986).
45) Pukite, P.R., and Cohen, P.I.: Suppression of Anti-phase Domains in the Growth of GaAs on Ge(100) by Molecular Beam Epitaxy. *J. Cryst. Growth*, **81**, pp. 214-220 (1987).
46) Kawabe, M., Ueda, T., and Takasugi, H.: Initial Stage and Domain Structure of GaAs Grown on Si(100) by Molecular Beam Epitaxy. *Jpn. J. Appl. Phys.*, **26**, 2, pp. L114-L116 (1987).
47) Tanoue, T., and Sakaki, H.: A New Method to Control Impact Ionization Rate Ratio by Spatial Separation of Avalanching Carriers in Multilayered

Heterostructures. *Appl. Phys. Lett.*, **41**, 1, pp.67-70 (1982).

48) Nakata, Y., Fujii, T., Sandhu, A., Sugiyama, Y., and Miyauchi, E.: Growth and Characterization of $Ga_{0.5}As_{0.5}Sb$ Lattice-Matched to InP by Molecular Beam Epitaxy. *J. Cryst. Growth*, **91**, 4, pp. 655-658 (1988).

49) Akimoto, K., Dohsen, M., Arai, M., and Watanabe, N.: Origin of Oval Defects in GaAs Layers Grown by Molecular Beam Epitaxy. *J. Cryst. Growth*, **73**, 1, pp. 117-122 (1985).

50) Kakibayashi, H., Nagata, F., Katayama, Y., and Shiraki, Y.: Structure Analysis of Oval Defect on Molecular Beam Epitaxial GaAs Layer by Cross-Sectional Transmission Electron Microscopy Observation. *Jpn. J. Appl. Phys.*, **23**, 11, L846-L848 (1984).

51) Long. J.A., Riggs, V.G., Johnston, Jr., W.D.: Growth of Fe-doped Semi-Insulating InP by MOCVD. *J. Cryst. Growth*, **69**, 1, pp. 10-14 (1984).

52) Tanaka, K., Nakai, K., Aoki, O., Sugawara, M., Wakao, K., and Yamakoshi, S.: Fe-Doped Semi-Insulating InP Grown by Chloride Vapor-Phase Epitaxy. *J. Appl. Phys.*, **61**, 9, pp. 4698-4700 (1987).

53) Huang, K., and Wessels, B.W.: Electronic and Optical Properties of Fe-Doped InP Prepared by Organometallic Vapor-Phase Epitaxy. *J. Appl. Phys.*, **60**, 12, pp. 4342-4344 (1986).

54) Nakai, K., Ueda, O., Odagawa, T., Takanohashi, T., and Yamakoshi, S.: Epitaxial Growth and Characteristics of Fe doped InP by MOCVD. Proc. Int. Symp. GaAs and Related Compounds, Heraklion, Greece, 1987, Inst. Phys. Conf. Ser., 91, 1988, pp. 199-202.

55) Nakahara, S., Chu, S.N.G., Long, J.A., Riggs, V.G., and Johnston, Jr., W.D.: A Transmission Electron Microscope Study of Iron Phosphide Precipitaters in InP Crystals. *J. Cryst. Growth*, **72**, 3, pp. 693-698 (1985).

56) Cahn, J.W.: Phase Separation by Spinodal Decomposition in Isotropic Systems. *J. Chem. Phys.*, **42**, 1, pp. 93-99 (1965).

57) Henoc, P., Izrael, A., Quillec, M., and Launois, H.: Composition Modulation in Liquid Phase Epitaxial $In_xGa_{1-x}As_yP_{1-y}$ Layers Lattice Matched to InP Substrates. *Appl. Phys. Lett.*, **40**, 11, pp. 963-965 (1982).

58) Ueda, O., Isozumi, S., and Komiya, S.: Composition-Modulated Structures in InGaAsP and InGaP Liquid Phase Epitaxial Layers Grown on (001)GaAs Substrates. *Jpn. J. Appl. Phys.*, **23**, 4, pp. L241-L243 (1984).

59) Treacy, M.M.J., Gibson, J.M., and Howie, A.: On Elastic Relaxation and Long Wavelength Microstructures in Spinodally Decomposed $In_xGa_{1-x}As_yP_{1-y}$ Epitaxial Layers. *Philos. Mag. A*, **51**, 3, pp. 389-417 (1985).

60) Ueda, O., Takechi, M., and Komeno, J.: Generation of Strong Composition-Modulated Structures and Absence of Ordered Structures in InGaP Crystals Grown on (110) GaAs Substrates by Metalorganic Chemical Vapor Deposition. *Appl. Phys. Lett.*, **54**, 23, pp. 2312-2314 (1989).

61) Gomyo, A., Suzuki, T., Kobayashi, K., Kawata, S., and Hino, I.: Evidence for the Existence of an Ordered State in $Ga_{0.5}In_{0.5}P$ Grown by Metalorganic Vapor Phase Epitaxy and Its Relation to Band-Gap Energy. *Appl. Phys. Lett.*, **50**, 11, pp. 673-675 (1987).

62) Ueda, O., Takikawa, M., Komeno, J., and Umebu, I.: Atomic Structure of Ordered InGaP Crystals Grown on (001) GaAs Substrates by Metalorganic Chemical Vapor Deposition. *Jpn. J. Appl. Phys.*, **26**, 11, pp. L1824-L1827 (1987).

63) Kondow, M., Kakibayashi, H., and Minagawa, S.: Ordered Structure in OMVPE-Grown $Ga_{0.5}In_{0.5}P$. *J. Cryst. Growth*, **88**, 2, pp. 291-296 (1988).

64) Ueda, O., Takikawa, M., Takechi, M., Komeno, J., and Umebu, I.: Transmission Electron Microscopic Observation of InGaP Crystals Grown on (001)GaAs Substrates by Metalorganic Chemical Vapor Deposition. *J. Cryst. Growth*, **93**, pp. 418-425 (1988).

65) Gomyo, A., Suzuki, T., and Iijima, S.: Observation of Strong Ordering in $Ga_xIn_{1-x}P$ Alloy Semiconductors. *Phys. Rev. Lett.*, **60**, 25, pp. 2645-2648 (1988).

66) Suzuki, T., Gomyo, A., and Iijima, S.: Strong Ordering in GaInP Alloy Semiconductors; Formation Mechanism for the Ordered Phase. *J. Cryst. Growth*, **93**, pp. 396-405 (1988).

67) Kondow, M., Kakibayashi, H., Tanaka, T., and Minagawa, S.: Ordered Structure in $Ga_{0.7}In_{0.3}P$ Alloy. *Phys. Rev. Lett.*, **63**, 8, pp. 884-886 (1989).

68) Ueda, O., Hoshino, M., Kodama, K., Yamada, H., and Ozeki, M.: Atomic Ordering in InGaP Crystals Grown by Chloride-VPE Method. *J. Cryst. Growth*, **99**, pp. 560-565 (1990).

69) Ueda, O., Hoshino, M., Takechi, M., Ozeki, M., Kato, T., and Matsumoto, T.: Comparative Study of Atomic Ordering and Alloy Clustering in InGaP Crystals Grown by Metalorganic Vapor Phase

Epitaxy, Chloride-Vapor Phase Epitaxy, and Liquid Phase Epitaxy. *J. Appl. Phys.*, **68**, 8, pp. 4268-4271 (1990).

70) Shahid, M.A., Mahajan, S., Laughlin, D.E., and Cox, H.M.: Atomic Ordering in $Ga_{0.47}In_{0.53}As$ and $Ga_xIn_{1-x}As_yP_{1-y}$ Alloy Semiconductors. *Phys. Rev. Lett.*, **58**, 24, pp. 2567-2570 (1987).

71) Nakayama, H., and Fujita, H.: Direct Observation of an Ordered Phase in a Disordered $In_{1-x}Ga_xAs$ Alloy. Proc. Int. Symp. GaAs and Related Compounds, Karuizawa, Jpn., 1985, Inst. Phys. Conf. Ser., 79, 1986, pp. 289-294.

72) Norman, A.G., Mallard, R.E., Murgatroyd, I.J., Booker, G.R., Moore, A.H., and Scott, M.D.: TED, TEM and HREM Studies of Atomic Ordering in $Al_xIn_{1-x}As$ (x~0.5) Epitaxial Layers Grown by Organometallic Vapor Phase Epitaxy. Proc. Microsc. Semicond. Mater., Oxford, 1987, Inst. Phys. Conf. Ser., 87, 1987, pp. 77-82.

73) Ueda, O., Fujii, T., Nakada, Y., Yamada, H., and Umebu, I.: TEM Investigation of Modulated Structures and Ordered Structures in InAlAs Crystals Grown on (001)InP Substrates by Molecular Beam Epitaxy. *J. Cryst. Growth*, **95**, pp. 38-42 (1989).

74) Jen, H.R., Cheng, M.J., and Stringfellow, G.B.: Ordered Structures in $GaAs_{0.5}Sb_{0.5}$ Alloys Grown by Organometallic Vapor Phase Epitaxy. *Appl. Phys. Lett.*, **48**, 23, pp. 1603-1605 (1986).

75) Ihm, Y.E., Otsuka, N., Klem, J., and Morkoç, H.: Ordering in $GaAs_{1-x}Sb_x$ Grown by Molecular Beam Epitaxy. *Appl. Phys. Lett.*, **51**, 24, pp. 2013-2015 (1987).

76) Jen, H.R., Ma, K.Y. and Stringfellow, G.B.: Long-Range Order in InAsSb. *Appl. Phys. Lett.*, **54**, 12, pp. 1154-1156 (1989).

77) Jen, H.R., Cao, D.S., and Stringfellow, G.B.. Long-Range [111] Ordering in $GaAs_{1-x}P_x$. *Appl. Phys. Lett.*, **54**, 19, pp. 1890-1892 (1989).

78) Chen, G.S., Jaw, D.H., and Stringfellow, G.B.: Effects of Substrate Misorientation on Ordering in $GaAs_{0.5}P_{0.5}$ Grown by Organometallic Vapor Phase Epitaxy. *Appl. Phys. Lett.*, **57**, 23, pp. 2475-2477 (1990).

79) Murgatroyd, I.J., Norman, A.G., Booker, G.R.: Observation of {111} Ordering and [110] Modulation in Molecular Beam Epitaxial $GaAs_{1-y}Sb_y$ Layers: Possible Relationship to Surface Reconstruction Occurring During the Growth. *J. Appl. Phys.*, **67**, 5, pp. 2310-2319 (1990).

80) Kuan, T.S., Kuech, T.F., Wang, W.I., and Wilkie, E.L.: Long-Range Order in $Al_xGa_{1-x}As$. *Phys. Rev. Lett.*, **54**, 3, pp. 201-204 (1985).

81) Kuan, T.S., Wang, W.I., and Wilkie, E.L.: Long-Range Order in $In_xGa_{1-x}As$. *Appl. Phys. Lett.*, **51**, 6, pp. 51-53 (1987).

82) Ueda, O., Nakata, Y., and Fujii, T.: Study on Microstructure of Ordered InGaAs Crystals Grown on (110)InP Substrates by Transmission Electron Microscopy. *Appl. Phys. Lett.*, **58**, 7, pp. 705-707 (1991).

83) Ueda, O., Nakata, Y., Nakamura, T., and Fujii, T.: TEM Investigation of CuAu-I Type Ordered Structures in MBE-Grown InGaAs Crystals on (110)InP Substrates. Proc. 7th Int. Conf. Vapor Growth and Epitaxy, Nagoya, 1991, to be published in a special issue of *J. Cryst. Growth*, (1992).

84) Khachaturyan, A.G.: The Problem of Symmetry in Statistical Thermodynamics of Substitutional and Interstitial Ordered Solid Solutions. *Phys. Status Solidi (b)*, **60**, pp. 9-37 (1973).

85) Nakata, Y., Ueda, O., and Fujii, T.: High Two-Dimensional Electron Gas Mobility Enhanced by Ordering in InGaAs/N-InAlAs Heterostructures Grown on (110)-Oriented InP Substrates by Molecular Beam Epitaxy. *Jpn. J. Appl. Phys.*, **30**, 2B, pp. L249-L251 (1991).

86) Nakata, Y., Ueda, O., and Fujii, T.: Two-Dimensional Electron Gas Mobility in Ordered InGaAs/N-InAlAs Heterostructures Grown on (110)-Oriented InP Substrates by Molecular Beam Epitaxy. Proc. 7th Int. Conf. Vapor Growth and Epitaxy, Nagoya, 1991, to be published in a special issue of *J. Cryst. Growth*, (1992).

87) Takeda, Y., and Sasaki, A: Calculated Electron Mobility of Two-Dimensional Electrons in AlInAs/InGaAs and InP/InGaAs Single Heterostructures. *Jpn. J. Appl. Phys.*, **24**, 10, pp. 1307-1311 (1985).

Osamu Ueda

Semiconductor Crystals Laboratory
FUJITSU LABORATORIES, ATSUGI
Bachelor of Physical Eng.
The University of Tokyo 1974
Dr. of Eng.
The University of Tokyo 1990
Specializing in Characterization of Compound Semiconductors

UDC 621.315.55:621.375.826

Pulsed-Jet Epitaxy of III-V Compounds

• Masashi Ozeki • Nobuyuki Ohtsuka • Yoshiki Sakuma

(Manscript received October 14, 1991)

Pulsed-jet epitaxy (PJE) for III-V compounds (GaAs, InP, GaP, and InAs) and its possibilities for process technology are described. A model involving selective reactions has been proposed to explain the self-limiting process in PJE. A reduction of carbon contamination has been achieved for GaAs growth using PJE and carrier concentrations ranging from $10^{14}\,cm^{-3}$ to $10^{20}\,cm^{-3}$ for *n*-type GaAs, and from $10^{15}\,cm^{-3}$ to $10^{21}\,cm^{-3}$ for *p*-type GaAs. These can be obtained by controlling growth conditions and doping levels. The growth of $(GaAs)_m(GaP)_n$ superlattices has demonstrated the high potential of PJE in superlattice growth. PJE offers unique possibilities for low temperature growth, selective growth, and uniform thickness growth.

1. Introduction

Atomic layer epitaxy (ALE) has many advantages over conventional growth methods such as molecular-beam epitaxy (MBE) and metalorganic vapor phase epitaxy (MOVPE)[1)-6)]. The current interest in quantum-effect devices has led to improved crystal growth now controllable at the atomic level. Such progress in MOVPE and MBE techniques now makes it almost possible to grow epitaxial layers at the atomic level. In this type of growth, the layer thickness is a function of growth time, and in most cases the function is proportional to growth time. To produce layers of the right thickness, the growth rate is controlled based on data on the preceding growth. However, the growth temperature, gas flow (molecular flux) and partial pressure of source gases change with growth time and from run to run. Even though this change is small, it makes it difficult to control the growth thickness within a monolayer level using conventional growth methods. At any one time, the source gas pressure (molecular flux) and substrate temperature are also different at different points on the substrate wafer, even at the same gas flow rate. In MOVPE and MBE, much work has been done to improve the uniformity of the layer thickness.

ALE provides a solution to these problems. Firstly, it is a self-limiting mechanism. The epitaxial growth automatically stops at exactly one monolayer. This distinguishes ALE from other epitaxial techniques and enables the thickness of the layer to be controlled precisely at the atomic level. The ALE technique makes it possible to grow epitaxial layers with an extremely uniform thickness with little fluctuation on large substrates.

Metalorganic ALE (MO-ALE), which uses metalorganic compounds for group III sources[6)], has several advantages in a flexible reactor design. It leads to fast exchange of group III and V source gases with a small gas manifold, it allows a number of highly pure metalorganic source to be used, and the techniques and concepts concerning the gas system and reactor developed for metalorganic vapor phase epitaxy can be applied.

MO-ALE has problems, however, for control of the self-limiting process and in crystal purity. Temperature ranges in which self-limited growth is possible are reportedly very narrow for many III-V compounds, and carbon contamination from metalorganic sources has been serious in GaAs ALE.

A new MO-ALE technique called pulsed-jet

epitaxy (PJE) was developed to solve many of the problems of conventional ALEs for III-V compounds. PJE enables high purity III-V thin films with a clear self-limiting mechanism to be grown under a wide range of conditions. This paper describes the principle of PJE and possible applications of the technique to device processes.

2. Self-limiting mechanism

A source molecule (precursor) introduced into a reactor arrives at the growth surface after thermal decomposition and chemical reactions with other molecules in the gas phase. The arrival rate of the molecule, r_{ar} per-second at a lattice site, i.e. adsorption site, is assumed to be proportional to the vapor pressure of the source molecule p_v, and can be written as

$$r_{ar} = K_{ar} p_v, \qquad \ldots\ldots (1)$$

where K_{ar} is a constant proportional to the inverse square root of temperature $T^{-1/2}$, and derived from detailed balance and statics.

The stability of a molecule at the adsorption site is determined from the total potential energy of the system including the adsorbed molecule and the adsorption site. When an adsorbed molecule in thermal equilibrium with the surface lattice desorbs from the surface in the gas phase, its thermal desorption rate, r_{ds} is written[7]

$$r_{ds} = K_{ds}(T)\nu \exp(-E_{ds}/kT), \qquad \ldots (2)$$

where ν is the thermal vibrational frequency of the adsorbed molecules, E_{ds} the dissociation energy (or band enthalpy), k the Boltzmann constant and K_{ds} the prefactor which involves the rotational and vibrational energies of the adsorbed molecule and is a function of temperature.

In the ALE of a binary compound composed of cation A and anion B, let A° be the source molecule for A (see Fig. 1). In some cases, A° may partly decompose or react with other chemicals in the gas phase. If the system can be described as a simple process where the source molecule A° is adsorbed (chemisorbed) at

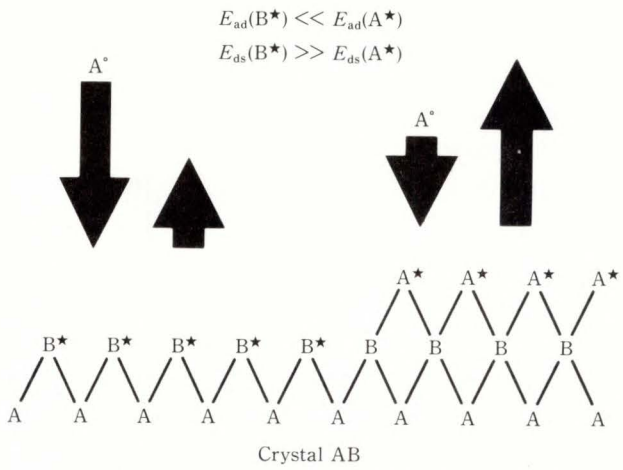

Fig. 1—Self-limiting process in ALE of crystal AB.

surface site B* with a relatively large adsorption energy E_{ad}, then a new adsorption site A* will be formed instead of site B*. Molecule A° reacts chemically with adsorption site B*, and usually partly or completely decomposes on the surface.

When the adsorption energy E_{ad} of molecule A° is sufficiently large at the new adsorption site A*, A° does not adsorb onto the site. If the surface chemical species involving cation atom A has a small desorption energy E_{ds} at adsorption site A*, it will easily desorb from the surface. In both cases, the "effective" adsorption rate of molecule A° appears to decrease as the surface density at site A* increases. This saturation effect of adsorption and desorption may be used to make self-limitation possible in ALE of compound AB.

A typical example of the saturation effect in effective adsorption is where A* has a stable methyl group or a chlorine which prevents gas phase molecules from approaching the A* site due to steric hindrance. However, the methyl group or chlorine is not necessarily needed for the self-limiting mechanism if site A*, which consists of only cation atom A, does not react with molecule A° (or has a large adsorption energy or a small desorption energy) at the growth temperature.

When a molecule approaches the crystal surface, the chemical bond of the molecule is sometimes broken and new chemical bonds are

formed between the adsorbed molecule and surface atoms. This type of adsorption, or dissociative adsorption, is an important chemisorption process and it plays an important role in ALE growth.

In dissociative adsorption, the valence electrons which form a chemical bond in the molecule transfer to the surface atom, while antibonding electrons transfer from the surface to the adsorbed molecule as the molecule approaches the surface. This weakens the strength of the chemical bond in the molecule. As the molecule approaches the surface, a strong chemical bond forms between surface atoms and atoms in the molecule, and finally the valence bond of the molecule is broken.

Generally, the electron distribution, and therefore the bond length in the adsorbed molecule, charge, even though the change is not big as in the case of dissociative adsorption. Some molecules tend to decompose more easily on the surface than in the gas phase, and decomposition of the adsorbed molecule in ALE often cannot be distinguished from dissociative adsorption.

3. Experiment

Epitaxial growth was carried out by depositing a monolayer of group III atoms followed by a monolayer of group V atoms. The gas sources for the group III atoms were trimethylgallium (TMGa), triethylgallium (TEGa), trimethylaluminum (TMAl) and trimethylindium (TMIn), and the gas sources for growth were contained in a low-pressure reactor designed so that thermal decomposition of the source gases was suppressed in the gas phase and proceeded only on the substrate surface. The reactor has a chimney-type structure where the carrier gas and reactants are introduced from the bottom and exhausted through the top by high capacity vacuum pumps. The reactor structure was determined by simulation to give smooth gas flow streamlines without vortices. The substrate was positioned in the fast gas stream emitted from a jet nozzle to prevent thermally decomposing source molecules building up in stagnant layers. The exchange of reactant gases was achieved using a pressure-balanced vent-and-run manifold. Alternating pulses of group III metalorganic and group V hydride gases were separated by a hydrogen purge pulse which prevented the reactants from mixing.

Growth thickness was estimated by measuring the step height between the epitaxial surface and a substrate whose surface was masked with SiO_2 which was removed before measurement. The growth rate was calculated by dividing the growth thickness by the gas cycle. A growth of 500 cycles was usually used for the growth rate experiments.

4. GaAs growth

Figure 2 shows the variation of growth rate of GaAs(001) as a function of the TMGa pulse

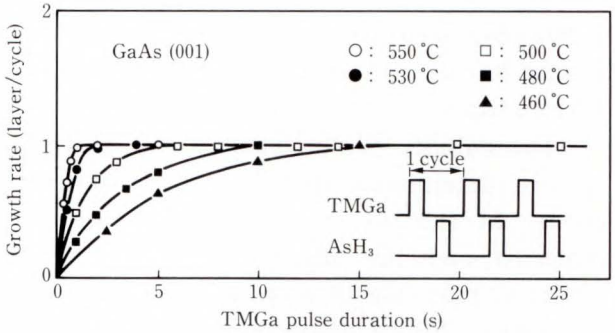

Fig. 2—Dependence of GaAs growth rate as a function of the TMGa pulse duration.

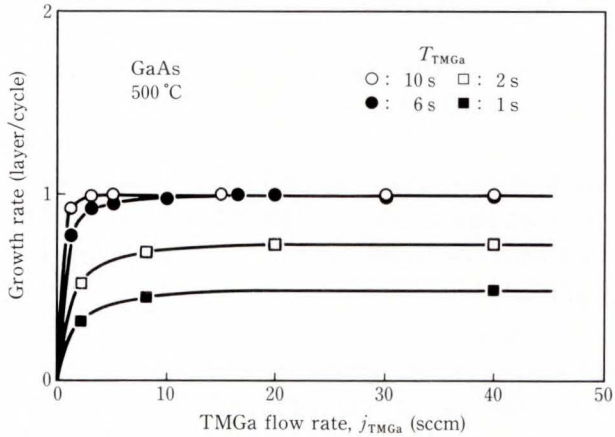

Fig. 3—Dependence of GaAs growth rate as a function of TMGa flow rate j_{TMGa} for different pulse durations. j_{TMGa} corresponds to TMGa partial pressure.

duration from 460 °C to 550 °C. The growth rate is defined as the epitaxial thickness by the gas cycle and is expressed in monolayers/cycle. The thickness of one monolayer corresponds to 0.283 nm (2.83 Å) for GaAs(100). The rise time to one monolayer thickness decreases as growth temperature increases. This occurs because the decomposition rate of TMGa molecules adsorbed on the surface increases as the temperature increases.

The GaAs growth rate was studied for different TMGa pulse duration as a function of TMGa flow rate j_{TMGa} defined as the flow rate of hydrogen carrier gas through the TMGa cylinder (see Fig. 3). TMGa partial pressure p_{TMGa} is proportional to flow rate j_{TMGa}, when the total flow rate of hydrogen carrier gas is constant in the reactor. The growth rate increases with j_{TMGa} for different saturation thicknesses, then levels off. The saturation thickness continuously increases with TMGa pulse duration up to one monolayer (2.83 Å). Figure 3 shows that the TMGa partial pressure corresponding to a TMGa flow rate above 10 standard cm^3 min^{-1} (sccm) is so high that the surface is completely covered with TMGa.

The steric hindrance effect due to the methyl group is significant when the dissociation energy E_{ds} of TMGa is very small at a surface site and TMGa therefore desorbs easily from the site at the growth temperature. After TMGa is supplied to the arsenic-coated surface, a TMGa molecule adsorbed on one site soon cannot occupy the nearest sites, because the molecule has a diameter of about 0.7 nm (7 Å) which involves the van der Waals repulsive force. The surface density of the TMGa molecule cannot reach the density of surface arsenic sites.

Figure 3 shows that the saturation thickness is one monolayer for a TMGa pulse duration over 6 s and no TMGa molecules exist on the surface. This suggests that the TMGa molecule is thermally decomposed or dissociatively adsorbed on the surface into di- or monomethylgallium, or atomic gallium. This decomposed state of TMGa is hereafter referred to as Ga*.

A rate equation can be used to describe the growth rate dependence in GaAs PJE. One of two things may happen to a TMGa molecule which arrives at the surface: one is desorption to the vapor phase, and the other is chemisorption (dissociative adsorption) onto surface arsenic atoms where TMGa decomposes into dimethyl, monomethyl or atomic gallium. We assume that TMGa molecules cannot chemisorb onto the Ga*.

Note that adsorbed TMGa quickly desorbs even on the arsenic atom around 500 °C. The desorption time constant τ_{ds} was reported to be 0.6 s for the TEGa molecule at 350 °C and much faster for TMGa[8]. This is consistent with the fact that, when the purge time following the TMGa pulse was changed from 0.1 s to 120 s, no variations in the growth rate were observed. These results show that TMGa molecules cannot be effectively observed on the surface at 500 °C after a TMGa gas pulse. The surface density of adsorbed TMGa n_{TMGa} and that of thermally decomposed methyl gallium or atomic gallium n_{Ga}* are calculated by the rate equations,

$$\begin{aligned} dn_{TMGa}/dt &= r_{ar}(1 - n_{TMGa} - n_{Ga}^*) \\ &\quad - (r_{cs} + r_{ds}) n_{TMGa}, \\ dn_{Ga}^*/dt &= r_{cs}\, n_{TMGa}. \end{aligned} \quad \cdots\cdots (3)$$

Neglecting the adsorbed TMGa at the end of the TMGa pulse, the growth thickness per gas cycle becomes n_{Ga}*.

The temperature dependence of growth rate was quantitatively compared with the rate equations using r_{cs} as the fitting parameter. r_{ar} is proportional to the mole fraction of TMGa, and a flow rate of 1 sccm through the TMGa bubbler corresponds to 5.6×10^2 s^{-1} for r_{ar}. The value of r_{ds} was of the order of 10^3 s^{-1} and its effect on the growth rate was small, because the growth carried out so that r_{ar} was much larger than r_{ds}. This condition may be satisfied if the TMGa flow rate j_{TMGa} is above 10 sccm at 500 °C (see Fig. 2). The solid curves in Figs. 2 and 3 were calculated from the rate equations. The fitting parameter $\tau_{cs} = r_{cs}^{-1}$ is plotted as a function of growth temperature in Fig. 3, and an activation energy of 42 kcal/mol

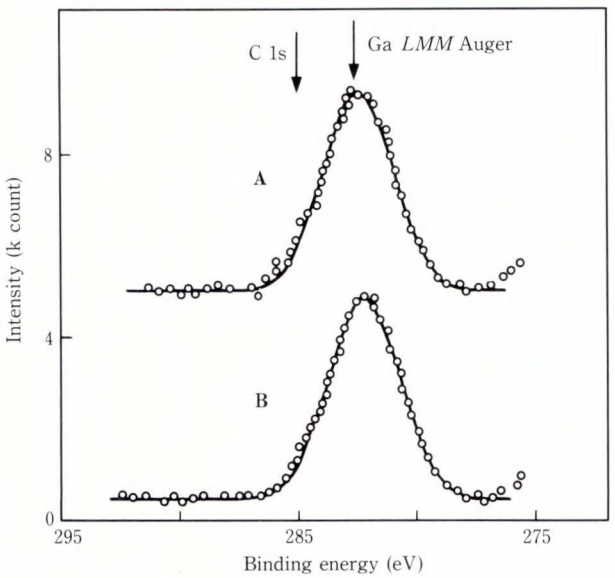

Fig. 4—Comparison of XPS spectra between AsH_3-exposed surface A and TMGa-exposed surface B. The dominant peak is due to the Auger *LMM* peak.

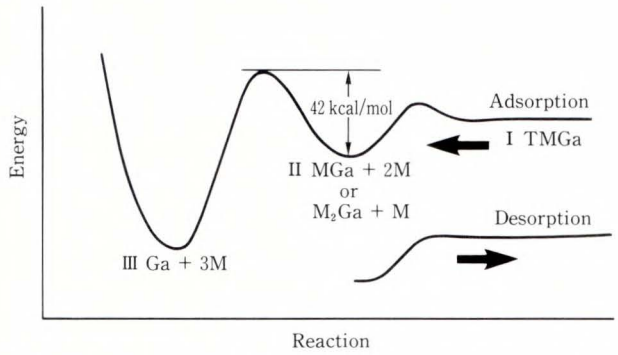

Fig. 5—Adsorption and desorption processes of TMGa molecule for GaAs (100) surface.

is obtained for the dissociative chemisorption of TMGa on a GaAs(100) surface from 450 °C to 560 °C. The saturation thickness below one monolayer for short pulse durations (see Fig. 2) is produced from the fast desorption of undecomposed TMGa after a TMGa gas pulse.

Surface adsorbates were identified using X-ray photoelectron spectroscopy (XPS) using an analysis chamber and growth chamber so that free movement from one chamber to another was possible out without exposure to air[8]. Figure 4 compares XPS spectra between an AsH_3-exposed surface A and a TMGa-exposed surface B. The GaAs(100) surface prepared by

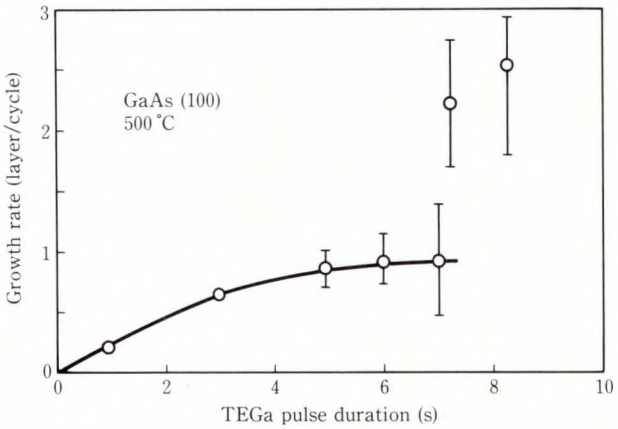

Fig. 6—Growth rate dependence of GaAs layer as a function of TEGa pulse duration (pulsed-jet epitaxy).

ALE growth was exposed to AsH_3 or TMGa vapor at 500 °C and cooled to room temperature for the XPS analysis. The observed peak was not due to XPS, but was due to a Ga *LMM* Auger emission. If there are carbon or carbon-related bonds on the surface, XPS emission associated with carbon should be observed at 285 eV on the higher energy side of the Ga *LMM* Auger peak. This shows that there were few methyl radicals on the TMGa exposed surface.

Figure 5 shows the adsorption and desorption of TMGa on the arsenic-coated (100)GaAs surface, which explains the atomic Ga model[9]. TMGa dissociatively adsorbs onto the GaAs surface and decomposes into monomethylgallium or dimethylgallium. These methylgalliums may desorb from the surface (the surface lifetime is very short, in the order of milliseconds), but some methylgalliums further decompose into Ga atoms (activation energy 42 kcal/mol).

TEGa is a typical gallium source, which decomposes at a lower temperature compared with TMGa and easily decreases the carbon contamination of the GaAs layer in conventional MOVPE or MOMBE growth. Figure 6 shows the growth rate variation in the GaAs layer as a function of the TEGa pulse duration in pulsed-jet epitaxy. Single monolayer saturation tended to occur for shorter pulse durations, but the growth rate increases beyond one monolayer when the pulse duration is above 7 s. A large fluctuation in the thickness profile was also

observed for an epitaxial layer. Error bars represent thickness variations within the epitaxial layer. When the growth rate increased beyond one monolayer of GaAs, the surface morphology of the layer changed drastically from a mirror-like to a rough surface. The surface was covered with gallium droplets when the growth rate was above one monolayer. Growth for the self-limiting mechanism was studied using TEGa under various growth conditions, which involved low temperature growth below 400 °C, but no self-limiting was observed in the growth rate. However, there is no definite model to explain this. Given that the vapor pressure of source molecules is closely related to the self-limiting mechanism, these phenomena may be produced more easily for source materials with a higher vapor pressure.

Tri-isobutylgallium (TIBGa), which is liquid at room temperature, was studied as a possible gallium source for low temperature ALE. TIBGa molecules decompose on the As-coated surface even at 200 °C. The vapor pressure of TIBGa is 200 Pa at 54 °C, thus it can be used in the conventional organometallic gas system. A GaAs layer was grown using TIBGa and AsH_3 in the pulsed-jet reactor. When growth was at 400 °C, the thickness per cycle increased with TIBGa pulse duration. Below 350 °C, growth was partly self-limited and saturated at one monolayer. GaAs layers with excellent surface morphology were grown by ALE using TIBGa and AsH_3, even at 250 °C.

In ALE, there has been little focus on the supply condition of AsH_3 because of the high As vapor pressure and the weak bonding between As atoms at the growth temperature. Below 350 °C, the growth rate strongly depends on the AsH_3 supply. Figure 7 shows the growth thickness per cycle (growth rate) as a function of AsH_3 pulse duration. After a quick rise in the growth rate at pulse durations below 1 s, the growth rate decreased with AsH_3 pulse duration. The surface morphology was very smooth and mirror-like for longer AsH_3 pulse durations. The same result was obtained when the AsH_3 partial pressure was changed, i.e. increasing the AsH_3 pressure decreased the growth rate. Another interesting feature is that the growth rate decreases for incremented steps of one monolayer of GaAs. This indicates that TIBGa is very sensitive to the atomic structure of the arsenic-coated surface.

5. InP, InAs and GaP

Figure 8 shows the dependence of the growth rate of InP on the TMIn pulse duration. At 600 °C, the thickness per cycle increased beyond one monolayer/cycle as pulse duration increased. At 350 °C, the growth rate remained constant for a pulse duration above 1 s. The saturation thickness was, however, 0.5 monolayers on the (100) face. A similar dependence was observed as the TMIn mole fraction was

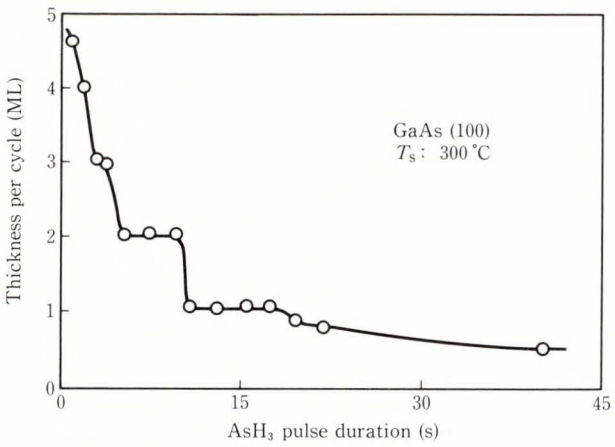

Fig. 7—Growth rate of GaAs as a function of AsH_3 pulse duration.

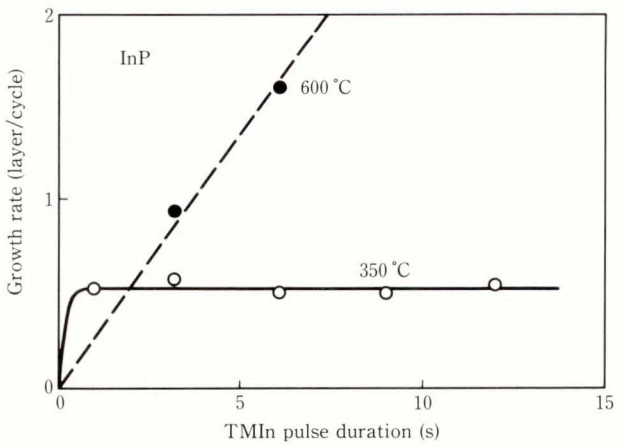

Fig. 8—Growth rate of dependence of InP as a function of the TMIn pulse duration.

varied. The thickness per cycle increased with TMIn mole fraction beyond 1 monolayer above 400 °C, while the thickness saturated at 0.5 monolayer below 400 °C[10].

XPS studies were made for the InP surface. No methylindium was observed on the surface around 350 °C as the GaAs surface. This suggests that the self-limiting process is due to selective adsorption and desorption on indium and phosphorus atoms, as in the pulsed-jet epitaxy of GaAs. The saturation thickness of about half a monolayer is probably due to a stable surface reconstruction of InP around 350 °C.

InAs and GaP ALE was studied using PJE. Figure 9 shows the growth rate dependence of GaP(100) as a function of the TMGa flow rate at 500 °C. A clear self-limiting condition was observed the growth rate saturated at just one monolayer when the pulse duration was higher than 5 s with increased TMGa flow rate. A self-limiting condition was also observed for the TMGa pulse duration dependence. Similar results were obtained for InAs ALE, where the growth rate saturated at just one monolayer with increased TMIn pulse duration and partial pressure. Figure 10 shows the temperature dependence of the saturation thickness for InAs, GaP, and GaAs. One monolayer saturation occurs over wide temperature ranges for these compounds[11].

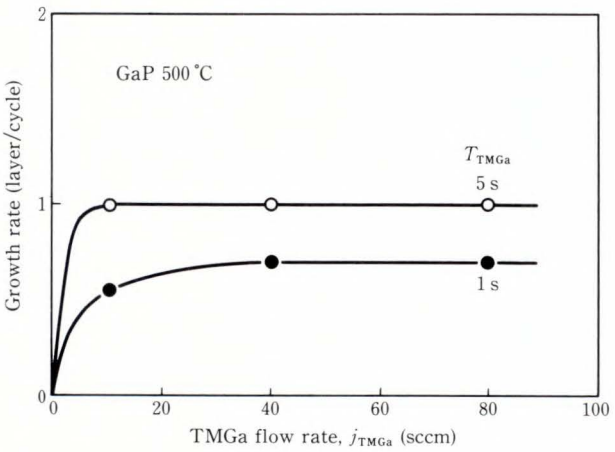

Fig. 9—Growth rate dependence of GaP on the TMGa flow rate.

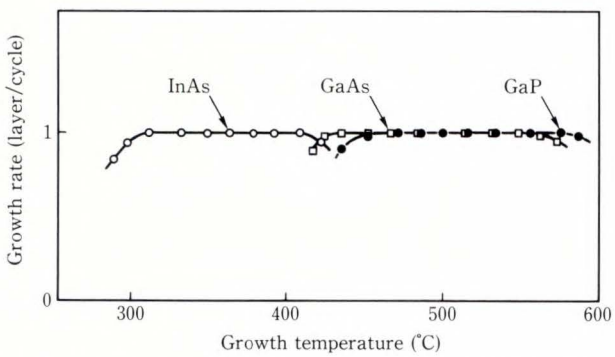

Fig. 10—Temperature dependence of saturation thicknesses for InAs, GaP and GaAs by PJE.

6. Purity and impurity doping

Purification and impurity doping techniques have been developed for PJE[12),13)]. GaAs

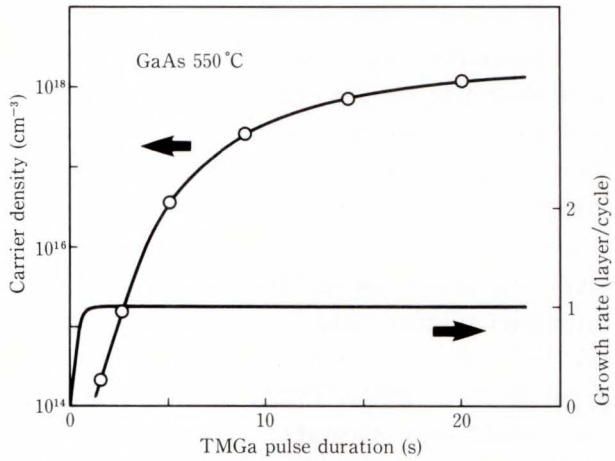

Fig. 11—Carrier (hole) density variation with TMGa pulse duration.

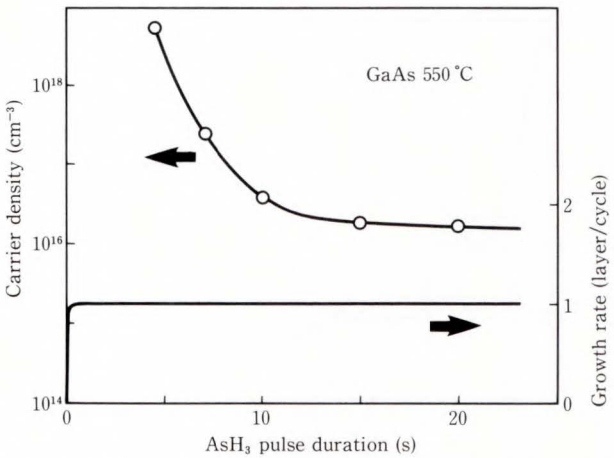

Fig. 12—Carrier (hole) density variation with AsH_3 pulse duration.

epitaxial growth under normal conditions exhibited *p*-type conductivity due to carbon acceptors. Figures 11 and 12 show the carrier (hole) densities of GaAs layers as a function of TMGa and AsH_3 pulse duration in PJE. The carrier density decreases drastically as TMGa pulse duration decreases or AsH_3 pulse duration increases. High-temperature growth above 550 °C can achieve one-monolayer saturation for a short TMGa pulse for a duration below 1 s (see Fig. 2). This allows highly pure GaAs layers to be grown by PJE. Figure 13 compares 4.2 K photoluminescence spectra for growth at 500 °C and TMGa pulse duration of 20 s, and 550 °C, and TMGa pulse duration of 0.8 s. The first sample was a *p*-type (hole density: 3×10^{18} cm^{-3}) and it showed broad luminescence at 830 nm due to donor-acceptor (carbon acceptor) pair recombination. The second sample was an *n*-type (carrier density: 3×10^{14} cm^{-3}). It exhibited sharp emission peaks due to the free and bound excitation peaks near the band gap energy but no emissions associated with the carbon acceptor, which reflects the high purity of the epitaxial layer.

It was possible to adjust the carrier density from 3×10^{14} cm^{-3} to 1×10^{21} cm^{-3} for *p*-type GaAs by varying the growth conditions, and from 1×10^{14} cm^{-3} to 2×10^{19} cm^{-3} for *n*-type by doping control using H_2Se, resulting in good surface morphology (see Fig. 14). These show that doping control in PJE is sufficient for growing GaAs layers for conventional devices.

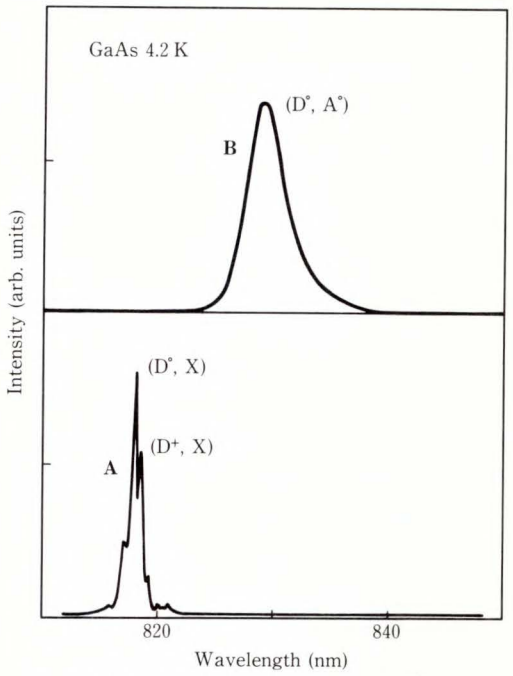

Fig. 13—Photoluminescence spectra for GaAs layers
A: 550 °C, TMGa pulse duration of 0.8 s,
B: 500 °C, TMGa pulse duration of 20 s.

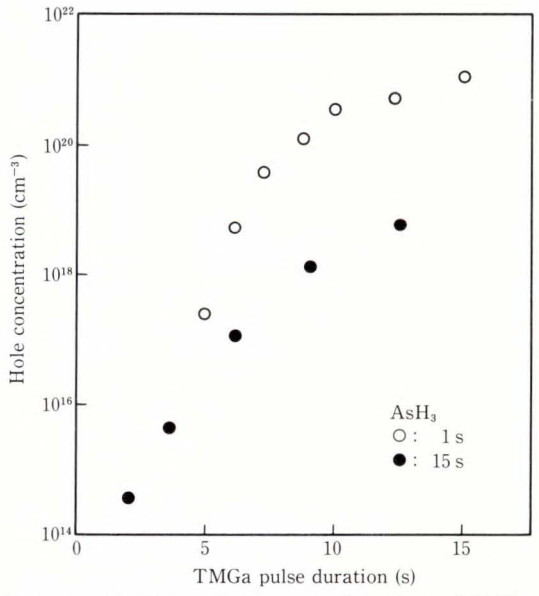

a) Hole concentration variations as a function of TMGa pulse duration for different arsine pulse durations

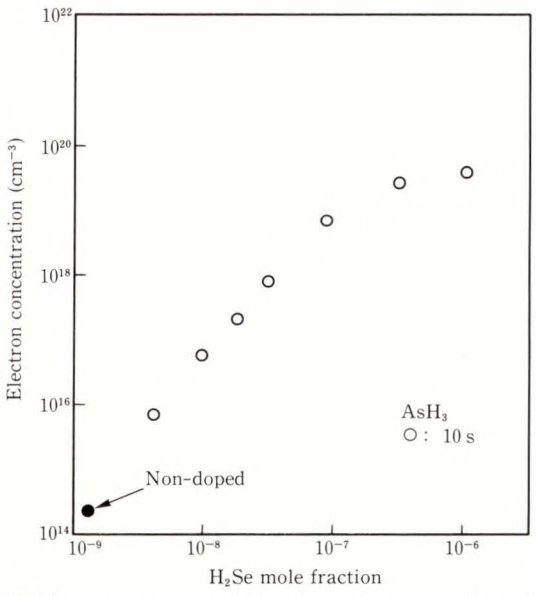

b) Electron concentration dependence as a function of H_2Se mole fraction

Fig. 14—Carrier concentrations of ALE-GaAs.

7. Selective growth and thickness uniformity

In ALE, ideal selective growth is possible, since growth proceeds two-dimensionally. Figure 15 compares the thickness variation of GaAs epitaxial layers from the SiO_2 mask edge for MOVPE and ALE growth. The epitaxial thickness of ALE shows the same surface level, while that of MOVPE gradually deceases for the SiO_2 edge because of faceted or lateral growth at the edge. It was also found that growth on stripes narrower than 1 μm was with a completely flat surface with no abnormal growth. Epitaxial patterns had perfectly mirror-like surfaces, although the substrate surface underwent several processes. This is important for the precise masking process using planar techniques.

It is easy for ALE to grow an epitaxial layer with an extremely uniform thickness. Figure 16 shows the thickness variations of ALE and MOVPE epitaxial layers on 2-inch wafers. Both epitaxial layers were grown in the same chamber, without any rotation of the GaAs substrate. The thickness variation for ALE grown layer was within 1.5 percent which is comparable to error in measuring thickness.

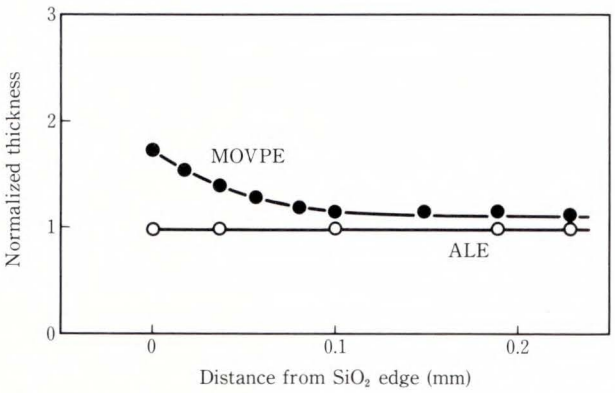

Fig. 15—Thickness variations of MOVPE and ALE (PJE) grown GaAs epitaxials from SiO_2 edge.

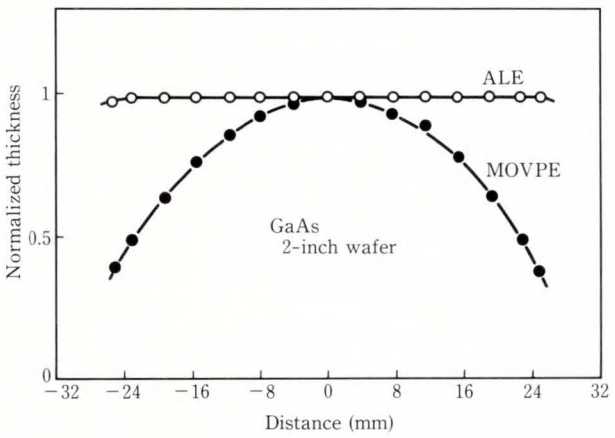

Fig. 16—Thickness variations of MOVPE and ALE (PJE) grown GaAs epitaxials on 2-inch substrates.

8. Heteroepitaxy and superlattices

Heteroepitaxy requires a much more complex procedure for ALE than homoepitaxy. The growth mechanism of the first layer for compound AB is not the same as that of the homoepitaxy for AB, because desorption, migration, and decomposition of precursors on the surface differ for crystal AB and substrate A′B′. Interface stress due to lattice mismatch greatly affects the growth mode of epitaxy and sometimes compromises the self-limiting mechanism.

The growth of strained-layer superlattices by ALE is an important test to examine the potential of ALE, because many complex procedures are involved. We grew $(GaAs)_m(GaP)_n$ strained-layered superlattices using PJE[14], because both crystals are self-limited at just one monolayer in the same temperature region, around 500 °C (see Fig. 10).

In ALE, the partial pressure and pulse duration of the sources were changed depending on the nature of the top surface. When the surface was coated with arsenic (phosphorus), TMGa was supplied to the surface under conditions

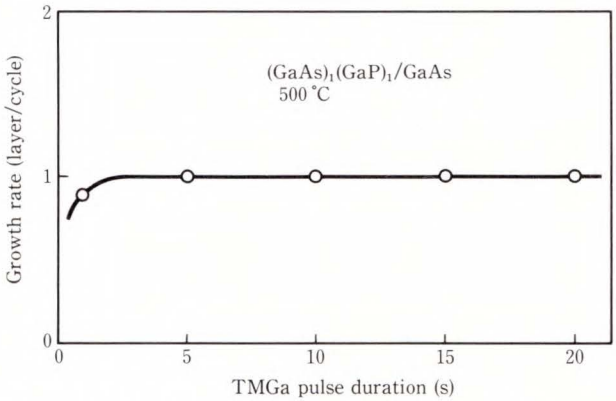

Fig. 17—Growth rate dependence of monolayer superlattice $(GaAs)_1(GaP)_1$ as a function of TMGa pulse duration after a PH_3 pulse. One monolayer is equal to 5.55 Å (0.555 nm).

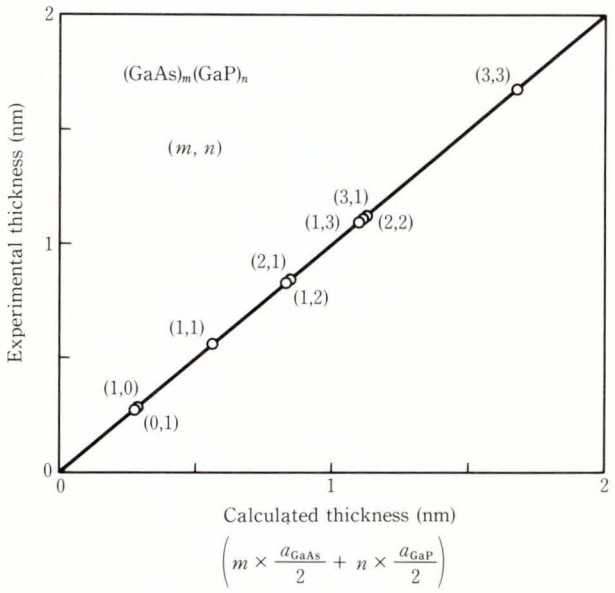

Fig. 18—Comparison of one-period experiment and calculated thicknesses for various superlattices $(GaAs)_m(GaP)_n$.

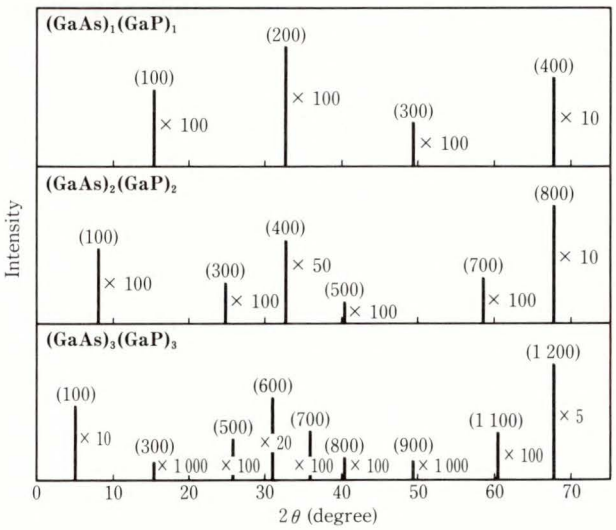

Fig. 19—X-ray rocking curves for $(GaAs)_m(GaP)_n$ $(m = n = 1, 2, 3)$.

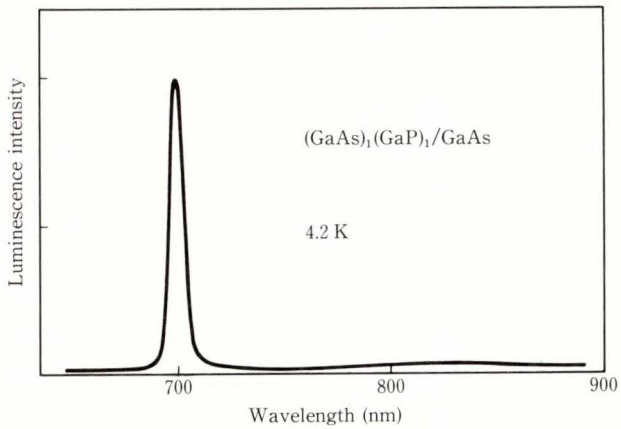

Fig. 20—4.2 K photoluminescence spectrum for $(GaAs)_1(GaP)_1$.

similar to GaAs (GaP) homoepitaxy. AsH_3 and PH_3 were supplied with a pulse duration and partial pressure high enough to attain one monolayer for GaAs and GaP homoepitaxies.

Figure 17 shows the growth rate of one period of $(GaAs)_1(GaP)_1$ for different pulse durations of TMGa onto the arsenic-coated surface. One monolayer is defined as the sum of a GaAs and GaP single-monolayer thickness and is equal to 0.555 nm (5.55 Å). A self-limiting mechanism was maintained for growth of the strained-layered superlattice. A self-limiting condition in the growth rate was also observed for variations in other growth parameters (TMGa partial pressure, AsH_3 pulse duration and partial pressure) involving the gallium-coated surface. Figure 18 compares the calculated and experimental one-period thickness of $(GaAs)_m(GaP)_n$ superlattices. The calculated thickness is defined as $m \times$ (GaAs lattice constant)/2 + $n \times$ (GaP lattice constant)/2 according to Vegard's law. The two sets of values agree well, indicating that the growth of each layer is self-limited to one monolayer.

We analyzed layer structures for superlattices using X-ray rocking curves and Raman scattering measurements. $(GaAs)_1(GaP)_1$, $(GaAs)_2(GaP)_2$, and $(GaAs)_3(GaP)_3$ show many diffraction peaks in addition to the (400) and (200) peaks which are allowed for the $GaAs_{0.5}P_{0.5}$ alloy (see Fig. 19). Their diffraction angles agree precisely with the calculated ones, as do their intensities. Raman scattering showed new vibrational modes resulting from Brillouin zone folding at the zone center for $(GaAs)_m(GaP)_n$. The periodicity of the superlattice causes Brillouin zone folding of the acoustic phonon branch and the confinement of optical phonons. The observed peak energies agree with those calculated when based on an elastic continuum model[15].

Electronic properties were studied by photoluminescence and photo-reflectance measurements[16]. Figure 20 shows a photoluminescence spectrum for the monolayer superlattice $(GaAs)_1(GaP)_1$. A strong luminescence peak occurs at about 700 nm with a relatively narrow half-width. Other superlattices (m, n = 2, 3, 4, 5) and a $GaAs_{0.5}P_{0.5}$ alloy exhibit no such sharp luminescence. Photo-reflectance measurements also showed that the band-gap energy abruptly decreased with layer number from $m = n = 2$ to 1, although the band-gap energy slowly increased as the layer number decreased above m, $n > 2$. These findings suggest that $(GaAs)_1(GaP)_1$ has a direct band-gap energy differing from other superlattices and $GaAs_{0.5}P_{0.5}$.

9. Conclusion

We showed PJE to be effective in ALE for III-V compounds. A self-limiting mechanism in PJE is explained by dissociative adsorption of TMGa molecules onto surface arsenic atoms. Atomic gallium may be responsible for the self-limiting condition in ALE. The activation energy of TMGa decomposition on the GaAs surface was found to be 42 kcal/mol around 500 °C, which is smaller than that in the gas phase because of the surface catalytic effect. Very pure GaAs films were produced, together with a wide range of carrier concentrations for n-type and p-typed doping of GaAs layers. Selective growth on fine patterns and uniform growth on large sugstrates show great promise for process techniques. Optical studies by photoluminescence and reflectance measurements of strained-layered superlattices $(GaAs)_m(GaP)_n$ grown on GaAs substrates by PJE suggest that the monolayer superlattice $(GaAs)_1(GaP)_1$ had a direct-band gap structure.

References

1) Suntola, T.: Atomic Layer Epitaxy. *Materials Sci. Rep.*, **4**, pp. 261-312 (1989).
2) Goodman, C.H.L., and Pessa, M.V.: Atomic layer epitaxy. *J. Appl. Phys.*, **60**, 3, pp. R65-R81 (1986).
3) Ozeki, M., Mochizuki, K., Ohtsuka, N., and Kodama, K.: Growth of GaAs and AlAs Thin Films by a New Atomic Layer Epitaxy Technique. *Thin Solid Films*, **174**, pp. 63-70 (1989).
4) Bedair, S.M., McDermott, B.T., Ide, Y., Karam, N.H., Hashemi, H., Tischler, M.A., Timmons, M., Tarn, J.C.L., and EL-Masry, N.A.: Recent Progress in Atomic Layer Epitaxy of III-V Compounds. *J. Crystal Growth*, **93**, pp. 182-189 (1988).
5) Watanabe, H., and Usui, A.: Atomic Layer Epitaxy. Proc. Int. Symp. GaAs and Related Compounds, Las Vegas, 1986, Inst. Phys. Conf. Ser. 83, Inst. Phys., Bristol and New York, 1987, pp. 1-8.
6) Nishizawa, J., and Kokubun, Y.: Recent Progress in Low Temperature Photochemical Processes. Ext. Abst. 16th Int. Conf. Solid State Devices Mater., Kobe, 1984, pp. 1-4.
7) Zeiri, Y., Redondo, A., and Goddard, W.A.: Classical Stochastic Diffusion Theory for Desorption from Solid Surfaces. *Surface Sci.*, **131**, pp. 221-238 (1983).
8) Kodama, K., Ozeki, M., Sakuma, Y., Mochizuki, K., and Ohtsuka, N.: *In-situ* X-ray Photoemission Spectroscopy for Atomic Layer Epitaxy of InP and GaAs. *J. Crystal Growth*, **99**, pp. 535-539 (1990).
9) Ozeki, M., Mochizuki, K., Ohtsuka, N., and Kodama, K.: New approach to the atomic layer epitaxy of GaAs using a fast gas stream. *Appl. Phys. Lett.*, **53**, 16, pp. 1509-1511 (1988).
10) Sakuma, Y., Kodama, K., and Ozeki, M.: Self-Limited Growth in InP Epitaxy by Alternate Gas Supply. *Jpn. Appl. Phys.*, **27**, 11, pp. L2189-L2191 (1988).
11) Sakuma, Y., Kodama, K., and Ozeki, M.: Atomic layer epitaxy of GaP and elucidation for self-limiting mechanism. *Appl. Phys. Lett.*, **56**, 9, pp. 827-829 (1990).
12) Mochizuki, K., Ozeki, M., Kodama, K., and Ohtsuka, N.: Carbon incorporation in GaAs layer grown by atomic layer epitaxy. *J. Crystal Growth*, **93**, pp. 557-561 (1988).
13) Takanohashi, T., Mochizuki, K., and Ozeki, M.: n and p-type doping in atomic layer epitaxy of GaAs. Proc. Int. Symp. GaAs and Related Compounds, Karuizawa, 1989, Inst. Phys. Conf., Ser. 106, Inst. Phys., Bristol and New York, 1990, pp. 39-44.
14) Ozeki, M., Kodama, K., Sakuma, Y., Ohtsuka, N., and Takanohashi, T.: GaAs/GaP strained-layer superlattices grown by atomic layer epitaxy. *J. Vac. Sci. Technol.*, **B8**, 4, pp. 741-746 (1990).
15) Kodama, K., Ozeki, M., Sakuma, Y., and

Ohtsuka, N.: Raman scattering of $(GaAs)_m(GaP)_n$ short-period superlattices prepared by pulsed jet epitaxy. *J. Appl. Phys.*, **69**, 9, pp. 6713-6715 (1991).
16) Takanohashi, T., and Ozeki, M.: Exiton-Transition Energies and Band Structure of $(GaP)_n(GaAs)_m$/GaAs Atomic-Layer Superlattices. *Jpn. J. Appl. Phys.*, **30**, 6A, pp. L956-L958 (1991).

Masashi Ozeki
Semiconductor Crystals Laboratory
FUJITSU LABORATORIES, ATSUGI
Bachelor of Electronic Eng.
Shizuoka University 1968
Dr. of Material Science
Osaka University 1979
Specializing in Semiconductor Materials

Nobuyuki Ohtsuka
Semiconductor Crystals Laboratory
FUJITSU LABORATORIES, ATSUGI
Bachelor of Science
Keio University 1986
Specializing in Semiconductor Crystals

Yoshiki Sakuma
Semiconductor Crystals Laboratory
FUJITSU LABORATORIES, ATSUGI
Bachelor of Electronic Eng.
Tohoku University 1985
Master of Electronic Eng.
Tohoku University 1987
Specializing in Semiconductor Crystals

UDC 548.522:621.315.55

Metalorganic Vapor Phase Epitaxy Using Organic Group-V Sources

• Toshihide Kikkawa • Hitoshi Tanaka • Junji Komeno

(Manuscript received November 22, 1991)

Safer MOVPE growth of GaAs, AlGaAs, and InGaAs on 3-inch GaAs substrates was investigated using organic group-V sources.

Tertiarybutylarsine (TBAs) and monoethylarsine (EtAs) were used with a horizontal atmospheric pressure reactor. GaAs and AlGaAs grown using TBAs were of high purity and extremely uniform, equivalent to those using arsine. With either silane or disilane doping, Si incorporation efficiency using TBAs or EtAs was always higher than that using arsine. The group-V pyrolysis simulation implies that H_2AsSiH_3 dominates in the gas phase when using TBAs, corresponding to high doping efficiency. High quality, high electron-mobility transistors were achieved with TBAs. These results verify that epitaxial layers grown using TBAs are of sufficiently high quality for device applications.

1. Introduction

Metalorganic vapor phase epitaxy (MOVPE) is a key technique in growing large-area III-V semiconductor materials for high-speed and optoelectronic devices, because it provides highly uniform, top quality materials having abrupt compositional changes on an atomic monolayer scale. The drawback is the danger posed by the use of highly toxic group-V hydrides, i.e. arsine (AsH_3) and phosphine (PH_3). Since they are stored in high-pressure cylinders, careful handling, especially when changing cylinders is required to avoid dangerous leakage. Safety apparatus, i.e. special exhaust equipment, is also required in case of accidental release.

Given the danger involved, many studies have been made in the search for less toxic As and P sources alternative to arsine and phosphine, as Stringfellow has reviewed[1]. Recently, less hazardous organic group-V precursors have attracted much attention. They are less toxic than arsine and phosphine, and are liquid at room temperature. Should a large leakage occur, the danger of exposure should be limited due to the lower toxicity and lower cylinder pressure. Early studies with trimethylarsine (TMAs) were hampered by significant impurity in the source materials[2),3)]. Using ^{13}C-labeled TMAs, Lum et al. showed that carbon from TMAs was incorporated at a concentration of 5×10^{16} cm^{-3} in GaAs layers[4]. The carbon background concentration could be reduced by using a graphite thermal precracker for TMAs[5]. Some researchers used TMAs with arsine as a carbon dopant source for the growth of heavily *p*-type GaAs[6]. Using triethylarsine (TEAs), GaAs layers were contaminated with carbon in the 10^{17} cm^{-3} range[7)-9)]. Using layers grown with TEAs, Fujita et al. fabricated a double-heterojunction laser diode that operated in pulse mode at room temperature[10].

In contrast with fully substituted organoarsines, i.e. TMAs and TEAs, partially hydrogen-substituted organoarsines have given more promising results. High quality GaAs layers were obtained using diethylarsine (DEAs)[11], phenylarsine (PhAs)[12], monoethylarsine (EtAs)[13),14)], and tertiarybutylarsine (TBAs)[15)-26)]. Using TBAs, Haacke et al. obtained the purest GaAs layers among non-arsine group-V sources[25),26)].

The GaAs layers had an electron mobility of 160 000 $cm^2 V^{-1} s^{-1}$ at 77 K. These results verify that partially substituted organoarsines, as As sources safer than arsine, are promising candidates for obtaining high-quality GaAs films with negligible carbon incorporation due to the effect of the As-H bond[27]. However, there has been little research into the growth of AlGaAs and InGaAs on GaAs substrate under various conditions, or into uniformity across a 3-inch substrate, due to limited quantities of organoarsine.

Several researchers have reported differences in Si-doping characteristics in GaAs between TBAs and arsine[28)-32)]. However, the mechanism responsible for these differences in doping efficiency was unknown. With arsine, many studies have been reported using silane (SiH_4) and disilane (Si_2H_6)[33)-52)].

Experimental device fabrication using a hydrogen-substituted organoarsine is essential for developing MOVPE manufacturing. Many successful results were achieved with TBAs, such as GaAs metal semiconductor field effect transistors (MESFETs)[30),53),54)], *p-i-n* photodiodes[28),55),56)], lasers[57)-59)], and solar cells[60)]. Recently, Sundaram et al.[61)] reported GaAs MESFETs exhibiting high performance. However, no high-speed devices consisting of both AlGaAs and GaAs have yet been fabricated by MOVPE using TBAs.

In this paper, we describe the use of TBAs as an arsenic source for the growth of high-quality uniform GaAs, AlGaAs, InGaAs, and selectively doped heterostructures on 3-inch GaAs substrates in an atmospheric pressure reactor under various conditions, and compare the properties of epitaxial layers grown using TBAs with those grown using arsine[23),24)]. EtAs was also used, and appears to be another promising source for GaAs growth[24)]. We investigated silane and disilane doping of GaAs with organoarsine and arsine[31)] to clarify the role of As-precursors, because doping control is indispensable to the reproducible production of high-performance devices. Furthermore, we demonstrated effective planar doping of Si into GaAs with TBAs to eliminate the effect of group-III sources[32)]. The comparison between our results and previous reports is addressed. We applied a kinetic simulation on the pyrolysis of the group-V sources, using the results to propose a precise Si-doping model. Electron traps in GaAs grown using TBAs were measured by deep level transient spectroscopy (DLTS)[62)], because the stoichiometric deviation in a crystal also provides useful information about the type of reactant on a substrate, and deep levels, such as EL2, are strongly affected by stoichiometric deviation.

We fabricated *n*-AlGaAs/GaAs high electron mobility transistors (HEMTs) and *n*-AlGaAs/InGaAs/GaAs pseudomorphic HEMTs with wafers grown using TBAs[63)]. The growth of a selectively doped heterostructure[64)] and the fabrication of HEMTs are landmarks in feasibility checks for device applications. High quality GaAs and AlGaAs films and abrupt compositional transitions are required to obtain high quality two-dimensional electron gas (2DEG) at the heterointerface[64)]. HEMTs are potentially superior to GaAs MESFETs due to the superior electron transport in HEMT channels and the unique electrical properties of the HEMT structure, which results in high-speed performance and low power dissipation[65)]. Furthermore, the HEMT structure suppresses the short channel effect[66)]. The *n*-AlGaAs/InGaAs/GaAs pseudomorphic HEMTs are more promising than *n*-AlGaAs/GaAs conventional HEMTs because they perform better in dc and microwave applications, due to a higher sheet carrier concentration and higher saturated velocity in the InGaAs channel layer[67),68)].

The natural convection induced by buoyancy which occurs in all conventional horizontal atomspheric pressure reactors promoted deposition onto the ceiling, degrading film uniformity. We designed an inverted horizontal atmospheric pressure reactor to demonstrate the growth of highly-uniform epitaxial layers. The inverted reactor eliminated buoyancy-induced flow, reducing source consumption due to wall deposition.

2. Experimental

We used two types of horizontal atmos-

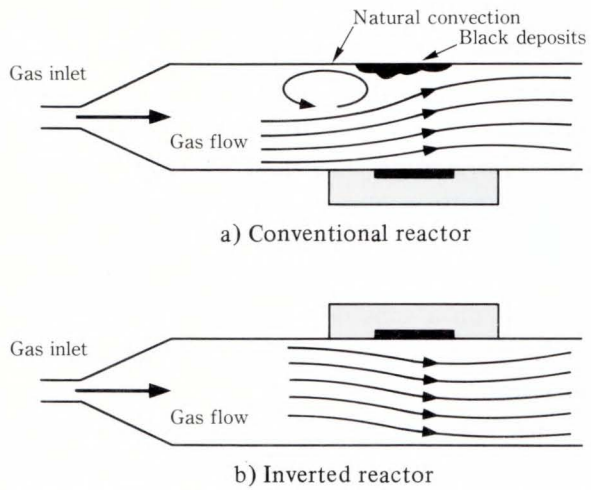

Fig. 1 – Schematic drawing indicating the expected flow line[24].

pheric pressure reactor using rectangular cross-section fused quartz of 10 cm to 14 cm wide by 2 cm tall as shown in Fig. 1. The first, Fig. 1a), was a common conventional reactor[24]. The other, Fig. 1b), was an inverted reactor we developed in this study. The stream lines in Fig. 1 schematically represent the gas flow we speculated.

Epitaxial layers were grown on stationary or rotated 2- or 3-inch GaAs substrates oriented 2.5 ° off (100) toward <110>, which were brought to growth temperature from 425 °C to 700 °C by radio frequency (RF) induction. Group-III sources were trimethylgallium (TMGa), trimethylaluminum (TMAl), and trimethylindium (TMIn). Organometallic precursors were contained in stainless steel bubblers in cooling baths. The TBAs bubbler (American Cyanamid Company) was kept at 4 °C or 10 °C with a vapor pressure of 63 Torr or 96 Torr[70]. Those for EtAs (Morton International) were at 10 °C and 311 Torr[71]. Three different lots of TBAs were used in this section, to investigate growth reproducibility from batch to batch of TBAs[23]. Lot A, lot B and lot C were produced in 1987, 1989, and 1990. The group-V flow rate ranged from 4×10^{-4} mol/min to 6×10^{-2} mol/min. GaAs, $Al_{0.28}Ga_{0.72}As$, and $In_{0.15}Ga_{0.85}As$ were grown with V/III ratios of 5 to 40, 20 to 120, and 2.5 to 90, respectively. Typical growth rates at 650 °C for GaAs, $Al_{0.28}Ga_{0.72}As$, and $In_{0.15}Ga_{0.85}As$ were 1 μm/h to 3.6 μm/h, 1.5μm/h, and 1.2 μm/h, respectively. Silane or disilane was used as the *n*-type dopant source. Hydrogen gas diffused through a palladium cell was used as the carrier gas. All species were mixed just before putting them into the reactor. The flow velocity was varied from 8.5 cm/s to 30 cm/s.

The surface morphology was observed by Normarski interference contrast optical microscopy, and by a surface contamination analyzer (Surfscan 4500, Tencor Instruments) that could count the density of irregular particles on the surface as a function of the laser scattering cross section. The donor concentration (N_d) was determined using the capacitance-voltage (*C-V*) and van der Pauw-Hall methods. GaAs growth rates were determined using a stylus profiler to measure GaAs thickness after selectively removing an unmasked GaAs layer on an $Al_{0.65}Ga_{0.35}As$ stopper layer using citric acid[72]. AlGaAs growth rates were determined by the *C-V* method while observing the depth of the peak which appeared at the heterointerface of the *n*-AlGaAs/*n*-GaAs structures. The optical properties of the epitaxial layers were evaluated by photoluminescence (PL) spectroscopy performed at 77 K and 4.2 K. The samples were excited using multiline emissions of an argon ion laser and PL signals were detected with a Si *p-i-n* photodetector or a photomultiplier. Electron traps were measured by the DLTS method[73] from −180 °C to +150 °C. A double-crystal X-ray diffractometer was also used to evaluate the quality of the AlGaAs. Both the 77 K PL and X-ray diffractometer measurements were performed to determine the AlAs mole fraction of the $Al_xGa_{1-x}As$. We used the results of Baliga et at.[74] for the relationship between band gap energy and the InAs mole fraction for $In_yGa_{1-y}As$ growth ($y \leq 0.2$). The residual impurities in the epitaxial layers were characterized by secondary ion mass spectroscopy (SIMS) using Cs^+ ions as the primary ion source. The self-compensation of Si into GaAs was estimated using PL measurements at 77 K, observing the self-activated (SA) center peak appearing around 1 μm[75].

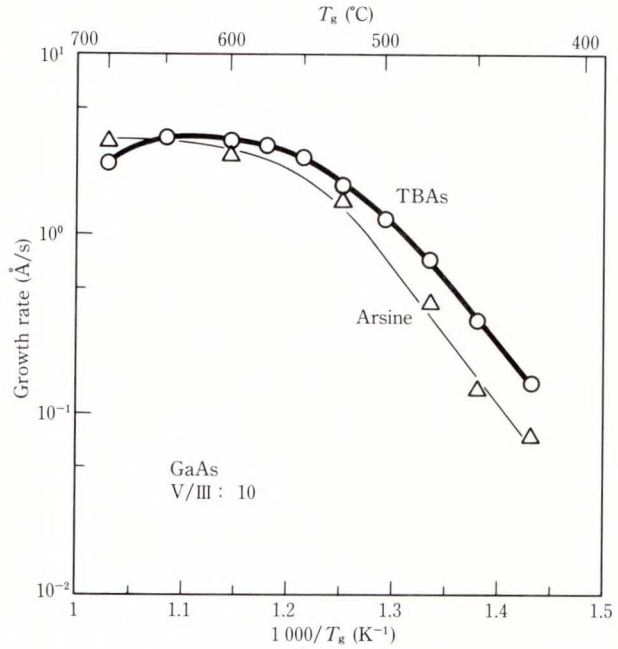

Fig. 2—Growth rate dependence on growth temperature with a V/III ratio of 10 for GaAs films grown using TBAs and arsine[23].

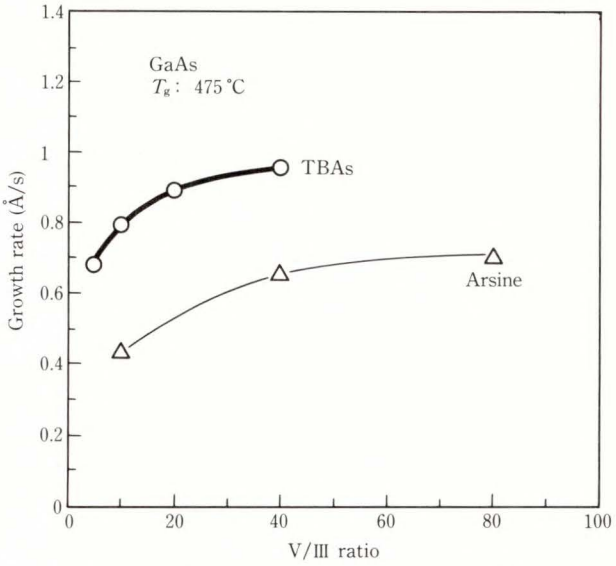

Fig. 3—Growth rates as a function of the V/III ratio for GaAs layers grown at 475 °C using TBAs and arsine.

3. Results and discussion

3.1 Undoped GaAs

First, we investigate carbon incorporation and impurity contamination in undoped GaAs. Differences in growth rate due to different growth mechanisms between TBAs and arsine will be addressed.

The surface morphology of GaAs grown using TBAs was excellent, as good as that grown using arsine. There was no difference among the TBAs lots. Figure 2 shows the growth rates of the GaAs epitaxial layers for TBAs and arsine as a function of growth temperature (T_g). The growth rate using TBAs increases with increasing temperature below 550 °C, but is fairly independent of temperature between 550 °C and 650 °C. The behavior at temperatures below 650 °C is similar to that observed using arsine. In the former region (below 550 °C), called the kinetically controlled region, the growth rate is controlled by the decomposition rate of group-III species. In the latter region (between 550 °C and 650 °C), called the transport-controlled region, it is controlled by the diffusion of the decomposed metalorganic components[76]. The activation energies of the growth rates observed in the kinetically controlled region were 145 kJ/mol using arsine. The activation energies for both sources are extremely close, although the value of the growth rate using TBAs in the kinetically controlled region is about twice that of the rate using arsine. Above 650 °C, the growth rate for TBAs decreases slightly with increasing temperature. In contrast, the growth rate for arsine is independent of temperature. There was no difference in growth rate among the TBAs lots.

The growth rate dependence on the V/III ratio at 475 °C is shown in Fig. 3. At 475 °C, the growth rate using TBAs increases with increasing V/III ratio. If this is due only to the difference in decomposition temperatures of TBAs and arsine[17)-19),77], the growth rate at a higher V/III ratio should saturate at the same value for both TBAs and arsine. Since these values seem to be different, as shown in Fig. 3, we suppose that there must be a different growth mechanism for each source under these growth conditions. At low temperatures, the reaction between TMGa and arsine takes place heterogeneously and may proceed via the Langmuir-Hinshelwood mechanism[78]. If this is the case, we must consider the reversible excluded-volume chemisorption mechanism

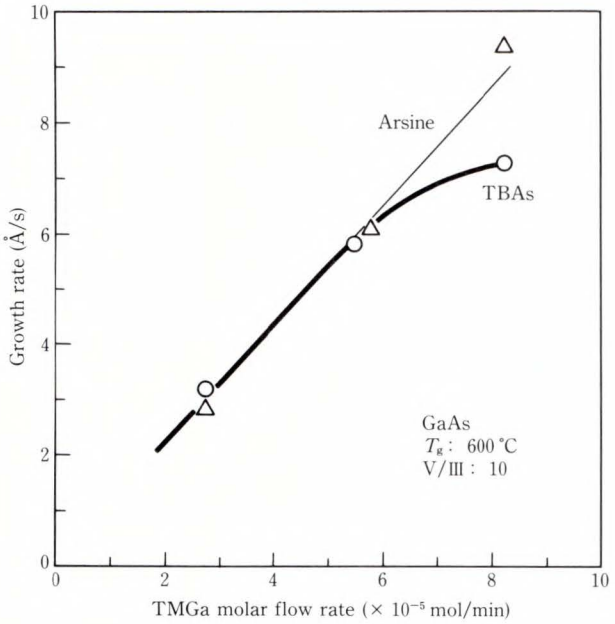

a) Dependence on TMGa flow rate

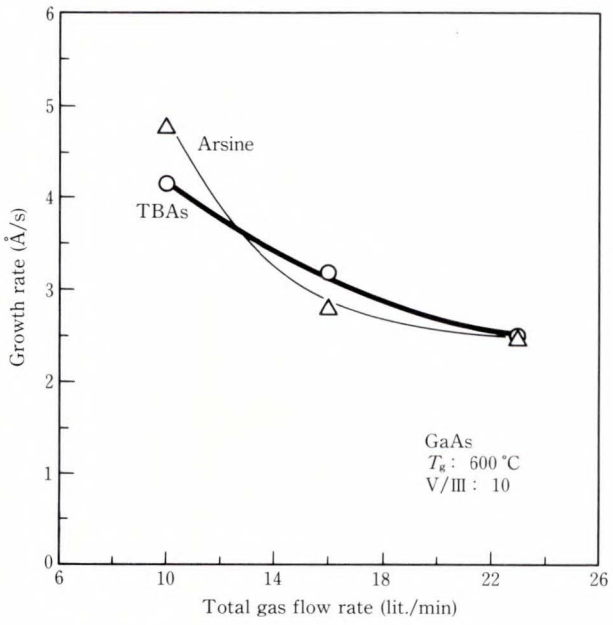

b) Dependence on total gas flow rate

Fig. 4—Growth rates for GaAs films. Growth temperature is 600 °C and V/III ratio is 10[23].

presented by Aspnes et al[79]. In this mechanism, an undecomposed TMGa molecule chemisorbed at a specific lattice site on an initially arsine-stabilized surface hides several adjacent sites, causing decreased growth efficiency. TBAs is expected to be a stronger adduct former than arsine due to the electron-donating nature of the tertiarybutyl substitute. Therefore, the TMGa-TBAs adducts chemisorb on the surface. Either the reversible excluded-volume mechanism does not play an important role in the growth, or the excluded volume of the TMGa-TBAs adducts is smaller than that of TMGa due to the deformation of TMGa from a planar to a pyramidal structure with adduct formation. We believe that the difference in growth rates of both sources should be observable at 475 °C.

In addition, we obtained two significant results pertinent to GaAs growth rates at 600 °C. First, the growth rate using arsine is a linear function of the TMGa flow rate, as shown in Fig. 4a). On the contrary, the growth rate using TBAs saturates at a high TMGa flow rate over 5×10^{-5} mol/min. Second, growth rates depend strongly on the total gas flow rate at 600 °C, and different for each source, as shown in Fig. 4b). The growth rate for TBAs varies in inverse proportion to flow rate, while that for arsine varies inversely with the square root of the flow rate. It is remarkable that the growth rates for higher total flow rates are the same for TBAs and arsine. This suggests that the species residence time for gas flow over the wafer has a significant effect on GaAs growth. According to the boundary layer theory, the growth rate should be approximately proportional to $v^{-1/2}$, where v is the velocity of total gas flow[80]. The growth rate for arsine can only be predicted theoretically. We speculate that gas phase reactions, i.e. adduct formation and homogeneous nucleations among metalorganic components, play an important role in the growth of GaAs using TBAs. Lower TMGa flow rates and higher total gas flow rates reduce the gas phase reaction between TMGa and TBAs. In addition, the results of growth uniformity agree with this interpretation. We discuss AlGaAs growth uniformity in sections 3.3 and 3.4.

Figure 5 shows the free carrier concentration and electron mobility at 77 K, using lot A, as a function of growth temperature for a V/III ratio of 10. The epitaxial layers showed n-type conductivity under all growth conditions. The best crystal was obtained at 700 °C. The highest electron mobilities were 6 700 $cm^2 V^{-1} s^{-1}$ at

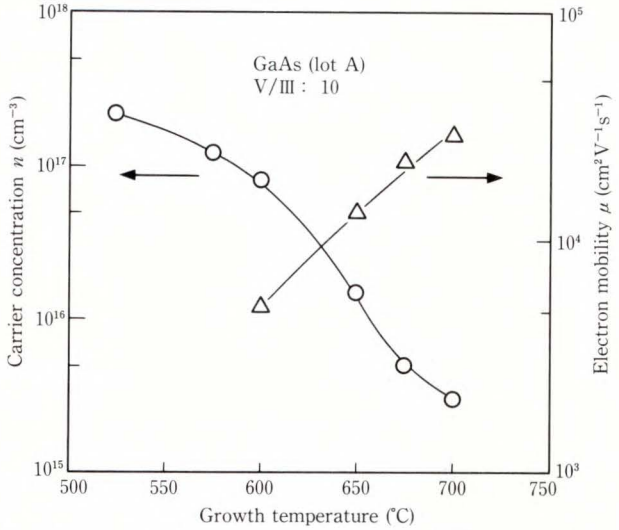

Fig. 5—Free carrier concentration at 300 K and electron mobility at 77 K of GaAs films using lot A with a V/III ratio of 10 as a function of growth temperature[23].

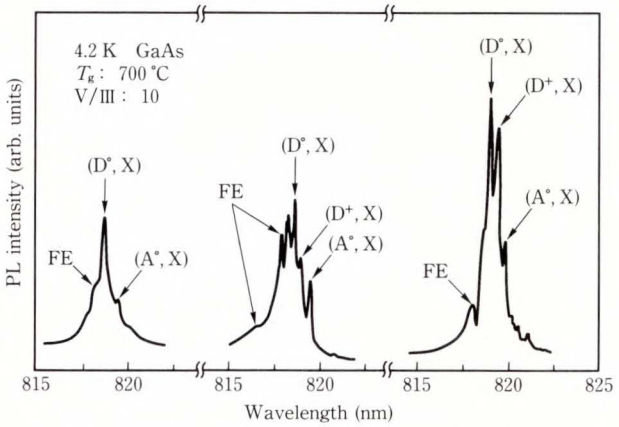

a) Lot A TBAs b) Lot B TBAs c) Arsine

Fig. 6—Photoluminescence (PL) spectra in the exiton region measured at 4.2 K for GaAs layers grown at 700 °C with a V/III ratio of 10.

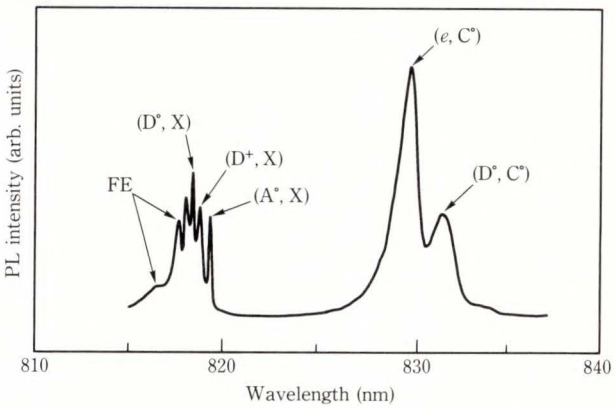

a) Lot C TBAs at 600 °C with a V/III ratio of 20

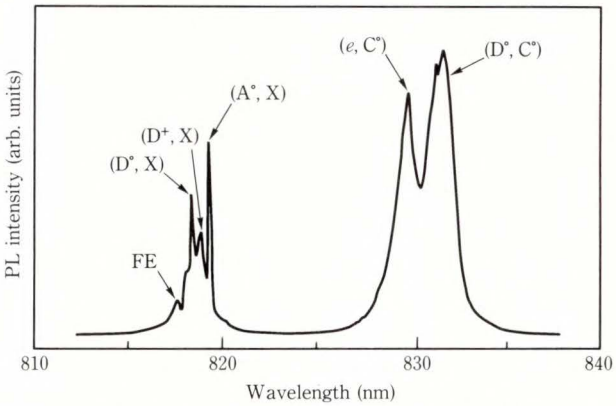

b) EtAs at 650 °C with a V/III ratio of 20[24]

Fig. 7—PL spectra at 4.2 K for GaAs layers.

room temperature and 30 000 cm^{2}V^{-1}s^{-1} at 77 K with a carrier concentration of 3×10^{15} cm^{-3} at room temperature for the 2 μm-thick GaAs layer. The carrier concentration decreases and the electron mobility increases with increasing growth temperature. The residual dopant was identified as sulfur only by SIMS analysis. The compensation ratio, defined as the ratio of ionized acceptor concentration to ionized donor concentration, was assessed as 0.3 at growth temperatures of 600 °C to 700 °C by Hall measurements[81]. This ratio for films grown using arsine with an electron mobility of 120 000 cm^{2}V^{-1}s^{-1} at 77 K was about 0.28.

The 8 μm-thick epitaxial layer grown at 650 °C with a V/III ratio of 10, using lot B TBAs, showed p-type conductivity with hole mobilities of 400 cm^{2}V^{-1}s^{-1} at room temperature and 7 600 cm^{2}V^{-1}s^{-1} at 77 K, with a carrier concentration of 3×10^{14} cm^{-3} at room temperature. The other epitaxial layers grown at temperatures between 600 °C and 700 °C were 2 μm thick and were too thin for electrical property measurements, indicating high purity films.

Figure 6 shows PL spectra in the exciton region measured at 4.2 K for films using lot A, lot B, and arsine, and grown under the same conditions. The various sharp lines which appear just below the band gap correspond to the recombination of free and bound excitons. The

spectrum for lot A is insufficient compared with that of arsine due to the contamination of lot A with sulfur. The excition peaks of the lot B film with high resistivity are as well resolved as those of the arsine film with an electron mobility of 120 000 $cm^2V^{-1}s^{-1}$ at 77 K. The emissions from free excitons (FEs) for the lot B layer are very strong. These results show that the lot B GaAs epitaxial layers are of high purity.

The best PL spectrum using lot C which contains acceptor-related peaks is shown in Fig. 7a). This film was grown at 600 °C with a V/III ratio of 20. The intensity of carbon-acceptor-related peaks are comparable to that of exciton peaks. The full-width at half-maximum (FWHM) of the emission corresponding to band to acceptor (e, C^0) transition is 1.7 meV for the films using TBAs and 1.5 meV for those using arsine. The Zn detected by PL comes from the TMGa. This is known because Zn also remains in GaAs films grown using arsine. Therefore, we conclude that lot B is much purer than lot A and carbon incorporation into GaAs grown using TBAs is negligible. As well as lot B, GaAs layers grown using lot C (the most recent batch) exhibit high quality with excellent reproducibility from run to run.

GaAs layers were grown using EtAs at 650 °C. The surface morphology was good. The 5 μm epitaxial layer grown with a V/III ratio of 10 had p-type conductivity showing a hole concentration of 2.5×10^{14} cm^{-3} with a hole mobility of 400 $cm^2V^{-1}s^{-1}$ at 300 K and 5 700 $cm^2V^{-1}s^{-1}$ at 77 K, and that grown with a V/III ratio of 20 showed high resistivity. Figure 7b) shows the PL spectrum at 4.2 K for the film with a V/III ratio of 20. Exciton and acceptor peaks were well resolved, suggesting that highly pure GaAs equivalent to arsine-grown and TBAs-grown GaAs were obtained using EtAs. Through the carrier concentration depends on the V/III ratio, we suppose that a higher V/III ratio will reduce the amount of carbon incorporation.

3.2 Si-doped GaAs

The purity of undoped GaAs is not the only important factor for device fabrication. Controllability of n-type doping of GaAs is also required. In this section, we describe detailed doping research using silane or disilane as a Si dopant source. Differences in Si doping efficiency between TBAs and arsine will be discussed, proposing a doping mechanism using simulation of group-V source decomposition. Only pure lot C TBAs {see Fig. 7a)} was used in the doping study.

3.2.1 Bulk doping

Our experiments compared several group-V sources in respect of the dependence of the donor concentration on Si mole fraction, growth temperature, V/III ratio, growth rate, total gas flow velocity and substrate misorientation[31]. We used an inverted horizontal reactor to eliminate apparatus issues related to non-uniform distribution[37),49]. Detailed discussion about the inverted horizontal reactor will be addressed in the section on AlGaAs. The growth rate and donor concentration varied within ±1-2 % across a 3-inch substrate. The reproducibility of the measured donor concentration value from run to run was within ±1 %.

Figure 8 shows the dependence of the donor concentration (N_d) on the disilane flow rate using TBAs or arsine for GaAs at 650 °C. Using

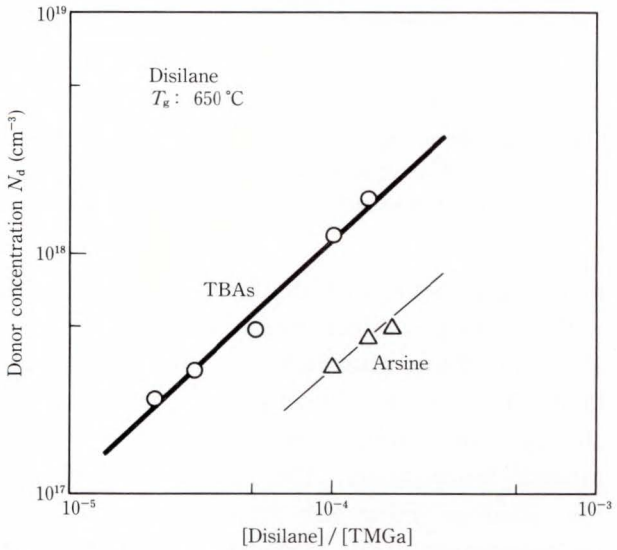

Fig. 8—Dependence of the donor concentration N_d on the disilane flow rate divided by the TMGa flow rate using lot C TBAs and arsine. The V/III ratio is 20. The group-V flow rate is 8×10^{-4} mol/min[31].

TBAs, N_d is always about three times higher than when using arsine. As the disilane flow increases, N_d increases in proportion for both group-V sources. A similar difference was observed when silane was used. We confirmed by SIMS that N_d was the same as the Si concentration. Hall measurements for samples having the same N_d demonstrate that the electron mobility and compensation ratio values are the same for each group-V source[81]. These results indicate that the difference in N_d was attributable to the Si incorporation itself and that most Si atoms reside at Ga sublattice sites. SIMS also confirmed that no other residual impurity such as a carbon acceptor is present in the epitaxial layers. This proves that TBAs enhances Si incorporation.

The effective distribution coefficient,

$$k_d \equiv \{N_d/2.21 \times 10^{22}\} / \{[\text{Si input}]/[\text{Ga input}]\}, \quad \ldots\ldots (1)$$

is estimated at 0.1 for growth with TBAs and 0.03 with arsine. In the treatment of [Si input] in Equation (1) when using disilane, it is postulated that two atoms per molecule of disilane contribute to Si doping reactions. This is because in the case of arsine-grown GaAs at a high growth temperature[47], when the disilane flow was set to half the value of the silane flow, the doping efficiency with disilane was the same as with silane.

Figure 9 shows N_d as a function of the growth temperature.

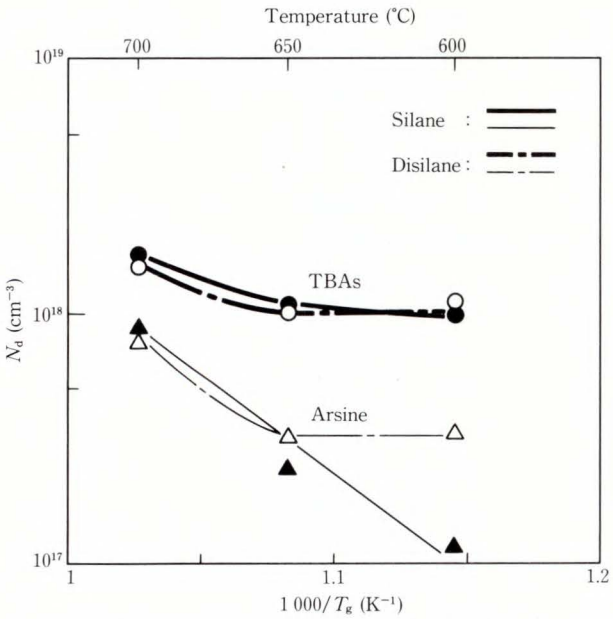

Fig. 9—Donor concentration as a function of the growth temperature. The solid lines show N_d for layers doped with silane, and the broken lines with disilane. The Si mole fraction is 2×10^{-8} mol/min for both silane and disilane. The V/III ratio is 20. The growth rates are constant at 1 μm/h in this temperature range for both group-V sources[31].

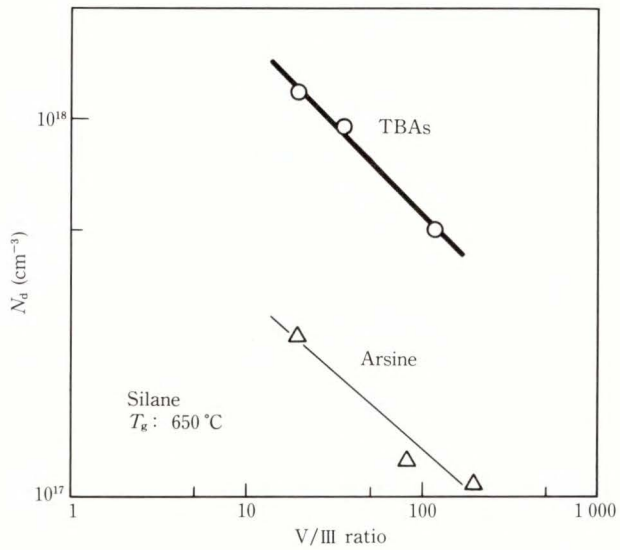

a) Silane

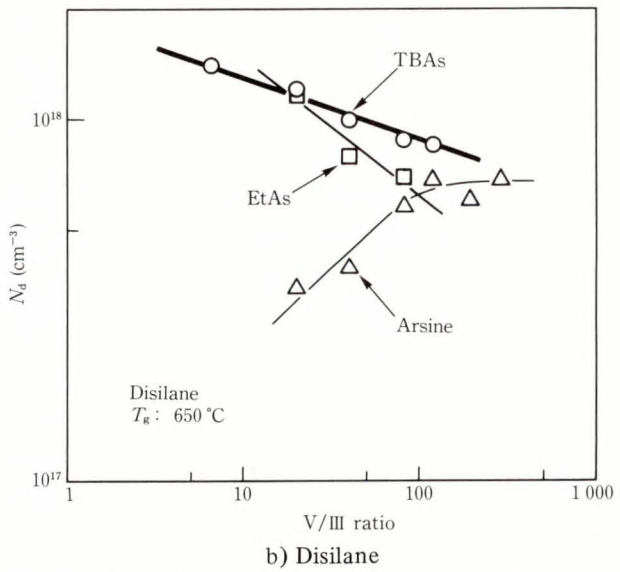

b) Disilane

Fig. 10—Dependence of N_d on the V/III ratio at 650 °C with a growth rate of 1 μm/h. The Si mole fraction is 2×10^{-8} mol/min. The results for EtAs using disilane are included for comparison[31].

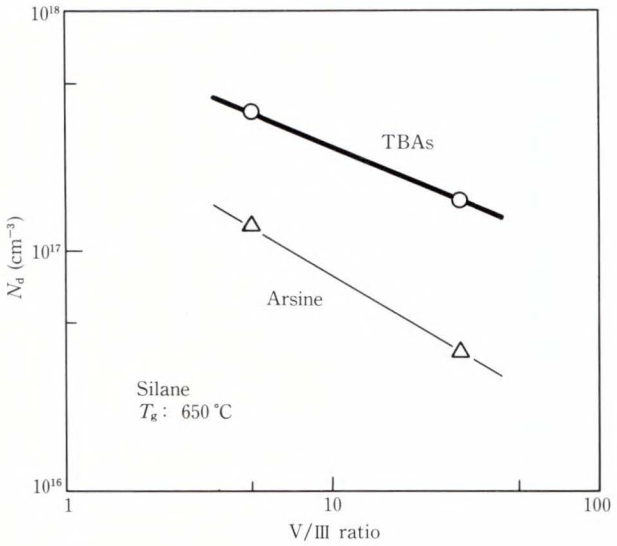

a) Silane

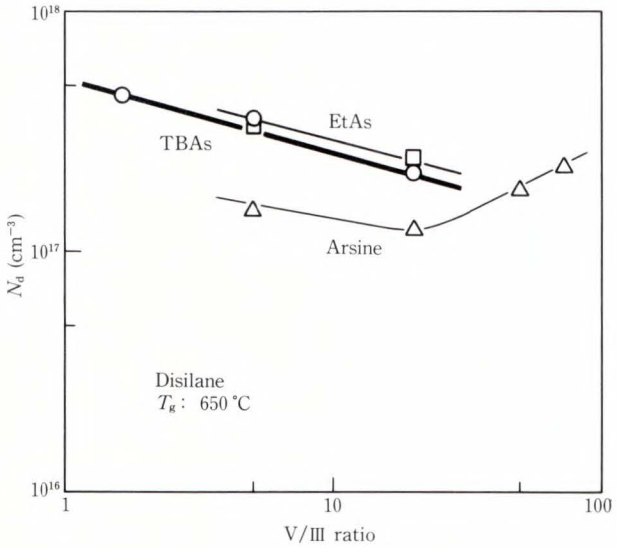

b) Dislane

Fig. 11—Effect of growth rate: The dependence of N_d on the V/III ratio at 650 °C with a growth rate of 3.6 μm/h. The group-V flow rate and the total flow rate are the same as in Fig. 3, while only the TMGa flow rate is varied to increase the growth rate[31].

Using TBAs, N_d is always higher than when using arsine with either silane or disilane. When using arsine, the incorporation efficiency with silane increases exponentially with the growth temperature, approaching that for TBAs.

Figure 10a) shows the dependence of N_d on the V/III ratio at 650 °C when silane is used as a dopant source. With TBAs, N_d is always higher

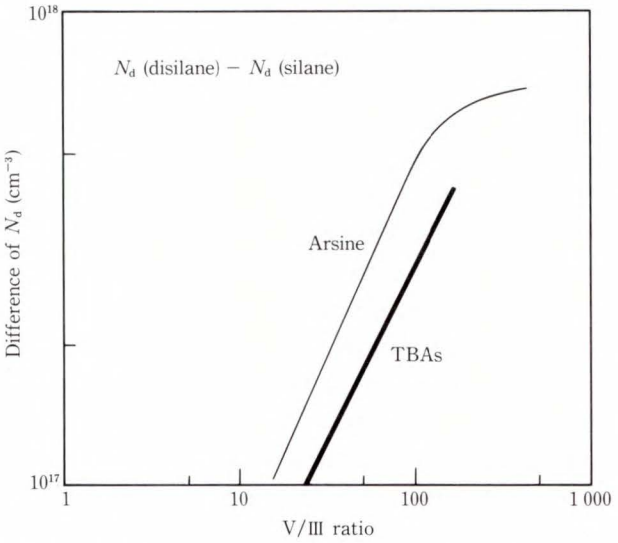

Fig. 12—Difference between Si dopant sources derived from Figs. 10a) and b). The N_d for a layer doped with silane subtracted from one doped with disilane is shown as a function of the V/III ratio[31].

than with arsine for all V/III ratios. N_d decreases with either group-V precursor as the V/III ratio increases. In contrast, when we use disilane {see Fig. 10b)}, N_d decreases with TBAs or EtAs, and increases with arsine, with an increasing V/III ratio. Interestingly enough, the trends for EtAs match those using TBAs.

The growth rate should drastically affect doping efficiency[34),35),39),42),50)]. When the growth rate was increased in this study, the H_2 carrier gas and dopant source flow rates held constant while the TMGa flow rate was increased. With silane, using either TBAs or arsine, N_d decreases with an increasing V/III ratio when the growth rate is 3.6 μm/h, as shown in Fig. 11a). The same phenomena are found when the growth rate is 1 μm/h {see Fig. 10a)}. With disilane, the N_d for arsine-grown layers decreases as the V/III ratio increases to 20, as shown in Fig. 11b). When the V/III ratio exceeds 20, the N_d increases with the V/III ratio. This behavior for the arsine-disilane combination differs from that observed when the growth rate is slower {see Fig. 10b)}. Using TBAs or EtAs, the behavior of N_d as a function of the V/III ratio is independent of the growth rate. When disilane is used, the increase of growth rate from 1 μm/h

to 3.6 μm/h elevates the effective distrubution coefficient k_d from 0.1 to 0.17 with TBAs and from 0.03 to 0.08 with arsine.

Figure 12 shows the difference between the silane results {see Fig. 10a)} and the disilane results {see Fig. 10b)}. We found that, at a higher V/III ratio, the N_d in the case of disilane is higher than that of silane using either TBAs or arsine. This trend is independent of the growth rate.

Figure 13 shows the N_d dependence on the V/III ratio for epitaxial layers grown using disilane at 700 °C. Using TBAs, N_d decreases as the V/III ratio increases. The N_d with arsine is independent of the V/III ratio in Fig. 13. We surmise that this is the same behavior as that observed when the V/III ratio exceeds 100 at 650 °C {see Fig. 10b)}, because the pyrolysis rate of the As-species increases at higher temperatures[19].

Figure 14 shows the dependence of N_d on flow velocity. The flow velocity is varied by modifying only the hydrogen carrier gas flow under atmospheric pressure, while all precursor mole flow rates are constant. As the flow velocity increases, N_d with TBAs increases and that with arsine decreases using either silane or disilane, as shown in Fig. 14.

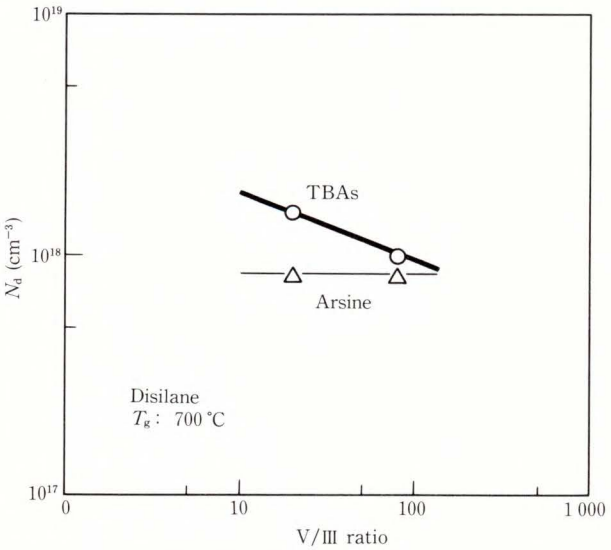

Fig. 13—N_d using disilane at 700 °C as a function of the V/III ratio. Except for the growth temperature, the growth parameters are the same as in Fig. 10b)[31].

Figure 15 shows N_d as a function of the substrate misorientation towards <110> for (100) substrates using disilane. The Si incorporation for the epitaxial layer grown on the on-axis substrate is more efficient than on the misoriented substrate using both TBAs and arsine.

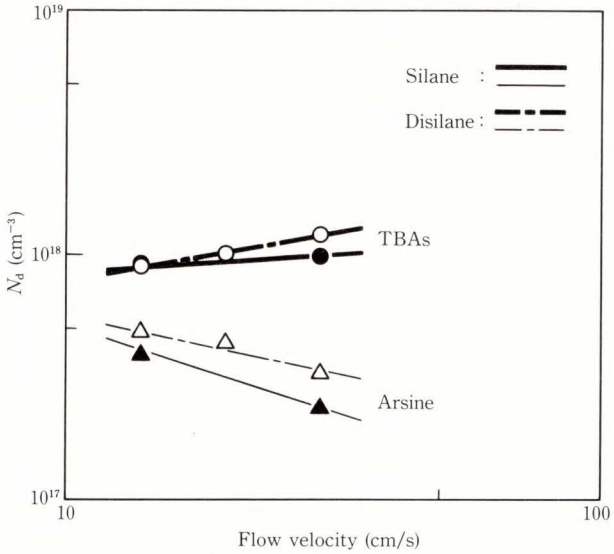

Fig. 14—The solid lines show N_d as a function of the flow velocity for layers doped with silane at 600 °C. The broken lines show that with disilane. The V/III ratio is 20. The Si mole fraction is 2×10^{-8} mol/min. The growth rate decreases as the flow velocity increases[31].

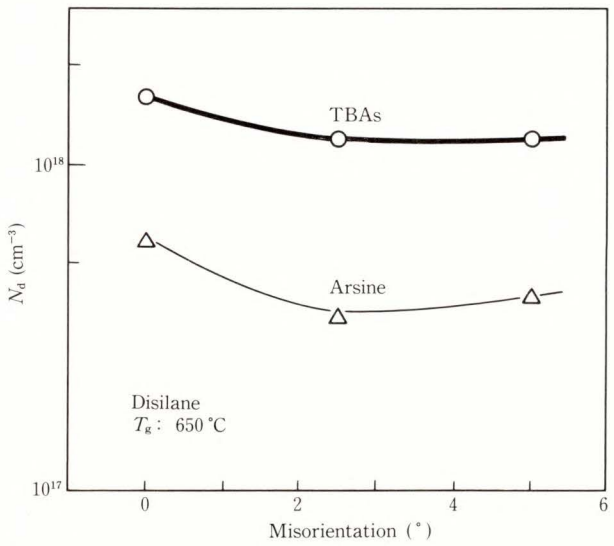

Fig. 15—Dependence of N_d on substrate misorientation from the (100) surface at 650 °C. The dopant source is disilane only. The V/III ratio is 20. The disilane flow rate is 2×10^{-8} mol/min. The growth rate is 1 μm/h[31].

3.2.2 Planar doping

It is important to know whether this different efficiency is due to the group-V precursor alone or to the reactions between group-V and group-III precursors. We also examined planar doping of Si into GaAs using TBAs or arsine to eliminate the effect of the group-III precursor, and we discuss the role of the group-V precursor in the Si doping process. Si planar doping is a promising technique for obtaining high carrier concentrations for high performance FETs[82)-84)]. Therefore, before using it practically, we must clarify the effect of TBAs on planar doping[24)].

GaAs layers consisted of a 100 nm undoped GaAs layer, a planar-doped atomic layer, and a 100 nm undoped GaAs layer. The growth rate of GaAs was 1 μm/h using either group-V precursor. Planar doping was carried out during an interruption in the GaAs growth[37)], and was conducted by supplying disilane under a group-V flow without a Ga-precursor for 2 min to 10 min.

Figure 16 shows the dependence of the sheet carrier concentration (N_s) on the disilane flow rate when either TBAs or arsine is used for a two-minute planar-doped layer. The group-V flow rate is 8×10^{-4} mol/min. Although a monotonic increase in N_s is observed for disilane flows of up to 1.5×10^{-6} mol/min, N_s seems to saturate at higher disilane flow rates for both group-V precursors. The N_s for TBAs is always higher than that for arsine. The higher N_s of 2.2×10^{13} cm^{-2} is obtained for TBAs, even though, because of the increase in the number of L-band electrons[85)], Hall measurements could not account for the extremely high electron carrier concentration. For arsine, a high disilane flow rate exceeding 10^{-6} mol/min is required to obtain a high N_s exceeding 10^{13} cm^{-2}. From the C-V method, the FWHM in the depth profile of carrier concentration for TBAs-grown layers with an N_s of 6×10^{13} cm^{-2} is only 5 nm. The peak wave-length of the PL spectrum for this layer is the same as that for undoped GaAs layers grown with TBAs, indicating an abrupt doping profile and no Si diffusion into the GaAs layers.

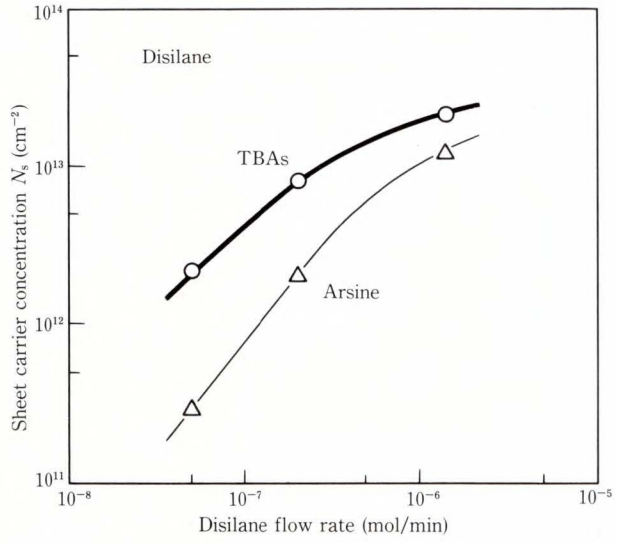

Fig. 16—Dependence of sheet carrier concentration N_s on the disilane flow rate for two-minute planar doped layers using lot C TBAs or arsine. The group-V flow rate is 8×10^{-4} mol/min[32)].

As the growth temperature increased from 650 °C to 670 °C, N_s increased for TBAs from 1.55×10^{13} cm^{-2} to 2×10^{13} cm^{-2}. As the planar doping time increased from 2 min to 10 min under the same disilane flow rate, N_s for TBAs increased from 1.6×10^{13} cm^{-2} to 2.2×10^{12} cm^{-2}, and that for arsine from 7.5×10^{12} cm^{-2} to 1.6×10^{13} cm^{-2}. Either the high growth temperature or long planar doping time, however, degrades the surface morphology for both group-V precursors, indicating that it is difficult to obtain high sheet carrier concentration with good morphology using arsine. The optimum growth conditions for heavy planar doping are restricted for arsine. Thus, we conclude that TBAs is very useful in heavy planar doping of Si into GaAs.

Figure 17 shows N_s as a function of group-V flow rate for a disilane flow rate of 2×10^{-7} mol/min for a two-minute planar-doped layer. As the As-precursor flow rate increased from 8×10^{-4} mol/min to 4×10^{-3} mol/min, the N_s for TBAs decreased from 8×10^{12} cm^{-2} to 6.9×10^{12} cm^{-2}, while that for arsine increased from 2×10^{12} cm^{-2} to 5.9×10^{12} cm^{-2}. This is the same trend as observed in the dependence of N_d on the V/III ratio in bulk doping as shown in Fig. 10b), confirming that the reactions with

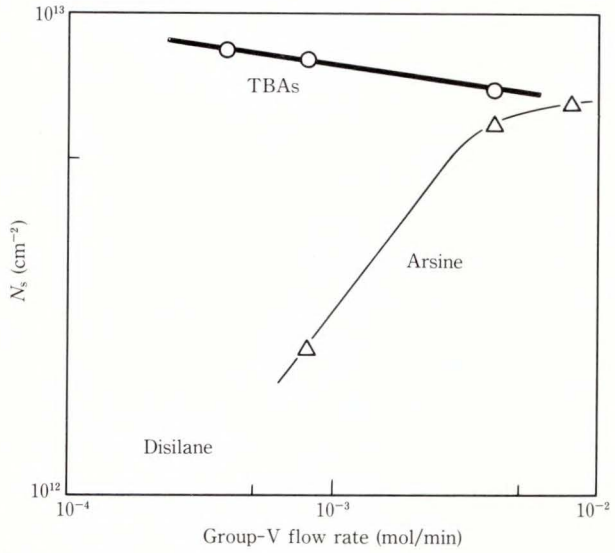

Fig. 17—N_s as a function of the group-V precursor flow rate with a disilane flow rate of 2×10^{-7} mol/min for two-minute planar doped layers[32].

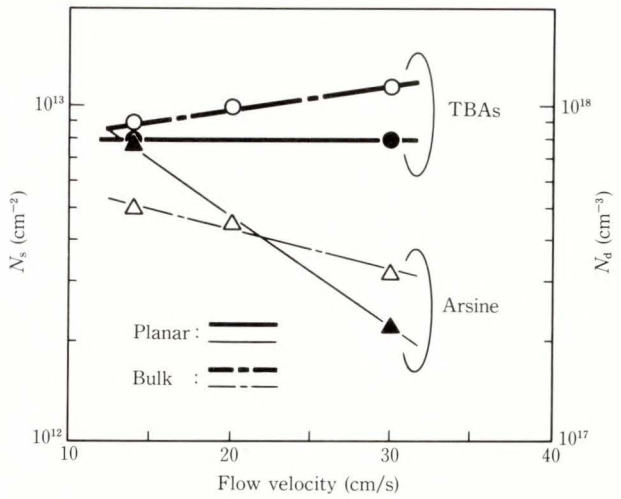

Fig. 18—Solid lines show N_s as a function of gas flow velocity for two-minute planar doped layers. Broken lines show carrier concentration as a function of flow velocity for bulk doped layers. The disilane and group-V flow rates are 2×10^{-7} mol/min and 8×10^{-4} mol/min for both planar doping and bulk doping. The growth rate for bulk-doped layers is 1 μm/h[32].

group-III species have little effect on the carrier concentration dependence. We investigated the Si concentration in the epitaxial layer using SIMS profile as a function of depth from the surface. The Si concentrations measured by SIMS correspond exactly to the differences in N_s shown in Fig. 17. This indicates that the difference in N_s is only due to Si incorporation itself and that most of the Si atoms reside at Ga sublattices. Since only the group-V precursor and disilane were supplied during the planar doping sequence, the reactions between the group-V species and the Si-species should affect the Si doping mechanism, regardless of the group-III precursor. This could be influenced by the pyrolysis rate of the group-V precursor.

The dependence of N_s on the gas flow velocity for a two-minute planar doped layer is shown in Fig. 18. The gas flow velocity greatly affects N_s. This behavior is very similar to that for bulk doping. The Si concentrations for high flow velocities are relatively high when using TBAs for both planar and bulk doping. Since the planar doping was carried out under atmospheric pressure, there is no effect of pressure.

The flow velocity determines the duration that the precursors remain adjacent to the surface. The duration affects gas phase reactions between precursors. As flow velocity increases, the concentrations of As-species and Si-species in the gas phase decrease, reducing gas phase reactions. Therefore, flow velocity should significantly control gas phase reactions. The opposite trend in behavior between the group-V precursors in Fig. 18 verifies that the progress of the gas phase reactions between As-species and Si-species will also differ greatly between group-V precursors.

3.2.3 Doping model

1) Conventional models of Si-doping

To predict the Si-doping of GaAs, a simple equilibrium model represents all Si dopant reaching the surface to be incorporated into the epitaxial layer due to the low vapor pressure of the Si dopant[41]; this is called the mass-transport limited case[86]. Si incorporation efficiency is predicted to be independent of the growth temperature and group-V flow rate in this model[86]. From experimental results, however, incomplete decomposition of silane causes a strong temperature dependence[37),38),40),43),46),47]. Stringfellow has already pointed out that the simple

equilibrium model is too simple and inadequate[86].

Many researchers have reported experiments on silane and disilane decomposition[87)-94)]. Roenigk et al.[95] calculated the silane decomposition using the Rice, Ramsperger, Kassel and Marcus (RRKM) theory. Field et al.[42], De Croon et al.[48] and Moffat et al.[46] reported numerical modeling for the growth of Si-doped GaAs using two reversible reactions A and B, as listed below:

$$Si_2H_6 \leftrightarrow SiH_2 + SiH_4, \quad \ldots (A)$$

$$SiH_4 \leftrightarrow SiH_2 + H_2. \quad \ldots\ldots (B)$$

They obtained good agreement with experimental results. Reactions A and B describe the doping process by SiH_2 (silylene) insertion into epitaxial layers[43),45),46),48),50)]. These reactions can be applied to model Si epitaxy using silane and disilane[96)-98)].

2) Arsine as the group-V source

First, we discuss the silane doping into GaAs using arsine as a group-V source. Using silane, we observed that Si incorporation shows a strong temperature dependence (see Fig. 9). The temperature-dependent behavior for arsine-grown layers is the same as previously reported[37),38),40),43),46),47)]. The pyrolysis of silane is incomplete for growth temperatures between 600 °C and 650 °C[88]. Thus, the increased incorporation efficiency for arsine-grown layers reflects the more effective decomposition of silane at higher growth temperatures[86]. The apparent activation energy for the arsine-silane process evaluated from the slope in Fig. 9 is 1.5 eV, similar to previously reported values[37),38),40)]. In our reactor, Si incorporation is inversely proportional to the V/III ratio at constant group-III partial pressure {see Figs. 10a) and 11a)}. Bass[34] and Sakaguchi et al.[47], using atmospheric pressure reactors, reported the same behavior as in our results. On the contrary, Kuech et al.[38] and Moffat et al.[46], using reduced pressure reactors, observed that V/III ratio had only a weak effect or no effect on Si incorporation. This difference could be attributed to the growth pressure[43].

Using disilane, we observed that, below 650 °C, the Si incorporation is independent of the growth temperature (see Fig. 9). But above 650 °C, Si incorporation efficiency increases with increasing growth temperature as when using silane. Furuhata et al.[45] reported the same trends as ours. However, Shimazu et al.[43] and Moffat et al.[46] reported different trends. Field et al.[42] and Shimazu et al.[43] observed that the dependence of Si incorporation on the growth temperature strongly depends on the growth pressure. The growth pressure affects the Si incoporation activation energy[43]. Under atmospheric pressure, the reactants have a long residence time and the gas phase reactions probably play an important role. In our reactor, we speculate that below 650 °C, reaction A proceeds rapidly in the gas phase and the diffusion of SiH_2 radicals controls Si incorporation efficiency. Reaction B proceeds at a temperature above 650 °C, increasing Si incorporation efficiency[47].

For the V/III ratio dependence using disilane, we found that, contrary to when using silane, Si incorporation efficiency increases with an increasing V/III ratio {see Figs. 10b) and 11b)} or group-V partial pressure (see Fig. 17). This trend is opposite to the silane results {see Figs 10a) and 11a)}. Furuhata et al.[45] also reported the same trends with disilane as in our results. Figure 12 shows the difference between silane and disilane. With an increasing V/III ratio, the difference increases and tends to saturate. Thus, we speculate that there is an enhancement effect with increased V/III ratios when using arsine with disilane. Moffat et al.[46] introduced reaction C when using arsine as the group-V source.

$$AsH_3 + SiH_2 \rightarrow H_2AsSiH_3. \quad \ldots (C)$$

They consider H_2AsSiH_3 (silylarsine) to be an additional doping component which can explain the V/III ratio dependence.

3) TBAs as the group-V source with silane

When using TBAs as the group-V source, Si incorporation efficiency of GaAs is always higher than that using arsine with either silane or disilane under all growth conditions. Serreze et al.[28] and Stolz et al.[29] reported high doping efficiency using TBAs with silane. Lum et al.[30]

also reported both high Si doping efficiency with $(CH_3)_6Si_2$ and high sulfur doping efficiency with H_2S for TBAs-grown GaAs layers. Below 650 °C, the Si incorporation using TBAs is independent of the growth temperature, and remarkably enough at 600 °C, N_d using TBAs is almost ten times that using arsine. In this temperature range, no previous research has observed such mass-transport-limited behavior using silane with arsine. This behavior with TBAs indicates that components contributing effectively to the doping chemical reactions are being formed in the gas phase, in spite of the low pyrolysis rate of silane, and that their diffusion to the surface controls Si incorporation efficiency. At a higher growth temperature, silane decomposes due to thermal energy, resulting in an increased N_d at 700 °C using TBAs (see Fig. 9).

Si incorporation decreases with an increasing V/III ratio as observed for the TBAs-silane combination {see Figs. 10a) and 11a)}. This trend is independent of the growth rate. Serreze et al.[28] also found the same trend as in our results with TBAs, but Stolz et al.[29] reported the opposite trend. We conclude that there is a suppression effect with increased V/III ratio using silane as a dopant source with either group-V source under our conditions.

4) TBAs and EtAs as the group-V source with disilane

Using disilane, the dependence on the growth temperature is similar for each group-V source, but with different incorporation efficiencies (see Fig. 9). Si incorporation decreases with an increasing V/III ratio (group-V partial pressure) using TBAs or EtAs {see Figs. 10b) and 17)}. This trend is opposite to the arsine-disilane combination. Figure 12 shows, however, that the difference between silane and disilane using TBAs has the same trend as in the case of arsine. With an increasing V/III ratio, Si incorporation efficiency with disilane becomes higher than that with silane, using either TBAs or arsine. Thus, we conclude that, with disilane, enhancement occurs in addition to the suppression observed with silane.

Figures 14 and 18 show an opposite dependence of Si incorporation on the total gas flow velocity between TBAs and arsine using either silane or disilane. In this study, flow velocity was varied by controlling the hydrogen carrier flow rate. The flow velocity affects the growth rate and boundary layer thickness. However, these dependences were the same for both group-V sources[23]. The flow velocity determines the residence time of precursors adjacent to the surface, affecting the reaction time in the gas phase. Thus, according to Fig. 14, we conclude that rates of gas phase reactions between As-species and Si-species should differ greatly between the group-V sources.

Figure 15 shows that Si incorporation efficiency is high for on-axis substrates. Tang et al.[50] reported the same dependence on misorientation as in Fig. 15 in the case of the arsine-silane combination. Smooth epitaxial growth requires atomic steps and kink sites at the growth fronts and few steps contributing to the growth process could exist on the on-axis substrate during growth, increasing the Ga-vacancy[50),52]. Consequently, the probability of Si adsorption at the Ga sublattice increases, leading to increased Si incorporation efficiency[50]. The relative increment of the on-axis substrate sample compared to the misoriented sample is the same for both group-V sources, supporting our interpretation.

To verify the influence of self-compensation, we investigated SA center peaks in PL spectra, which are identified as a mixture of Ga-vacancies and Si-donors at the Ga-site[75]. An SA peak appears at a wavelength of around of 1 μm in PL spectra for Si-doped GaAs layers. We examined disilane-doped GaAs layers with an N_d of 5×10^{17} cm^{-3} grown using TBAs or arsine. We observed a broad peak at 1 μm in 77 K PL for both layers. The peak wavelength and integrated intensity are the same for both group-V sources. Since no difference arises between group-V sources and the evaluated layers have the same N_d, the probability of Ga-vacancy formation during growth is the same for both group-V sources. We conclude that the difference in N_d is not attributable to a difference in self-compensation, but to a difference in

the amount of active Si-species on the growth surface which could contribute to the doping process.

5) Decomposition of group-V sources

The strong dependence on the V/III ratio and flow velocity supports the concept that the simple equilibrium model cannot be adapted to Si doping with either silane or disilane, and that non-equilibrium conditions control doping features. We speculate that differences in doping efficiency among the group-V sources are due to the difference in gas phase reactions between As-species and Si-species. Even though group-III sources are supplied during growth, and the effect of reactions associated with group-III sources should be taken into account in discussing the doping mechanism, the most significant difference in the growth process with the different group-V sources is the pyrolysis of the group-V sources, not of group-III sources[17)-21)]. We simulated the group-V source pyrolysis kinetically, to illuminate the relationship between the doping efficiency and the product of As-species, and to represent realistic conditions.

Recently, MOVPE models have been expanded to fully three-dimensional descriptions of horizontal reactors due to the rapid developments in computation speed and memory. Model predictions have shown good agreement with experimental data, such as growth rate, impurity levels and composition variation across a wafer aligned with the gas flow in horizontal reactors. Tirtowidjojo et al.[99),100)] performed the equilibrium calculations for the growth of GaAs from TMGa and arsine. They considered the effects of temperature, flow rate and inlet gas composition at the different reactor pressures. The theoretical calculations showed that reaction pathways and rate-controlling steps are sensitive to reactor pressure. Buchan et al.[101)] calculated the unimolecular rate constants using the RRKM theory. Giling et al.[102)] focused on the maximum coverage values for the growth species adsorbed on the surface under near-equilibrium conditions. Coltrin et al.[103)] treated rotating-disk reactors based on ideal flow geometry. This simulation revealed the relative roles of the different reactions, but could not describe the spatial variations in films. Jensen et al.[104)] and Fotiadis et al.[105),106)] demonstrated fully three-dimensional GaAs growth predictions in both horizontal reactors and vertical reactors. They concluded that the gas phase and surface chemistry, as well as transport descriptions, must be included in models to obtain accurate predictions.

Our simulation addressed the As-species concentration adjacent to the surface as a function of reaction time and input group-V flow rate, including gas phase and surface reactions, and diffusion of the species in the gas phase perpendicular to the surface, as reported previously[107),108)]. The inverted horizontal reactor was used in the simulation. We assumed that the gas flow in the reactor is well developed and unchanging. Since the mole fractions of precursors in the reactor are small, the influence of energy release on gas flow dynamics due to growth is negligible. The change in the concentration of species in 20 mesh elements in the boundary layer is calculated with gas phase reactions and the diffusions of species between meshes. The height of each mesh element is fixed at 1 mm and the thickness of the boundary layer is 20 mm. It is postulated that the temperature of the inverted substrate and the floor of the reactor are 650 °C and 300 °C. The gas flow velocity and gas temperature in each mesh element increase and decrease linearly from the substrate to the floor. The simple finite differential method was used to solve the differential equations. Calculations of the 50 μs gas phase and surface reactions are iterated ten times followed by 500 μs diffusion. The initial concentration of precursors is the same in all mesh elements. The rate constant k, for kinetic simulation, is written as:

$$k \equiv AT^{\beta} \exp(-E_a/RT). \quad \ldots (2)$$

The reactions considered are given in Table 1. Reactions T-1 to T-6 are taken into account only for TBAs pyrolysis. We assume that the first step of TBAs pyrolysis is a first order unimolecular reaction, dissociating into tertiarybutyl radicals and AsH_2 radicals[19),62)], and that the rate constant of this fission is the same as for

the dissociation of C_4H_9NO into tertiarybutyl radicals and NO radicals[109]. Li et al.[14] and Speckman et al.[110] reported that the first step of EtAs pyrolysis is the dissociation into an ethyl radical and an AsH_2 radical. On the contrary, Mountziaris et al.[111] reported the kinitic simulation of TBAs pyrolysis and postulated that production of both AsH and AsH_3 was the first step of TBAs pyrolysis. They treated the gas flow, temperature distribution, and surface reactions very carefully, but considered only two gas phase reactions corresponding to TBAs pyrolysis, and ignored the effect of C_4H_9. Our simulation treats the gas phase reactions more precisely, but other factors are simplified. Li et al.[21] reported that the reaction between the TBAs and C_4H_9 produces ditertiarybutylarsine. However, we could not introduce this

Table 1. Gas phase reactions for As-species considered in this study

Reaction	Gas phase reactions for As-species			Log A (mol, K, cm, s)	β	E_a (kcal/mol)
T-1:	TBAs	→	$AsH_2 + C_4H_9$	16	0	52
T-2:	$AsH_2 + C_4H_9$	→	$AsH_3 + C_4H_8$	12	0	0
T-3:	$C_4H_9 + C_4H_9$	→	C_8H_{18}	12	0	0
T-4:	$C_4H_9 + C_4H_9$	→	$C_4H_8 + C_4H_{10}$	12	0	0
T-5:	$C_4H_9 + H_2$	→	$C_4H_{10} + H$	11	0	10
T-6:	C_4H_9	→	$C_3H_8 + CH_3$	16	0	46.1
A-1:	$AsH_3 + M$	→	$AsH_2 + H + M$	17.5	0	75
A-2:	$AsH_2 + M$	→	$AsH + H + M$	17.1	0	69
A-3:	$AsH_3 + H$	→	$AsH_2 + H_2$	13	0	2
A-4:	$AsH_3 + AsH_2$	→	$As_2H_4 + H$	13	0	36.5
A-5:	$AsH_2 + AsH_2$	→	$AsH_3 + AsH$	12	0	10
A-6:	As_2H_4	→	$AsH_2 + AsH_2$	15	0	34.6
A-7:	$AsH_2 + H_2$	→	$AsH_3 + H$	11	0	27.5
A-8:	$AsH_3 + CH_3$	→	$AsH_2 + CH_4$	11.8	0	1.65
A-9:	$AsH_2 + CH_3$	→	$AsH + CH_4$	11	0	0
A-10:	$AsH_3 + AsH$	→	As_2H_4	13	0	2
A-11:	$AsH + H_2$	→	AsH_3	11	0	0
A-12:	$H + H + M$	→	$H_2 + M$	17	−0.6	0

The units of A depend on the reaction order, but are given in terms of mols, cubic centimeters, Kelvin, and seconds. E_a is in kcal/mol. M means third-body species that are buffers of thermal energy[31].

Table 2. Gas phase reactions for Ga-species considered in this study

Reaction	Gas phase reactions for Ga-species			log A (mol, K, cm, s)	β	E_a (kcal/mol)
G-1:	$(CH_3)_3Ga$	→	$(CH_3)_2Ga + CH_3$	17.5	0	59.5
G-2:	$(CH_3)_2Ga$	→	$CH_3Ga + CH_3$	7.94	0	35.4
G-3:	CH_3Ga	→	$Ga + CH_3$	16	0	77.6
G-4:	$(CH_3)_3Ga + H$	→	$(CH_3)_2GaCH_2 + H_2$	13.3	0	5
G-5:	$(CH_3)_2GaCH_2 + H_2$	→	$(CH_3)_3Ga + H$	11	0	6.6
G-6:	$(CH_3)_2Ga + H$	→	$CH_3GaCH_2 + H_2$	13.1	0	5
G-7:	$CH_3GaCH_2 + H_2$	→	$(CH_3)_2Ga + H$	11	0	6.6
G-8:	$CH_3Ga + H$	→	$CH_2Ga + H_2$	12.8	0	5
G-9:	$CH_2Ga + H_2$	→	$CH_3Ga + H$	11	0	6.6
G-10:	$(CH_3)_2GaCH_2$	→	$CH_3GaCH_2 + CH_3$	17.5	0	59.5
G-12:	$CH_3GaCH_2 + H$	→	$CH_2Ga + CH_3$	17.5	0	40
G-11:	$CH_3 + CH_3$	→	C_2H_6	13.9	−0.4	0
G-13:	$CH_3 + H + M$	→	$CH_4 + M$	36.9	−3	0
G-14:	$CH_3 + H_2$	→	$CH_4 + H$	11.9	0	10.9
G-15:	$CH_4 + H$	→	$CH_3 + H_2$	4.34	3	8.75

The simulation for As-species pyrolysis calculates Ga-species pyrolysis at the same time[31].

reaction into the simulation due to the absence of knetic data for it. Since the rate of AsH_2 formation is predicted to be fast for TBAs, many gas phase reactions must be considered, as listed in Table 1. The unimolecular reaction for arsine is calculated using the RRKM theory[101]. Reactions A-8 and A-9 with the CH_3 radical are introduced to consider the effect of group-III sources[27]. To estimate the concentration of CH_3 radicals, TMGa pyrolysis is also simulated considering the reactions in Table 2. We assume that no adduct formation between Ga- and As-species contribute to the growth reactions in the inverted horizontal reactor, as mentioned in the following AlGaAs section[19),62)]. The surface reaction is considered only for the As-species with hydrogen (see Table 3). The adsorption and desorption steps are also considered using rate equations.

Table 3. Surface reactions for As-species considered in this study

Surface reactions for As-species				
AsH_3		→	AsH_2	+ H
AsH_2		→	AsH	+ H
AsH_3	+ H	→	AsH_2	+ H_2
AsH_2	+ H	→	AsH_3	
AsH_2	+ H	→	AsH	+ H_2
AsH		→	As (growth)	

Interactions between As-species are not involved[31].

Figure 19 shows the results of our simulation; in it we plot the time dependencies of the chemical species concentration in the gas phase adjacent to the surface. We calculated that As-species radicals are abundant when using TBAs, suggesting to us that As-species radicals are responsible for the enhanced Si incorporation.

6) Doping mechanism with TBAs and EtAs

We propose the following scheme:

$$AsH_2 + SiH_4 \rightarrow H_2AsSiH_3 + H, \quad \ldots (D)$$

$$AsH + SiH_4 \rightarrow H_2AsSiH_3. \quad \ldots\ldots (E)$$

In our proposed mechanism, reactions D and E control Si doping efficiency rather than reactions A and B. The following reactions are introduced to explain the difference between group-V sources from our simulation:

$$TBAs \rightarrow AsH_2 + C_4H_9, \quad (T\text{-}1)$$

$$AsH_2 + C_4H_9 \rightarrow AsH_3 + C_4H_8, \quad (T\text{-}2)$$

$$AsH_3 + M \rightarrow AsH_2 + H + M. \quad (A\text{-}1)$$

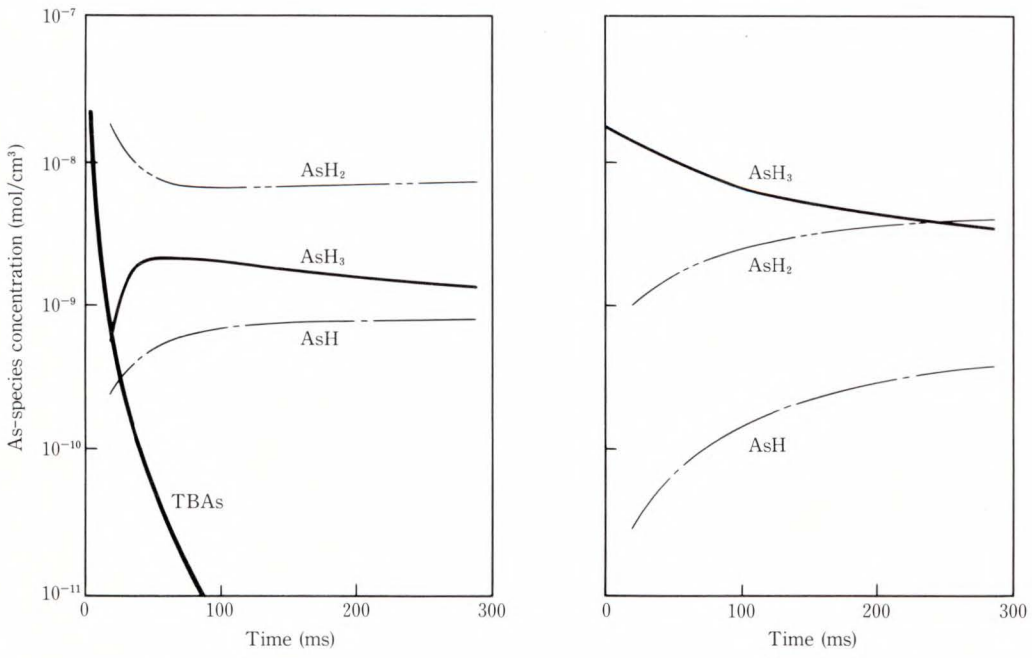

Fig. 19—Results of simulation: As-species concentration in the gas phase adjacent to the surface as a function of the reaction time for GaAs growth.
The initial input condition represents a V/III ratio of 20 and a growth temperature of 650 °C[31].

Our simulation indicates that large amounts of As-species radicals exist adjacent to the surface, resulting in rapid rates of reaction for reactions D and E. These reactions produce a large amount of silylarsine. Moffat et al.[46] has modified a doping model associated with an additional effect of reaction C. In contrast, we speculate that silylarsine formed via reactions D and E mainly controls doping efficiency, resulting in a higher donor concentration using TBAs (see Figs. 8 and 16), because silylarsine is stable in the gas phase due to its low standard heat of formation of 37 kcal/mol and its high dissociation energy of 73 kcal/mol[112], whereas the standard heat of formation for AsH_2 is 41 kcal/mol[113] and for SiH_2 is 63.5 kcal/mol[98].

As-species radicals can adsorb at the Ga-sublattice during As-rich growth, resulting in an As-stabilized surface[114]. Si-precursors must decompose and then break the As-dimerized bond to incorporate into the epitaxial layers. This difficulty causes a low distribution coefficient, typically 0.03 when arsine is used. When silylarsine is formed in the gas phase and reaches the growth surface, dissociation should occur immediately, producing activated As- and Si-species radicals at the same place. Moffat et al.[46] assumed that the surface reaction probability of silylarsine is 1. After the dissociation reaction on the surface, we speculate that most As-species radicals incorporate into an As-site and that Si-species should adsorb on the Ga-sublattice sites without difficulty, resulting in a higher distribution coefficient. However, silylarsine can also adsorb effectively near Ga-sites due to the nature of the Si-atom, producing As_{Ga} in the epitaxial layer. We observed a large amount of As_{Ga} for TBAs-grown GaAs layers using the DLTS (deep level transient spectroscopy) method, suggesting the existence of silylarsine on the surface[109]. Even in this case, we speculate that few Si atoms can incorporate into the As-sublattice sites due the intrinsic property of GaAs. Thus, we concluded that the silylarsine, predicted to be abundant with TBAs, should enhance Si incorporation into the Ga-sublattice sites. The rates of reactions D and E are expected to be fast at 600 °C because reaction T-1 occurs at quite a lower temperature. We surmise that the doping process between 600 °C and 650 °C is in the silylarsine transport limited region, consistent with the observed tempera-

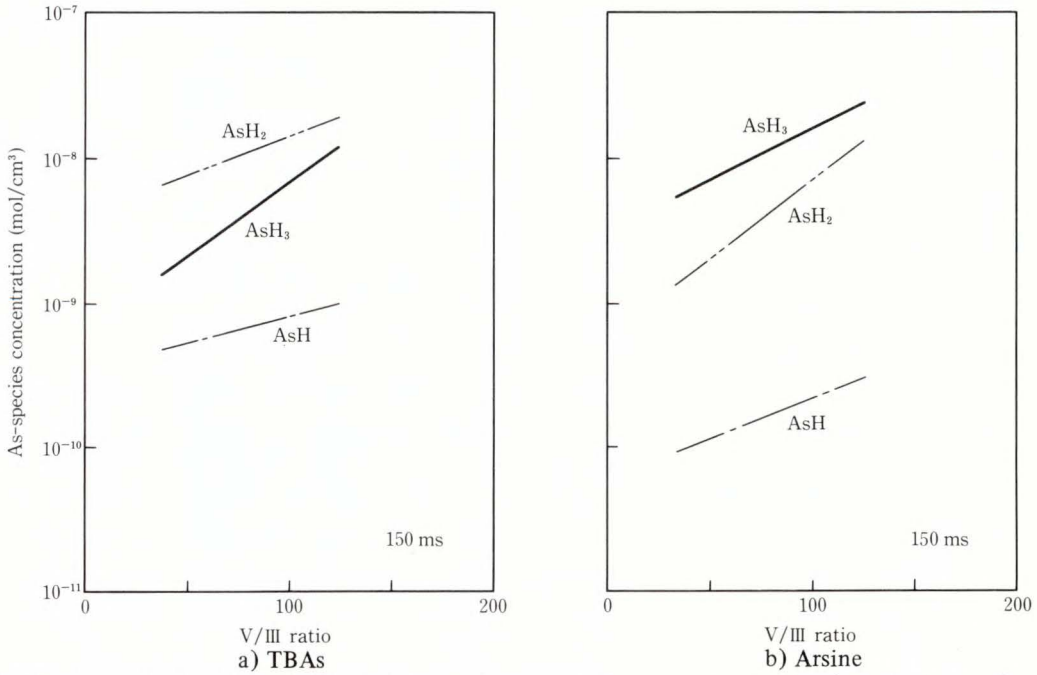

Fig. 20—Results of simulation: Dependence of As- species concentration in the gas phase adjacent to the surface for the V/III ratio.
The reaction time is fixed at 150 ms. The growth tempera- ture is 650 °C[31].

ture-independent trends for silane doped TBAs-grown layers (see Fig. 9).

We also propose the surface reaction mechanisms related to the AsH_3 molecule. Most silane decomposes on the surface via adsorption[50] similar to arsine. Tang et al.[50] also reported that the decomposition of silane happens very close to the hot surface. Silane should compete with AsH_3 in adsorbing[33), 34]. Excess AsH_3 adsorption inhibits Si-species adsorption to break the As-dimerized bond on the As-stabilized surface and to incorporate into the epitaxial layer. We speculate that this mechanism is responsible for the depletion effect with the V/III ratio when using silane {see Figs. 10a) and 11a)}. Figure 20 shows the As-species concentration adjacent to the surface after 150 ms as a function of the V/III ratio from our simulation. The AsH_3 concentration adjacent to the surface increases with increasing As-precursor flow rate with either arsine or TBAs. We speculate that reaction T-2 is predominantly responsible for the production of a large amount of AsH_3 in TBAs pyrolysis.

Using disilane produces more complicated situations. Disilane rapidly dissociates into SiH_2 and SiH_4 via reaction A. Thus, due to a large amount of SiH_2, Si incorporation when using arsine is controlled by the diffusion of SiH_2 (see Fig. 9). We speculate that, even using disilane, reactions D and E proceed effectively with TBAs, resulting in enhancement {see Figs. 10b) and 17}. Moreover, we have to consider reaction C to be significant for the case of disilane. In reaction C, an SiH_2 radical reacts with AsH_3, producing silylarsine[46]. AsH_3 increases with an increasing V/III ratio (see Fig. 18). Therefore, using only disilane, as the V/III ratio increases, the rate of reaction C increases, producing a large amount of silylarsine and enhancing Si incorporation not only using TBAs but also using arsine (see Fig. 12).

The only difference in growth conditions between Figs. 10b) and 11b) is the TMGa flow rate. The group-V flow rate and disilane flow rate are the same. According to our proposed mechanism, the concentrations of both silylarsine and silylene are the same. However, the effective distribution coefficient k_d in Fig. 11b), higher growth rate case, is higher than that in Fig. 10b). Sakaguchi et al.[47] reported similar results. On the contrary, Tang et al.[50] observed the opposite trend. In our experiment, the increase in growth rate corresponds to a decrease in the V/III ratio, increasing the probability of Ga-vacancy formation during growth. We speculate that the increase of Ga-vacancies is responsible for the high doping efficiency under a constant doping component concentration.

Our simulation indicates that the rate of formation of the As-species in the gas phase differs between the group-V sources by about 150 ms (see Fig. 19). Precursors pass beyond the hot susceptor of 46 mm before reaching measurement point: in this study 153 ms under atmospheric pressure with a flow velocity of 30 cm/s. As the reaction proceeds, AsH_3 production with TBAs increases, while that with arsine decreases (see Figs. 14 and 18). A higher flow velocity corresponds to a shorter residence time of reactants in the gas phase; a slower flow to a longer residence time. Thus, comparing Fig. 19 with Figs. 14 and 18, we conclude that different dependencies on the flow velocity (or on the reaction time) are due to differences in the rates of As-species formation between the group-V sources.

We speculate that the same discussion as for TBAs should be used for the EtAs-disilane combination because of the similarity in the decomposition reactions. Li et al.[14] and Speckman et al.[110] have noted that the dominant reaction in the decomposition of EtAs is:

$$EtAs \rightarrow C_2H_5 + AsH_2. \quad \ldots\ldots (F)$$

This reaction occurs at a lower temperature than for the pyrolysis of TBAs[110].

3.2.4 Deep level concentration

Two lots of TBAs, i.e. lot A (contaminated by sulfur) and lot B (as pure as the recent batch) as mentioned in section 3.1, were used in the DLTS[73] study. Disilane was used as a dopant during growth using lot B. Doping was intentionally not done during growth using lot A. The V/III ratio was 10 for all samples. The growth temperature was between 575 °C and 700 °C.

The growth rate was almost constant in this temperature range as shown in Fig. 2. The EL2 concentration was thus not affected by the growth rate in this study.

In a typical DLTS spectrum of GaAs with TBAs, one negative peak was detected. The activation energy is 0.83 eV and the capture cross-section is 6.5×10^{-3} cm^2. The Arrhenius plot for this trap falls near those for EL2[115], ETI[116], and EB2[117]. These are identified as the same trap[118], the so-called EL2. EL2 is a dominant electron trap in GaAs, and we believe that the trap observed here is EL2. EL2 was also detected in GaAs with arsine.

Figure 21 shows the growth temperature dependence of the EL2 concentration in GaAs with TBAs or arsine. With TBAs, the EL2 concentration decreases with an increasing growth temperature below 675 °C, and is constant above 675 °C. This does not depend on the type of donor impurity. The EL2 concentration is constant for GaAs with arsine in this growth temperature range.

Much work and time have gone into clarifying the origin of EL2, a native defect in GaAs. It has been attributed to substitutional As, (As_{Ga})[119], or a complex of As_{Ga} and interstitial As, (As_I)[120]. EL2 concentration is affected by excess incorporation of As into the crystal[121] and, therefore, depends on the type of reactant on the substrate. We speculate that no EL2 is introduced when the As-As bond dissociates on the surface. When using TBAs, AsH_2 radicals dominate the gas phase as mentioned in subsection 3.2.3. Thus, at temperatures below 650 °C, excess As is supplied on the surface with TBAs, resulting in high EL2 concentration (see Fig. 21). EL2 is completely absent in GaAs grown by molecular-beam epitaxy (MBE), where the dominant arsenic source is As_2[122]. Taking the origin of EL2 into consideration, this fact shows the possibility that excess incorporation of As decreases when As_2 molecules are supplied on the surface of the epitaxial layer. Thus, at temperatures above 650 °C, As_2 molecules are formed by AsH_2 consumption with TBAs[62], resulting in low EL2 concentration (see Fig. 21).

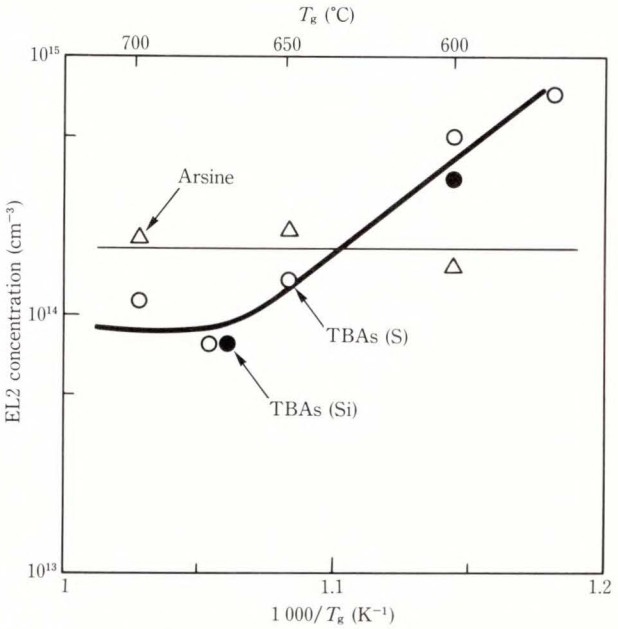

Fig. 21—Growth temperature dependence of the EL2 concentration[62].

The 50 percent decomposition temperature of arsine is 675 °C[15]. Since this is much higher than that of TBAs, the gas phase reaction does not seem to contribute to the As_2 formation before reaching the substrate, resulting in the constant EL2 concentration between 575 °C and 700 °C (see Fig. 21).

3.3 Undoped AlGaAs

Growth of ternary or quaternary alloys is required to fabricate many kinds of device. Not only purity of epitaxial layers but also uniformity of solid composition, growth rate, and carrier concentration are key features in this growth. In this section, we discuss AlGaAs growth on GaAs. AlGaAs has proven to be a more difficult material to grow by MOVPE than GaAs due to the high reactivity of aluminum, forming strong bonds with carbon and oxygen and degrading uniformity.

3.3.1 Conventional horizontal reactor

The surface morphology of the AlGaAs epitaxial layers was excellent under all growth conditions[23]. Figures 22a) and b) show the uniformity of the growth rate and the AlAs mole fraction (x value of $Al_xGa_{1-x}As$ epitaxial layer) along a wafer grown using TBAs and arsine at

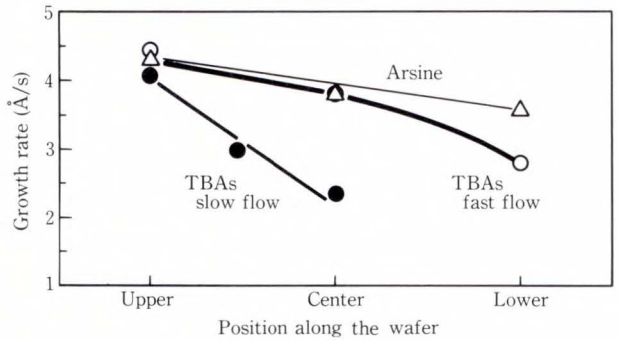

a) Growth rate

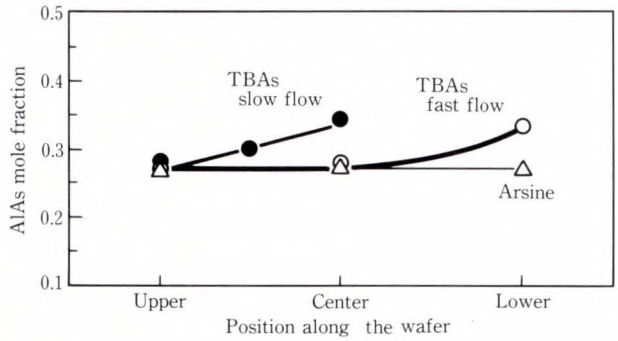

b) AlAs mole fraction

Fig. 22—Uniformity of AlGaAs along a wafer parallel to gas flow for $Al_{0.28}Ga_{0.72}As$ epitaxial layers grown at 680 °C with a V/III ratio of 60. AlAs mole fraction in vapor is fixed at 0.24. The uniformity of films using arsine is independent of the total gas flow rate[23].

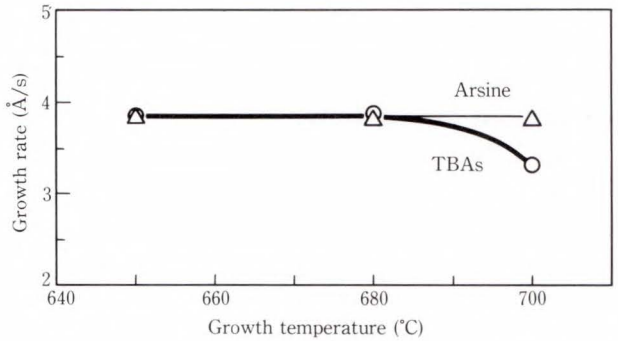

a) Growth rate

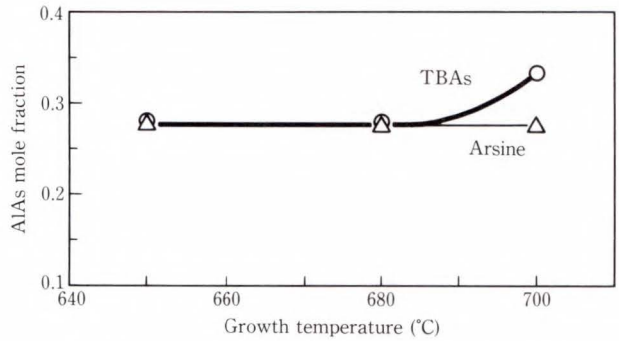

b) AlAs mole fraction

Fig. 23—Dependence of AlGaAs growth on growth temperature for $Al_{0.28}Ga_{0.72}As$ epitaxial layers grown with a V/III ratio of 60. AlAs mole fraction in vapor is fixed at 0.24. Only data for the center of the wafer is given in this figure[23].

680 °C. The growth was less uniform for TBAs than for arsine. We found that γ, defined as the x value in the solid form divided by the x value in the vapor form, varied from 1.1 to 1.5 across the wafer for TBAs and was constant at 1.1 for arsine under the same growth conditions. Increasing the flow rate, decreasing the growth temperature, and cooling the ceiling of the reactor improved γ uniformity across the wafer. The growth uniformity for films using arsine does not depend significantly on the total gas flow rate. Figures 23a) and b) show the dependence of the growth rate and x value on growth temperature at the center of the wafer. The growth rate decreases and the x value increases with increasing temperature using TBAs with a fixed x value of 0.24 in vapor. On the other hand, for arsine, the growth rate

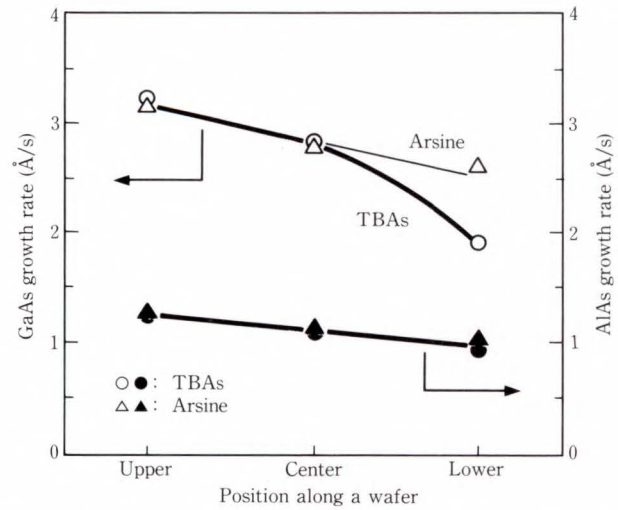

Fig. 24—Calculated AlAs growth rate and calculated GaAs growth rate profile along a wafer for films grown at 680 °C. AlAs and GaAs growth rates are determined by multiplying the $Al_xGa_{1-x}As$ growth rate and the x value or $1-x$ value shown in Fig. 23[23].

decreases slowly with increasing temperature and the x value is quite independent of temperature.

The calculated growth rate profile of AlAs along the wafer parallel to the gas flow for TBAs is the same as that for arsine, as shown in Fig. 24. Here, the AlAs growth rate was determined from the product of the AlGaAs growth rate and the AlAs mole fraction shown in Fig. 22. The growth rate of GaAs using TBAs decreases more rapidly in the direction of flow than that using arsine. A higher γ and a less uniform growth rate for TBAs compared with arsine are caused by depletion of Ga-sources in vapor. Black deposits on the ceiling of the horizontal reactor were notable. A gas phase reaction resembling adduct formation should occur as mentioned above. In addition, TMAl is unlikely to react with TBAs to form an adduct in vapor, since TMAl is a dimmer in vapor[123]. The gas phase reactions between TMGa and TBAs promoted Ga-group deposits, i.e. $(GaCH_3)_n$[78], to form on the ceiling of the reactor, causing the GaAs growth rate to decrease along the wafer. Thus, we have to reduce gas phase reactions to control growth strictly. Possible options using a conventional horizontal reactor are to increase the flow velocity or to reduce the reactor pressure.

The FWHM of the X-ray diffractometer rocking curves for AlGaAs films using TBAs at 700 °C with a V/III ratio of 60 was 27 arcs. This value is equivalent to that of 30.4 arcs for arsine. This suggests that films grown with TBAs are good crystals. Undoped AlGaAs epitaxial layers grown at 670 °C to 700 °C with an x value of 0.24 in the vapor phase showed n-type conductivity with a carrier concentration of 10^{15} cm^{-3} to 10^{16} cm^{-3}, and high resistivity at 650 °C. Si was detected as an n-type dopant with a concentration of 10^{16} cm^{-3} by SIMS analysis. The Si concentration is close to the carrier concentration. Thus, we conclude that Si is the main n-type dopant. The behavior of the carrier concentration is similar to that using arsine. We speculate that Si comes from TMAl since the GaAs epitaxial layers grown using TBAs and TMGa are of high quality.

Figure 25 shows the carrier concentration

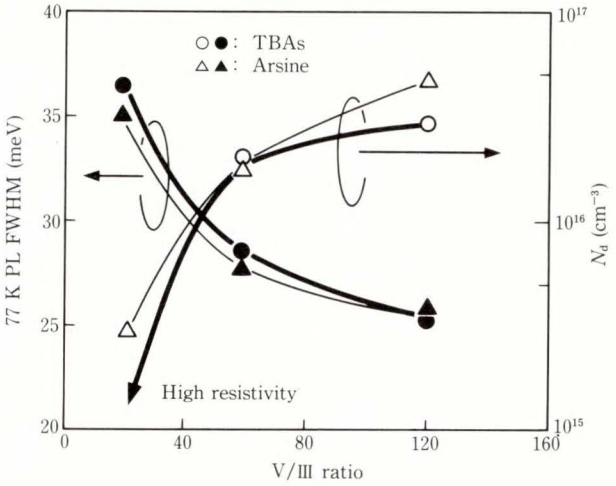

Fig. 25—Carrier concentration and full-width at half-maximum (FWHM) of PL band edge emission at 77 K for $Al_{0.28}Ga_{0.72}As$ grown using lot B at 680 °C as a function of the V/III ratio[23].

and the FWHM of the PL spectra measured at 77 K for films grown at 680 °C, as a function of the V/III ratio. The carrier concentration increased slightly with increasing V/III ratio for films using not only TBAs but also arsine. The FWHM decreased with increasing V/III ratio. From the FWHM results, we conclude that a larger V/III ratio produces better AlGaAs epitaxial layers.

Figure 26 shows the PL spectra at 4.2 K of undoped $Al_{0.28}Ga_{0.72}As$ layers grown at 680 °C with V/III ratios of 20, 60, and 120. The spectra for films using TBAs and arsine are quite similar for the same V/III ratios. The carbon-related peak is prominent for epitaxial layers grown with small V/III ratios. We suppose that the higher binding energy between aluminum and carbon forces the carbon in organometallics to incorporate into AlGaAs epitaxial layers, while carbon incorporation is negligible in the GaAs epitaxial layers. We speculate that hydrogen radicals hardly remove hydrocarbons that bind with aluminum from the surface. However, the ratio of the exciton peak intensity to the carbon acceptor peak intensity increases with increasing V/III ratio. The exciton emission for films grown with a V/III ratio of 120 is quite strong. The SIMS analysis showed that the

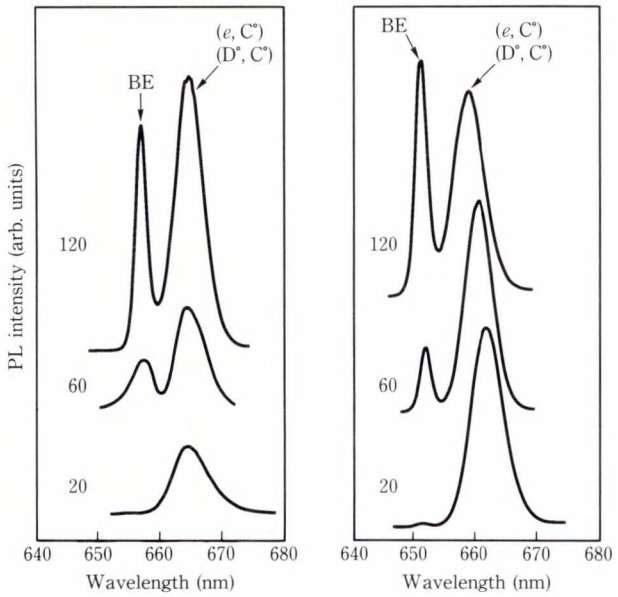

Fig. 26—PL spectra measured at 4.2 K for $Al_{0.28}Ga_{0.72}As$ layers grown at 680 °C with three V/III ratios[23].

concentration of residual carbon had a magnitude of 10^{16} cm^{-3} for films with a V/III ratio of 20. Since undoped AlGaAs films showed *n*-type conductivity with a free carrier concentration of 10^{16} cm^{-3}, we suppose that carbon incorporation as a *p*-type dopant is as low as 10^{15} cm^{-3} to 10^{16} cm^{-3}. An increased gas flow rate also improved the quality of the AlGaAs. At the beginning of this work, we expected that high quality AlGaAs layers would be grown with even a small V/III ratio when using TBAs, since the decomposition temperature of TBAs was quite a lot lower than that of arsine. From this work, however, it seems that a higher V/III ratio is important for the growth of high quality AlGaAs when using TBAs as well as when using arsine.

3.3.2 Inverted horizontal reactor

In AlGaAs growth using TBAs with conventional horizontal atmospheric pressure reactors, epitaxial layers showed poor growth uniformity as discussed in subsection 3.3.1. Increasing the total gas flow rate improves uniformity slightly but decreasing the growth temperature has no apparent effect. This was mainly due to the atmospheric pressure apparatus. Because black deposits on the ceiling of the reactor just above the substrate consumed group-III species and decreased the source supply over the entire substrate surface, the uniformity in growth became worse. Deposits were more prominent for TBAs than for arsine. The natural convection induced by buoyancy in all conventional atmospheric pressure reactors promoted deposition onto the ceiling, especially when used TBAs.

We estimated the influence of natural convection using the Rayleigh number (Ra), defined as follows[124]:

$$\mathrm{Ra} \equiv (g\beta h^3 \Delta T)/\nu D_T, \qquad \ldots\ldots\ldots (3)$$

where g is the acceleration due to gravity, β the coefficient of thermal expansion, h the typical length of flow, ΔT the typical difference in temperature, ν the kinetic viscosity, and D_T the coefficient of thermal diffusion. Natural convection strongly affects the flow when Ra exceeds 1 708[125]. Ra was evaluated at 311 for our horizontal reactor at atmospheric pressure. Convection does not disorder the flow completely, but the influence cannot be ignored for an Ra of 311. Thus, we developed an inverted horizontal atmospheric pressure reactor, as shown in Fig. 1b), to eliminate the buoyancy-induced flow and reduce parasitic deposition so that epitaxial growth affected only by the nature of the materials themselves could be carried out easily under atmospheric pressure. No parasitic deposition was observed in the inverted reactor for either source. Puetz et al. obtained uniform InGaAs with an inverted horizontal reduced-pressure reactor [126]. We found an additional advantage to using the inverted reactor. Excellent morphology could be obtained easily for all epitaxial layers, because few particles were adsorbed on the substrate due to face-down growth. We obtained epitaxial layers with a total particle density of 3 cm^{-2} larger than 0.24 μm^2 using TBAs.

The uniformity of $Al_xGa_{1-x}As$ films was greatly improved using the new inverted reactor. In the PL spectrum at 77 K, the variation in the wavelength of the band edge emission line was within ±0.5 nm across the substrate, showing excellent x uniformity. Figure 27 shows the distribution of thickness across a stationary

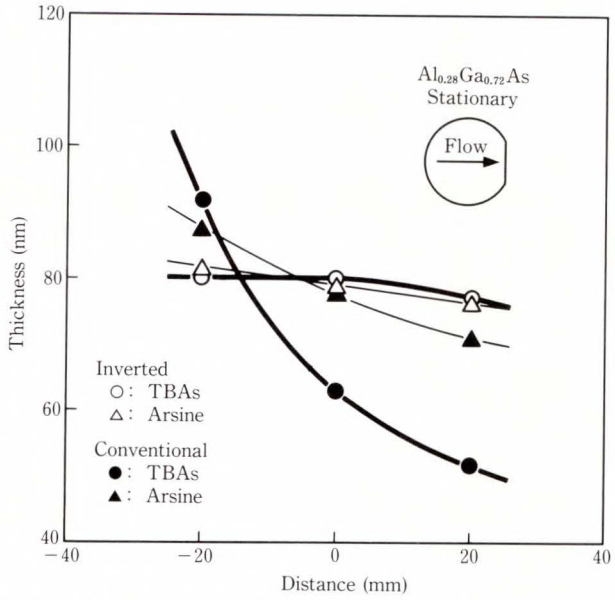

Fig. 27—Variation of $Al_{0.28}Ga_{0.72}As$ thickness using lot B TBAs and arsine across a 3-inch stationary substrate parallel to the gas flow at 650 °C with a V/III ratio of 60 in a conventional and inverted reactor[24].

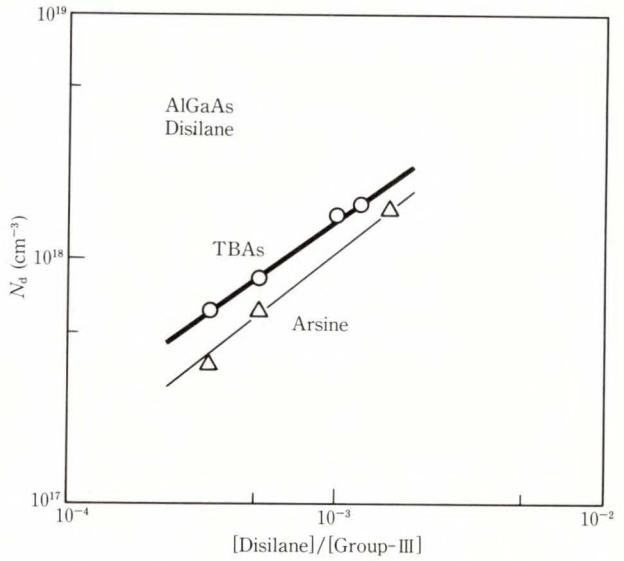

Fig. 28—N_d of $Al_{0.28}Ga_{0.72}As$ grown using TBAs or arsine as a function of the disilane flow rate. The V/III ratio is 60. The growth rate is 1.3 μm/h[31].

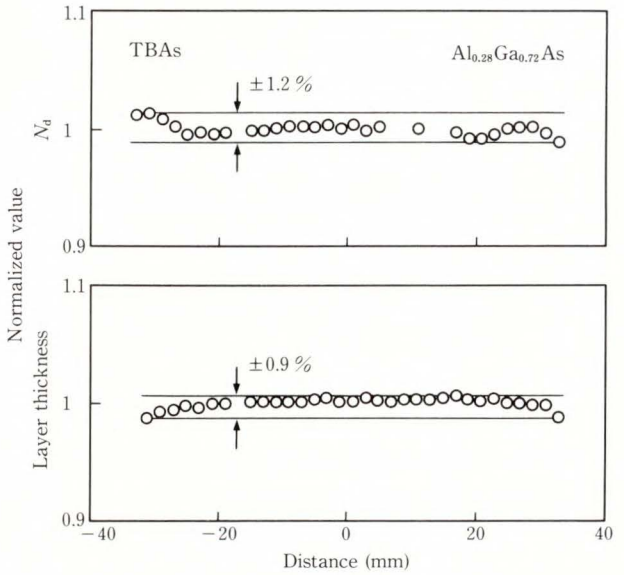

Fig. 29—Distribution of N_d and layer thickness of Si-doped $Al_{0.28}Ga_{0.72}As$ layers grown using TBAs at 650 °C with a V/III ratio of 60 across a rotated 3-inch substrate. The average N_d is 1.81×10^{18} cm^{-3}. The average layer thickness is 90.4 nm[24].

3-inch substrate at 650 °C with a V/III ratio of 60. A high V/III ratio is important for AlGaAs growth as shown in Fig. 26. With the inverted reactor, the uniformity of AlGaAs using TBAs and arsine was virtually the same.

3.4 Si-doped AlGaAs

An *n*-type AlGaAs with a carrier concentration greater than 10^{17} cm^{-3} is essential to fabricate HEMTs or lasers consisting of AlGaAs.

An initial study on Si-doping for $Al_{0.28}Ga_{0.72}As$ has been completed using disilane. Undoped $Al_{0.28}Ga_{0.72}As$ grown with a high V/III ratio using TBAs or arsine possesses a low carrier concentration as shown by the Hall measurement and low carbon incorporation according to the PL spectra (see Fig. 26). AlGaAs grown using EtAs at 650 °C, however, resulted in poor morphology due to intermediate reactions and to residual impurities such as water. Figure 28 shows the dependence of the Si incorporation efficiency on the disilane flow rate for epitaxial layers grown using TBAs or arsine at 650 °C. The N_d using TBAs is always 1.5 times higher than using arsine. This occurs in the case of GaAs growth, indicating that the same mechanism controls Si incorporation for both GaAs and AlGaAs.

AlGaAs layers were grown on substrates rotated at 12 r/min. Figure 29 shows the distribution of N_d and the layer thickness using

TBAs. Despite atmospheric pressure growth and a vapor phase reaction between TMGa and TBAs caused by the low decomposition temperature of TBAs[19),23)], variations in N_d and the layer thickness were less than ±1.2 % and ±0.9 %. An edge effect due to protuberances on the susceptor for holding substrates slightly decreased layer thickness at the edge region. This result is not optimized but already similar to that using arsine, suggesting that a uniformity sufficient for device fabrication can be obtained using TBAs with this inverted reactor even at atmospheric pressure. Thus, we believe that improving the reactor to eliminate deposits should produce excellent AlGaAs uniformity using TBAs.

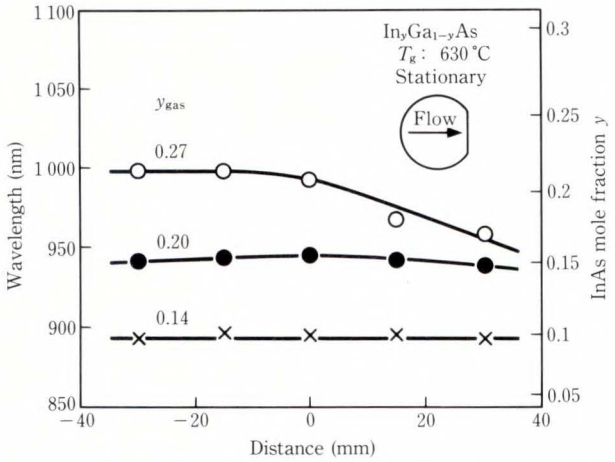

Fig. 30—Distribution of band edge emission in PL spectra at 77 K for $In_yGa_{1-y}As$ layers across a stationary GaAs substrate using TBAs grown at 630 °C. Only TMIn flow rate is varied[24)].

3.5 InGaAs on GaAs

In this section, $In_yGa_{1-y}As$ layers were grown on GaAs substrates aiming to AlGaAs/InGaAs/GaAs pseudomorphic heterostructures. All layers were 1.2 μm thick in order to minimize the distortion caused by lattice mismatch. The V/III ratios of InGaAs grown were 2.6 to 10 for TBAs and 5 to 95 for arsine. The surfaces of InGaAs layers grown using arsine with a V/III ratio of 5 were milky due to insufficient decomposition of arsine.

Figures 30 and 31 show the distributions of band edge emissions in PL spectra at 77 K (corresponding to InAs mole fraction; y) across stationary 3-inch substrates grown at 630 °C and 650 °C, respectively. In Fig. 30, only TMIn flow rate was varied and the V/III ratio was around five. Excellent y uniformity was obtained for the layers with y up to 0.15. In Fig. 31, InAs mole fraction in gas phase (y_{gas}) was kept

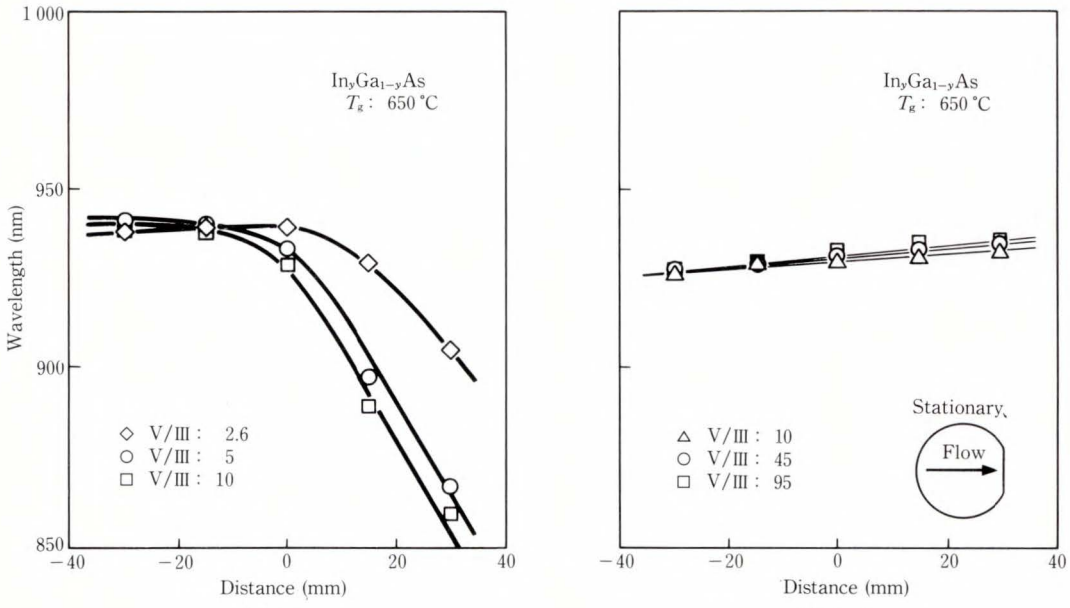

Fig. 31—Distribution of band edge emission in PL spectra at 77 K for $In_yGa_{1-y}As$ layers across a stationary GaAs substrate with various V/III ratios grown at 650 °C[24)].

to 0.2. An increase of only 20 °C deteriorated the y uniformity significantly using TBAs. There are substantial differences between sources. The y uniformity for TBAs became worse with increasing V/III ratio. However, y was almost constant in the region upstream from the center and the InGaAs thickness was also confirmed to be uniform in that region from the growth of GaAs/InGaAs/GaAs quantum well structures. For arsine, y increases slightly downstream from the top, regardless of V/III ratio, up to 95.

No deposit was left on the reactor ceiling just under a substrate nor on the injector for either source. Depositions on the cool wall downstream for TBAs were more abundant than those for arsine. It should be noted that, in AlGaAs growth at 650 °C, only reducing source consumption due to wall deposition resulted in highly uniform AlAs mole fraction and highly uniform layer thickness. Thus, InGaAs growth distributions across a substrate are affected only by the material itself.

Since there was no deposition on the injector, there is no apparent reaction between TMIn and arsenic sources at room temperature. Therefore, we speculate that different reaction mechanisms operate in the vapor phase only around substrates including TMIn at atmospheric pressure. They may be reactions involving adduct formation or a parasitic reaction, which does not contribute to the growth reaction directly like triethylindium (TEIn)-arsine adduct formation[127]; either may eliminate In-containing species from the vapor just below the substrate. This is because the temperature of the vapor around the substrate is only 200 °C to 500 °C, even if the growth temperature is 700 °C[105]. TBAs begins to decompose at 300 °C[19),21)], and is expected to react with TMIn in vapor at that temperature. This unclarified vapor phase reaction must be eliminated to fabricate pseudomorphic structures. Since InGaAs layers are already uniform in the upstream region for TBAs (about 40 mm length), we believe that improved source injection or reduced pressure should produce uniform InGaAs across a 3-inch substrate.

3.6 Selectively doped heterostructures

The quality of selectively doped heterostructures is very sensitive to the abruptness at the heterointerface, the purity of materials, and doping concentration. Thus, we investigated the growth of selectively doped heterostructures with TBAs, comparing that with arsine. These results were utilized for HEMT fabrication as described in section 3.7.

3.6.1 *n*-AlGaAs/GaAs

Selectively doped n-AlGaAs/GaAs heterostructures consist of a 700 nm undoped GaAs layer, a 0 nm to 7 nm undoped $Al_{0.28}Ga_{0.72}As$ spacer layer, a 37 nm Si-doped $Al_{0.28}Ga_{0.72}As$ layer, and a GaAs cap layer, The electron concentration of the n-AlGaAs layer was maintained at 1.4×10^{18} cm^{-3}. The V/III ratios of GaAs and AlGaAs for TBAs were 40 and 60 and those for arsine were 10 and 60.

Strong oscillations of the Shubnikov-de Haas (SdH) effect in a transverse magnetoresistance were observed at 4.2 K for the heterostructures of the 5 nm spacer layer grown using TBAs as shown in Fig. 32. The magnetic field was applied perpendicular to the heterointerface. These oscillations confirm the existence of high-quality 2DEG at the heterointerface.

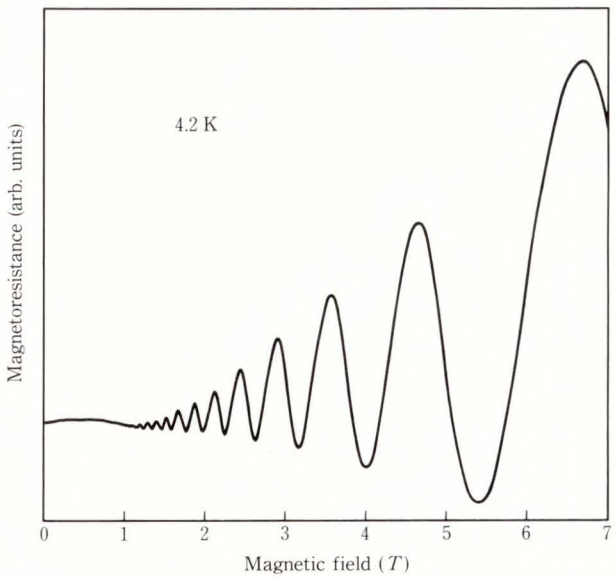

Fig. 32—Shubnikov-de Haas oscillations observed at 4.2 K for a selectively doped n-$Al_{0.28}Ga_{0.72}As$/GaAs heterostructure grown using TBAs[64].

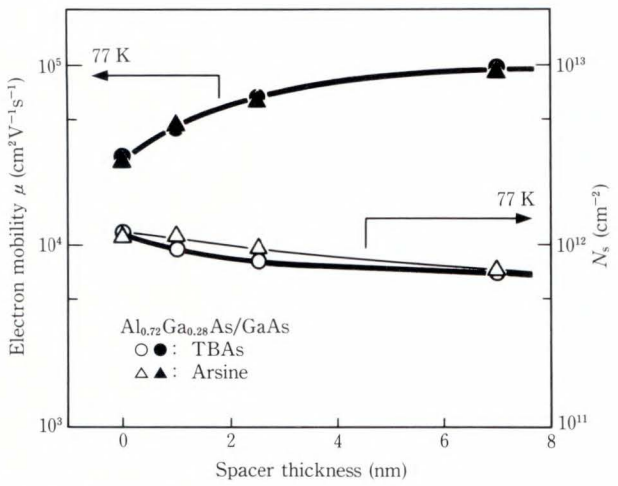

Fig. 33—Electron mobility and sheet carrier concentration at 77 K for selectively doped n-$Al_{0.28}Ga_{0.72}As/GaAs$ heterostructures grown at 650 °C as a function of AlGaAs spacer layer thickness[24].

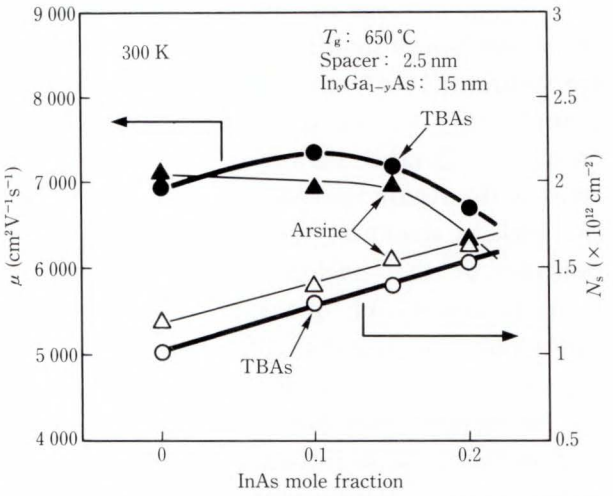

Fig. 34—Electron mobility and sheet carrier concentration of n-$Al_{0.28}Ga_{0.72}As/In_yGa_{1-y}As/GaAs$ pseudomorphic heterostructures at 300 K as a function of the InAs mole fraction in the InGaAs channel layer[63].

Figure 33 shows electron mobility (μ) and sheet carrier concentration (N_s) at 77 K as a function of spacer layer thickness for films grown using lot C (produced in 1990). The inverted horizontal reactor was used. There is no difference between the group-V sources. We obtained high-quality n-AlGaAs/GaAs heterostructures using TBAs with a μ of 98 000 $cm^2V^{-1}s^{-1}$ and an N_s of 6.9×10^{11} cm^{-2} at 77 K for the 7 nm spacer layer. This proves that an abrupt interface between the AlGaAs spacer layer and GaAs buffer layer was formed using the inverted reactor. The excellent performance of the heterostructures also verifies the purity of these epitaxial layers.

3.6.2 n-AlGaAs/InGaAs/GaAs

In the growth of n-AlGaAs/InGaAs/GaAs pseudomorphic heterostructures, a 15 nm InGaAs channel layer was grown between the undoped GaAs layer and the undoped AlGaAs spacer layer. In the atmospheric pressure reactor, the InAs mole fraction in the InGaAs layer using TBAs was less uniform than that in the layer using arsine as described in section 3.5. A V/III ratio of less than 5 was required to obtain better uniformity with TBAs. However, with arsine, InGaAs grown with such a low V/III ratio resulted in a milky surface due to insufficient arsenic source supply on the substrate. Thus, when pseudomorphic HEMTs were grown, the InGaAs channel layers had a V/III ratio of 2.5 for TBAs and 10 for arsine. The growth parameters (e.g. growth rate) were optimized at the center of the substrate.

Figure 34 shows μ and N_s of selectively doped n-AlGaAs/InGaAs/GaAs pseudomorphic heterostructures at room temperature as a function of the InAs mole fraction (y). The AlGaAs spacer layer was 2.5 nm thick. As the InAs mole fraction increased, N_s increased monotonically, while the μ remained almost constant when the InAs mole fraction was below 0.15. At 300 K, N_s and μ were 1.4×10^{12} cm^{-2} and 7 200 $cm^2V^{-1}s^{-1}$ respectively for the film grown using TBAs with an InAs mole fraction of 0.15. The N_s and μ at 77 K for this film were 1.25×10^{12} cm^{-2} and 45 000 $cm^2V^{-1}s^{-1}$ respectively, demonstrating an abrupt interface between the AlGaAs spacer layer and the InGaAs channel layer. The μ resulting from using TBAs was higher than that when arsine was used. On the other hand, when TBAs was used, N_s was lower than that for arsine. In the growth of pseudomorphic heterostructures, the V/III ratio for the growth of the InGaAs channel layer is different between the group-V sources, because the V/III ratio for optimum uniformity is different, as shown in Fig. 31. The Si incorporation

efficiency also differs between sources[28)-32)]. Thus, we speculate that the difference in electrical properties is attributed to the difference in the quality of both Si-doped AlGaAs and InGaAs layers.

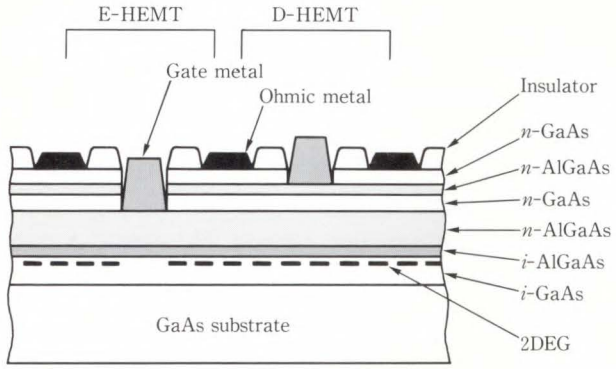

Fig. 35—Circuit structure of n-AlGaAs/GaAs HEMT DCFL.

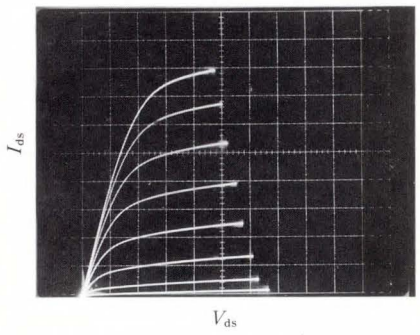

Fig. 36—Source-drain I-V characteristics at 300 K for n-$Al_{0.28}Ga_{0.72}As$/GaAs E-HEMTs with a 0.5-μm gate using TBAs. The step of source-gate voltage V_{gs} is 0.1 V[63)].

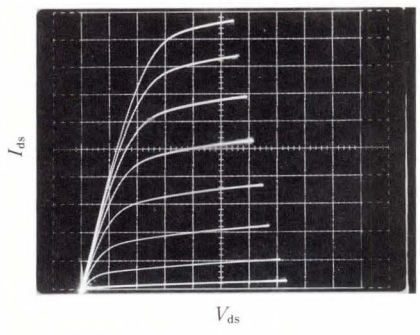

Fig. 37—Source-drain I-V characteristics at 300 K for n-$Al_{0.28}Ga_{0.72}As/In_{0.15}Ga_{0.85}As$/GaAs E-HEMTs with a 0.5-μm gate using TBAs. The step of source-gate voltage V_{gs} is 0.1 V[63)].

3.7 HEMT fabrication

In this chapter, we describe the fabrication of HEMTs using the heterostructures grown as described in section 3.6.

3.7.1 n-AlGaAs/GaAs HEMT

Figure 35 shows an n-AlGaAs/GaAs HEMT direct-coupled-FET-logic (DCFL) circuit structure. The gate length is 0.5 μm and the width is 60 μm. A very thin AlGaAs layer is embedded in the GaAs cap layer to stop selective dry etching during the fabrication of enhancement-mode HEMTs (E-HEMTs) and depletion-mode HEMTs (D-HEMTs). The source-drain current-voltage (I-V) characteristics of n-AlGaAs/GaAs HEMTs grown using TBAs are shown in Fig. 36. Excellent saturation and pinch-off were observed using TBAs. We achieved high performance HEMTs, with an extrinsic transconductance (g_m) of 324 $mSmm^{-1}$ and K-valve of 418 $mSV^{-1}mm^{-1}$.

3.7.2 n-AlGaAs/InGaAs/GaAs HEMT

We also fabricated n-$AlGaAs/In_yGa_{1-y}As$/GaAs pseudomorphic HEMTs using TBAs and arsine. A 15 nm $In_{0.15}Ga_{0.85}As$ layer was grown for this structure, because the dependence of the InAs mole fraction on various properties of the pseudomorphic heterostructures, as shown in Fig. 34, implies that $In_{0.15}Ga_{0.85}As$ is most suitable for the 15 nm channel layer. Figure 37 shows the I-V characteristics, measured at 300 K, of n-AlGaAs/InGaAs/GaAs pseudomor-

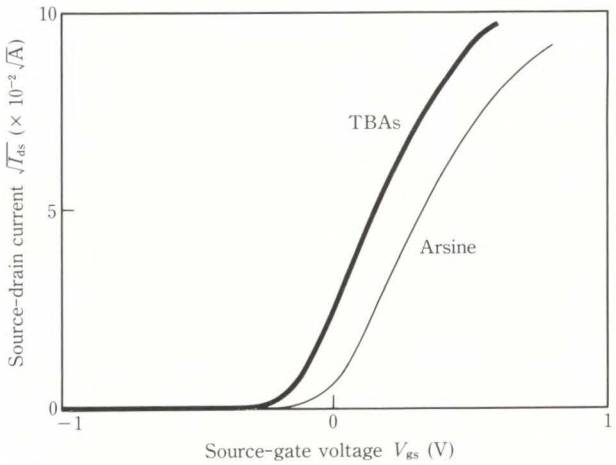

Fig. 38—Square-root of source-drain current versus source-gate voltage for pseudomorphic HEMTs. The source-drain voltage V_{ds} is 1 V[63)].

phic HEMTs grown using TBAs. Excellent saturation characteristics were observed.

In addition to the good electrical properties of selectively doped heterostructures, complete isolation of the active region is indispensable for the development of HEMT LSIs. A high-resistance buffer layer is required to obtain complete isolation. It is a significant issue whether the buffer layer grown using TBAs is resistive enough to isolate the adjacent transistor. Figure 38 shows the square root of the source-drain current ($\sqrt{I_{ds}}$) plotted as a function of the source-gate voltage (V_{gs}) for pseudomorphic HEMTs grown using a) TBAs and b) arsine. The source-drain voltage (V_{ds}) was 1 V. Figure 38 verifies that the pinch-off characteristics are excellent for both sources, which indicates that the TBAs-grown buffer layer has sufficient isolation capability for sub-micron gate HEMTs. For pseudomorphic HEMTs, the values of g_m and the K-value were 350 $mSmm^{-1}$ and 480 $mSV^{-1}mm^{-1}$ for TBAs; and 308 $mSmm^{-1}$ and 423 $mSV^{-1}mm^{-1}$ for arsine. The results for pseudomorphic HEMTs confirm better performance than conventional AlGaAs/GaAs HEMTs with both TBAs and arsine. The performance for TBAs was superior to that for arsine. However, the Si incorporation efficiency into AlGaAs and GaAs[28)-32)], and the quality of the InGaAs layer[24)] were quite different between precursors having the same V/III ratio. We speculated that, since the performance of HEMTs depends on N_d of the AlGaAs layers and on the InGaAs purity, slight differences in HEMT performance should occur between group-V sources. Detailed research into InGaAs growth on GaAs with TBAs must improve the performance of pseudomorphic HEMTs.

4. Conclusion

We have investigated undoped and Si-doped GaAs and AlGaAs, InGaAs, and selectively doped AlGaAs/GaAs heterostructures using TBAs in conventional or inverted horizontal atmospheric pressure reactors. EtAs was also used for comparison.

The surface morphology of the GaAs and AlGaAs epitaxial layers grown using TBAs was comparable to that of layers grown using arsine. PL measurements at 4.2 K revealed well-resolved emissions in the exciton region of the GaAs films which suggested that the GaAs films grown using TBAs and EtAs were of high quality, and that carbon incorporation into the GaAs epitaxial layer was as low as achieved with arsine. X-ray analysis showed that AlGaAs epitaxial layers grown using TBAs were as good as those grown using arsine. Carbon incorporates into the AlGaAs epitaxial layers with a concentration of 10^{15} cm^{-3} to 10^{16} cm^{-3}. We interpret this as resulting from the stronger binding energy between aluminum and carbon. However, increasing the V/III ratio reduces carbon incorporation, producing high-quality AlGaAs. In this study, the purity of EtAs was insufficient for AlGaAs growth.

It was difficult to assure a uniform AlGaAs layer across the wafer using a conventional horizontal atmospheric pressure reactor. Gas phase reactions between TMGa and TBAs form adducts and other intermediates, causing the growth efficiency to vary markedly over the wafer surface. However, with an inverted horizontal atmospheric pressure reactor, we eliminated buoyancy-induced flow, thus reducing the source deposition onto the reactor wall, and obtained high quality, highly uniform AlGaAs layers using TBAs. The uniformity of AlGaAs films using TBAs across a 3-inch substrate was within ±1.2 % for N_d and ±0.9 % for the layer thickness with an inverted horizontal reactor.

Our study (bulk doping and planar doping of Si) revealed Si-doping to have seven significant key features:

1) Using TBAs and EtAs enhances Si incorporation.
2) Diffusion of the doping component controls Si-doping using TBAs, even using silane.
3) Using silane, Si-doping efficiency decreases as the V/III ratio increases.
4) Using disilane, Si-doping efficiency decreases as the V/III ratio increases in the case of TBAs and EtAs, but increases in the case of arsine. At a higher V/III ratio, the doping efficiency using disilane is higher than that

using silane not only for arsine but also for TBAs. This increment is similar with TBAs and with arsine.

5) The growth rate affects Si-doping efficiency.
6) The dependence of Si-doping efficiency on the gas flow velocity is opposite for TBAs and for arsine, indicating that the gas phase reactions between As-species and Si-species dominate the Si-doping process and that the rate of reaction in the gas phase is different for different group-V sources.
7) The dependence of Si-doping efficiency on substrate misorientation is the same for TBAs and arsine.

To verify the relationship between the pyrolysis of As-species and the doping efficiency, we applied a kinetic simulation on group-V decomposition including the gas and surface reactions. The TBAs pyrolysis produces a large amount of As-species radicals. We propose that a large amount of silylarsine is formed by reaction between As-species radicals and SiH_4. Silylarsine is predicted to be prominent when using organoarsine, and silylarsine rather than silylene is the most effective contributor to Si doping reactions. We also introduced the hindrance of Si-species adsorption on the surface due to AsH_3. The mixture of enhancement and suppression could explain the complicated doping features. Using TBAs, EL2 concentration of GaAs decreases as growth temperature increases. This also suggests that AsH_2 formation dominates the gas phase when using TBAs.

Uniform $In_{0.15}Ga_{0.85}As$ on GaAs was obtained using TBAs at 630 °C. Increasing the InAs mole fraction, growth temperature, and V/III ratio resulted in poor uniformity, signifying an active vapor phase reaction between TMIn and TBAs.

The electron mobility of the selectively doped *n*-AlGaAs/GaAs heterostructures with a 7 nm spacer layer was as high as 98 000 $cm^2V^{-1}s^{-1}$. The existence of 2DEG at the heterointerface was confirmed by the observation of Shubnikov-de Haas oscillations. Selectively doped *n*-AlGaAs/InGaAs/GaAs pseudomorphic heterostructures were grown using TBAs or arsine, resulting in comparably good electrical properties. We demonstrated the first fabrication of 0.5 μm-gate *n*-AlGaAs/GaAs HEMTs and *n*-AlGaAs/InGaAs/GaAs pseudomorphic HEMTs using TBAs. Sharp pinch-off and excellent saturation characteristics were observed for HEMTs made from either source. $\sqrt{I_{ds}}$ vs V_{gs} characteristics verified that the buffer layer had high resistance. We obtained high-performance HEMTs using either TBAs or arsine. These results demonstrate that GaAs, AlGaAs, and InGaAs layers grown using TBAs are very pure and are suitable for HEMT LSI fabrications.

References

1) Stringfellow, G.B.: Non-Hydride Group V sources for OMVPE. *J. Electron. Mater.*, **17**, 4, pp. 327-335 (1988).
2) Dietze, W.T., Ludowise, M.J., and Cooper, C.B.: Improved Mobility in OM-VPE-Grown $Ga_{1-x}In_xAs$. *Electron. Lett.*, **17**, 19, pp. 698-699 (1981).
3) Kuo, C.P., Cohen, R.M., and Stringfellow, G.B.: OMVPE Growth of GaInAs. *J. Cryst. Growth*, **64**, 3, pp. 461-470 (1983).
4) Lum, R.M., Klingert, J.K., Kisker, D.W., Tennant, D.M., Morris, M.D., Malm, D.L., Kovalchick, J., and Heimbrook, L.A.: Investigation of Carbon Incorporation in GaAs Using ^{13}C-Enriched Trimethylarsenic and $^{13}CH_4$. *J. Electron. Mater.*, **17**, 2, pp. 101-104 (1988).
5) Vook, D.W., Reynolds, S., and Gibbons, J.F.: Growth of GaAs by Metalorganic Chemical Vapor Deposition Using Thermally Decomposed Trimethylarsenic. *Appl. Phys. Lett.*, **50**, 19, pp. 1386-1387 (1987).
6) Kuech, T.F., Tischler, M.A., Wang, P.-J., Scilla, G., Potemski, R., and Cardone, F.: Controlled Carbon Doping of GaAs by Metalorganic Vapor Phase Epitaxy. *Appl. Phys. Lett.*, **53**, 14, pp. 1317-1319 (1988).
7) Speckman, D.M., and Wendt, J.P.: Alternatives to Arsine: The Atmospheric Pressure Organometallic Chemical Vapor Deposition Growth of GaAs Using Triethylarsenic. *Appl. Phys. Lett.*, **50**, 11, pp. 676-678 (1987).
8) Fujita, S., Uemoto, Y., Araki, S., Imaizumi, H., Takada, Y., and Sasaki, A.: Organometallic Vapor-Phase Epitaxy of GaAs Using Triethylarsenic as Arsenic Source. *Jpn. J. Appl. Phys.*, **27**, 7, pp. 1151-1155 (1988).
9) Lum, R.M., Klingert, J.K., Wynn, A.S., and Lamont M.G.: Investigation of Triethylarsenic as

a Replacement for Arsine in the Metalorganic Chemical Vapor Deposition of GaAs. *Appl. Phys. Lett.*, **52**, 18, pp. 1475-1477 (1988).

10) Fujita, S., Imaizumi, M., Araki, S., Takeda, Y., and Sasaki, A.: Crystal Growth of GaAs and AlGaAs by OMVPE Using Triethylarsenic as Arsenic Source. *J. Cryst. Growth*, **93**, pp. 1-6 (1988).
11) Bhat, R., Koza, M.A., and Skromme, B.J.: Growth of High-Quality GaAs Using Trimethylgallium and Diethylarsine. *Appl. Phys. Lett.*, **50**, 17, pp. 1194-1196 (1987).
12) Brauers, A., Kayser, O., Kall, R., Heinecke, H., and Balk, P.: The Use of Organic As Precursors in the Low Pressure MOCVD of GaAs. *J. Cryst. Growth*, **93**, pp. 7-14 (1988).
13) Speckman, D.M., and Wendt, J.P.: Vapor Deposition of High-Purity GaAs Epilayers Using Monoethylarsine. *Appl. Phys. Lett.*, **56**, 12, pp. 1134-1136 (1990).
14) Li, S.H., Larsen, C.A., and Stringfellow, G.B.: Comparative Pyrolysis Studies of Ethylarsines. *J. Cryst. Growth*, **107**, pp. 32-36 (1991).
15) Chen, C.H., Larsen, C.A., and Stringfellow, G.B.: Use of Tertiarybutylarsine for GaAs Growth. *Appl. Phys. Lett.*, **50**, 4, pp. 218-220 (1987).
16) Lum, R.J., Klingert, J.K., and Lamont, M.G.: Use of Tertiarybutylarsine in the Metalorganic Chemical Vapor Deposition Growth of GaAs. *Appl. Phys. Lett.*, **50**, 5, pp. 284-286 (1987).
17) Larsen, C.A., Buchan, N.I., Li, S.H., and Stringfellow, G.B.: GaAs Growth Using Tertiarybutylarsine and Trimethylgallium. *J. Cryst. Growth*, **93**, pp. 15-19 (1988).
18) Omstead, T.R., Van Sickle, P.M., Lee, P.W., and Jensen, K.F.: Gas Phase and Surface Reactions in the MOCVD of GaAs from Triethylgallium, Trimethylgallium, and Tertiarybutylarsine. *J. Cryst. Growth*, **93**, pp. 20-28 (1988).
19) Lee, P.W., Omstead, T.R., McKenna, D.R., and Jensen, K.F.: *In Situ* Mass Spectroscopy Studies of the Decomposition of Organometallic Arsenic Compounds in the Presence of $Ga(CH_3)_3$ and $Ga(C_2H_5)_3$. *J. Cryst. Growth*, **93**, pp. 134-142 (1988).
20) Larsen, C.A., Li, S.H., Buchan, N.I., and Stringfellow, G.B.: Mechanisms of GaAs Growth Using Tertiarybutylarsine and Trimethylgallium. *J. Cryst. Growth*, **94**, 3, pp. 673-682 (1989).
21) Li, S.H., Buchan, N.I., Larsen, C.A., and Stringfellow, G.B.: The Effect of Supplemental *t*-butyl Radicals on the Pyrolysis of Tertiarybutylarsine, Tertiarybutylphosphine, and Ditertiarybutylarsine. *J. Cryst. Growth*, **98**, 3, pp. 309-316 (1989).
22) Lum, R.M., Klingert, J.K., and Kisker, D.W.: Effects of Methylarsine Homologs $(CH_3)_nAsH_{3-n}$ on the Metalorganic Vapor-Phase Epitaxy of GaAs. *J. Appl. Phys.*, **66**, 2, pp. 652-655 (1989).
23) Kikkawa, T., Tanaka, H., and Komeno, J.: The Growth of GaAs, AlGaAs, and Selectively Doped AlGaAs/GaAs Heterostructures by Metalorganic Vapor Phase Epitaxy Using Tertiarybutylarsine. *J. Appl. Phys.*, **67**, 12, pp. 7576-7582 (1990).
24) Kikkawa, T., Tanaka, H., and Komeno, J.: MOVPE Growth of Uniform AlGaAs and InGaAs Using Organoarsine with Inverted-Horizontal Atmospheric Pressure Reactor. *J. Cryst. Growth*, **107**, pp. 370-375 (1991).
25) Haacke, G., Watkins, S.P., and Burkhard, H.: Epitaxial Growth of High-Mobility GaAs Using Tertiarybutylarsine and Triethylgallium. *Appl. Phys. Lett.*, **56**, 6, pp. 478-480 (1990).
26) Haacke, G., Watkins, S.P., and Burkhard, H.: Control of Residual Impurity Incorporation in Tertiarybutylarsine-Grown GaAs. *J. Cryst. Growth*, **107**, pp. 342-347 (1991).
27) Kuech, T.F., and Veuhoff, E.: Mechanism of Carbon Incorporation in MOCVD GaAs. *J. Cryst. Growth.*, **68**, pp. 148-156 (1984).
28) Serreze, H.B. Baumann, J.A., Bunz, L., Schachter, R., and Esman, R.D.: GaAs *p-i-n* Photodiodes Made by Metalorganic Chemical Vapor Deposition Using Tertiarybutylarsine and Arsine. *Appl. Phys. Lett.*, **55**, 24, pp. 2532-2534 (1989).
29) Stolz, W., Protzmann, H., Göbel, E.O., Hostalek, M., and Pohl, L.: Alternative Precursors for the Growth of (AlGa)As/GaAs Modulation Doped Heterostructures by Metalorganic Vapour Phase Epitaxy. Proc. 17th Int. Symp. on GaAs and Related Compounds, Inst. Phys. Conf. Ser. 112, 1990, pp. 155-160.
30) Lum, R.M., Klingert, J.K., and Stevie, F.A.: Controlled Doping of GaAs Films Grown with Tertiarybutylarsine. *J. Appl. Phys.*, **67**, 10, pp. 6507-6512 (1990).
31) Kikkawa, T., Tanaka, H., and Komeno, J.: Special Issue: Proc. 5th Biennial Workshop on OMVPE; Differences in Si doping Efficiency in Tertiarybutylarsine, Monoethylarisne and Arsine for GaAs and AlGaAs Grown by MOVPE. *J. Electron. Mater.*, **21**, 3, pp. 305-315 (1992).
32) Kikkawa, T., Ohori, T., Tanaka, H., Kasai, K., and

Komeno, J.: Effective Si Planar Doping of GaAs by MOVPE Using Tertiarybutylarsine. *J. Cryst. Growth*, **115**, pp. 448-454 (1991).

33) Pogge, H.B., and Kemlage, B.M.: Doping Behavior of Silicon in Vapor-Grown III-V Epitaxial Films. *J. Cryst. Growth*, **31**, pp. 183-189 (1975).

34) Bass, S.J.: Silicon and Germanium Doping of Epitaxial Gallium Arsenide Grown by the Trimethylgallium-Arsine Method. *J. Cryst. Growth*, **47**, 4, pp. 613-618 (1979).

35) Duchemin, J.P., Bonnet, M., Koelsch, F., and Huyghe, D.: A New Method for the Growth of GaAs Epilayer at Low H_2 Pressure. *J. Cryst. Growth*, **45**, pp. 181-186 (1978).

36) Druminski, M., Wolf, H.-D., Zshauer, K.-H., and Wittmaack, K.: Unexpectedly High Energy Photoluminescence of Highly Si Doped GaAs Grown by MOVPE. *J. Cryst. Growth*, **57**, 2, pp. 318-324 (1982).

37) Ohno, H., Ikeda, E., and Hasegawa, H.: Planar Doping by Interrupted MOVPE Growth of GaAs. *J. Cryst. Growth*, **68**, pp. 15-20 (1984).

38) Kuech, T.F., Veuhoff, E., and Meyerson, B.S.: Silicon Doping of GaAs and AlGaAs Using Disilane in Metalorganic Chemical Vapor Deposition. *J. Cryst. Growth*, **68**, 1, pp. 48-53 (1984).

39) Azoulay, R., Dugrand, L., Ankri, D., and Rao, E.V.K.: MOCVD n-type Doping of GaAs and AlGaAs Using Silicon and Selenium and Fabrication of Double Heterostructure Bipolar Transistor. *J. Cryst. Growth*, **68**, pp. 453-460 (1984).

40) Veuhoff, E., Kuech, T.F., and Meyerson, B.S.: A Study of Silicon Incorporation in GaAs MOCVD Layers. *J. Electrochem. Soc.*, **132**, 8, pp. 1958-1961 (1985).

41) Stringfellow, G.B.: The Role of Impurities in III/V Semiconductors Grown by Organometallic Vapor Phase Epitaxy. *J. Cryst. Growth*, **75**, 1, pp. 91-100 (1986).

42) Field, R.J., and Ghandhi, S.K.: Doping of Gallium Arsenide in a Low Pressure Organometallic CVD System I. Silane. *J. Cryst. Growth*, **74**, 3, pp. 543-550 (1986).

43) Shimazu, M., Kamon, K., Kimura, K., Mashita, M., Mihara, M., and Ishii, M.: Silicon Doping Using Disilane in Low-Pressure OMVPE of GaAs. *J. Cryst. Growth*, **83**, 3, pp. 327-333 (1987).

44) Liu, C.-N., Chen, S.-L., Lay, J., Lee, S.-C., and Lin, H.-H.: Characteristics of Si-Doped GaAs Epilayers Grown by Metalorganic Chemical Vapor Deposition Using a Silane Source. *Appl. Phys. Lett.*, **51**, 20, pp. 1634-1636 (1987).

45) Furuhata, N., Kakimoto, K., Yoshida, M., and Kamejima, T.: Heavily Si-Doped GaAs Grown by Metalorganic Chemical Vapor Deposition. *J. Appl. Phys.*, **64**, 9, pp. 4692-4695 (1988).

46) Moffat, H.K., Kuech, T.F., Jensen, K.F., and Wang. P.-J.: Gas Phase and Surface Reactions in Si Doping of GaAs by Silanes. *J. Cryst. Growth*, **93**, pp. 594-601 (1988).

47) Sakaguchi, H., Suzuki, R., and Meguro, T.: Systematic Study of Si and Se Doping of MOVPE GaAs. *J. Cryst. Growth*, **93**, pp. 602-606 (1988).

48) De Croon, M.H.J.M. and Giling, L.J.: Chemical Boundary Layers in MOCVD. *Prog. Crystal Growth and Charact.*, **19**, pp. 125-136 (1989).

49) Hageman, P.R., Tang, X., de Croon, M.H.J.M., and Giling, L.J.: Temperature Dependence of Silicon Doping of GaAs by SiH_4 and Si_2H_6 in Atmospheric Pressure Metalorganic Chemical Vapour Deposition. *J. Cryst. Growth*, **98**, 3, pp. 249-254 (1989).

50) Tang, X., Lochs, H.G.M., Hageman, P.R., de Croon, M.H.J.M., and Giling, L.J.: Si-Doping of MOCVD GaAs: Closer Analysis of the Incorporation Process. *J. Cryst. Growth*, **98**, 4, pp. 827-837 (1989).

51) Keizer, L.C., Tang, X., Van Meerten, R.Z.C., and Giling, L.J.: Doping of Gallium Arsenide in MOCVD: Equilibrium Calculations. *J. Cryst. Growth*, **102**, pp. 667-677 (1990).

52) Tang, X., te Nijenhuis, J., Li, Y., and Giling, L.J.: The Influence of Substrate Orientation and Mis-Orientation on the Si-Doping of GaAs Grown by MOVPE. *J. Cryst. Growth*, **107**, pp. 263-267 (1991).

53) Lum, R.M., Klingert, J.K., Ren, F., and Shah, N.J.: Epitaxial Growth of n^+-n GaAs Metal-Semiconductor Field-Effect Transistor Structures Using Tertiarybutylarsine. *Appl. Phys. Lett.*, **56**, 4, pp. 379-381 (1990).

54) Baumann, J.A., Michel, C., Marek, H., Serreze, H.B., and Schachter, R.: High Temperature MOVPE Growth of GaAs/AlGaAs Device Structures with Tertiarybutylarsine. *J. Electron. Mater.*, **19**, 4, pp. 363-366 (1990).

55) Baker, D.M., Duncan, W.J., Learmouth, M.D., and Lynch, T.G.: High-Quality GaInAs Photodiodes Grown Using Tertiarybutylarsine by Atmospheric-Pressure MOVPE. *Electron. Lett.*, **25**, 23, pp. 1598-1600 (1989).

56) Kuramata, A., Kobayashi, H., Ogita, S., and Yamazaki, S.: Fabrication of InGaAsP Laserdiodes Grown by MOVPE Using Tertiarybutylarsine and Tertiarybutylphosphine. Proc. 18th Int. Symp. on GaAs and Related Compounds, Inst. Phys. Conf. Ser. (to be published 1992).
57) Duncan, W.J., Baker, D.M., Harlow, M., English, A., Burness, A.L., and Haigh, J.: BH Lasers with GaInAsP and GaInAs Active Layers Grown by MOVPE Using Tertiarybutylarsine and Tertiarybutylphosphine. *Electron. Lett.*, **25**, 23, pp. 1603-1604 (1989).
58) Miller, B.I., Young, M.G., Oron, M., Koren, U., and Kisker, D.: High Quality Long-Wavelength Lasers Grown by Atmospheric Organometallic Vapor Phase Epitaxy Using Tertiarybutylarsine. *Appl. Phys. Lett.*, **56**, 15, pp. 1439-1441 (1990).
59) Hummel, S.G., Beyler, C.A., Zou, Y., Grodzinski, P., and Dapkus, P.D.: Use of Tertiarybutylarsine in the Fabrication of GaAs/AlGaAs Quantum Wells and Quantum Well Lasers. *Appl. Phys. Lett.*, **57**, 7, pp. 695-697 (1990).
60) Sundaram, V.S., Arau, B.A., Avery, J.E., Bailey, A.L., Girarad, G.R., Hager, H.E., Thompson, A.G., and Fraas, L.M.: Tertiary Butylarsine Grown GaAs Solar Cell. *Appl. Phys. Lett.*, **54**, 7, pp. 671-673 (1989).
61) Sundaram, V.S., Mao, B.-Y., Zurek, S.J., Levy, H.M., Lee, G.Y., and Fraas, L.M.: High Performance 0.5 and 0.25 μm Gate MESFET Grown by MOCVD Using Tertiarybutylarsine. Mater. Res. Soc. Symp. Proc., **204**, 1991, pp. 123-127.
62) Okabe, T., Kikkawa, T., Tanaka, H., Takikawa, M., and Komeno, J.: Growth Temperature Dependence of EL2 Concentration in GaAs Grown by Metalorganic Vapor-Phase Epitaxy Using Tertiarybutylarsine. *J. Appl. Phys.*, **68**, 8, pp. 4064-4067 (1990).
63) Kikkawa, T., Ohori, T., Mitani, E., Suzuki, M., Tanaka, H., and Komeno, J.: AlGaAs/GaAs and AlGaAs/InGaAs/GaAs High Electron Mobility Transistors Grown by Metalorganic Vapor Phase Epitaxy Using Tertiarybutylarsine. *Jpn. J. Appl. Phys.*, **30**, 10A, pp. L1718-L1721 (1991).
64) Tanaka, H., Kikkawa, T., Kasai, K., and Komeno, J.: MOVPE Growth of Selectively Doped AlGaAs/GaAs Heterostructures with Tertiarybutylarsine. *Jpn. J. Appl. Phys.*, **28**, 5, pp. L901-L903 (1989).
65) Abe, M., Mimura, T., Kobayashi, N., Suzuki, M., Kosugi, M., Nakayama, M., Odani, K., and Hanyu, I.: Recent Advances in Ultrahigh-Speed HEMT LSI Technology. *IEEE Trans. Electron Devices*, **ED-36**, 10, pp. 2021-2031 (1989).
66) Awano, Y., Kosugi, M., Kosemura, K., Mimura, T., and Abe, M.: Short-Channel Effects in Subquarter-Micrometer-Gate HEMTs: Simulation and Experiment. *IEEE Trans. Electron. Devices*, **ED-36**, 10, pp. 2260-2266 (1989).
67) Okamoto, A., Toyoshima, H., and Ohata, K.: Strained N-$Ga_{0.7}Al_{0.3}As/In_xGa_{1-x}As$/GaAs Modulation-Doped Structures. *Jpn. J. Appl. Phys.*, **26**, 4, pp. 539-542 (1987).
68) Pan, N., Carter, J., Zheng, X.L., Hendriks, H., Hoke, W.E., Feng, M.S., and Hsieh, K.C.: Growth of Pseudomorphic High Electron Mobility Heterostructures by Atmospheric Pressure Metalorganic Chemical Vapor Deposition. *Appl. Phys. Lett.*, **56**, 3, pp. 274-276 (1990).
69) Tanaka, H., Itoh, H., Ohori, T., Takikawa, M., Kasai, K., Takechi, M., Suzuki, M., and Komeno, J.: Multi-Wafer Growth of HEMT LSI Quality AlGaAs/GaAs Heterostructures by MOCVD. *Jpn. J. Appl. Phys.*, **26**, 9, pp. L1456-L1458 (1987).
70) American Cyanamid Company: Application Note. No. 1, (1987).
71) Morton International: Vapor Pressure Data. (1991).
72) Frijlink, P.M.: A New Versatile, Large Size MOVPE Reactor. *J. Cryst. Growth.*, **93**, pp. 207-215 (1988).
73) Lang, D.V.: Deep-Level Transient Spectroscopy: A New Method to Characterize Traps in Semiconductors. *J. Appl. Phys.*, **45**, 7, pp. 3023-3032 (1974).
74) Baliga, B.J., Bhat, R., and Ghandhi, S.K.: Composition Dependence of Energy Gap in GaInAs Alloys. *J. Appl. Phys.*, **46**, 10, p. 4608 (1975).
75) Williams, E.W., and Bebb, H.B.: "5. Photoluminescence II: Gallium Arsenide". Semiconductors and Semimetals, Vol. 8, New York and London, Academic Press, 1972, pp. 321-392.
76) Leys, M.R., and Veenvliet, H.: A Study of the Growth Mechanism of Epitaxial GaAs as Grown by the Technique of Metal Organic Vapor Phase Epitaxy. *J. Cryst. Growth.*, **55**, pp. 145-153 (1981).
77) Nishizawa, J., and Kurabayashi, T.: On the Reaction Mechanism of GaAs MOCVD. *J. Electrochem. Soc.*, **130**, 2, pp. 413-417 (1983).
78) Larsen, C.A., Buchan, N.I., and Stringfellow, G.B.: Reaction Mechanisms in the Organometallic Vapor Phase Epitaxial Growth of GaAs. *Appl. Phys. Lett.*, **52**, 6, pp. 480-482 (1988).
79) Aspnes, D.E., Colas, E., Studna, A.A., Bhat, R., Koza, M.A. and Keramidas, V.G.: Kinetic Limits of Monolayer Growth on (001) GaAs by Organometallic

Chemical-Vapor Deposition. *Phys. Rev. Lett.*, **61**, 24, pp. 2782-2785 (1988).

80) Komeno, J., Ohkawa, S., Miura, A., Dazai, K., and Ryuzan, O.: Variation of GaAs Epitaxial Growth Rate with Distance along Substrate within a Constant Temperature Zone. *J. Electrochem. Soc.*, **124**, 9, pp. 1440-1443 (1977).

81) Walukiewicz, W., Lagowski, J., and Gatos, H.C.: Electron Mobility in *N*-Type GaAs at 77 K; Determination of the Compensation Ratio. *J. Appl. Phys.*, **53**, 1, pp. 769-770 (1982).

82) Ishikawa, H., Shibata, H., and Kamada, M.: Excellent Uniformity of Threshold Voltage of Si Planar-Doped AlInAs/GaInAs Heterointerface Field-Effect Transistors Grown by Metalorganic Chemical Vapor Deposition. *Appl. Phys. Lett.*, **57**, 5, pp. 461-462 (1990).

83) Pan, N., Carter, J., Jackson, G.S., Hendriks, H, Huang, J.C., and Zheng, X.L.: Si Delta-Doped FET by Atmospheric Pressure Metalorganic Chemical Vapor Deposition. Proc. 17th Int. Symp. on GaAs and Related Compounds, Inst. Phys. Conf. Ser. 112, 1990, pp. 401-406.

84) Ishibashi, A., Fukano, K., and Mori, Y.: Ultra-Thin-Channelled GaAs MESFET with Double-δ-Doped Layers. *Electron. Lett.*, **24**, 16, pp. 1034-1035 (1988).

85) Schubert, E.F., Fisher, A., and Ploog, K.: The Delta-Doped Field-Effect Transistor (δFET). *IEEE Trans. Electron. Devices*, **ED-33**, 5, pp. 625-632 (1986).

86) Stringfellow, G.B.: "3. Thermodynamics". Organometallic Vapor-Phase Epitaxy Theory and Practice, 1st ed., New York and London, Academic Press, 1989, pp. 126-132.

87) Purnell, J.H. and Walsh, R.: The Pyrolysis of Monosilane. *Proc. Roy. Soc. London Ser.* A, **293**, pp. 543-561 (1966).

88) Newman, C.G., O'Neal, H.E., Ring, M.A., Leska, F., and Shipley, N.: Kinetics and Mechanism of Silane Decomposition. *Inter. J. Chem. Kinet.*, **11**, 6, pp. 1168-1182 (1979).

89) Dzarnoski, J. Rickborn, S.F., O'Neal, H.E., and Ring, M.A.: Shock-Induced Kinetics of the Disilane Decomposition and Silylene reactions with trimethylsilane and butadiene. *Organometallics*, **1**, pp. 241-242 (1982).

90) O'Keefe, J.F., and Lampe, F.W.: Spectroscopic Detection of Silylene in the Infrared Multiphoton Decomposition of Silane. *Appl. Phys. Lett.*, **42**, 3, pp. 217-219 (1983).

91) Robertson, R., Hills, D., and Gallagher, A.: Silane Pyrolysis. *Chem. Phys. Lett.*, **103**, 4, pp. 397-404 (1984).

92) Inoue, G., and Suzuki, M.: Reactons of $SiH_2(X^1A_1)$ with H_2, CH_4, SiH_4 and Si_2H_6 at 298 K. *Chem. Phys. Lett.*, **122**, 4, pp. 361-364 (1985).

93) Gordon, M.S., Gano, D.R., Binkley, J.S., and Frisch, M.J.: Thermal Decomposition of Silane. *J. Amer. Chem. Soc.*, **108**, 4, pp. 2191-2195 (1986).

94) Meyerson, B.S., and Jasinski, J.M.: Silane Pyrolysis Rates for the Modeling of Chemical Vapor Deposition. *J. Appl. Phys.*, **61**, 2, pp. 785-787 (1987).

95) Roenigk, K.F., Jensen, K.F., and Carr, R.W.: Rice-Ramsperger-Kassel-Marcus Theoretical Prediction of High-Pressure Arrhenius Parameters by Nonlinear Regression: Application to Silane and Disilane Decomposition. *J. Phys. Chem.* **91**, 22, pp. 5732-5739 (1987).

96) Farrow, R.F.: The Kinetics of Silicon Deposition on Silicon by Pyrolysis of Silane. *J. Electrochem. Soc.*, **121**, 7, pp. 899-907 (1974).

97) Coltrin, M.E., Kee, R.J., and Miller, J.A.: A Mathermatical Model of Silicon Chemical Vapor Deposition. *J. Electrochem. Soc.*, **133**, 6, pp. 1206-1213 (1986).

98) Moffat, H.K., and Jensen, K.F.: Three-Dimensional Flow Effects in Silicon CVD in Horizontal Reactors. *J. Electrochem. Soc.*, **135**, 2, pp. 459-471 (1988).

99) Tirtowidjojo, M., and Pollard, R.: Elementary Process and Rate-Limiting Factors in MOVPE of GaAs. *J. Cryst. Growth*, **93**, pp. 108-114 (1988).

100) Tirtowidjojo, M., and Pollard, R.: The Influence of Reacor Pressure on Rate-Limiting Factors and Reaction Pathways in MOVPE of GaAs. *J. Cryst. Growth*, **98**, 3, pp. 420-438 (1989).

101) Buchan, N.I., and Jasinski, J.M.: Calculation of Unimolecular Rate Constants for Common Metalorganic Vapor Phase Epitaxy Precursors via RRKM Theory. *J. Cryst. Growth*, **106**, 2/3, pp. 227-238 (1990).

102) Giling, L.J., and de Croon, M.H.J.M.: Surface Process During Growth of GaAs by MOCVD. *J. Cryst. Growth*, **107**, pp. 56-61 (1991).

103) Coltrin, M.E., and Kee. R.J.: A Mathematical Model of the Gas-Phase and Surface Chemistry in GaAs MOCVD. Mater. Res. Soc. Symp. Proc., Vol. 145, 1989, pp. 119-124.

104) Jensen, K.F., Fotiadis, D.I., and Mountziaris, T.J.: Detailed Models of the MOVPE Process. *J. Cryst. Growth*, **107**, pp. 1-11 (1991).

105) Fotiadis, D.I., Boekholt, M., Jensen, K.F., and Richter, W.: Flow and Heat Transfer in CVD Reactors: Comparison of Raman Temperature

Measurements and Finite Element Model Predictions. *J. Cryst. Growth,* **100**, pp. 577-599 (1990).
106) Fotiadis, D.I., Kieda, S., and Jensen, K.F.: Transport Phenomena in Vertical Reactors for Metalorganic Vapor Phase Epitaxy-I. Effects of heat transfer characteristics, reactor geometry, and operating conditions. *J. Cryst. Growth,* **102**, pp. 441-470 (1990).
107) Tanaka, H., and Komeno, J.: Gas Phase Reactions in Horizontal MOCVD Reactors. Mater. Res. Soc. Symp. Proc., Vol. 94, 1987, pp. 255-259.
108) Tanaka, H., and Komeno, J.: Kinetic Simulation of Gas Phase Reactions in MOVPE Growth. *J. Cryst. Growth,* **93**, pp. 115-119 (1988).
109) Benson, S.W.: Thermochemical Kinetics. 2nd ed., New York, Wiley-Interscience, 1976, 320p.
110) Speckman, D.M., and Wendt, J.K.: Organoarsine Pyrolysis Mechanisms and Their Influence on GaAs Epilayer Purity. *J. Appl. Phys.,* **69**, 5, pp. 3316-3323 (1991).
111) Mountziaris, T.J., Ingle, N.K., and Kalyanasundaram, S.: Modeling of Gas-Phase and Surface Kinetics in MOVPE of GaAs and $Al_xGa_{1-x}As$. Mater. Res. Soc. Symp. Proc., Vol. 204, 1991, pp. 219-224.
112) Saalfeld, F.E., and McDowell, M.V.: The Mass Spectra of Volatile Hydrides. V. Silylarsine. *Inorganic Chemistry,* **6**, 1, pp. 96-98 (1967).
113) Belkowitz, J.: Photoionization Mass Spectrometric Studies of AsH_n (n = 1-3). *J. Chem. Phys.,* **89**, 12, pp. 7065-7076 (1988).
114) Asai, H.: Anisotropic Lateral Growth in GaAs MOCVD Layers on (001) Substrates. *J. Cryst. Growth,* **80**, 2, pp. 425-433 (1987).
115) Ashby, A., Roberts, G.G., Ashen, D.J., and Mullin, J.B.: Non Extrinsic Conduction in Semi-Insulating GaAs. *Solid State Commun.,* **20**, pp. 61-63 (1976).
116) Sakai, K., and Ikoma, T.: Deep Levels in GaAs by Capacitance Methods. *Appl. Phys.,* **5**, pp. 165-171 (1974).
117) Lang. D.V., and Logan, R.A.: A Study of Deep Levels in GaAs by Capacitance Spectroscopy. *J. Electron. Mater.,* **4**, 5, pp. 1053-1066 (1975).
118) Martin, G.M., Mitonneau, A., and Mircea, A.: Electron Traps in Bulk and Epitaxial GaAs Crystals. *Electron. Lett.,* **13**, 7, pp. 191-193 (1977).
119) Lagowski, J., Gatos, H.C., Parsey, J.M., Wada, K., Kaminska, M., and Walukiewicz, W.: Origin of the 0.82-eV Electron Trap in GaAs and Its annihilation by Shallow Donors. *Appl. Phys. Lett.,* **40**, 4, pp. 342-344 (1982).
120) Wada, K., and Inoue, N.: Effects of Heat Treatments of GaAs on the Near-Surface Distribution of EL2 Defects. *Appl. Phys. Lett.,* **47**, 9, pp. 945-947 (1985).
121) Bhattacharya, P.K., Ku, J.W., Owen, S.J.T., Aebi, V., Cooper, III, C.B., and Moon R.l.: The Trend of Deep States in Organometallic Vapor-Phase Epitaxial GaAs with Varying As/Ga Ratios. *Appl. Phys. Lett.,* **36**, 4, pp. 304-306 (1980).
122) Neave, J.H., Blood, P., and Joyce, B.A.: A Correlation between Electron Traps and Growth Processes in N-GaAs Prepared by Molecular Beam Epitaxy. *Appl. Phys. Lett.,* **36**, 4, pp. 311-312 (1980).
123) Stringfellow, G.B.: "2. Source Molecules". Organometallic Vapor-Phase Epitaxy Theory and Practice, 1st ed., New York and London, Academic Press, 1989, pp. 26-29.
124) Giling, L.J.: Gas Flow Patterns in Horizontal Epitaxial Reactor Cells Observed by Interference Holography. *J. Electrochem. Soc.,* **129**, 3, pp. 634-644 (1982).
125) Visser, E.P., Kleijn, C.R., Govers, C.A. M., Hoogendoorn, C.J., and Giling, L.J.: Return Flows in Horizontal MOCVD Reactors Studied with the Use of TiO_2 Particle Injection and Numerical Calculations. *J. Cryst. Growth,* **94**, 4, pp. 929-946 (1989).
126) Puetz, N., Hillier, G., and Springthorpe, A.J.: The Inverted Horizontal Reactor: Growth of Uniform InP and GaInAs by LPMOCVD. *J. Electron. Mater.,* **17**, 5, pp. 381-386 (1988).
127) Agnello, P.D., and Ghandhi, S.K.: A Mass Spectrometric Study of the Reaction of Triethylindium with Arsine Gas. *J. Electrochem. Soc.,* **135**, 6, pp. 1530-1534 (1988).

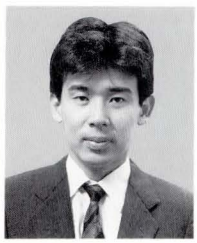

Toshihide Kikkawa

Compound Semiconductor Devices Laboratory
FUJITSU LABORATORIES, ATSUGI
Bachelor of Applied Physics Eng.
The University of Tokyo 1988
Specializing in Semiconductor Materials

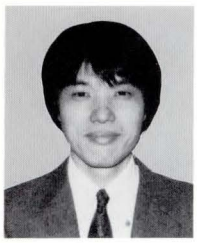

Hitoshi Tanaka

Compound Semiconductor Devices Laboratory
FUJITSU LABORATORIES, ATSUGI
Bachelor of Chemical Eng.
The University of Tokyo 1979
Dr. of Chemical Eng.
The University of Tokyo 1988
Specializing in Semiconductor Materials

Junji Komeno

Compound Semiconductor Devices Laboratory
FUJITSU LABORATORIES, ATSUGI
Bachelor of Metallurgical Eng.
Osaka University 1970
Dr. of Electrical Eng.
Osaka University 1983
Specializing in Semiconductor Materials

UDC 621.3.049.73:681.327.17

Molecular Dynamics Simulation on an AP1000 Distributed Memory Parallel Computer

• Hiroyuki Sato • Yasumasa Tanaka • Toru Yao

(Manuscript received June 6, 1991)

Parallel processing techniques have been applied to the molecular dynamics calculation module of AMBER developed by the University of California. The target machine is the AP1000 distributed memory parallel computer developed at Fujitsu Laboratories Limited. AP1000 consists of up to 1 024 processor elements connected with three different networks. To obtain a higher degree of parallelism and better load balance between processors, a particle division method was developed to randomly allocate particles to processors. Experiments showed that a problem with 41 095 atoms can be processed 226 times faster with a 512-processor AP1000 than by one processor.

1. Introduction

Molecular dynamic simulation is becoming an important technique in physics and chemistry and now plays a key role in protein engineering[1]. This technique will become more important as computer technology improves, eventually enabling the handling of larger molecules with added precision. Computing power is crucial to the analysis of proteins, and the speed and memory size of computers currently limit the size of proteins that can be studied. If we were also to consider the water molecules and counter ions surrounding a given protein and simulate biological phenomena, we would need a much faster machine.

Molecular dynamics uses Newton's equation of motion and performs an integration for each particle. This is very time consuming especially as the number of particles increases. Moreover, tens of thousands of integration steps are often necessary. For example, a 10 000-step calculation for a 40 000-atom problem would take seven days on the large-scale FUJITSU M-780 mainframe. The most time-consuming part is the force calculation, which accounts for over 90 percent of the total runtime. Vector processors have been used to speed up this calculation by factors of five to fifteen times, and have made simulation practical for small to medium-size problems. However, this is still insufficient for larger problems consisting of over ten-thousand particles.

In this paper, we study a parallel processing approach to speed up the force calculation where certain problems such as communication and load balancing must be solved. We parallelized a molecular dynamics module of AMBER[2)-4)], a widely used program for analyzing molecular dynamics and mechanics of proteins and DNAs. AMBER was developed at the University of California in San Francisco. The machine used is a highly parallel computer, a 512-processor AP1000[5),6)], developed by Fujitsu Laboratories. AP1000 accommodates up to 1 024 processor elements and has a peak performance of 8.53 GFLOPS.

2. Molecular dynamics

2.1 Molecular dynamics method

In molecular dynamics, the force on each

particle is the sum of the forces from all mutually interacting particles. Each particle is usually treated as a mass point, often having an electrical charge.

The position and velocity of each particle are calculated by numerically integrating Newton's equations of motion

$$F_i = m_i \frac{d^2 X_i}{dt^2}, \qquad \ldots\ldots\ldots\ldots\ldots (1)$$

where F_i is the force vector of particle i, m_i is the mass of particle i, X_i is the position vector of particle i, and t is the time. Force vector F_i is calculated as the summation of the gradient of potential E.

$$F_i = -\sum_{j \neq i} \Delta_i E\{X_{ij}(t)\}, \qquad \ldots\ldots\ldots\ldots (2)$$

where, $X_{ij}(t)$ is the distance between particle i and particle j at time t.

The potential energy function of AMBER is described as follows:

$$\begin{aligned} E_{\text{total}} = & \sum_{\text{bonds}} K_R (R - R_0)^2 + \sum_{\text{angles}} K_\theta (\theta - \theta_0)^2 \\ & + \sum_{\text{dihedrals}} \frac{V_n}{2} \{1.0 + \cos(n\phi - \gamma)\} \\ & + \sum_{i<j} \left(\frac{A_{ij}}{R_{ij}^{12}} - \frac{B_{ij}}{R_{ij}^{6}} + \frac{q_i q_j}{\epsilon R_{ij}} \right) \\ & + \sum_{\text{H-bonds}} \left(\frac{C_{ij}}{R_{ij}^{12}} - \frac{D_{ij}}{R_{ij}^{10}} \right). \qquad \ldots (3) \end{aligned}$$

The first three terms are for the energy of bonded atoms, and the remaining terms for nonbonded interaction by van der Waals or Coulomb energy (see Fig. 1).

Newton's equation of motion is time-integrated using the Leapfrog method[7]. The Leapfrog method is an alternate version of Verlet's method[8] and has been adopted for AMBER. It is described as below.

First, the velocity of each atom is obtained by

$$V_i(t + \frac{\Delta t}{2}) = V_i(t - \frac{\Delta t}{2}) + \Delta t \frac{F_i(t)}{m_i}. \qquad (4)$$

Then, coordinates are obtained by

$$X_i(t + \Delta t) = X_i(t) + \Delta t V_i(t + \frac{\Delta t}{2}). \qquad \ldots (5)$$

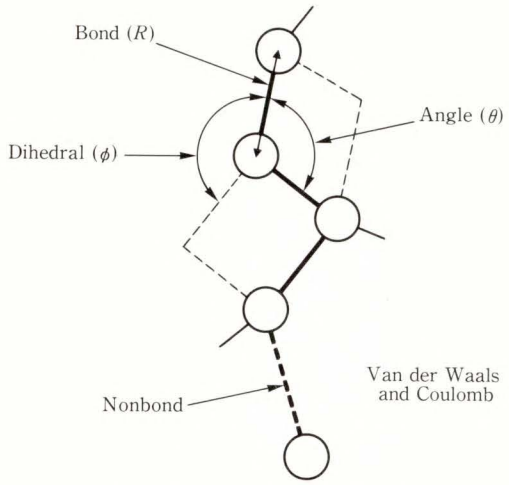

Fig. 1—Force field parameters.

The time step Δt is usually 0.5×10^{-15} s (0.5 femtoseconds), an increment obtained by considering the periodicity of the vibrating motion of bonds involving hydrogen atoms. However, this time step can be maximized to 2 femtoseconds by stopping the stretching motion of the hydrogen atoms using the SHAKE method of Ryckaert et al[9].

The scaling method[10] is used to maintain the pressure and temperature at desired values. Temperature is adjusted by scaling the velocity of atoms. Pressure is adjusted by scaling the length of each side of the basic cell that is the cubic region in which particles are held.

Initial velocity is given according to the Boltzman distribution for a given temperature. Initial coordinates are given at those of a minimum energy structure obtained through molecular mechanics.

2.2 Molecular dynamics module of AMBER

The module used to execute molecular dynamics is called MOLDYN. Figure 2 shows the program flow of the original MOLDYN module.

For calculating nonbonded forces, MOLDYN first makes a list of atom pairs, where the atom of each pair lie within the cutoff radius. This pair list generation is usually done every 20-30 time-steps. Bond connection information is used for bonded force calculation, and is constant throughout the calculation. Most

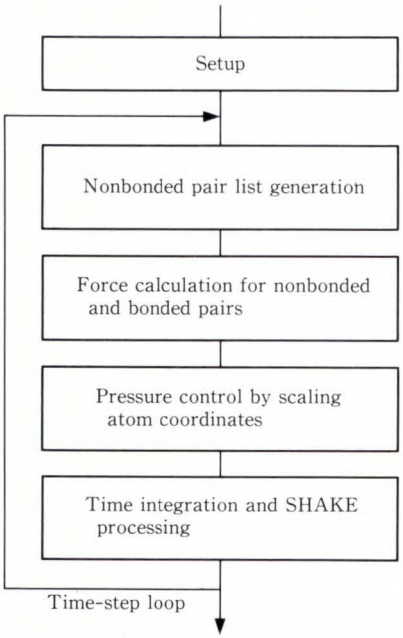

Fig. 2—Flow of original MOLDYN.

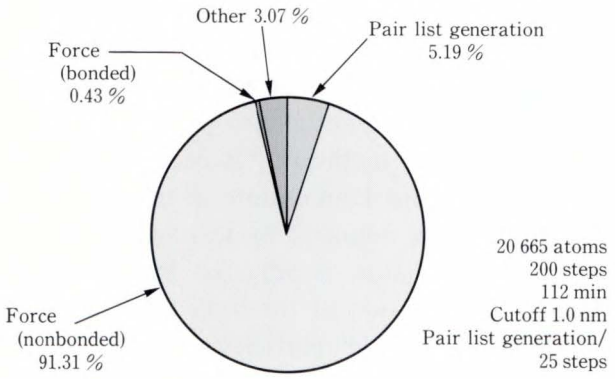

Fig. 3—Timing result of original MOLDYN on M-780.

of the computing time is spent calculating nonbonded forces. Ninety-one percent of the calculation time is spent executing 200 time-steps of dynamics for a 20 665-atom problem (see Fig. 3).

3. Parallelization of molecular dynamics

3.1 AP1000 architecture

Figure 4 shows the architecture of the AP1000 and Table 1 lists the specifications. Processor elements, called cells, are connected with three networks, called the broadcast network (B-net), torus network (T-net), and synchronization network (S-net). A SUN 4-workstation host controls the AP1000.

The host, or any cell, can broadcast data to

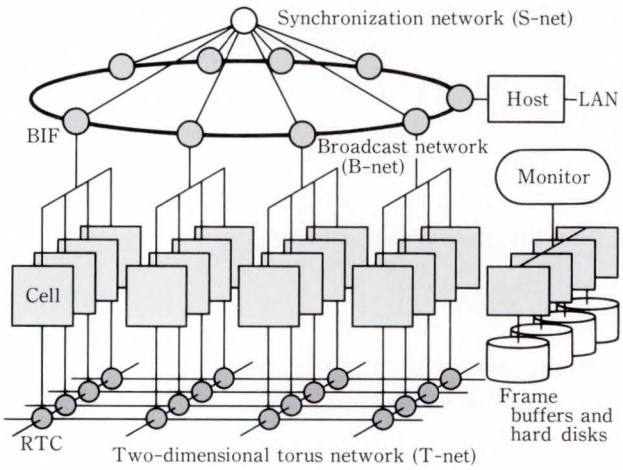

Cell : Cell processor BIF : Broadcast network interface
RTC : Routing controller

Fig. 4—AP1000 architecture.

Table 1. AP1000 specifications

Item		Specifications
System	Architecture	Distributed memory, MIMD parallel computer
	Number of processors	64-1 024 cells (0.53-8.53 GFLOPS)
S-net	Structure	Tree
	Function	Barrier synchronization and satus (40 events)
B-net	Structure	Ring + hierarchical bus (50 Mbyte/s)
	Function	Broadcast, scattering, and gathering
T-net	Structure	Two-dimensional torus (25 Mbyte/s)
	Routing method	Wormhole routing with structured buffer pool
	Special function	Broadcast to specified cells

MIMD: Multiple instruction stream multiple data stream

all cells through the B-net, which is implemented with a ring and hierarchical connections. It also scatters and gathers data to and from cells directly by hardware. The broadcast network interface (BIF) chip handles these functions. The peak transfer rate is 50 Mbyte/s.

The T-net is used for communication between any two cells. The topology is a two-dimensional mesh with boudary wires connected to the other sides. The routing controller (RTC) on each mesh point performs automatic message routing using wormhole routing and a structured

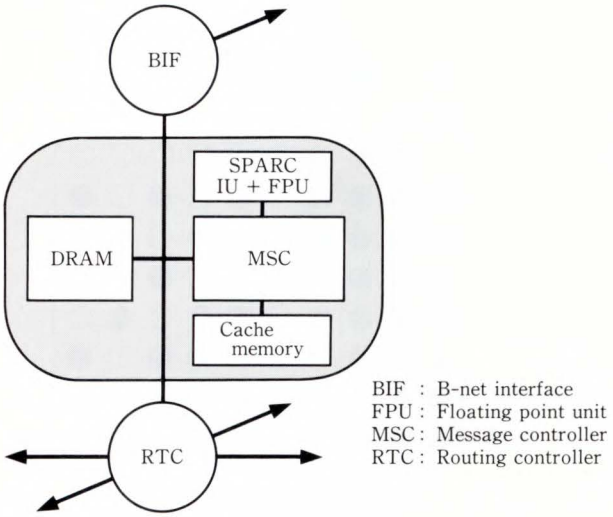

Fig. 5—Cell processor configuration.

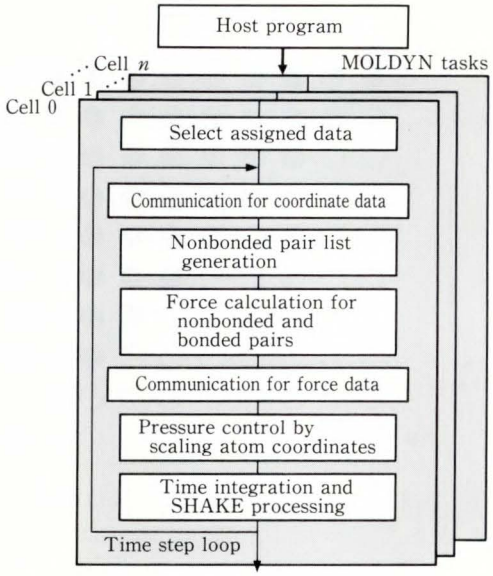

Fig. 6—Program structure of MOLDYN.

buffer pool algorithm. The transfer speed is 25 Mbyte/s per channel.

Figure 5 shows the configuration of a cell processor, which consists of a 25 MHz SPARC integer unit (IU) with a Weitek 3170 floating-point processor, 128 Kbyte of cache memory, and communication devices. The message controller (MSC) supports DMA transfer functions.

The AP1000 software runs under Cell OS[5] which resides in all cells and schedules multiple tasks in cells. The application software is written in C and FORTRAN, and communication and synchronization functions are provided as callable functions. An application program consists of the host program and various cell tasks.

4. Implementation of particle division method

The MOLDYN module was parallelized using the particle division method which partitions the ensemble of atoms into groups and assigns them to processors. This method makes it possible to use more than several hundred processors for large problems which contain more than several thousand atoms. A degree of parallelism (the number of atoms) much greater than the number of processors is used to balance the load by assigning randomly selected multiple atoms to processors. The calculation load is evenly distributed in a statistical sense by this allocation method.

4.1 Structure of the parallelized MOLDYN

Figure 6 shows the program structure of AMBER converted for use on parallel machines. The original MOLDYN program was split into host and cell task programs. The host program sets up initial data and broadcasts them to all cells. The time-step loop is performed in cells without host program intervention.

4.2 Data division and allocation.

Data is broadcast from the host program to all cells. Each cell selects the data necessary for itself and discards any unnecessary data. Model data consists of protein molecules and many water molecules as solvent. We chose residues of proteins and water molecule as units of data allocation because they are treated as units in MOLDYN. These are called submolecules. Residues and water molecules are distributed to cells in such a way that each cell holds an equal number of residues and water molecules.

A bond list of atoms is read at the beginning of calculation from the input file and distributed to cells. This information does not change throughout the molecular dynamics calculation.

4.3 Nonbonded pair list generation

A nonbonded pair list is generated for assigned residues and water molecules. A cutoff

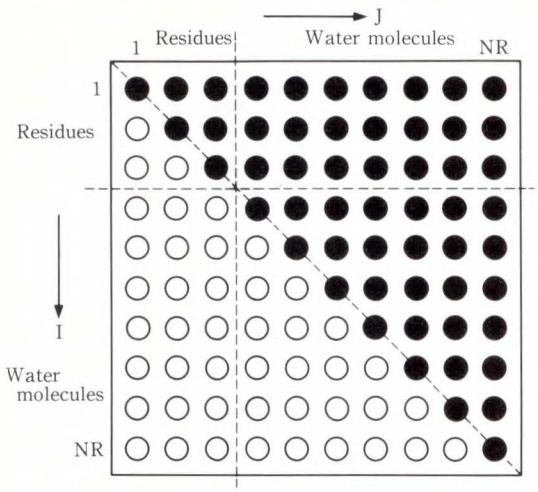

Fig. 7—Selection of submolecule pairs (original).

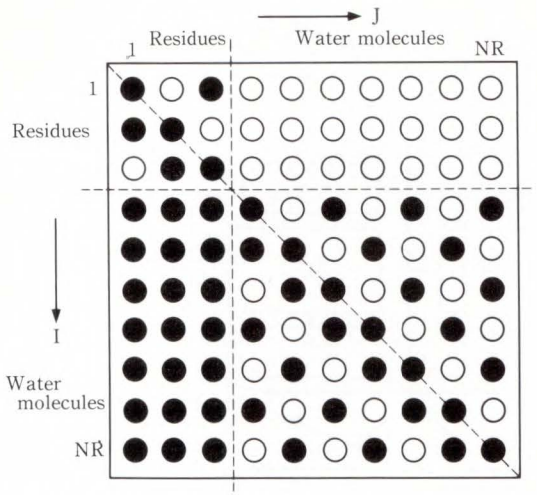

Fig. 8—Selection of submolecule pairs (parallel version).

distance check is not done between individual atoms but instead is done between submolecules (residues or water molecules). If the minimum of the distances of all atom pair between two submolecules is less than the cutoff radius, all the pairs are registered in the pair list. This is called residue-based pair list generation and is often used in the MOLDYN program.

In the original code, the pair-list is generated by nested DO loops indexed by submolecule numbers as shown below (see Fig. 7).

```
DO I = 1, NR
        DO J = I, NR
        Check minimum distance between
        submolecules I and I
        IF distance < cutoff
            THEN generate pair list between
            atoms in two submolecules
        END DO
END DO
```

where NR is the total number of residues and water molecules.

Before parallelizing MOLDYN, this code is changed to

```
DO I = 1, NR
        DO J = 1, NR
        Check minimum distance between
        submolecules I and J
        IF distance < cutoff
            THEN generate pair list between
            atoms in two submolecules
        END DO
END DO
```

When this nested loop is executed, each submolecule pair is checked twice. We avoided this using a selection rule determined by considering even load distribution. It is shown in Fig. 8.

In Fig. 8, circles show pairs of submolecules I and J. Pairs shown as black circles are selected and white ones are discarded for distance checking. For residue-residue and water-water pairs (circles in the top-left and right-bottom rectangle areas in Fig. 8), even numbered pairs (I + J is an even integer) are selected when I is less than J, odd numbered pairs (I + J is an odd integer) are selected when I is greater than J. When I is equal to J, the pair is always selected.

The changed code is then parallelized by breaking up outer DO loop index I into segments and assigning them to processors. In other words, each processor executes a different set of rows in Fig. 8.

The distance check of submolecules I and J is done by the processor assigned to the submolecule. If the distance is less than the cutoff, atom pairs between the submolecule pair are registered in the pair list in each cell for later force calculation. Cyclic allocation of submolecules to processors (submolecule I is assigned to processor K = I modulo P, where P is the total number of processors) allows the number of nonbonded atom pairs to be distributed fairly evenly.

The coordinate data of all atoms are stored in each cell for pair list generation (performed every 20-30 time steps) and force calculation. Coordinate data of all atoms can be collected efficiently by broadcasting data assigned to each cell to all other cells through the B-net. As a result, each cell holds a copy of the coordinate data for all atoms. The amount of coordinate data sent is 48 bytes (6 double precision words) per atom.

4.4 Force calculation and summation

The force between two atoms is accumulated to form the force data for each individual atom. One of these two atoms is possibly assigned to another cell. After force calculation is finished, this force data is sent to cells to which interacting atoms are assigned (see Fig. 9). This point-to-point (cell-to-cell) communication is done using the T-net. Force data to be sent to the same atom is summed up before being sent. This reduces the amount of data sent.

There are 24 bytes (3 double-precision words) of force data per atom. The amount of force data sent to other cells depends on the number of interacting atoms allocated to other cells.

4.5 Visualization

The AP1000 can be used to display simulation results. A parallel display program was also developed to show atoms and bonds as full-color images.

The visualization software consists of two types of tasks. OBJECT tasks receive geometric data from MOLDYN tasks and generate images of shaded spheres and lines with z values (distance from the eye point). Generated images are redistributed to IMAGE tasks which remove hidden surfaces using the z-buffer algrorithm. Image space is divided and processed in the IMAGE tasks[11), 12)] (see Fig. 10). Running this program concurrently with MOLDYN makes possible the visual simulation of molecular

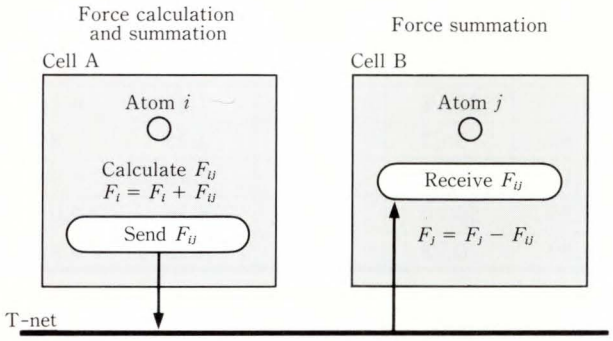

Fig. 9—Force calculation and summation.

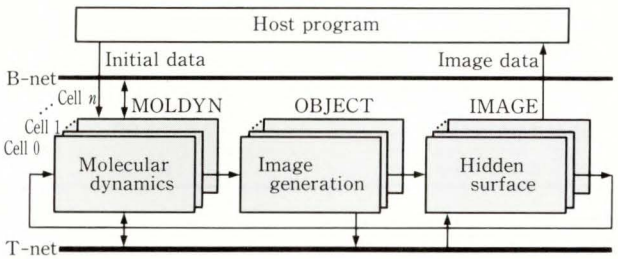

Fig. 10—Visual simulation program.

Table 2. Test model data

Data item \ Test model	Lysozyme-A	Lysozyme-B	Hemoglobin
Protein	Lysozyme	Lysozyme	Hemoglobin
Atoms (total)	20665	41095	88384
Atoms (protein)	2041	2041	9082
Atoms (water)	18624	39024	79302
Residues	130	130	578
Water molecules	6208	13008	26434
Box size (mm)	7.03 x 5.89 x 5.44	7.51 x 7.51 x 7.51	11.26 x 11.26 x 11.26
Cut-off radius (nm)	1.00	1.00	1.00
Cut-off checking	residue base	residue base	residue base
Pair list generation interval	every 25 steps	every 25 steps	every 25 steps
Number of nonbonded pairs (initial)	4711181	8965917	18888552

dynamics. Computer animation can easily be produced by recording generated images.

5. Experiments

5.1 Test data

We used three problems to evaluate the performance of MOLDYN. Two of them contain a human lysozyme and the other a hemoglobin at the center of a pressure control cubic box filled with water molecules. Human lysozymes consist of 130 residues and hemoglobin 578. The sizes of cubes and the number of water molecules are different between these three data items (see Table 2). These problems were also solved using an M-780 for comparison. Average execution times per time step are listed in Table 5.

5.2 Results and performance analysis

We experimented with these model problems using the AP1000 with 512 cells. Tables 3 and 4 list the timing results for a single time step. Experiments using less than 512 cells were also done using subsets of the 512 cells. Communica-

Table 3. Timing results of Lysozyme-A

Results \ Number of cells	1*	16*	32	64	128	256	512
Pair list generation (s)	971.80	60.74	30.37	16.56	8.65	4.96	2.31
Nonbonded force calculation (s)	265.30	16.58	8.29	4.15	2.08	1.04	0.52
Other calculation (s)	10.60	0.66	0.33	0.20	0.13	0.07	0.04
Communication (total) (s)	0	0.79	0.77	0.72	0.68	0.78	0.96
Coordinate data (s)	0	0.30	0.30	0.31	0.32	0.35	0.41
Force summation (s)	0	0.40	0.38	0.31	0.24	0.21	0.13
Other (s)	0	0.09	0.09	0.10	0.11	0.22	0.42
Idle time (s)	0	0.50	0.49	0.55	0.30	0.36	0.32
Step time (with pair list gen.) (s)	1 247.70	79.27	40.21	22.18	11.80	7.21	4.16
Step time (s)	275.90	18.53	9.89	5.62	3.19	2.25	1.85
Average step time (s)	314.77	20.96	11.10	6.28	3.53	2.45	1.94
Speed-up ratio	1.00	15.02	28.35	50.10	89.06	128.56	162.05
Efficiency (%)	100.00	0.94	0.89	0.78	0.70	0.50	0.32

Table 4. Timing results of Lysozyme-B

Results \ Number of cells	1*	16*	32*	64	128	256	512
Pair list generation(s)	3 764.00	235.00	118.00	58.81	30.20	11.56	8.24
Nonbonded force calculation (s)	506.00	31.60	15.80	7.91	3.96	1.97	0.99
Other calculation (s)	19.20	1.20	0.60	0.31	0.19	0.10	0.07
Communication (total) (s)	0	1.48	1.41	1.36	1.17	1.19	1.39
Coordinate data (s)	0	0.60	0.60	0.61	0.62	0.64	0.70
Force summation (s)	0	0.80	0.73	0.59	0.42	0.31	0.32
Other (s)	0	0.08	0.08	0.17	0.12	0.24	0.38
Idle time (s)	0	0.80	0.78	0.50	0.38	0.32	0.22
Step time (with pair list gen.) (s)	4 289.00	270.00	137.00	68.89	35.90	15.14	10.90
Step time (s)	525.00	35.08	18.59	10.08	5.70	3.58	2.66
Average step time (s)	675.56	44.48	23.33	12.43	6.91	4.04	2.99
Speed-up ratio	1.00	15.19	28.96	54.34	97.79	167.12	225.97
Efficiency (%)	100.00	0.95	0.91	0.85	0.76	0.65	0.44

*: The data for the number of cells indicated was not executable due to memory limitations; values are estimated by extrapolating experimental data.

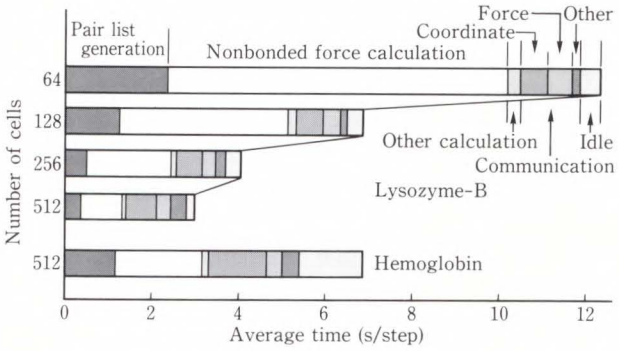

Fig. 11—Timing results of Lysozyme-B and Hemoglobin.

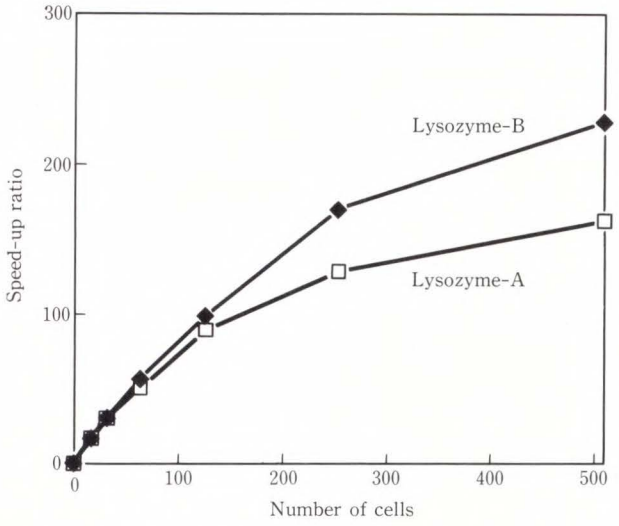

Fig. 12—Performance of MOLDYN on the AP1000.

tion time was measured for coordinate data, force data, and other communication for global summation of scalar values such as energy, weight, and minor communications.

Figure 11 shows the timing analysis of Lysozyme-B and Hemoglobin. Pair list generation and nonbonded force calculation time were efficiently decreased by increasing the number of cell processors. When a small number of cells are used, each atom interacts with atoms in almost every cell. This is because we allocated atoms randomly to processors irrespective of their coordinates. The time for sending force data decreases slightly as the number of cells increases. This shows that the number of atoms for which force data is sent decreases as the number of cells increases.

Communication time for coordinates increases slightly with the number of cells

Table 5. Performance comparison

Test model / Test system	Lysozyme-A Time(s) (Prfm. ratio)	Lysozyme-B Time(s) (Prfm. ratio)	Hemoglobin Time(s) (Prfm. ratio)	
M-780	33.57 (1.00)	66.95 (1.00)	100.00 (1.00)	
AP1000-64	6.28 (5.35)	12.43 (5.39)	NA	NA
AP1000-128	3.53 (9.51)	6.91 (9.69)	NA	NA
AP1000-256	2.45 (13.70)	4.04 (16.57)	NA	NA
AP1000-512	1.94 (17.30)	2.99 (22.39)	7.02 (14.25)	

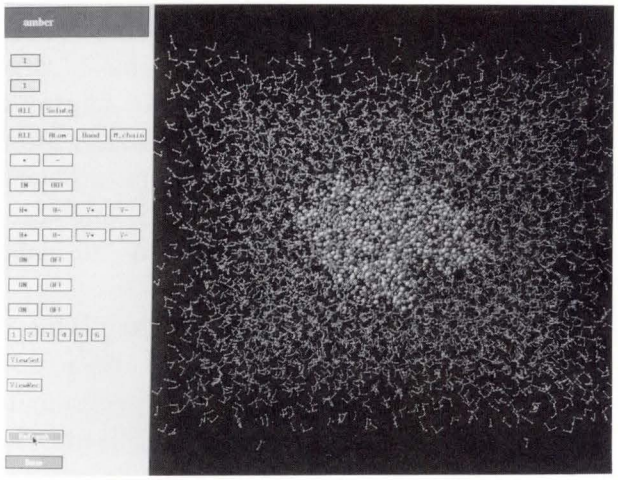

Fig. 13—Example of a generated image (Lysozyme-A).

The right hand side shows an image of the configuration of a human lysozyme molecule (center) with water molecules displayed with ball-and-stick models. The left hand side are buttons for controlling molecular dynamics simulation and visualization. Users can start and stop molecular dynamics simulation and can change the point of view, select display items (protein or/and water, main chain only or all, etc.), and display styles (ball-and-stick or stick only).

because of an increase in the broadcast communication overhead. The amount of data received by each cell is constant because coordinate data for all atoms are collected. This communication reduces the performance improvement when over 256 cell are used (see Fig. 12).

The 512-cell AP1000 executes Lysozyme-A 17.3 times faster the M-780 (see Table 5), and Lysozyme-B runs 22.4 times faster. One problem is the large memory requirement for coordinate data. Model data containing more than 100 000 atoms cannot be processed. This problem is left for future work.

Figure 13 shows a generated image for a Lysozyme-A model containing 20 665 atoms.

6. Conclusion

This paper examined parallel processing of molecular dynamics. The AMBER molecular dynamics calculation program was parallelized using a particle division technique for execution by a distributed memory parallel computer consisting of several hundred processor elements. The parallelized program was implemented on an AP1000 and tested with reasonably large problems. Using 512 processors, we improved performance by factor of 162 for a 20 665 atom problem and 226 for 41 095 atom problem. Performance was respectively 17.3 and 22.4 times faster than on the FUJITSU M-780 mainframe.

Two problems remain to be solved. One is improving performance for more than 256 processors. The sequential part of coordinate data communication must be minimized. The other is to reduce the memory requirements for coordinate data. To solve these problems, we are studying a method that avoids copying coordinate data for each cell.

References

1) Kuroki, R. et al.: Design and Creation of a Ca^{2+} Binding Site in Human Lysozyme. Proc. Natl. Acad. Sci., **USA 86**, 1989, pp. 6903-6907.
2) Weiner, P.K., and Kollman, P.A.: AMBER: Assisted Model Building with Energy Refinement. A General Program for Modeling Molecules and Their Interactions. *J. Comput. Chem.*, **2**, 3, pp. 287-303 (1981).
3) Weiner, S.J., Kollman, P.A., et al.: A new Force Field for Molecular Mechanical Simulation of Nucleic Acids and Proteins. *J. Am. Chem. Soc.* **106**, 3, pp. 765-784 (1984).
4) Weiner, S.J., and Kollman, P.A.: An All Atom Force Field for Simulations of Proteins and Nucleic Acids. *J. Comput. Chem.*, **7**, 2, pp. 230-252 (1986).
5) Ishihata, H., Horie, T., Inano, S., Shimizu, T. and Kato, S.: An Architecture of Highly Parallel Computer AP1000. Proc. IEEE Pacific Rim Conf. Commun. Comput. Signal Processing, 1991, pp. 13-16.
6) Ishihata, H., Horie, T., Inano, S., Shimizu, T., Kato, S., and Ikesaka, M.: Third Generation Message Passing Computer AP1000. Proc. Int. Symp. Supercomputing, 1991, pp. 46-55.
7) Berendsen, H.J.C., and van Gunsteren, W.F.: "Molecular Dynamics Simulations: Techniques and approaches", *Molecular Liquids – Dynamics and Interactions*, Barnes, A.J., ed., D. Reidel Publishing Company, 1984, pp. 475-500.
8) Verlet, L.: Computer "Experiments" on Classical Fluids. I. Thermodynamical Properties of Lennard-Jones Molecules. *Phys. Rev.*, **159**, 1, pp. 98-103 (1967).
9) Ryckaert, J.P., Ciccotti, G., and Berendsen, H.J.C.: Numerical Integration of the Cartesian Equation of Motion of a System with Constraints; Molecular Dynamics of N-alkane. *J. Comput. Phys.* **23**, pp. 327-341 (1977).
10) Berendsen, H.J.C. et al.: Molecular Dynamics with Coupling to an External Bath. *J. Chem. Phys.*, **81**, 8, pp. 3684-3690 (1984).
11) Ishii, M., Sato, H., Murakami, K., Ikesaka, M. and Ishihata, H.: Cellular Array Processor and Applications. *J. VLSI Signal Processing*, **1**, pp. 57-67 (1989).
12) Sato, H., Ishii, M., Sato. K., Ikesaka, M., Ishihata, H., Kakimoto, M., Hirota, K. and Inoue, K.: Fast Image Generation of Constructive Solid Geometry Using A Cellular Array Processor. *ACM Comput. Graphics*, **19**, 3, pp. 95-102 (1985).

Hiroyuki Sato

Computer-Based Systems Laboratory
FUJITSU LABORATORIES KAWASAKI
Bachelor of Electrical Eng.
Waseda University 1975
Master of Electrical Eng.
Waseda University 1977
Specializing in Parallel Processing, Scientific Computing and Visualization

Yasumasa Tanaka

Manufacturing Systems Engineering Dept.
FUJITSU LIMITED
Bachelor of Physics
Kyushu University 1972
Master of Physics
Kyushu University 1975
Specializing in Biosystems Engineering

Toru Yao

Formerly: Research Dept.
Protein Engineering Research Institute
(Presently: Systems and Computing Group
Mitsubishi Kasei Corporation)
Bachelor of Applied Physics Eng.
The University of Tokyo 1958
Specializing in Protein Engineering

UDC 548.52:621.315.5

Automated Visual Inspection System for Bonded IC Wires

• Hiroyuki Tsukahara • Masato Nakashima • Takehisa Sugawara

(Manuscript received October 31, 1991)

This paper discusses an automated visual inspection system for bonded IC wires. The system uses high-contrast image capture, an algorithm for accurately measuring the bonding balls, and a wire inspection algorithm. The high-contrast image capture system consists of a wide-area camera and two types of lighting optics, one for ball sensing and the other for wire sensing. The algorithm for measuring the bonding balls is based on morphological techniques, and the wire inspection algorithm is based on a border following algorithm. The automated inspection system measures ball diameters to within ±5 μm accuracy, which corresponds to half a pixel of the captured picture. The system takes 0.2 seconds to inspect a wire and ball. Combining the inspection system with an automatic wire bonder enables a fully automatic bonding system.

1. Introduction

Automated visual inspection is vital to wire bonding to ensure a high product yield. In the wire bonding process, gold wire 20 to 38 μm in diameter is bonded to IC pads and package leads. Gold balls 70 to 110 μm in diameter are bonded to IC pads ranging in size from 90 × 90 to 120 × 120 μm^2. One IC chip may have as many as 300 bonding points. A wire bonder bonds one wire within 0.2 seconds.

Visual inspection can detect defects in a wire and ball, and can evaluate bonding quality. The detected wire defects include broken wires, wires that are too close together and incorrect wiring paths. The ball defects that can be detected include deformation and incorrect placement. The inspection can also measure bonding location and ball deformation, which reflect the performance of a bonder. Thus, the inspection can find symptoms which cause the performance of the bonder to deteriorate. The detected symptoms are analyzed and bonding parameters, such as bonding location and force, are modified. This prevents a large number of defective ICs from being produced. Because the location tolerance is within ±10 μm, a measurement accuracy of ±5 μm is needed.

The bonding quality can be monitored by combining the inspection system and bonding system in-line. This guarantees the bonding quality, resulting in improved yield.

To achieve the objectives, a visual inspection system must meet two basic requirements:

1) Accurate evaluation of bonding quality

The ball measurement must be accurate to within ±5 μm.

2) Real-time inspection

The inspection of a wire and ball must be completed within 0.2 seconds to keep up with the wire bonder.

2. Background

Three technical problems must be solved:

1) Obtaining clear images of both the wires and balls (see Figs. 1 and 2)

The gold balls are bonded onto aluminum pads. Because both the balls and the pads are shiny, it is difficult to distinguish the ball images from the pad images.

2) Measuring ball size and shape

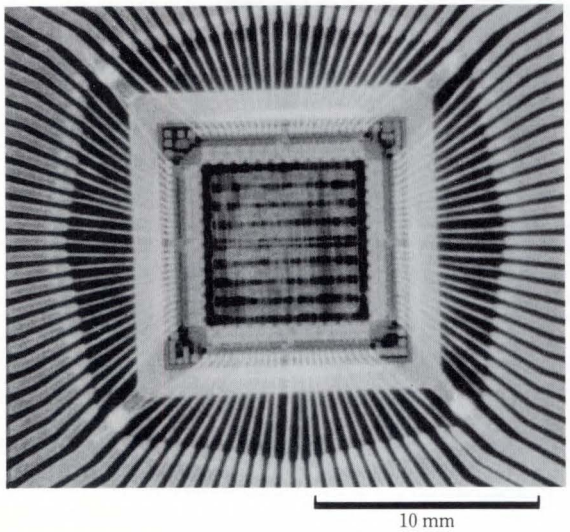

Fig.1 – Wire bonded lead-frame seen from the top.

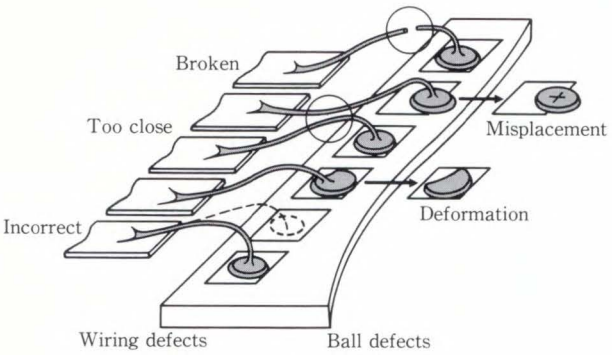

Fig.2 – Typical wire and ball defects.

Wire images overlapping the ball patterns make it difficult to measure ball shapes accurately.

3) Inspecting wire shapes

Wire paths are not completely straight, and their deviation makes it difficult to measure the distance between the wires.

To solve these problems, the authors developed high-contrast image capture, an accurate ball measurement algorithm, and a versatile wire shape inspection algorithm.

3. Image capture system

The authors developed a high-contrast wire and ball image capture system consisting of a wide-area camera and two types of lighting optics.

Table 1. Megacamera specifications

Item	Specifications
Sensor	2 048-element CCD linear sensor
Resolution	10 μm/pixel
Density	256 gray levels
Area	2 048 x 2 048 pixels (20 x 20 mm^2)
Input time	2 s

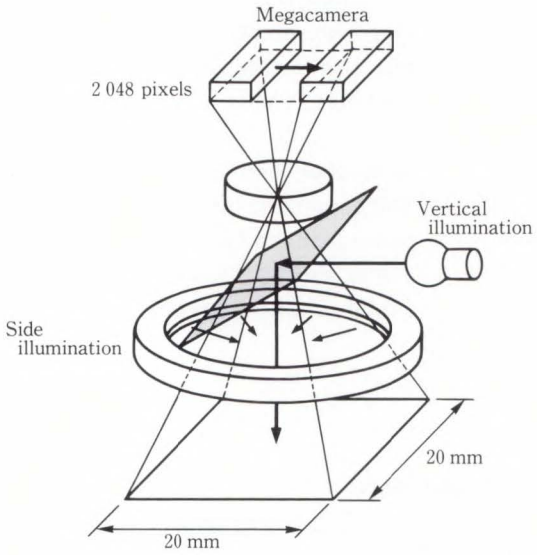

Fig.3 – High-contrast image capture system.

3.1 Wide-area camera

A wide-area camera called a megacamera[1] can capture a 2 048 x 2 048 pixel image using a mechanically operated CCD linear image sensor. Table 1 shows the specifications of this camera. The resolution is 10 μm, and the capture area is 20 x 20 mm^2. This camera can capture an image in two seconds.

3.2 High-contrast lighting system

High-contrast imaging is essential for correct inspection. The system uses two types of lighting optics. They are vertical illumination and side illumination (see Fig. 3).

Vertical illumination is used for ball pattern sensing. The light goes down to the pad and ball vertically. While the pad is flat, the ball is round, thus only the pad reflects the light back to the camera. This makes the ball image dark, and the pad image light.

Side illumination is used for wire sensing. The side illumination apparatus consists of optical fibers and a halogen lamp. Figure 4 shows the side illumination optics. Each optical fiber is arranged in a circle facing inward. The camera is set vertically above the side illumination optics and views wires through the circle. The wires are illuminated from all sides. The pad does not reflect light, but the wires do, regardless of their direction.

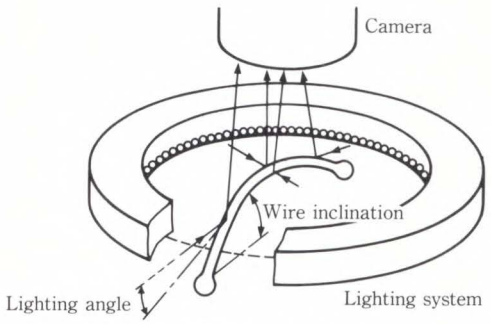

Fig.4– Side illumination optics.

Figure 5 shows the lighting characteristics of the side illumination optics. The wire image clarity depends on the lighting angle. This angle is defined as the angle between lighting and the horizontal plane. The solid line is a clear image boundary, and is based on experiment. As the lighting angle decreases, the range of clear images increases. Usually, the wire inclinations range from 0 to 40 degrees. The lighting angle was therefore set at 10 degrees to cover the whole angle.

Figure 6 shows the signal-to-noise ratio (SNR) of the wire images. The signal-to-noise ratio of wire images also depends on the lighting

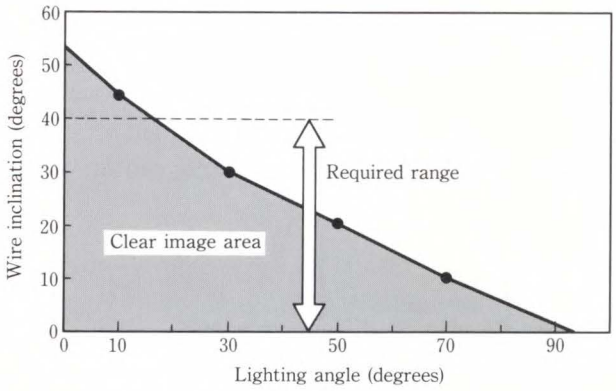

Fig.5– Lighting characteristics.

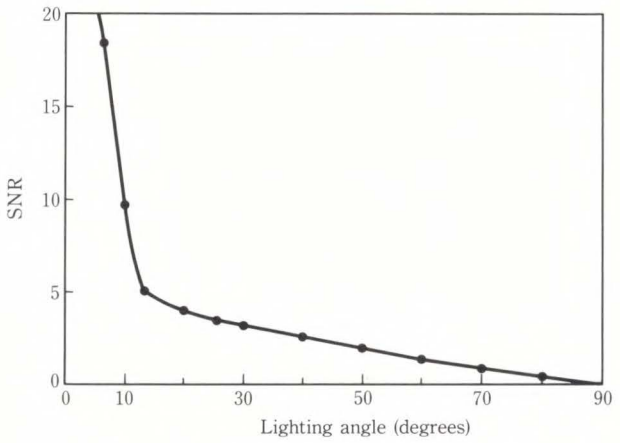

Fig.6– SNR of wire-image capture.

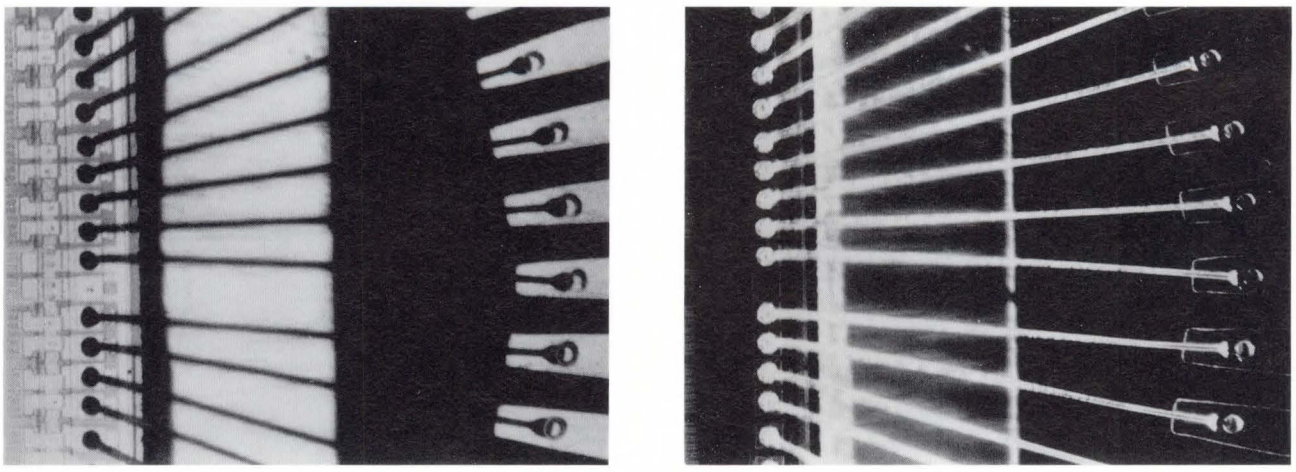

a) Vertical illumination

b) Side illumination

Fig.7– Ball and wire image.

angle. In this case, noise is caused by a chip's surface pattern. As the lighting angle decreases, the signal-to-noise ratio increases. This result indicates that a lighting angle of 10 degrees is sufficient for high contrast at an acceptable signal-to-noise ratio as well as wire image clarity.

Figure 7 is IC image taken using this illumination system. In Fig. 7a), only vertical illumination was used. The ball patterns are dark, while the pad patterns are light. In Fig. 7b), side illumination was used. The wires are clearly visible against the dark background.

4. Inspection algorithm

4.1 Ball measurement algorithm[2)]

4.1.1 Requirements for ball measurement

There are two requirements for ball measurement. The first is accurate edge detection from a low-resolution image. The resolution of the original image is 10 μm. The required accuracy for ball measurement is ± 5 μm, which corresponds to half a pixel on the original image.

The second requirement is ball outline reconstruction. With vertical illumination, as shown in Fig. 8, the wire pattern overlaps the ball. This wire pattern must be eliminated before the ball pattern diameter can be measured.

4.1.2 Edge detection

Subpixel accuracy is needed for edge detection[3),4)]. Figure 9 shows a ball edge detection technique the authors developed.

The original image, which has a resolution of 10 μm, is sensed at 256 gray levels. A finer edge pattern is produced by interpolating pixels between pixels. Given digital error, the intervals of interpolated pixels must be 2.5 μm to measure ball diameters within a ± 5 μm accuracy. The gray-level value of the interpolated pixels is calculated by the gray levels of the four nearest neighbors. Applying a Laplacian operator to the interpolated image, it is possible to produce a second-derivative image. Zero-crossing points[5)] in the second-derivative image indicate edge locations, and are detected from the ball center.

These zero-crossing points correspond to ball edges with a ± 2.5 μm accuracy. As a result, the diameter can be measured within an accuracy of ± 5 μm.

4.1.3 Reconstruction of ball outlines

Preprocessing for ball outline detection is shown in Fig. 10. The orthogonal coordinates of the ball image are transformed to polar coordinates. The origin is at the center of the

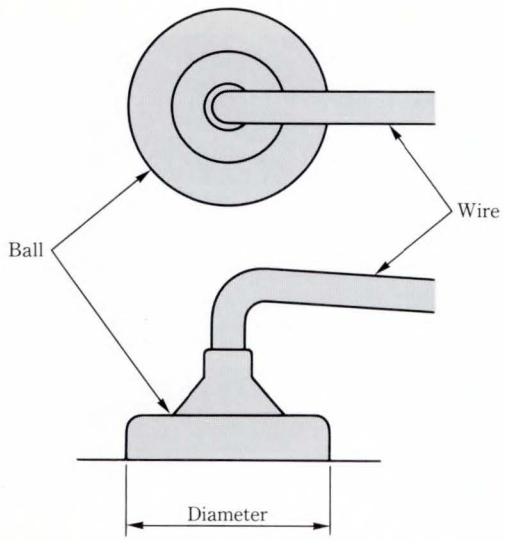

Fig.8– Side and top view of ball and wire.

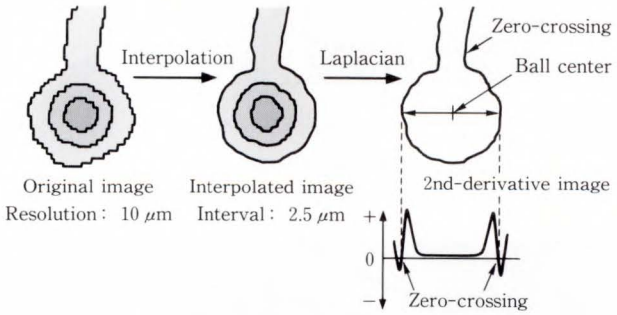

Fig.9– Edge detection algorithm.

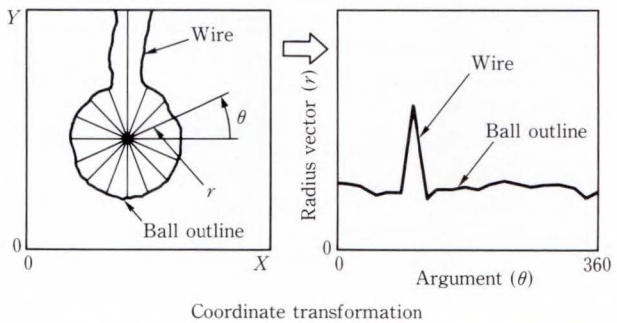

Fig.10–Ball outline detection preprocessing.

ball. In Fig. 10, plane envelopes are made to correspond to ball outlines. The jutting envelope is a wire outline. The solution to the problem of deleting the wire pattern is to delete the large convex of the envelope.

To distinguish the ball outline from the wire image, a morphological transformation[6)-9)] is used, called opening. Opening compares an object pattern with a disk structuring element and removes the sharp convex part where the outline does not fit the structuring element.

Figure 11 shows ball outline reconstruction. Applying this to polar coordinates, the disk structuring element rolls beneath the envelope of the ball outline. The transformed edge in polar coordinates is transformed back to orthogonal coordinates, reconstructing only the ball outline. The ball shape is then inspected by measuring the ball diameters in all directions.

4.2 Flexible wire shape inspection algorithm

The authors used the border following technique to inspect the wire shape (see Fig. 12). Masks consisting of a 3 x 3 pixel matrix detect the right and left border locations. The current left border position is pixel L. The next border position is detected by checking the contents of the pixels in the matrix. The pixel is checked counterclockwise starting from the last border pixel L'. Position 5, where the space changes to the pattern, is detected as the next border position in this case. The position of the right border is detected the same way in the clockwise direction.

The wire width, the distance between neighboring wires, and deviation from the standard line are calculated during border following. The distance is checked against the standard at every line, and wires that are either shorted or too close together are detected. Deviation is checked to detect broken wires, lifted balls, and lifted crescents. Missing wires are detected at the beginning of border following.

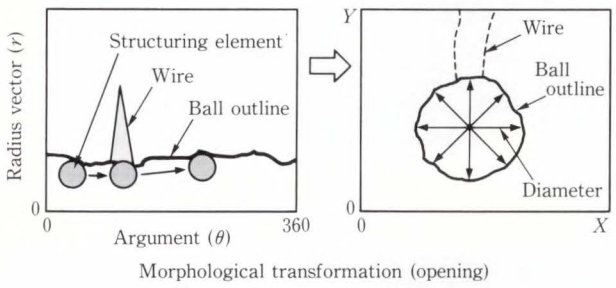

Fig.11—Morphological ball outline reconstruction.

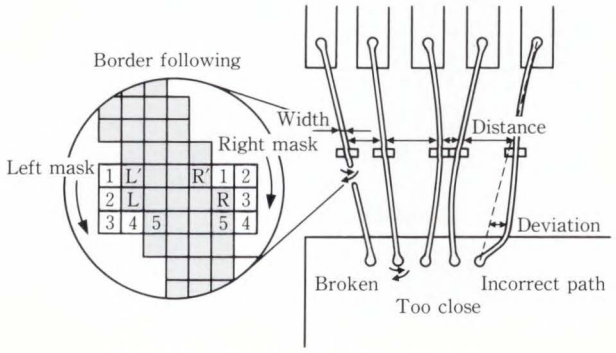

Fig.12—Wire inspection algorithm.

4.3 Results

The results of the ball measurement algorithm and wire inspection algorithm are given below.

Figure 13 shows an original image and its interpolated image. The original image, Fig. 13a), is a 256-level image of the bonding ball on the pad, magnified four times. The resolution of the original image is 10 μm. The interpolated image, Fig. 13b), is obtained by using bilinear interpolation. The gray-level values on every 2.5 μm grid are computed from the values of the neighboring pixels.

Figure 14 shows an example of the ball outline reconstruction process. Figure 14a) is the gray level representation of the interpolated

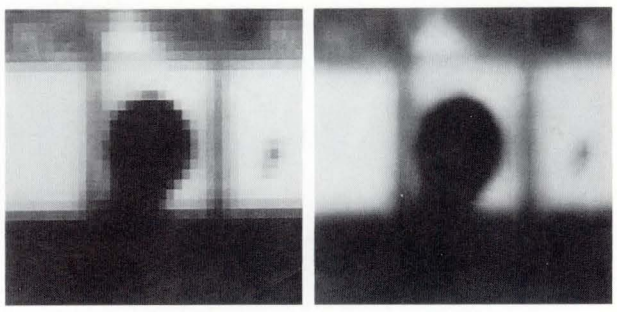

a) Original image b) Interpolated image

Fig.13—Pixel interpolation.

image. The resolution is 100 x 100, coded in 8 bits. Figure 14b) shows the second-derivative image, obtained by applying a 3 x 3 Laplacian mask to Fig. 14a). Figure 14c) shows the zero-crossings detected at quarter-pixel accuracy. These zero-crossings indicate the pad, wire, and ball outlines. Figure 14d) shows the coordinate transformation of the ball zero-crossings. The radius vectors represent the lines radiating from bell center to the zero-crossings on the ball outline. Figure 14e) shows the results of ball outline reconstruction, obtained by applying morphological opening operators to the polar coordinates. The cross in Fig. 14e) is the ball center detected from the ball outline. Finally, the ball diameters are measured by using the reconstructed outlines and the detected center.

The experimental results for ball measurement indicate that the measurement algorithm measured the ball diameters to an accuracy of ±5 μm (see Fig. 15).

Figure 16 shows some examples of defective wires detected by the wire inspection algorithm. In these applications, three wires are inspected at a time. While following the wire borders, the wire width and the distance between wires are measured. Figure 16a) shows a broken wire. The mark indicates where the wire width became zero in the middle of the wire. Figure 16b)

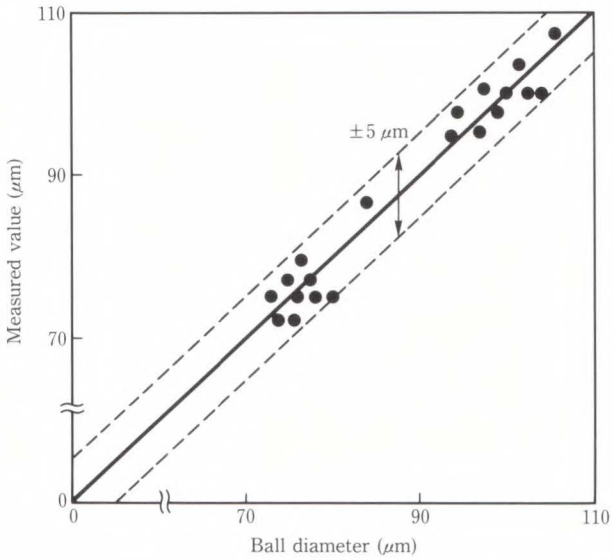

Fig.15—Ball measurement accuracy.

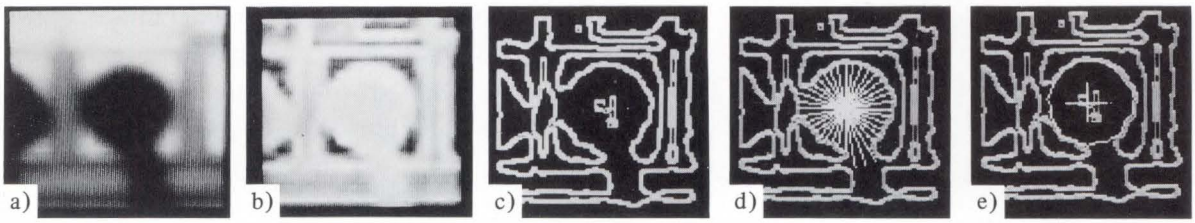

Fig.14—Ball outline reconstruction.

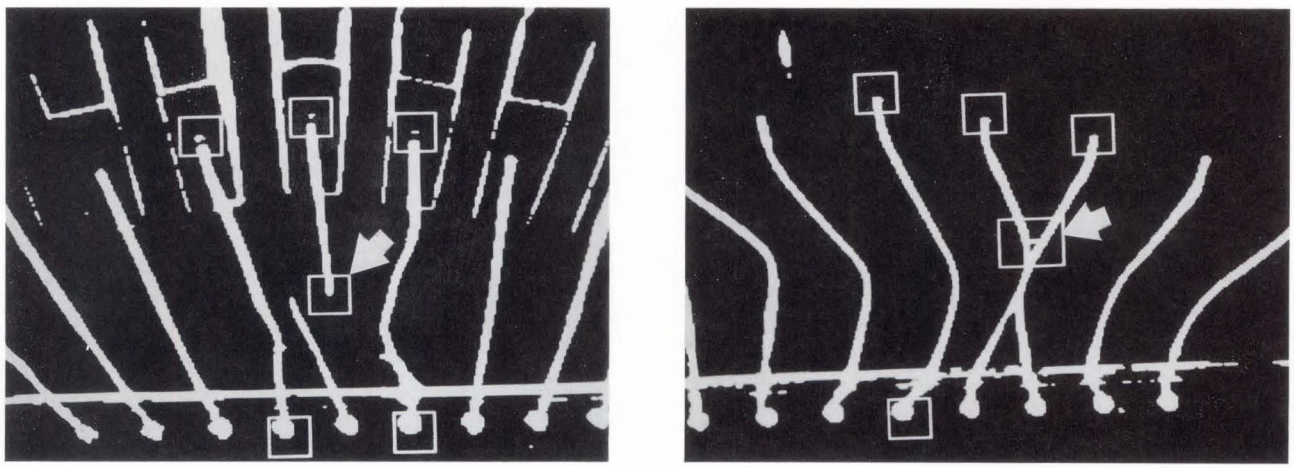

a) Broken wire

b) Shorted wires

Fig.16—Detected wiring defects.

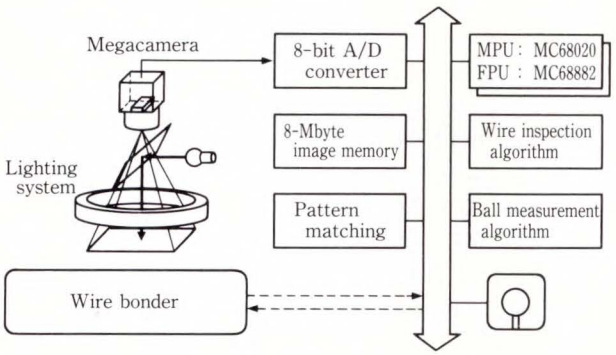

Fig. 17—System configuration.

shows shorted wires. The mark indicates where the distance between neighboring wires became zero.

5. Automated inspection system

5.1 System configuration

In the system configuration, the mega-camera captures the wire image by side illumination and the ball pattern by vertical illumination (see Fig. 17). The video signal is converted by an 8-bit analog-digital converter. Of the total 8-Mbyte image memory, 4 Mbytes are used for wire images and 4 Mbytes for ball images. The system is controlled by 32-bit microprocessors and co-processors. The wire bonder and inspection system exchange bonding addresses and bonding quality. The wire bonder parameters can be adjusted based on the bonding quality.

Figure 18 shows the wire inspection system. A wire bonder can be combined with a frame feeder. A CRT displays inspection results.

5.2 Specifications

The system is used to inspect bonded wires on lead-frame ICs and can detect wires which are broken, too close together or shorted. The system can also detect incorrect wiring, deformed balls, and incorrect ball placement. Bonding reliability is calculated by measuring the size and shape of the deformed balls. The measurement accuracy is ±5 μm which corresponds to half a pixel. It takes 0.2 seconds to inspect each wire (see Table 2).

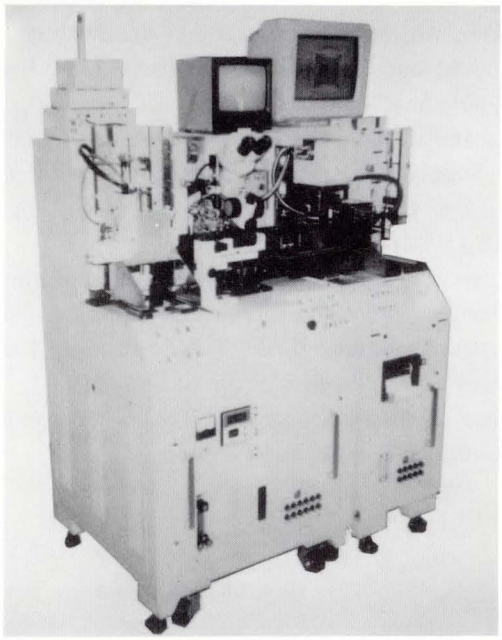

Fig. 18—Wire inspection system.

Table 2. Specifications

Object	Bonded wires on lead frame IC
Defects	Wires that are broken, too close together, or shorted; incorrect wiring; deformed balls; and incorrect ball placement
Quality	Ball size and shape
Accuracy	±5 μm
Time	0.2 s/wire

6. Conclusion

This automated visual inspection system uses high-contrast imaging, an accurate measurement algorithm, and a versatile wire shape inspection algorithm. It can inspect a wire in 0.2 seconds and can work in unison with the wire bonder. A fully automatic bonding system can be constructed by combining this inspection system with a wire bonder.

References

1) Tsukahara, H., Nakashima, M., and Inagaki, T.: Automatic Visual Inspection System for IC Bonding Wires. Proc. SPIE, Hybrid Image and Signal Processing, **939**, Florida, 1988, pp. 140-146.
2) Tsukahara, H., Nakashima, M., and Sugawara, T.: Automated Visual Inspection System for IC bond-

ing Wires Using Morphological Processing. Proc. SPIE, High-Speed Inspection Architectures, Bar Coding, and Character Recognition, **1384**, Boston, 1990, pp. 15-26.
3) Tabatabai, A.J., and Mitchell, O.R.: Edge Location to Subpixel Values in Digital Imagery. *IEEE Trans. Pattern Anal. & Mach. Intell.*, **PAMI-6**, 2, pp.188-201 (1984).
4) Huertas, A., and Medioni, G.: Detection of Intensity Changes with Subpixel Accuracy Using Laplacian-Gaussian Masks. *IEEE Trans. Pattern Anal. & Mach. Intell.*, **PAMI-8**, 5, pp. 651-664 (1986).
5) Marr, D.: Vision. 1st ed., Tokyo, Sangyo-Tosho Publishing Co., Ltd., 1987, 448p.
6) Serra, J.: Image analysis and mathematical morphology. 1st ed., London, Academic press inc., 1982, 610p.
7) Haralick, R.M., Sternberg, S.R., and Zhuang, X.: Image Analysis Using Mathematical Morphology. *IEEE Trans. Pattern Anal. & Mach. Inrell.*, **PAMI-9**, 4, pp. 532-550 (1987).
8) Vogt, R.C.: Formalized Approaches to Image Algorithm Development Using Mathematical Morphology. Proc. VISION '86 Conf., Detroit. 1986, pp. 5.17-5.37.
9) Esselman, T.R., and Verly, J.G.: Some applications of mathematical morphology to range imagery. Proc. ICASSP, Dallas, 1987, pp. 7.10.2-7.10.4.

Hiroyuki Tsukahara
Sensing Technology and Robotics Laboratory
FUJITSU LABORATORIES, ATSUGI
Bachelor of Communications Eng.
The University of Electro-Communications 1981
Specializing in Sensing Technology and Image Processing

Masato Nakashima
Holography and Color-Imaging Laboratory
FUJITSU LABORATORIES, ATSUGI
Bachelor of Chemistry
Tohoku University 1969
Specializing in Sensing Technology and Image Processing

Takehisa Sugawara
Equipment Development Dept.
FUJITSU VLSI LIMITED
Bachelor of Precision Machine Eng.
Ibaragi University 1965
Specializing in Development of Machine Vision Systems for IC Assembly Equipment

UDC 577.322:681.32

Low Drive Voltage and Low Chirp Modulator Integrated DFB Laser Light Source for Multiple-gigabit Systems

• Toru Watanabe • Keiji Sato • Haruhisa Soda

(Manuscript received November 1, 1991)

This paper discusses a low drive voltage and low chirp modulator integrated DFB laser (MI-DFB laser). In this research, the composition of the absorption layer was adjusted experimentally to obtain a low drive voltage, and the absorption layer thickness was analytically optimized. The drive voltage for an extinction ratio of -13 dB is found to be -3 V, which is small enough for high-speed IC drivers. A SiN film on the front facet is optimized for an antireflective (AR) coat, and gives a low chirp width of 0.016 nm at -15 dB (0.004 nm at -3 dB) under 10 Gbit/s NRZ pseudo random modulation. The low drive voltage and low chirp performance is promising for use in the next generation of multiple-gigabit long-haul optical fiber transmission systems.

1. Introduction

Current fiber optic transmission systems directly modulate the intensity of DFB lasers. Directly modulated DFB lasers exhibit large wavelength chirp caused by relaxation oscillation. This large chirp limits the bit-rate and span product because of the dispersion of a fiber. But, due to the need to transmit increasing amounts of information, multiple-gigabit optical fiber transmission systems are in demand. To achieve multiple gigabit transmission over large distances, low-chirp light sources are essential. An MI-DFB laser is a promising device for reducing the chirp because it has an external modulation scheme which gives very low chirp.

The authors previously reported the MI-DFB laser having an absorption layer whose photoluminescence (PL) wavelength was 1.4 μm[1]. The device had a drive voltage of -5 V and a chirp width of 0.01 nm at 3 dB down. This drive voltage of -5 V is high for practical use. Although a chirp width of 0.01 nm is lower than that in a directly modulated laser (LD), it is not sufficient for long-haul and multiple-gigabit transmissions. Therefore, a reduction in the drive voltage and in the chirp are important for multiple-gigabit optical fiber transmissions.

This paper describes the design for a low drive voltage and a low chirp width, and then discusses the performance of the improved MI-DFB laser.

2. Structure

A schematic structure of the device is shown in Fig. 1. The monolithic device has three regions on one n-InP substrate. To operate the device, a constant current is injected into the DFB laser (EA-MOD) region and a modulated voltage is applied to the electro-absorption modulator (DA-MOD) region. The DFB-LD region is 300 μm long and the EA-MOD region is 200 μm long. A buffer region was introduced without a contact layer between the DFB-LD region and the EA-MOD region for electric isolation. A good optical coupling between the DFB-LD region and the EA-MOD region was

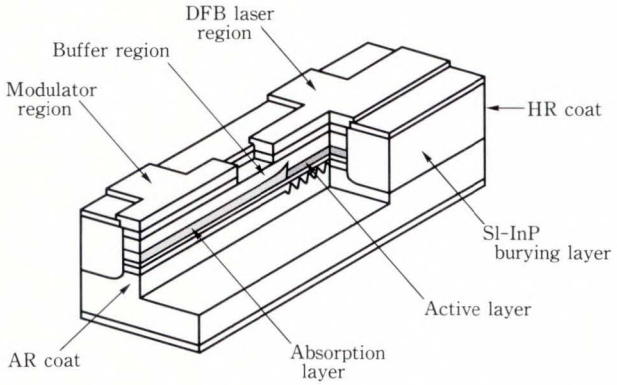

Fig. 1—Schematic structure of the MI-DFB laser.

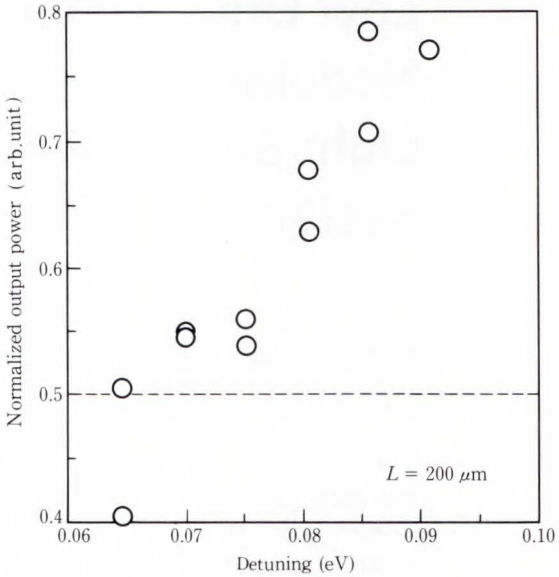

Fig. 2—Loss of waveguide under no applied voltage.

achieved by the butt-joined waveguide. The stripe was buried with semi-insulating InP for low parasitic capacitance[1].

The front facet was coated with a SiN film to reduce reflectivity. The reduced reflectivity gives a flat frequency response and low chirp width without any influence from the relaxation oscillation of the laser region[2]. The back facet was coated with two pairs of SiO_2 film and an amorphous Si film for a high reflective (HR) coat to achieve high slope efficiency and large side-mode suppression.

3. Design for low operating voltage

The EA-MOD uses the Frantz-Keldysh effect, which is photon absorption assisted by tunneling electrons under an electric field[3]. This effect is enhanced by both small detuning between the photon energy and the band gap energy, and a large applied field. Taking this into consideration, the authors designed the composition and the thickness of the absorption layer to obtain a low drive voltage.

Detuning between the light energy and band gap energy introduces a trade-off between high output power and low drive voltage. This is because as detuning decreases, the absorption loss under no applied voltage increases.

Firstly, the composition of the absorption layer was chosen considering the output light power. The authors experimentally evaluated the absorption loss of a solitary EA-MOD whose both facets were cleaved. The reflectivity of the facet was estimated to be 31 percent. The length of the waveguide was 200 μm. The absorption layer had a PL wavelength of 1.4 μm. Transmission light power was measured through the EA-MOD waveguide changing the incident light wavelength with an F-center laser. The absorption loss was calculated from this spectrum using Hakki and Paoli's method[4].

These results indicate that the absorption loss increases as the detuning between the band gap energy of an absorption layer and light energy decreases (see Fig. 2). A PL wavelength of 1.40 μm for a light wavelength of 1.55 μm corresponds to a detuning of 0.08 eV, and is expected to have a loss of 30 percent. For this result and the previous data of the 1.4-μm absorption layer[1], the average effective output power from the DFB region is expected to be 14 mW at 150 mA. When the detuning is 0.067 eV, the output power from DFB region is halved to 7 mW at the front facet.

If detuning is smaller than 0.067 eV, the output power is too small for practical use. Detuning of 0.067 eV is equivalent to a PL wavelength of 1.43 μm for light wavelength of 1.55 μm. Because the detuning for a PL wavelength of 1.43 μm is smaller than that for a 1.4 μm absorption layer which has a drive voltage of -5 V, the drive voltage of EA-MOD having a 1.43-μm absorption layer is expected to be lower than -5 V[1]. Thus the PL wavelength of

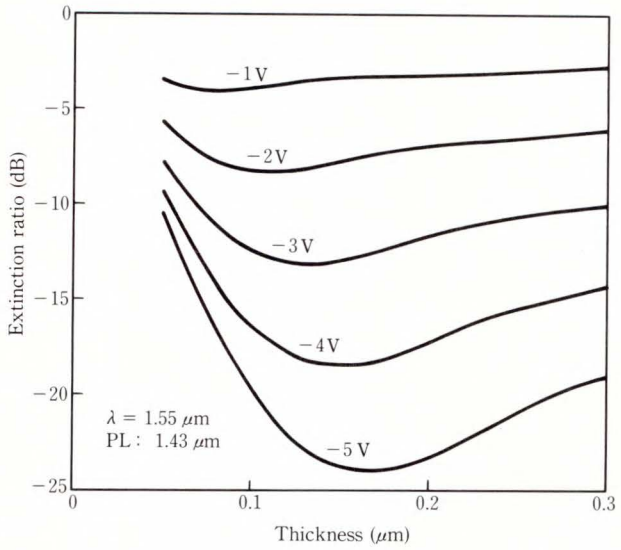

Fig. 3—Dependence of extinction ratio on the thickness of the absorption layser.

the absorption layer was fixed to 1.43 μm[5].

The authors then calculated the dependence of the extinction ratio on the absorption layer thickness in an EA-MOD taking account of the applied electric field and optical field. The device model for this calculation was solitary two dimensional EA-MOD. The thickness and PL wavelength of the InGaAsP guide layer model was assumed to be 0.15 μm and 1.1 μm respectively. Concentration of the p-clad layer was 5×10^{17} cm^{-3}, and one of the n-substrates was 2×10^{18} cm^{-3}. The incident light wavelength was 1.55 μm. Under these conditions, the applied electric field was obtained by solving the Poisson equation. From the applied electric field, the envelope carrier wavefunction was calculated. The wavefunction was expressed with the Airy function. The absorption coefficient was obtained from the wavefunction and the optical field[3].

Figure 3 shows the results of the calculations. If the layer is too thin, a small light confinement in absorption layer reduces the extinction ratio. However, if the layer is too thick, the absorption is also reduced because the electric field applied to the absorption layer is weak. According to the above results, the operating voltage is expected to be -3 V when the PL wavelength of the absorption layer is 1.43 μm and the thickness is 0.13 μm.

4. Design for low chirp characteristic

Practical MI-DFB lasers have a finite front facet reflectivity. A feedback light does greatly affect the lasing condition of a DFB laser. Therefore the authors modelled the MI-DFB laser to be equivalent to a DFB laser whose complex front facet reflectivity is changed by applying a voltage to be EA-MOD region. The complex front facet reflectivity is represented by an absorption coefficient, the reflectivity of the real front facet, and a light wave propagation constant in the EA-MOD region.

To analyze the chirp behavior of the DFB laser, the authors calculated the dependence of the lasing wavelength on DC applied voltage, and then applied these results to the chirp behavior with a frequency response of the wavelength shift[6]. To calculate a lasing wavelength change for an extinction ratio of -10 dB, the authors considered the change in complex front reflectivity, the threshold carrier density in the DFB-LD region, and κL, where κ is the coupling coefficient of the corrugation and L is the length of the DFB-LD region. The frequency response is calculated by rate equations which included a photon lifetime modulation scheme. The α-parameter of the EA-MOD region and the DFB-LD region was 1[7] and 4 respectively. Heat effects were neglected.

According to the calculated frequency response of a lasing wavelength shift, the chirp behavior under modulation was almost the same as the dependence of the lasing wavelength on DC voltage applied to the EA-MOD region, when the relaxation frequency of the DFB-LD region was sufficiently higher than the modulation frequency. The calculated chirp behavior agreed well with observed temporal behaviors using the streak camera system[6]. Therefore, the calculation is valid for designing low-chirp devices.

As the lasing wavelength depends on the facet phases, the low-chirp operation was estimated using the yield of a wavelength shift for -10 dB DC attenuation. The chirp was found to decrease as the front facet reflectivity decreased and as κL increased. However a large κL induces multi-mode operation due to a strong spatial hole burning[8], and there is difficulty in

achieving a reflectivity of less than 0.1 percent using conventional techniques. Then according to the above analysis, a κL of 1.5 and a reflectivity of 0.1 percent was used because the yield of the maximum wavelength shift of less than 0.01 nm was estimated to be over 50 percent.

5. Fabrication

The device was fabricated in four steps, three of which were liquid phase epitaxy (LPE) and one of which was metalorganic vapor phase epitaxy (MOVPE) as shown in Fig. 4[1].

First, the DFB-LD region was fabricated. The first order corrugation for a wavelength of 1.55 μm was fabricated partially on the substrate of the DFB-LD area. Next, a guide layer, a thin InP etch-arresting layer, an active layer, and a clad layer were fabricated with LPE. The guide layer and the active layer were InGaAsP having a PL wavelength of 1.1 μm and 1.54 μm respectively. The clad layer and the etch-arresting layer were InP.

Next the EA-MOD region was fabricated. The clad and the active layer on the EA-MOD area were etched off using a SiO_2 mask over the DFB-LD area. The guide layer was left selectively because of the etch-arresting layer. After etching, an InGaAsP absorption layer having a PL wavelength of 1.43 μm and an InP clad layer were refabricated using LPE. A p-clad layer and a contact layer were fabricated entirely using LPE after removing the SiO_2 mask over the DFB-LD area.

Next a stripe structure was fabricated with selective etching on both the DFB-LD and the EA-MOD parts using the same SiO_2 mask. This stripe was buried in semi-insulate InP using MOVPE. Next the clad layer in the joint area was removed to establish sufficient electrical isolation. The resistance was 2 MΩ by removing the contact layer at the region.

Finally SiN film was fabricated on the front facet using a well-controlled deposition process. To achieve a reflectivity of 0.1 percent, the authors optimized the thickness of the SiN film on the front facet, taking into account again the two-dimensional optical field and the refractive index of the absorption layer whose PL wavelength was 1.43 μm.

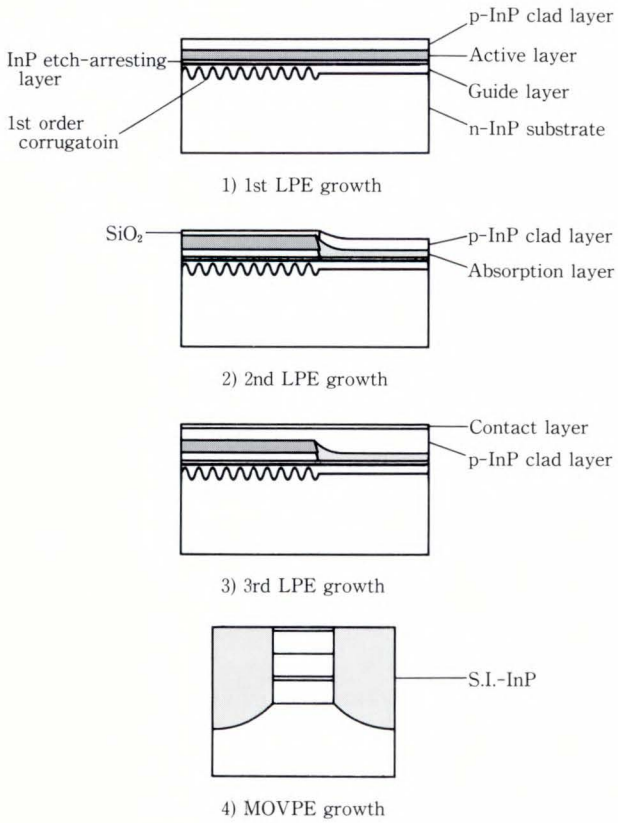

Fig. 4—Growth procedure.

6. Characteristics

Figure 5 shows the total light output power versus the injection current characteristic. The threshold current of the device is 24 mA. Out-

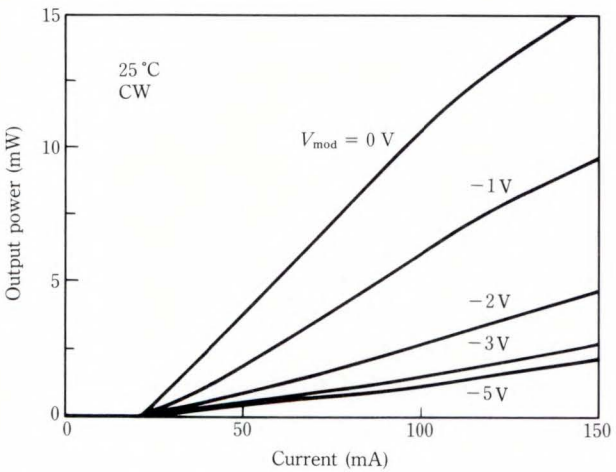

Fig. 5—Dependence of total light output power on the applied voltage.

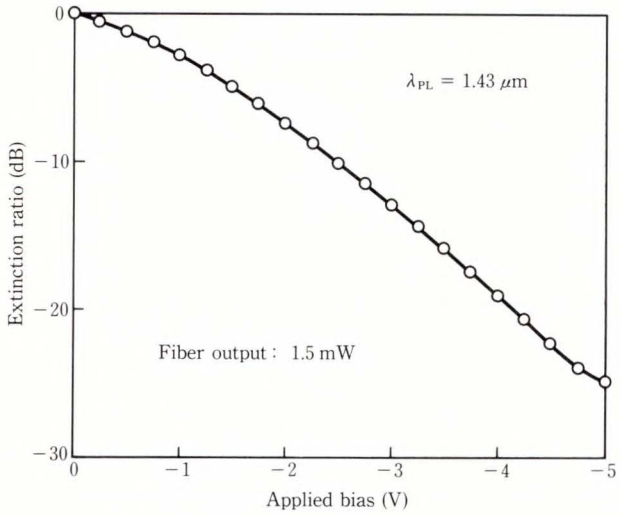

Fig. 6—Extinction ratio of fiber coupled power.

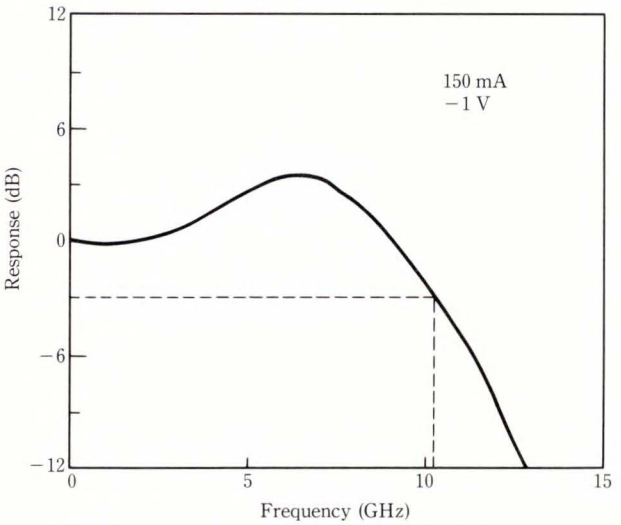

Fig. 7—Small signal frequency response.

put power is 11 mW at 100 mA. The slope efficiency is 0.14 mW/mA. The total output power from the front facet includes the leak power and the guided power. The guided power is almost all absorbed under enough applied voltage, about -5 V, and most of the other power is the leak power. The coupling efficiency is estimated to be 90 percent from the output power at no applied voltage and one at -5 V. The effective output power is 10 mW at 100 mA. These values are comparable to those of the previously reported device[1].

Only the effective guided power can coupled with fiber. The fiber output power is 1.5 mW. The extinction ratio of the fiber coupled output power is shown in Fig. 6. The required voltage for the extinction ratio of -13 dB is only -3 V[5]. These results almost agree with the calculated extinction ratio of a solitary EA-MOD. This is a significant improvement over the previous result[1].

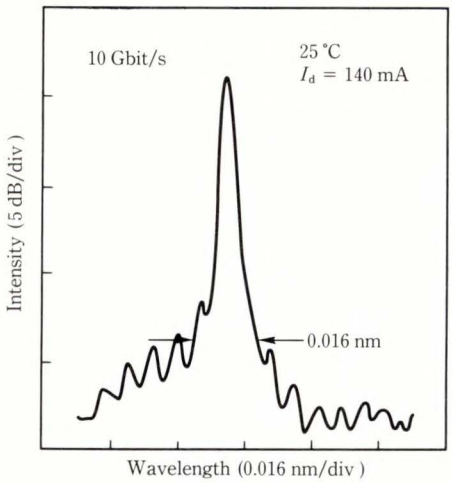

Fig. 8—Light spectrum under 10 Gbit/s NRZ random modulation.

Figure 7 shows the small signal frequency response under an applied voltage of -1 V and an injection current of 150 mA. The cutoff frequency is 10.3 GHz, which is almost equal to the estimated cutoff frequency of the parasitic capacitance of 0.55 pF.

Figure 8 shows the spectrum of the device under 10 Gbit/s NRZ pseudo random modulation. The measured chirp width at 15 dB down is only 0.016 nm (0.004 nm at -3 dB). This is a drastic reduction of the chirp of 0.4 to 0.8 nm in direct modulation of a DFB-LD.

The temporary wavelength chirp is also important for optical transmission. Figure 9 shows the temporary image of the wavelength chirp under 10 Gbit/s NRZ (1,0) fixed pattern. The current injected to the DFB-LD region is 100 mA. The shift width of the chirp is very small.

Figure 10 shows the eye pattern of the integrated device under 10 Gbit/s NRZ pseudo random modulation. The eye pattern of the integrated device has no peaking and no jitter. These results indicate that the integrated device can be used in high bit-rate long-haul systems.

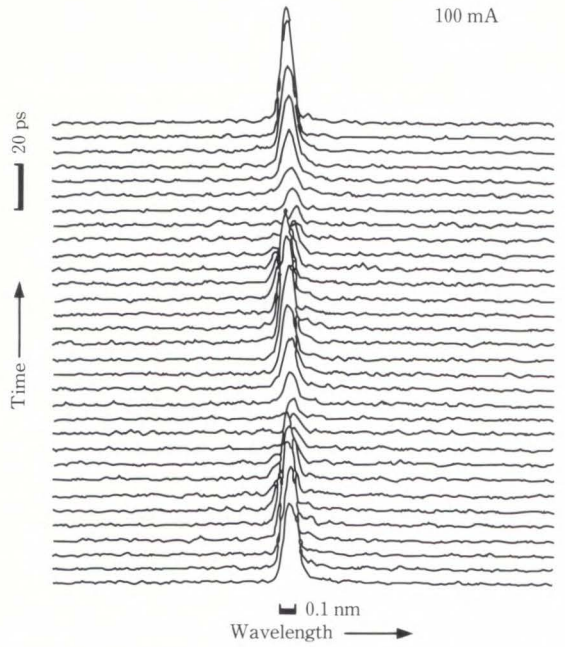

Fig. 9—Temporary image of wavelength chirping at 10 Gbit/s (1,0) fixed modulation.

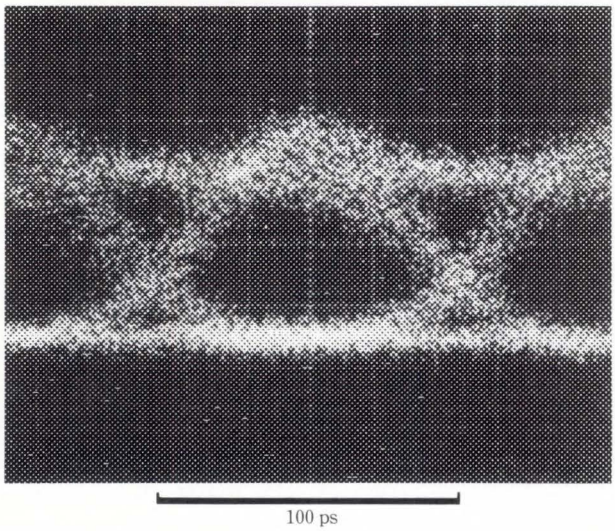

Fig. 10—Eye pattern at 10 Gbit/s NRZ random modulation.

7. The transmission span

The authors considered a tolerable dispersion in transmission for the optimized MI-DFB laser. Okiyama et. al. previously reported bit error rate (BER) characteristics using our previous MI-DFB laser for 10 Gbit/s transmission over 64.8 km of dispersion shift fiber[8]. This MI-DFB laser had a large chirp width of 0.01 nm at 3 dB down, but there was no power penalty for a dispersion of 63 ps/nm.

A tolerable dispersion for a power penalty of 0.5 dB was estimated to be 230 ps/nm. The newly developed MI-DFB laser has a very low chirp width of 0.016 nm at -15 dB (0.004 nm at -3 dB). The measured chirp width is drastically reduced compared to that of the previous MI-DFB laser' Therefore a tolerable dispersion of much larger than 230 ps/nm can be expected for the latest ultra-low chirp MI-DFB.

8. Conclusion

This report discusses a low drive voltage and low chirp modulator integrated DFB laser. The authors optimized the composition and thickness of the absorption layer taking into account the absorption loss and absorption efficiency.

As a result, the effective output power was 10 mW at an injection current of 100 mA, and the extinction ratio was -13 dB at -3 V. A drive voltage of -3 V is usable for practical systems. The AR film on a front facet was optimized taking account of the two-dimensional optical field and the reflective index of the optimized absorption layer. The optimization of AR film gives a chirp of 0.016 nm at -15 dB under 10 Gbit/s NRZ pseudo random modulation. This low chirp is acceptable for a dispersion of larger than 230 ps/nm with 10 Gbit/s NRZ pseudo random modulation.

The new MI-DFB laser having low drive voltage and low chirp performance is promising for use in the generation of multiple-gigabit, long-haul optical fiber transmission systems.

References

1) Soda, H., Furutsu, M., Sato, K., Okazaki, N., Yamazaki, S., Nishimoto, H., and Ishikawa, H.: High-power and high-speed semi-insulating BH structure monolithic electroabsorption modulator/DFB laser light source. *Electron. Lett.*, **26**, 1, pp. 9-10 (1990).

2) Ishikawa, H., Soda, H., Watanabe, T., Sudo, H., and Sato, K.: Low-threshold current and high-efficiency operation of electro-absorption modulator/DFB laser light source with AR-HR coating. Proc. IEEE Int. Semiconductor Laser Conf. K-6. Switz., 1990, pp. 170-171.

3) Tharamalingam, K.: Optical absorption in the presence of uniform field. *Phys. Rev.*, **130**, 6, pp. 2204-2206 (1963).
4) Hakki, B. W., and Paoli, T.L.: CW degration at 300 k of GaAs double-heterostructure junction lasers, 2. Electric gain. *J. Appl. Phys.*, **44**, 9, pp. 4113-4119 (1973).
5) Soda, H., Furutsu, M., Sato, K., Okazaki, N., Yamazaki, S., and Ishikawa, H.: Low drive voltage semi-insulating BH structure monolithic electro-absorption modulator/DFB laser light source. Proc. OFC '90 TH12, 1990, pp. 180-180.
6) Soda, H., Sato, K., Sudo, H., Takeuchi, H., and Ishikawa, H.: Ultra-low chirp characteristics of monolithic electro-absorption modulator/DFB laser light sources. Proc. ECOC '91 WeB7-2, 1991, pp. 433-436.
7) Soda, H., Sato, K., Nakai, K., Ishikawa, H., and Imai, H.: Chirp behavior of high-speed GaInAsP/InP optical intensity modulator. *Electron. Lett.*, **24**, 19, pp. 1194-1195 (1988).
8) Soda, H., Kotaki, Y., Sudo, H., Ishikawa, H., Yamakosi, S., and Imai, H.: Stability in Single Longitudinal Mode Operation in GaInAsP/InP Phase-Adjusted DFB Lasers. *IEEE J. Quantum Electronics.*, **QE-23**, 6, pp. 804-814 (1987).
9) Okiyama, T., Yokota, I., Nishimoto, H., Hironoshi, K., Horimatsu, T., Tongue, T., and Soda, H.: A 10-Gbit/s, 65-km optical fiber transmission experiment using a monolithic electro-absorption modulator/DFB laser light source. Proc. ECOC '89 MoA1-3, 1989, pp. 1-3.

Toru Watanabe
Optical Semiconductor Devices Laboratory
FUJITSU LABORATORIES, ATSUGI
Bachelor of Applied Phisics Eng.
Tohoku University 1986
Master of Applied Physics Eng.
Tohoku University 1988
Specializing in Semiconductor Lasers

Keiji Sato
Optical Semiconductor Devices Laboratory
FUJITSU LABORATORIES, ATSUGI
FUJITSU Technical College 1990
Specializing in Semiconductor Lasers

Haruhisa Soda
Optical Semiconductor Devices Laboratory
FUJITSU LABORATORIES, ATSUGI
Bachelor of Physical Electronics Eng.
Tokyo Institute of Technology 1978
Dr. of Engineering Eng.
Tokyo Institute of Technology 1983
Specializing in Semiconductor Lasers

International Network

Offices

Abu Dhabi Office
P.O. Box 47047 Suite 802.
A1 Masadood Tower, Sheikh Hamdan Street, Abu Dhabi. U.A.E.
Telephone : (971-2)-333440
FAX : (971-2)-333436

Algiers Office
9 Rue Louis Rougie Chateau Neuf.
El Biar, Alger 16030. Algeria
Telephone : (213)-2-78-5542
Telex : 408-67522

Amman Project Office
P.O. Box 5420, Ammán. Jordan
Telephone : (962)-6-662417
FAX : (962)-6-673275

Bangkok Office
3rd Floor, Dusit
Thani Bldg., 1-3, Rama IV.
Bangkok10500, Thailand
Telephone : (66-2)-236-7930
FAX : (66-2)-238-3666

Beijing Office
Room 2101, Fortune Building,
5 Dong San Huan Bei-lu,
Chao Yang District, Beijing,
People's Republic of China
Telephone : (86-1)-501-3261
FAX : (86-1)-501-3260

Sucursal de Colombia
Cra. 13 No. 27-50.
Edificio Centro Internacional
Tequendama, Oficina 326/328
Bogotá. D.E. Colombia
Telephone : (57-1)-286-7061
FAX : (57-1)-286-7148

Brussels Office
Avenue Louise 176, Bte 2
1050 Brussels, Belgium
Telephone : (32-2)-648-7622
FAX : (32-2)-648-6876

Hawaii Branch
6660 Hawaii Kai Drive, Honolulu,
Hawaii 96825, U.S.A.
Telephone : (1-808)-395-2314
FAX : (1-808)-396-7111

Indonesia Project Office
16th Floor, Skyline Bldg.,
Jalan M.H. Thamrin No.9,
Jakarta, Indonesia
Telephone : (62-21)-3105710
FAX : (62-21)-3105712

Jakarta Representative Office
16th Floor, Skyline Bldg.,
Jalan M.H. Thamrin No.9,
Jakarta, Indonesia
Telephone : (62-21)-333245
FAX : (62-21)-327904

Kuala Lumpur Office
Letter Box No.47, 22nd Floor,
UBN Tower No.10, Jalan P.
Ramlee, 50250, Kuala Lumpur,
Malaysia
Telephone:(60-3)-238-4870
FAX : (60-3)-238-4869

Munich Office
c/o Siemens Nixdorf Informationsysteme
AG, D8 SC,
Otto-Hang Ring 6, D-8000,
München 83, F.R. Germany
Telephone:(49-89)-636-3244
FAX : (49-89)-636-45345

New Delhi Liaison Office
1st Floor, 15 Katsurba
Gandhi Marg
New Delhi-110001, India
Telephone : (91-11)-331-1311
FAX : (91-11)-332-1321

New York Office
680 Fifth Avenue, New York,
N.Y. 10019, U.S.A.
Telephone : (1-212)-265-5360
FAX : (1-212)-541-9071

Paris Office
Bâtiment Aristote,
Rue Olof Palme 94006,
Creteil Cedex, France
Telephone : (33-1)-4-399-0897
FAX : (33-1)-4-399-0700

Shanghai Office
Room 1504, Ruijin Bldg.,
205 Maoming Road South,
Shanghai, People's Republic of China
Telephone : (86-21)-433-6462
FAX : (86-21)-433-6480

Taipei Office
Sunglow Bldg., 66, Sung Chiang Road, Taipei, Taiwan
Telephone : (886-2)-551-0233
FAX : (886-2)-536-7454

Washington, D.C. Office
1776 Eye Street, N.W.,
Suite 880, Washington, D.C.,
20006, U.S.A.
Telephone : (1-202)-331-8750
FAX : (1-202)-331-8797

Subsidiaries

ASIA AND OCEANIA

Fujitsu Australia Ltd.
Fujitsu Australia Software Technology. Pty. Ltd.
Fujitsu Component(Malaysia)Sdn. Bhd.
Fujitsu Electronics(Singapore)Pte. Ltd.
Fujitsu Hong Kong Ltd.
Fujitsu Korea Ltd.
Fujitsu Microelectronics Asia Pte. Ltd.
Fujitsu Microelectronics(Malaysia)Sdn. Bhd.
Fujitsu Microelectronics Pacific Asia Ltd.
Fujitsu New Zealand Ltd.
Fujitsu(Singapore)Pte. Ltd.
Fujitsu(Thailand)Co., Ltd.
Fujitsu Trading Ltd.

NORTH AMERICA

Fujitsu America, Inc.
Fujitsu Business Communication Systems, Inc.
Fujitsu Canada, Inc.
Fujitsu Computer Packaging Technologies, Inc.
Fujitsu Computer Products of America, Inc.
Fujitsu Customer Service of America, Inc.
Fujitsu Imaging Systems of America, Inc.
Fujitsu Microelectronics, Inc.
Fujitsu Network Switching of America, Inc.
Fujitsu Network Transmission Systems, Inc.
Fujitsu Systems Business of America, Inc.
Fujitsu Systems of America, Inc.
Intellistor, Inc.
Open Systems Solutions, Inc.
Poqet Computer Corp.

EUROPE

Fujitsu Deutschland GmbH.
Fujitsu España, S.A.
Fujitsu Europe Ltd.
Fujitsu Europe Telecom R&D Centre Ltd.
Fujitsu Finance(U.K.)PLC
Fujitsu France S.A.
Fujitsu International Finance(Netherlands)B.V.
Fujitsu Italia S.p.A.
Fujitsu Microelectronics Ireland Ltd.
Fujitsu Microelectronics Italia S.r.l.
Fujitsu Microelectronics Ltd.
Fujitsu Mikroelektronik GmbH.
Fujitsu Nordic AB
Fulcrum Communications Ltd.

LATIN AMERICA

Fujitsu Do Brasil Ltda.
Fujitsu Vitória Computadores e Serviços Ltda.

FUJITSU LIMITED

6-1, Marunouchi 1-chome, Chiyoda-ku, Tokyo 100, Japan
Phone: National (03) 3216-3211 International (Int'l Prefix) 81-3-3216-3211 Telex: J22833 Cable: "FUJITSULIMITED TOKYO"